

A SEARCH FOR SUPERSYMMETRY IN EVENTS WITH A Z BOSON,
JETS, AND MISSING TRANSVERSE ENERGY IN $p - p$ COLLISIONS
WITH $\sqrt{s}=13$ TEV WITH THE ATLAS DETECTOR

TOVA RAY HOLMES



Physics Department
University of California, Berkeley

August 2016 – version 1.0

Tova Ray Holmes: *A Search for Supersymmetry in Events with a Z Boson, Jets, and Missing Transverse Energy in $p - p$ Collisions with $\sqrt{s}=13$ TeV with the ATLAS Detector*, © August 2016

ABSTRACT

A search for new phenomena in final states containing a Z boson decaying to electrons or muons, jets, and large missing transverse momentum is presented. This search uses proton–proton collision data collected during 2015 and 2016 at a center of mass energy $\sqrt{s} = 13$ TeV by the ATLAS detector at the Large Hadron Collider, which correspond to an integrated luminosity of 3.3 fb^{-1} . The search targets the pair production of supersymmetric particles, squarks or gluinos, which decay via jets and a Z boson to the lightest Supersymmetric particle, which does not interact with the ATLAS detector. Results are interpreted in simplified models of gluino-pair (squark-pair) production, and provide sensitivity to gluinos (squarks) with masses as large as 1.3 (1.0) TeV.

PUBLICATIONS

Some results and ideas presented have previously appeared in the following publications:

[this_paper]

ACKNOWLEDGEMENTS

Put your acknowledgements here.

CONTENTS

I INTRODUCTION	1
1 INTRODUCTION	3
II THEORY AND MOTIVATION	7
2 THEORY AND MOTIVATION	9
2.1 The Standard Model	9
2.1.1 Matter	9
2.1.2 Forces	11
2.1.3 Phenomenology of Proton-Proton Collisions	20
2.1.4 Problems in the Standard Model	22
2.2 Supersymmetry	24
2.2.1 The Minimal Supersymmetric Standard Model	25
2.2.2 Solutions to Standard Model Problems	27
2.2.3 Simplified Models of Supersymmetry	28
2.3 Monte Carlo Event Generation	30
III THE EXPERIMENT	37
3 THE LARGE HADRON COLLIDER	39
3.1 The Injector Complex	40
3.2 Operation of the Large Hadron Collider	41
3.3 Luminosity	43
3.4 Pile-up in proton-proton Collisions	43
4 THE ATLAS DETECTOR	47
4.1 Coordinate System Used in the ATLAS Detector	47
4.2 The Inner Detector	48
4.2.1 The Pixel Detector	48
4.2.2 The Silicon Microstrip Tracker	50
4.2.3 The Transition Radiation Tracker	50
4.3 The Calorimeters	51
4.4 The Muon Spectrometer	52
4.5 The Magnet System	55
4.6 The Trigger System and Data Acquisition	56
5 OBJECT RECONSTRUCTION IN THE ATLAS DETECTOR	61
5.1 Electrons	61
5.2 Photons	64
5.3 Muons	66
5.4 Jets	68
5.5 Overlap Removal	71
5.6 Missing Transverse Momentum	73
6 APPLICATION OF A NEURAL NETWORK TO PIXEL CLUSTERING	77
6.1 Clustering in the Pixel Detector	77
6.1.1 Charge Interpolation Method	78

6.1.2	Improving Measurement with Neural Networks	78
6.2	Impact of the Neural Network	79
6.2.1	The Neural Network in 13 TeV Data	80
IV	SEARCHING FOR SUPERSYMMETRY	85
7	BACKGROUND PROCESSES	87
7.1	Data and Monte Carlo Samples	89
8	OBJECT IDENTIFICATION AND SELECTION	91
8.1	Electrons	91
8.2	Muons	92
8.3	Jets	92
8.4	Photons	93
9	EVENT SELECTION	95
9.1	Trigger Strategy	96
9.2	Signal Efficiency and Contamination	98
10	BACKGROUND ESTIMATION	101
10.1	Flavor Symmetric Processes	101
10.1.1	Flavor Symmetry Method	101
10.1.2	Sideband Fit Method	103
10.2	Z/γ^* + jets Background	105
10.2.1	Photon and Z Event Selection	107
10.2.2	Smearing of Photon Events	108
10.2.3	p_T Reweighting of Photon Events	110
10.2.4	Determining H_T and $m_{\ell\ell}$	111
10.2.5	Subtraction of $V\gamma$ Events	113
10.2.6	Validation in Data	115
10.3	Fake and Non-Prompt Leptons	117
10.4	Diboson and Rare Top Processes	118
11	SYSTEMATIC UNCERTAINTIES	125
11.1	Uncertainties on Data-Driven Backgrounds	125
11.1.1	Uncertainties on the Flavor Symmetry Method	125
11.1.2	Uncertainties on the γ + jets Method	129
11.1.3	Uncertainties on the Fakes Background	132
11.2	Theoretical and Experimental Uncertainties	133
11.3	Impact of Uncertainties on the Signal Region	134
12	RESULTS	139
13	INTERPRETATIONS	145
V	CONCLUSIONS	149
14	CONCLUSIONS AND OUTLOOK	151
	BIBLIOGRAPHY	153

LIST OF FIGURES

Figure 1	The Standard Model of particle physics, containing all known bosons and fermions, with the addition of the hypothetical graviton. [7]	10
Figure 2	Gluon self coupling Feynman diagrams involving 3- and 4-gluon interactions.	14
Figure 3	Quark couplings to the different types of gauge bosons. The $q_{u,d}$ labels represent any up- or down-type quarks.	14
Figure 4	The running of the strong coupling constant, α_s . [14]	15
Figure 5	Feynman diagrams of trilinear gauge couplings in the Standard Model (SM).	17
Figure 6	Feynman diagrams of weak couplings to leptons in the SM.	18
Figure 7	Feynman diagrams demonstrating Higgs couplings to the weak gauge bosons in the SM.	19
Figure 8	Feynman diagrams showing Higgs couplings to fermions in the SM.	20
Figure 9	2008 MSTW Parton Distribution Functions (PDFs) for various particle types given as a function of x and Q^2 , the square of the parton-parton momentum transfer. [15]	21
Figure 10	Cross-sections for many SM processes at the Tevatron and Large Hadron Collider (LHC) [16].	22
Figure 11	Galactic rotation curve of velocity as a function of radius in NGC 3198. Included is the observed data, as well as the expected velocity distribution from a disk-shaped galaxy corresponding to the expected density from electromagnetic observations. Another curve corresponding to a halo-shaped matter distribution is superimposed, and the halo and disk are summed and fit to the data. [20]	23
Figure 12	Two example vertices allowed by the Minimal Supersymmetric Standard Model (MSSM).	26
Figure 13	Running of the strong, weak, and electromagnetic coupling constants for the SM (left) and MSSM (right). [27]	27
Figure 14	Feynman diagram of the decay considered in the simplified models used in the analysis presented in Part iv.	29
Figure 15	13 TeV production cross-sections for sparticles, as a function of sparticle mass [32].	30

Figure 16	Results of an 8 TeV search performed by the ATLAS collaboration in a signal region targeting events like those in Figure 14. The events in the signal region are displayed as a function of $m_{\ell\ell}$, the invariant mass of the event's leading leptons. The SM backgrounds are shown with their full uncertainties based on data-driven background estimations, and two signals are superimposed on the distribution. The observed datapoints are higher than the expected background, with a total excess of 3.0σ [1].	31
Figure 17	Results of an 8 TeV search performed by the Compact Muon Solenoid (CMS) collaboration in a signal region including a broad range of $m_{\ell\ell}$. A 2.4σ local excess is seen in the low $m_{\ell\ell}$ region, and no excess of events is seen in the region with $m_{\ell\ell}$ consistent with an on-shell Z boson. The data is fit based on a data driven estimate of the flavor symmetric background (FS) and the Drell-Yan background (DY), with an additional component for the signal [34].	32
Figure 18	Preliminary results from a 13 TeV search targeting the same signal region as Figure 16, performed on 3.2 fb^{-1} of 2015 data. The events in the signal region are displayed as a function of $m_{\ell\ell}$, the invariant mass of the event's leading leptons. Flavor symmetric and $Z/\gamma^* + \text{jets}$ backgrounds are taken from data-driven methods, while the other backgrounds are taken from Monte Carlo simulation (MC). They are compared to the data, which shows a 2.2σ excess of events. Distributions from two signal points are superimposed [2].	33
Figure 19	Number of secondary vertices in a module in the first layer of the pixel detector in data (top) and MC (bottom). There are more events in the data than the MC [45].	35
Figure 20	The LHC main collider ring and pre-accelerator Super Proton Synchrotron (SPS) overlaid on a map of Switzerland and France, with the four main LHC experiments identified.	39
Figure 21	The pre-accelerators of the LHC.	40
Figure 22	Bunch structure in the Proton Synchrotron (PS), SPS, and LHC.	41
Figure 23	Cross-section of a cryodipole magnet in the LHC. . .	
Figure 24	Beam spot in the ATLAS detector for one run in 2015. Distributions show only the highest p_T vertex per event. Left is the $x - y$ distribution of vertices, while the right plot shows the $x - z$ distribution. . .	42

Figure 25	Instantaneous luminosity of one fill of 7 TeV data in 2011.	44
Figure 26	ATLAS luminosity for Run 1 and Run 2, as of September 2016.	44
Figure 27	Average number of interactions per crossing shown for 2015 and 2016 separately, as well as the sum of the two years.	45
Figure 28	Diagram of the ATLAS detector, with subsystems and magnets identified.	47
Figure 29	Diagram of the ATLAS Inner Detector, containing the Pixel, SCT, and TRT subsystems.	49
Figure 30	Diagram of one-quarter of the ATLAS Inner Detector in the $R - z$ plane, with lines drawn to indicate various η locations.	50
Figure 31	The calorimeter system of the ATLAS detector.	51
Figure 32	Layout of the LAr calorimeter module at central η [48].	52
Figure 33	An x - y view of the Muon Spectrometer (MS). In it, the three barrel layers are visible, as well as the overlapping, differently sized chambers. The outer layer of the MS is about 20m in diameter.	53
Figure 34	An r - z view of the MS. The three layers of the barrel and endcap MS are visible, and all muons at $ \eta < 2.7$ should traverse three detectors, assuming they propagate in an approximately straight line from the interaction point.	54
Figure 35	The magnet system of the ATLAS detector. The inner cylinder shows the solenoid which gives a uniform magnetic field in the Inner Detector (ID). Outside of that are the barrel and endcap toroids, which provide a non-uniform magnetic field for the MS.	55
Figure 36	Plots of the magnetic field within the ATLAS detector. Top is the field (broken into its R and z components) as a function of z for several different values of R . Bottom is the field integral through the Monitored Drift Tubes (MDTs) as a function of $ \eta $ for two different ϕ values.	57
Figure 37	Level One (L_1) trigger rates for a run in July 2016 as a function of luminosity block, an approximately 60-second long period of data-taking. The total rate is lower than the combined stack because of overlapping triggers.	58
Figure 38	High Level Trigger (HLT) trigger rates for a run in July 2016 as a function of luminosity block, an approximately 60-second long period of data-taking. The total rate is lower than the combined stack because of overlapping triggers.	59

Figure 39	Trigger efficiencies as a function of E_T for data and MC. Efficiencies are given for offline selected loose electrons.	59
Figure 40	Identification efficiencies from MC samples for Loose, Medium, and Tight working points. Left is the efficiency for identification of true electrons taken from $Z \rightarrow ee$ MC, and right is the efficiency for misidentification of jets as electrons taken from dijet MC [54].	62
Figure 41	Combined electron reconstruction and identification efficiencies measured as a function of η for data (using the tag-and-probe method on $Z \rightarrow ee$ events) and $Z \rightarrow ee$ MC. Distributions include all electrons with $E_T > 15$ GeV. [54].	63
Figure 42	Comparison of Tight identification efficiency measurements from data and $Z \rightarrow \ell\ell\gamma$ MC for unconverted (left) and converted (right) photons, with an inclusive η selection. The bottom of each figure shows the ratio of data and MC efficiencies. [57].	65
Figure 43	Muon reconstruction efficiency for the Medium and (for small $ \eta $) Loose working points measured with $Z \rightarrow \mu\mu$ events in data using the tag-and-probe method and in MC as a function of η . The ratio between the two is shown at the bottom. [59]	67
Figure 44	Muon reconstruction efficiency for the High- p_T working point measured with $Z \rightarrow \mu\mu$ events in data using the tag-and-probe method and in MC as a function of η . The ratio between the two is shown at the bottom. [59]	68
Figure 45	Distribution of event p_T density, ρ , taken from MC dijets for different numbers of primary vertices. [61]	70
Figure 46	Energy response as a function of energy and η for Electromagnetic (EM) jets in dijet MC. [61]	70
Figure 47	Dijet MC distributions of the number of pile-up jets passing the Jet Vertex Tagger (JVT) and Jet Vertex Fraction (JVF) cuts (left) and the efficiency for jets from the primary vertex (right) as a function of number of primary vertices in the event [62].	71
Figure 48	Distribution of MV2c20 output for b -jets, c -jets, and light-flavor jets in $t\bar{t}$ MC [63].	72
Figure 49	Distributions of the resolution of the x and y components of Track Soft Term (TST) E_T^{miss} in $Z \rightarrow \mu\mu$ events in data and MC [65].	73

Figure 50	Distributions of the jet term (top left), muon term (top right), and TST (bottom) E_T^{miss} in $Z \rightarrow \mu\mu$ events in data and MC . In the jet term distribution, the feature at zero is due to events with no jets, and the spike at 20 GeV corresponds to the minimum jet p_T considered for the analysis [65].	75
Figure 51	A few possible types of clusters in the Pixel Detector. (a) shows a single particle passing through a layer of the detector, (b) shows two particles passing through the detector, creating a single merged cluster, and (b) shows a single particle emitting a δ -ray as it passes through the detector [66].	77
Figure 52	One example of a two-particle cluster and its truth information compared with the output of the Neural Networks (NNs). The boxes represent pixels, with a color scale indicating Time Over Threshold (ToT). At top, the $p(N = i)$ values give the output of the Number NN , the probabilities that the cluster contains 1, 2, and 3 particles. Given the highest probability is for $N = 2$, the other NNs predict the position and errors of the two particles (in white). The black arrows and squares represent the truth information from the cluster, and the black dot and dotted line show the position measurement for the un-split cluster [66].	80
Figure 53	x resolutions for clusters with 3 (top) and 4 (bottom) pixels in the x direction in 7 TeV data for Connected Component Analysis (CCA) (using only charge interpolation to determine position) and NN clustering taken from MC [66].	81
Figure 54	Performance of the pixel neural network used to identify clusters created by multiple charged particles, as a function of constant coherent scaling of the charge in each pixel in the cluster. The top figure shows the rate at which the neural network wrongly identifies clusters with one generated particle as clusters with multiple particles. The bottom figure shows the rate at which the neural network correctly identifies clusters generated by multiple particles as such.	83
Figure 55	Fraction of cluster classes as a function of the distance between tracks for IBL (top) and 2nd pixel layer (bottom).	84
Figure 56	An example Feynman diagram of $t\bar{t}$ production and decay.	87
Figure 57	An example Feynman diagram of the production and decay of a WZ event.	88

Figure 58	An example Feynman diagram of the production and decay of a $Z/\gamma^* + \text{jets}$ event.	88
Figure 59	Schematic diagrams of the control, validation and signal regions for the on-shell Z (top) and edge (bottom) searches. For the on-shell Z search the various regions are shown in the $m_{\ell\ell} - E_T^{\text{miss}}$ plane, whereas in the case of the edge search the signal and validation regions are depicted in the $H_T - E_T^{\text{miss}}$ plane.	96
Figure 60	Signal region acceptance (left) and efficiency (right) in SRZ for the simplified model with gluino pair production with $\tilde{\chi}_2^0$ decays to $\tilde{\chi}_1^0$ and an on-shell Z boson with 1GeV neutralino LSP. Acceptance is calculated by applying the signal-region kinematic requirements to truth objects in MC, which do not suffer from identification inefficiencies or measurement resolutions.	98
Figure 61	Expected signal contamination in CRT (left) and CR-FS (right) for the signal model with gluino pair production, where the gluinos decay to quarks and a neutralino, with the neutralino subsequently decaying to a Z boson and a 1GeV neutralino LSP.	99
Figure 62	Expected signal contamination in VRS (left) and VRT (right) for the signal model with gluino pair production, where the gluinos decay to quarks and a neutralino, with the neutralino subsequently decaying to a Z boson and a 1GeV neutralino LSP.	99
Figure 63	Comparison of data and MC in a selection like SRZ, without the E_T^{miss} cut.	105
Figure 64	MC comparison of boson p_T in a selection of photon and $Z \rightarrow \ell\ell$ events with $H_T > 600$ GeV.	107
Figure 65	$E_{T,\parallel}^{\text{miss}}$ distributions in MC for $Z+\text{jets}$ ee (left) and $\mu\mu$ (right) channels compared to $\gamma + \text{jets}$ in an inclusive region with $H_T > 600$ GeV.	109
Figure 66	$E_{T,\parallel}^{\text{miss}}$ distributions in MC for $Z+\text{jets}$ ee (left) and $\mu\mu$ (right) channels compared to $\gamma + \text{jets}$ in an inclusive region with $H_T > 600$ GeV after the smearing procedure has been performed. These distributions have also been p_T reweighted, as described in Section 10.2.3.	110
Figure 67	Photon reweighting factors for the ee (left) and $\mu\mu$ (right) channels derived from data and MC.	111
Figure 68	E_T^{miss} distribution comparing MC distributions of photon and Z events before any smearing is applied (top), with only p_T reweighting applied (bottom left), and after p_T reweighting and smearing have both been applied (bottom right) in the ee channel of 2016 data.	112

Figure 69	E_T^{miss} distribution comparing MC distributions of photon and Z events before any smearing is applied (top), with only p_T reweighting applied (bottom left), and after p_T reweighting and smearing have both been applied (bottom right) in the $\mu\mu$ channel of 2016 data.	113
Figure 70	$Z/\gamma^* + \text{jets}$ MC $m_{\ell\ell}$ distribution compared to the prediction from $\gamma + \text{jets}$ method performed on MC (left) and the prediction from $\gamma + \text{jets}$ method performed on data (right).	114
Figure 71	Comparison of data and MC in CR- γ without any H_T cut, including the contributions from various $V\gamma$ processes.	114
Figure 72	Total $\gamma + \text{jets}$ data prediction in SRZ (excluding the E_T^{miss} cut) and the prediction after the $V\gamma$ subtraction.	115
Figure 73	E_T^{miss} distribution in VRZ ee (left) and $\mu\mu$ (right) with total data yield compared to the sum of the prediction from the $\gamma + \text{jets}$ method, the prediction from the flavor symmetry method, the prediction from the fake background estimation (included under “other”), and the remaining backgrounds taken from MC.	116
Figure 74	$\Delta\phi(\text{jet}, p_T^{\text{miss}})$ distribution in for the leading jet (left) and the subleading jet (right). The comparison is performed in VRZ with the cut on $\Delta\phi(\text{jet}_{12}, p_T^{\text{miss}})$ removed. The total data yield is compared to the sum of the prediction from the $\gamma + \text{jets}$ method, the prediction from the flavor symmetry method, the prediction from the fake background estimation (included under “other”), and the remaining backgrounds taken from MC.	116
Figure 75	Sub-leading lepton p_T for ee (left) and $\mu\mu$ (right) events in the tight-tight region used to measure the real-lepton efficiency for 2016.	118
Figure 76	Sub-leading lepton p_T for μe (left) and $\mu\mu$ (right) events in the tight-tight region used to measure the fake-lepton efficiency for 2016.	119
Figure 77	Same sign validation regions in the ee (top left), $\mu\mu$ (top right), $e\mu$ (bottom left) and μe (bottom right) channels combining 2015+2016 data. Uncertainty bands include both statistical and systematic uncertainties.	119
Figure 78	Distribtuions of data and MC in VR-WZ. Reconstructed transverse mass of the W (top) and mass of the Z (bottom).	121
Figure 79	Distribtuions of data and MC in VR-WZ. p_T of the W (top) and Z (bottom).	122

Figure 80	Distribtuions in VR-WZ. On the top, mass of the Z bosons in the event, and on the bottom, p_T of the Z bosons.	123
Figure 81	MC closure plots of VRS (top) and SRZ (bottom). The number of events from MC (black points) is compared to the number of events predicted from the flavor symmetry method (yellow histogram). The comparison is performed before the expanded $m_{\ell\ell}$ window is used to predict the on-Z bin, but because the shape is taken from the same MC , the result is identical.	126
Figure 82	Measurements of k , the ratio of electron to muon events, in bins of p_T and η . On the top is the measurements indexed by the leading lepton, while the measurements indexed by the subleading lepton are on the bottom. These efficiencies are for the 2016 dataset.	127
Figure 83	α , the trigger efficiency ratio, calculated as a function of E_T^{miss} from three different sources: data (blue), the usual skimmed $t\bar{t}$ MC (red), and an unskimmed $t\bar{t}$ MC (green).	129
Figure 84	Plots of the fraction of on-Z events with a VR-FS-like selection as a function of H_T . The top figure shows 2015 data and MC while the bottom figure shows the same for 2016.	130
Figure 85	E_T^{miss} distributions for $\gamma + \text{jets}$ predictions using different reweighting variables, as well as distributions with the nominal reweighting but with smearing functions taken from data and from MC in a ≥ 2 -jet region.	131
Figure 86	MC closure of the $\gamma + \text{jets}$ method as a function of E_T^{miss} comparing the MC prediction of the Z background with the $\gamma + \text{jets}$ method performed on $\gamma + \text{jets}$ MC . The uncertainty band includes both statistical and reweighting uncertainties.	132
Figure 87	Distributions of $m_T(\ell, E_T^{\text{miss}})$, the transverse mass of the lepton and the E_T^{miss} in a Validation Region (VR) designed to target $W\gamma$ processes. Top is the distribution with a E_T^{miss} cut at 100 GeV, and bottom is the same distribution with a E_T^{miss} cut of 200 GeV.	137

Figure 88	Comparison of background predictions and data yields in four validation regions, as well as the signal region. Definitions of all regions can be found in Table 7 , with both rare top and fake backgrounds grouped together under the “other” label. The uncertainty band includes all statistical and systematic uncertainties. Below is a panel of the one-sided statistical significances of the deviations between the predicted and observed quantities for each region.	139
Figure 89	Comparisons as a function of $m_{\ell\ell}$ of background predictions with observed data in an SRZ-like region, with the $m_{\ell\ell}$ cut removed. Left is the same-flavor channel, where all background shapes are taken from MC and scaled to their SRZ predictions, except for the $Z/\gamma^* + \text{jets}$ background, which is taken entirely from the data-driven background. Right is the different-flavor channel, in which the backgrounds are taken directly from MC , except for $t\bar{t}$, which is scaled to match the total data yield.	141
Figure 90	Distributions of observed data, background predictions, and simulated signals are shown in SRZ as a function of $m_{\ell\ell}$, $p_T^{\ell\ell}$, E_T^{miss} , H_T , number of jets, and number of b -jets. The two example signals have $(m(\tilde{g}), m(\tilde{\chi}_2^0)) = (1095, 205)$ GeV. All background shapes are taken from MC , and in the case of flavor symmetric and $Z/\gamma^* + \text{jets}$ backgrounds, their yields are scaled to match the data-driven predictions. Uncertainties include statistical and systematic components.	142
Figure 91	Comparisons as a function of $\Delta\phi(\text{jet}_{12}, p_T^{\text{miss}})$ of background predictions with observed data in an SRZ-like (left) and VRS-like (right) region, with the $\Delta\phi(\text{jet}_{12}, p_T^{\text{miss}})$ cut removed. All background shapes are taken from MC and scaled to their SRZ predictions, except for the $Z/\gamma^* + \text{jets}$ background, which is taken entirely from the data-driven background.	144

Figure 92	Expected and observed exclusion contours derived from the results in SRZ for the (top) $\tilde{g}-\tilde{\chi}_2^0$ on-shell grid and (bottom) $\tilde{q}-\tilde{\chi}_2^0$ on-shell grid. The dashed blue line indicates the expected limits at 95% CL and the yellow band shows the 1σ variation of the expected limit as a consequence of the uncertainties in the background prediction and the experimental uncertainties in the signal ($\pm 1\sigma_{\text{exp}}$). The observed limits are shown by the solid red line, with the dotted red lines indicating the variation resulting from changing the signal cross section within its uncertainty ($\pm 1\sigma_{\text{theory}}^{\text{SUSY}}$).	146
Figure 93	Expected and observed exclusion contours derived from the results in SRZ for the $\tilde{g}-\tilde{\chi}_1^0$ on-shell grid. The dashed blue line indicates the expected limits at 95% CL and the yellow band shows the 1σ variation of the expected limit as a consequence of the uncertainties in the background prediction and the experimental uncertainties in the signal ($\pm 1\sigma_{\text{exp}}$). The observed limits are shown by the solid red line, with the dotted red lines indicating the variation resulting from changing the signal cross section within its uncertainty ($\pm 1\sigma_{\text{theory}}^{\text{SUSY}}$).	147
Figure 94	Expected 95% Confidence Level (CL) exclusion contours (dashed) and 5σ discovery contours (solid) for $L_{\text{int}} = 300^{-1}$ (black) and 3000^{-1} (red) for gluino pair-production, with 1σ bands representing the uncertainty on the production cross-section. Superimposed is the observed 8 TeV exclusion for similar models. [105]	152

LIST OF TABLES

Table 1	Supermultiplets of supersymmetric and SM particles. Sfermions, on the first five rows, are all spin-0. Higgsinos and gauginos are all spin-1/2. Three sets of each fermion’s supermultiplet exist, one for each generation. [25]	25
Table 2	Simulated background event samples used in this analysis with the corresponding matrix element and parton shower generators, cross-section order in α_s used to normalise the event yield, underlying-event tune and PDF set.	90
Table 3	Summary of the electron selection criteria. The signal selection requirements are applied on top of the baseline selection.	91
Table 4	Summary of the muon selection criteria. The signal selection requirements are applied on top of the baseline selection.	92
Table 5	Summary of the jet and b -jet selection criteria. The signal selection requirements are applied on top of the baseline requirements.	93
Table 6	Summary of the photon selection criteria.	94
Table 7	Overview of all signal, control and validation regions used in the on-shell Z search. More details are given in the text. The flavour combination of the dilepton pair is denoted as either “SF” for same-flavour or “DF” for different flavour. All regions require at least two leptons, unless otherwise indicated. In the case of CR γ , VR-WZ, VR-ZZ, and VR-3L the number of leptons, rather than a specific flavour configuration, is indicated. The main requirements that distinguish the control and validation regions from the signal region are indicated in bold. Most of the kinematic quantities used to define these regions are discussed in the text. The quantity $m_T(\ell_3, E_T^{\text{miss}})$ indicates the transverse mass formed by the E_T^{miss} and the lepton which is not assigned to either of the Z-decay leptons.	97
Table 8	Lepton trigger requirements used for the analysis in different regions of lepton- p_T phase space.	98

Table 9	Yields in signal and validation regions for the flavor symmetric background. Errors include statistical uncertainty, uncertainty from MC closure, uncertainty from the k and α factors, uncertainty due to deriving triggers efficiencies from a DAOD, and uncertainty on the MC shape used to correct for the $m_{\ell\ell}$ expansion.	103
Table 10	Background fit results from the sideband fit method. The $t\bar{t}$ MC's normalization is taken as a free parameter in the fit to data in CRT, then that normalization factor is applied in SRZ. The results are shown here both divided between the ee and $\mu\mu$ channels and summed together. All other backgrounds are taken from MC in CRT, while in SRZ, the $Z/\gamma^* + \text{jets}$ contribution is taken from the $\gamma + \text{jets}$ method. The uncertainties quoted include both statistical and systematic components.	104
Table 11	Summary of the $t\bar{t}$ normalization factors calculated by the sideband fit to CRT and VRT for the 2015+2016 data.	105
Table 12	Comparison of Flavor Symmetric (FS) background predictions from the nominal method, the flavor symmetry method, and the cross-check, the sideband fit method. Uncertainties include statistical and systematic uncertainties in both cases.	106
Table 13	List of triggers used to collect photon events in 2015 and 2016 data-taking.	108
Table 14	Control regions used to measure efficiencies of real and fake leptons. The flavour combination of the dilepton pair is denoted as either "SF" for same-flavour or "DF" for different flavour. The charge combination of the leading lepton pairs are given as "SS" for same-sign or "OS" for opposite-sign.	118
Table 15	Yields in validation regions. In VRS, data-driven background estimates are used for $Z/\gamma^* + \text{jets}$, fakes, and FS processes. All other backgrounds are taken from MC, including all backgrounds in the multi-lepton VRS. Uncertainties include statistical and systematic components.	120

Table 16	Uncertainties in the on-Z signal and validation regions. Nominal predictions are given with statistical uncertainty (including uncertainty from subtracted backgrounds), MC Closure uncertainty, uncertainty on the prediction from varying k and α by their statistical uncertainties, comparing the efficiencies from AODs to that of DAODs, and on the $m_{\ell\ell}$ widening, which includes MC statistics and a data/MC comparison in a loosened region.	125
Table 17	Uncertainty breakdown for the $\gamma + \text{jets}$ method in SRZ. Uncertainties considered are the impact of MC uncertainty on $V\gamma$ backgrounds, MC closure, uncertainty on $m_{\ell\ell}$ shape (also determined via MC closure), reweighting uncertainties, smearing uncertainties, and statistical uncertainty on the $\gamma + \text{jets}$ events used in the method.	133
Table 18	Systematic uncertainties on the fake-lepton background for on-Z regions for 2015+2016 yields. The nominal yield includes statistical uncertainty from the baseline selection in a given region. The following rows indicate the results of varying the real and fake lepton efficiencies up and down by by their statistical uncertainty. Real cont. gives an uncertainty on the the contamination of real leptons in the fake lepton efficiency. b -jet and no b -jet indicate the impact of requiring or vetoing b -tagged jets in the regions used to measure the fake efficiency.	133
Table 19	Fractional uncertainties of dibosons in signal and validation regions from Sherpa scale variations. . .	135
Table 20	Comparison of yields in on-Z and off-Z regions in Sherpa and Powheg diboson MC at 14.7 fb^{-1} . . .	135
Table 21	Overview of the dominant sources of systematic uncertainty on the total background estimate in the signal regions. The values shown are relative to the total background estimate, shown in %.	136
Table 22	Number of events expected and observed in the ee , $\mu\mu$, and combined channels. Expected predictions include all systematic and statistical uncertainties discussed in Chapter 11 . Also shown is the discovery p -value for zero signal strength ($p(s = 0)$) [99], Gaussian significance, 95% CL observed and expected upper limits on the number of signal events (S^{95}), and the corresponding observed upper limit on the visible cross section ($\langle e\sigma \rangle_{\text{obs}}^{95}$).	140

LISTINGS

ACRONYMS

- IBL Insertable B-Layer
MS Muon Spectrometer
ID Inner Detector
SCT Silicon Microstrip Tracker
TRT Transition Radiation Tracker
NN Neural Network
CCA Connected Component Analysis
ToT Time Over Threshold
MDT Monitored Drift Tube
CSC Cathode-Strip Chamber
RPC Resistive Plate Chamber
TGC Thin Gap Chamber
L₁ Level One
HLT High Level Trigger
L₁Calo L₁ Calorimeter Trigger
L₁Topo L₁ Topological Trigger
CTP Central Trigger Processor
TTC Trigger Timing and Control
ROB Read Out Board
RoI Region of Interest
LHC Large Hadron Collider
LEP Large Electron-Positron
SPS Super Proton Synchrotron
CMS Compact Muon Solenoid
ALICE A Large Ion Collider Experiment
LHCb Large Hadron Collider beauty
RF Radiofrequency

PSB	Proton Synchrotron Booster
PS	Proton Synchrotron
OR	Overlap Removal
EM	Electromagnetic
LCW	Local Cluster Weighting
JES	Jet Energy Scale
JER	Jet Energy Resolution
JVT	Jet Vertex Tagger
JVF	Jet Vertex Fraction
CST	Calorimeter Soft Term
TST	Track Soft Term
MC	Monte Carlo simulation
SM	Standard Model
BSM	Beyond the Standard Model
SUSY	Supersymmetry
QCD	Quantum Chromodynamics
PDF	Parton Distribution Function
DM	Dark Matter
LO	Leading Order
NLO	Next to Leading Order
NLO+NLL	Next-to-Leading-Logarithmic Accuracy
SUSY	Supersymmetry
MSSM	Minimal Supersymmetric Standard Model
LSP	Lightest Supersymmetric Particle
AOD	Analysis Object Data
dAOD	derived AOD
SR	Signal Region
VR	Validation Region
CR	Control Region
FS	Flavor Symmetric

CL Confidence Level

HL-LHC High Luminosity Large Hadron Collider

¹

Part I

²

INTRODUCTION

³

4

5 INTRODUCTION

6 In 2010, the [LHC](#) began colliding protons in its 27 km ring, taking its place
7 as the most powerful in a long line of accelerators aimed at uncovering the
8 fundamental rules that govern particle physics. Its primary goal was to
9 complete the Standard Model of particle physics by discovering the Higgs
10 boson, the last remaining particle that physicists felt sure must exist. With
11 its presence, the Standard Model would be consistent, explaining every ob-
12 served interaction of known particles, with a complete mathematic frame-
13 work to describe each feature. However, even with a Higgs boson, the
14 Standard Model contained hints that it might be incomplete, suspicious
15 features that suggested that at a higher energy, there might be something
16 more.

17 In 2012, the [ATLAS](#) and [CMS](#) Experiments discovered the Higgs boson,
18 leaving the [LHC](#) physics community without a single primary goal, but
19 rather a host of theories to explore, each extending the Standard Model
20 in a different way. Each theory attempts to solve one of the mysteries left
21 by the Standard Model, providing an explanation for Dark Matter, sug-
22 gesting a mechanism that could explain Gravity's weakness, or explain-
23 ing the Higgs boson's mass. For decades, the most popular of these has
24 been Supersymmetry, which proposes a fermionic symmetry and requires
25 a menagerie of new Supersymmetric particles, none of which has yet been
26 observed.

27 Supersymmetry simultaneously solves more of the Standard Model's
28 problems than any other, making it appealing to theorists and experimen-
29 talists alike. But in order to do this, Supersymmetric particles must appear
30 with masses of approximately 1 TeV, precisely the range of energies the
31 [LHC](#) is capable of exploring. In 2015, after a three-year shutdown, the [LHC](#)
32 nearly doubled the energy of its collisions, opening up new territory to
33 be explored by analyzers, and providing data that could either discover or
34 exclude many Supersymmetric models.

35 The analysis presented in this thesis searches for Supersymmetry, seek-
36 ing to identify events in which Supersymmetric particles are produced in
37 proton-proton collisions, then decay via a Z boson to a chargeless Super-
38 symmetric particle which escapes ATLAS without detection. A similar AT-
39 LAS search, performed with data from the lower-energy collisions 2012,
40 observed a 3σ excess of events over the expected Standard Model back-
41 ground [1].

42 The excess generated a great deal of interest in this channel, and re-
43 investigating it became a top priority when the upgraded [LHC](#) turned back
44 on in 2015. A preliminary search, performed using the 2015 data only, was
45 released at the end of that year. Again an excess was observed, this time
46 with a significance of 2.2σ [2].

47 This thesis describes a search for Supersymmetry performed in this
48 channel using data taken by the ATLAS detector in 2015 and 2016, includ-
49 ing an explanation of the theory and motivation behind the search, and a
50 description of the LHC and the ATLAS detector. The remaining chapters
51 are laid out as follows:

52 CHAPTER 2 outlines the Standard Model of Particle Physics and the
53 benefits of extending it to include Supersymmetry, then continues on to
54 introduce the specific models used in the search presented in later chapters.
55 It also provides an overview of the process of generating MC for use in the
56 ATLAS experiment.

57 CHAPTER 3 describes the LHC and its operation, including the magnet
58 system, the preaccelerator complex, and some of the phenomenology of
59 collisions at 13 TeV.

60 CHAPTER 4 contains descriptions of the many pieces of the ATLAS de-
61 tector, and how they serve to detect particles coming from LHC collisions.
62 ATLAS’s magnet and trigger systems are also discussed.

63 CHAPTER 5 details the process of reconstruction, the procedure by which
64 the electric signals in the ATLAS detector are interpreted as particles to be
65 used for analysis.

66 CHAPTER 6 presents a neural network designed to improve tracking in
67 the ATLAS Pixel Detector, and describes the benefits of its implementation.

68 CHAPTER 7 lists the main backgrounds for the Supersymmetry search
69 described in this thesis, and provides general ideas of how they can be
70 reduced.

71 CHAPTER 8 outlines how objects are identified and selected for this anal-
72 ysis, referencing many of the working points defined in Chapter 5.

73 CHAPTER 9 explains the analysis’s search strategy, defining signal, con-
74 trol, and validation regions, and briefly describing how each contributes
75 to the search.

76 CHAPTER 10 describes, for each of the backgrounds described in Chap-
77 ter 7, how estimates of the Standard Model contributions to the signal
78 region are performed.

79 CHAPTER 11 builds off of Chapter 11, and continues to detail how the
80 uncertainties on each estimate are assessed.

81 CHAPTER 12 shows the results of the analysis, comparing expectations
82 based on background estimates to the observed data.

⁸³ CHAPTER 13 provides interpretations of the results, and explains the
⁸⁴ statistical procedure used to define exclusions on Supersymmetric models.

⁸⁵ CHAPTER 14 concludes with a summary of the results, and an outlook
⁸⁶ for future searches.

87

Part II

88

THEORY AND MOTIVATION

89

This section describes the theoretical foundation for the analysis presented in [Part iv](#). It includes an overview of the Standard Model, including its phenomenology in a pp collider. The theory of Supersymmetry is explained, and the motivation for extending the Standard Model to include it is presented. In addition, this section includes an explanation of Monte Carlo generators and details about the specific form of Supersymmetry searched for in this analysis.

90

91

92

93

94

95

96

97

98 THEORY AND MOTIVATION

99 The Standard Model ([SM](#)) of particle physics represents all particles and in-
100 teractions currently known. It is formulated using the principles of Quan-
101 tum Field Theory, with the constraints of several symmetries and physical
102 requirements to determine the rules for allowed interactions [3]. Devel-
103 oped in the 1960s and 70s [4–6], it has been immensely successful at pre-
104 dicting the existence of particles before their discovery, and has held up
105 to many high-precision tests. Despite this success, it has several shortcom-
106 ings. Though the [SM](#) is likely correct at the energies thus far probed, it
107 may be missing key components that become more important at higher
108 energies. Models supplementing the [SM](#) with additional particles and in-
109 teractions are referred to as Beyond the Standard Model ([BSM](#)) theories.

110 One possible extension of the [SM](#) is Supersymmetry ([SUSY](#)), a theory
111 which postulates an additional symmetry between bosons and fermions
112 to the [SM](#), creating a spectrum of [SUSY](#) particles (sparticles) which interact
113 with the particles of the [SM](#). This theory motivates the search performed
114 in [Part iv](#) of this thesis, and its theoretical appeals are discussed in this
115 section, along with specific models considered in the search.

116 2.1 THE STANDARD MODEL

117 The [SM](#) of particle physics describes the interactions of all of the particles
118 currently known to exist, and consists of matter particles and force carriers,
119 as well as the Higgs boson, which fits into neither category. This model has
120 been unprecedently successful in predicting new particles and phenom-
121 ena, including the prediction of the Higgs boson almost 50 years before its
122 discovery in 2012, which completed the [SM](#).

123 The particles of the [SM](#) are divided into two categories: fermions and
124 bosons [3]. The fermions comprise all the matter described by the [SM](#), and
125 are spin- $\frac{1}{2}$ particles. The bosons are integer spin-particles, most of which
126 are spin-1. These particles provide a mechanism to explain three of the four
127 forces known to physics, with gravity still lacking a quantum formulation.
128 The Higgs boson, the only spin-0 particle in the [SM](#), provides a mechanism
129 for giving mass to the other particles. The full [SM](#), with the addition of the
130 hypothetical graviton, is presented in [Figure 1](#).

131 2.1.1 *Matter*

132 The matter described by the [SM](#) is made up of fermions, spin- $\frac{1}{2}$ particles
133 which can be broken into two groups, quarks and leptons. The leptons all
134 interact weakly, while the quarks additionally interact strongly. Half the
135 leptons as well as all quarks are electromagnetically charged.

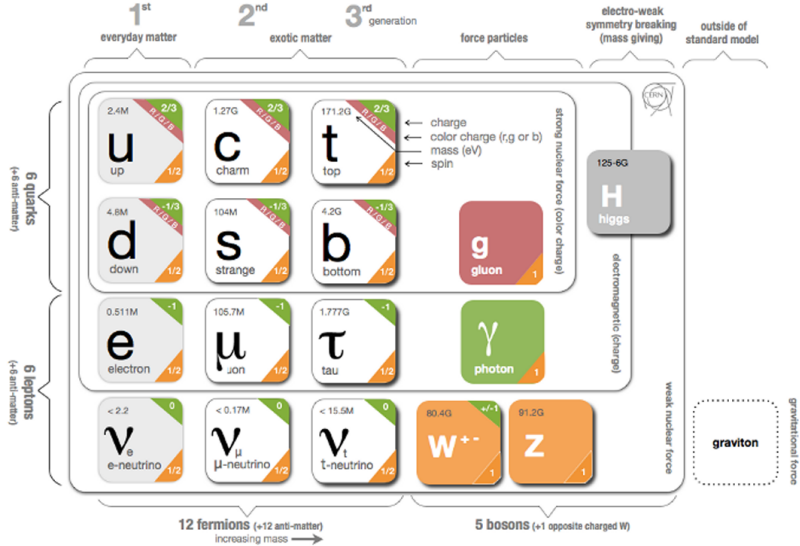


Figure 1: The Standard Model of particle physics, containing all known bosons and fermions, with the addition of the hypothetical graviton. [7]

136 2.1.1.1 Leptons

137 Leptons, as seen in the bottom left of Figure 1, exist in three generations,
 138 each labeled by a flavor: electron, muon, and tau. In the case of the massive
 139 leptons, these flavors are mass eigenstates, and the generations are placed
 140 in an order based on increasing mass. Each massive lepton is negatively
 141 electromagnetically charged and has a positively charged anti-particle.

142 The three neutrinos exist in the same flavors as the massive leptons, but
 143 these flavor eigenstates do not correspond exactly to mass eigenstates [8].
 144 As a consequence, neutrinos oscillate between flavors as they propagate
 145 through space. These oscillations are the only evidence of neutrino mass,
 146 which is bound from below by the mass splittings determined from the
 147 oscillation and bound from above by cosmological limits on the universe's
 148 mass density [9]. Though it is still uncertain if the masses of the neutrinos
 149 follow the same hierarchy as the massive leptons, that expected ordering
 150 is slightly experimentally preferred over the inverted hierarchy [10].

151 Unlike the massive leptons, the neutrinos are not electrically charged,
 152 and it is not yet known whether each neutrino has a separate anti-particle,
 153 or if it is its own antiparticle. Because they are not electromagnetically
 154 charged, they can only interact weakly, making them extremely difficult
 155 to detect. As a consequence of their ability to evade detection, neutrinos'
 156 properties are nearly impossible to study with general purpose particle
 157 detectors.

158 The SM conserves lepton number, L , which is defined as the number
 159 of leptons minus the number of anti-leptons in a state, and can also be
 160 defined for each lepton flavor. Though there are anomalies that appear in
 161 second order SM interactions which could provide very small violations
 162 of this conservation, it holds to great precision in experiment. $\mu \rightarrow e\gamma$

163 branching ratios, for example, have been constrained to 10^{-13} [11]. As a
164 consequence of this conservation, the lightest massive lepton, the electron,
165 is stable.

166 2.1.1.2 *Quarks*

167 Quarks, as seen in the top left of [Figure 1](#), are also electromagnetically
168 charged particles that interact weakly, but are differentiated from the lep-
169 tons by their strong interactions. They are also organized in three genera-
170 tions ordered by mass, and come in pairs of *up*-type and *down*-type quarks,
171 named after the lightest generation. Though the up quark is lighter than
172 the down, that rule is reversed in the subsequent two generations. Up-type
173 quarks are electromagnetically charged $+\frac{2}{3}$, while the down-type quarks
174 are charged $-\frac{1}{3}$. Quarks are also charged under the strong interaction,
175 whose three charges are often characterized by colors: red, green, and blue.
176 Each quark has an anti-particle with the opposite charges.

177 These fractional charges and individual colors are never seen in nature
178 because of the requirement (discussed further in [Section 2.1.2.2](#)) that stable
179 particle states be color-neutral. To accomplish this, quarks can create two-
180 particle bound states called *mesons* consisting of one quark and one anti-
181 quark with the same color charge, or three-particle bound states of quarks
182 or anti-quarks with the three different color charges, which are called
183 *baryons*. The lightest color neutral state containing only quarks, the pro-
184 ton (*uud*), is stable. Extremely unstable bound states consisting of higher
185 numbers of quarks can also exist, such as the pentaquark discovered in
186 2015 at the [LHC](#). [12] Collectively, these multi-quark bound states are called
187 *hadrons*.

188 Like leptons, the number of quarks in a state is conserved, up to very
189 small anomalies. However, because quarks cannot exist in an isolated state,
190 that conservation is described in terms of baryon number (B) defined simi-
191 larly to lepton number. Baryons are defined with $B = 1$, while anti-baryons
192 have the quantum number $B = -1$. Mesons have $B = 0$.

193 2.1.2 *Forces*

194 The fermions in the previous section interact via the electromagnetic, weak,
195 and strong forces. In a perturbative quantum field theory, interactions via
196 these forces are represented by mediating bosons. These force carriers in-
197 teract only with particles charged with their force's quantum numbers.
198 The photon, for example, interacts only with electromagnetically charged
199 particles. Gluons, mediators of the strong force, interact only with color
200 charged particles, quarks and gluons. All fermions are weakly charged
201 and interact with the weak force's mediators, the W and Z bosons.

202 The formulation for each of these forces is developed by requiring that
203 the [SM](#) Lagrangian be locally gauge invariant [8]. This can be accomplished
204 by adding gauge fields to the Lagrangian, whose behavior under gauge
205 transformations cancels out the gauge dependence of the free Lagrangian.

206 However, adding a mass term for these fields reintroduces gauge dependence,
 207 so this mechanism only creates forces mediated by massless gauge
 208 bosons. The addition of the Higgs field provides mass terms for the weak
 209 gauge bosons (as well as other particles) without interfering with the
 210 gauge invariance.

211 The total gauged symmetry group for the SM is $SU_C(3) \times SU_L(2) \times$
 212 $U_Y(1)$, where C stands for color, the charge of the strong force, L stands
 213 for left, because the weak force is left-handed, and Y is the hypercharge
 214 quantum number, the charge of the unified electroweak force.

215 **2.1.2.1 The Electromagnetic Force**

216 Electromagnetism provides the simplest example of a requirement of local
 217 gauge invariance generating a Lagrangian description of a force. Electromagnetism
 218 has one massless mediator, the photon, which interacts with
 219 all electromagnetically charged particles. What follows is a brief description
 220 of how enforcing this invariance generates a Lagrangian of the same
 221 form as the classical electromagnetic Lagrangian, which can be easily incor-
 222 porated into the SM.

223 The particles in Section 2.1.1 are fermions, and so the Lagrangian de-
 224 scribing their free propagation are Dirac Lagrangians and all follow the
 225 form

$$\mathcal{L} = i\bar{\psi}\gamma^\mu\partial_\mu\psi - m\bar{\psi}\psi. \quad (1)$$

226 Requiring that the free Lagrangians for these particles be invariant un-
 227 der a $U(1)$ local gauge transformation, $e^{iq\lambda(x)}$, can be accomplished by
 228 adding a term to the Lagrangian which cancels the derivative term arising
 229 from λ 's dependence on x :

$$\mathcal{L} = i\bar{\psi}\gamma^\mu\partial_\mu\psi - m\bar{\psi}\psi - (q\bar{\psi}\gamma^\mu\psi)A_\mu \quad (2)$$

230 where A_μ is a “gauge field” that transforms according to

$$A_\mu \rightarrow A_\mu + \partial_\mu\lambda. \quad (3)$$

231 This vector field must also come with a free term,

$$\mathcal{L} = -\frac{1}{16\pi}F^{\mu\nu}F_{\mu\nu} + \frac{1}{8\pi}m_A^2A^\nu A_\nu. \quad (4)$$

232 The mass term for this field would not itself be invariant under the
 233 transformation, but the field can simply be made massless to avoid this
 234 problem. The final Lagrangian, then, is

$$\mathcal{L} = i\bar{\psi}\gamma^\mu\partial_\mu\psi - m\bar{\psi}\psi - \frac{1}{16\pi}F^{\mu\nu}F_{\mu\nu} - (q\bar{\psi}\gamma^\mu\psi)A_\mu \quad (5)$$

which is precisely the original Lagrangian with the addition of terms replicating the form of the Maxwell Lagrangian. In a quantized interpretation, it describes a field that interacts with particles with non-zero electromagnetic charge q via interactions with a massless spin-1 boson, the photon. In the quantum formulation, this charge is dependent on the energy scale of the interaction, and the strength of the interaction is more typically described by the electromagnetic coupling constant

$$\alpha_{EM}(\mu) = q(\mu)^2 / 4\pi. \quad (6)$$

For the purpose of succinct notation, this Lagrangian is often rewritten in terms of the *covariant derivative*

$$D_\mu = \partial_\mu + iq\lambda A_\mu \quad (7)$$

which immediately cancels the gauge dependent term created by the transformation. This mechanism is mathematically simple in the $U(1)$ case, but can be replicated for more complicated gauge transformations with perturbative approximations.

2.1.2.2 The Strong Force

The strong force is generated by a similar process of requiring local gauge invariance, but in this case, for a $SU(3)$ transformation. The interactions of the strong force are described by the theory of quantum chromodynamics, which is given by the Lagrangian

$$\mathcal{L}_{strong} = -\frac{1}{4}G_{\mu\nu}^\alpha G^{\alpha\mu\nu} - \frac{1}{2}\bar{Q}_m D Q_m \quad (8)$$

where the α index runs from 1 to 8 and represents the eight force carriers of the strong force, the gluons. m indexes the three quark generations, and $G_{\mu\nu}^\alpha$ is the field strength tensor, defined as

$$G_{\mu\nu}^\alpha = \partial_\mu G_\nu^\alpha - \partial_\nu G_\mu^\alpha + g_s f_{\beta\gamma}^\alpha G_\mu^\beta G_\nu^\gamma \quad (9)$$

where g_s is a function of the energy scale of the interaction μ , and is related to the strong coupling constant by

$$\alpha_s(\mu) = g_s(\mu)^2 / 4\pi. \quad (10)$$

The first term of the Lagrangian gives the gluon self-coupling interactions, with terms involving 2, 3, and 4 gluon field terms. The 2-field portion is simply the field strength tensor, but the other terms give gluon self-interaction terms that can be described by the Feynman diagrams in [Figure 2](#). Unlike photons, gluons are charged by the force they carry, making self-interaction possible.

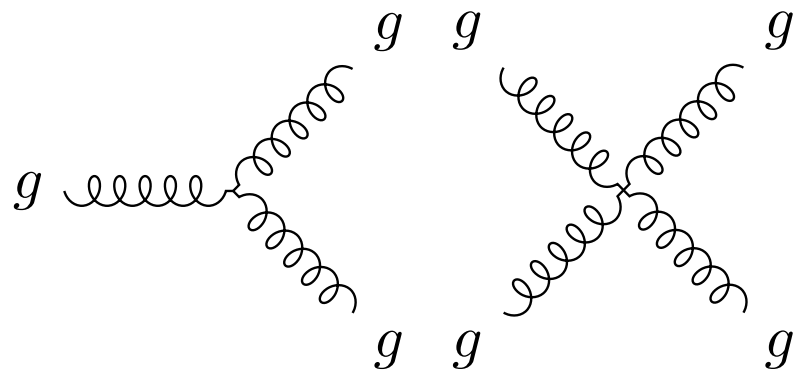


Figure 2: Gluon self coupling Feynman diagrams involving 3- and 4-gluon interactions.

264 In the second term, $\not{D}Q_m$ is the covariant derivative acting on the quark
 265 field. The quarks are in fact charged under all three forces, strong, electro-
 266 magnetic, and weak, so the covariant derivative includes terms to make
 267 each of the force's Lagrangians gauge invariant. Thus this term introduces
 268 quark-boson interactions of four types, seen in [Figure 3](#). The quarks' cou-
 269 pling to the gluon is the strongest, with the other couplings happening at
 270 lower rates. The couplings to the W and Z bosons are described in [Sec-](#)
 271 [tion 2.1.2.3](#).

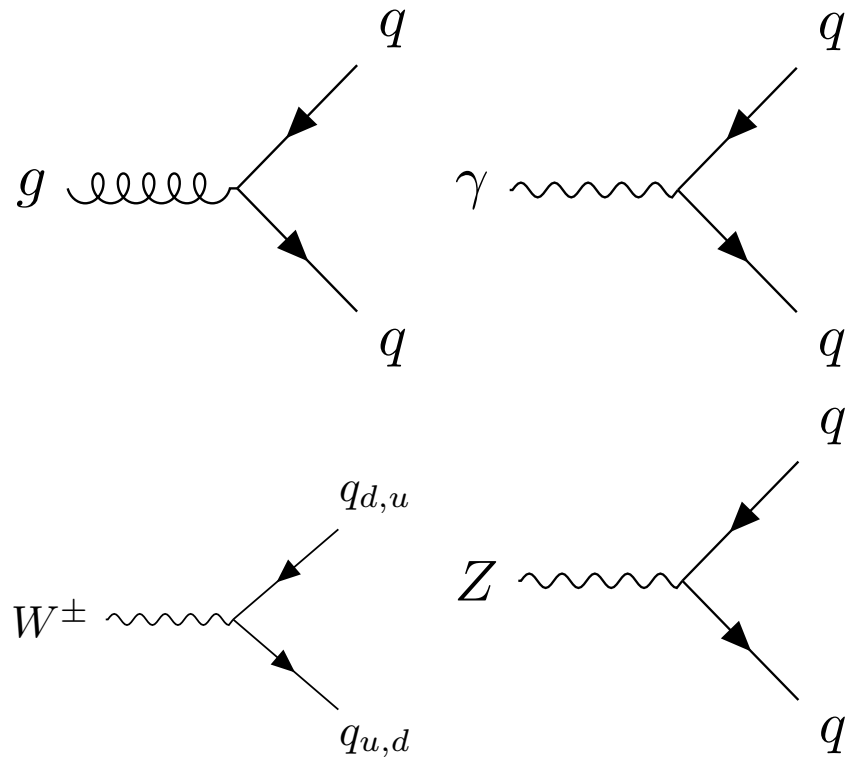


Figure 3: Quark couplings to the different types of gauge bosons. The $q_{u,d}$ labels represent any up- or down-type quarks.

Quantum Field Theory assumes that particles are essentially *free*, propagating without interaction, and considers all interactions as perturbations on a free theory. So long as multiple interactions are much less likely than a single interaction, or put another way, so long as the coupling constants for each force are much less than one, this perturbative approximation is essentially correct. However, the strong coupling constant, α_s , this assumption is not always valid. α_s changes as a function of the energy of an interaction according to its renormalization group equation

$$\mu_R^2 \frac{d\alpha_s}{d\mu_R^2} = \beta(\alpha_s) = -(b_0\alpha_s^2 + b_1\alpha_s^3 + b_2\alpha_s^4 + \dots) \quad (11)$$

where μ_R^2 gives the renormalization scale, and each b_n gives a correction to the β -function based on diagrams with n loops [13]. The overall negative sign produces the unique energy dependence of α_s , which becomes very small at high energy scales and asymptotically increases at low energies. Figure 4 shows this effect translated to distance scales, demonstrating that $\alpha_s \ll 1$ and can be considered perturbatively at small distance scales, but at large distance scales α_s approaches 1, and a perturbative approximation can no longer be used. Instead, for distances larger than 10^{-16} , the colorless hadrons introduced in Section 2.1.1.2 must be used to describe strong interactions.

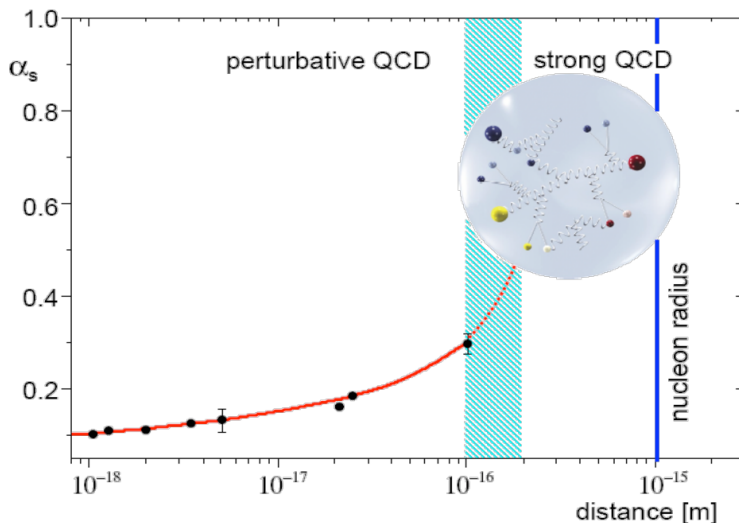


Figure 4: The running of the strong coupling constant, α_s . [14]

The boundary between these regimes is referred to as Λ_{QCD} and differentiates energies at which Quantum Chromodynamics (QCD) can be considered perturbatively and those at which it cannot. The LHC is capable of producing individual high-energy quarks in its hard scatterings, but they lose energy as they radiate gluons, eventually entering the energy regime below Λ_{QCD} . The transition between these two regimes is complex,

296 and dictates the way that strongly charged particles appear in the ATLAS
 297 detector. This is described in more detail in [Section 2.1.3.1](#).

298 **2.1.2.3 The Electroweak Force**

299 A similar process, using an $SU(2)$ gauge transformation, can produce a
 300 Lagrangian that would suffice to describe the W and Z bosons of the **SM**, if
 301 only they were massless. However, they are not, so an alternate mechanism
 302 is needed to generate massive force carriers.

303 Before a mechanism for their masses was understood, and before they
 304 were discovered, the large masses of the W and Z bosons were proposed
 305 in order to unify the electromagnetic and weak forces into the electroweak
 306 force [8]. The large masses were crucial to explain the discrepancy in the
 307 strength of the two forces.

308 The unified electroweak force is generated by a symmetry group written
 309 as $SU(2)_L \times U(1)_Y$, where L refers to left-handed fields, and Y is the
 310 quantum number for *hypercharge*. This new quantum number is defined as

$$Y = 2(Q - T_3) \quad (12)$$

311 where Q is the electromagnetic charge and T_3 is the third component
 312 of weak isospin \mathbf{T} , the quantum number relating to the weak interaction.
 313 In the unified theory, quark and lepton singlets interact according to their
 314 hypercharge, and left-handed quarks and leptons, grouped according to
 315 their generation, interact as doublets.

316 The gauge bosons resulting from this unified theory include a triplet, \mathbf{W} ,
 317 with coupling g_W , and a singlet field B , with coupling $g'/2$. However, the
 318 electroweak symmetry is broken, and mixing between these states occurs.
 319 Rewritten in their mass basis, the standard electroweak force carriers are
 320 produced: W^\pm , two states with identical coupling resulting from the first
 321 two states of the \mathbf{W} triplet, the Z and the photon field A resulting from
 322 the mixing of the last \mathbf{W} state and B .

323 The electroweak Lagrangian is much more complicated than the strong
 324 Lagrangian, and can be divided into several terms:

$$\mathcal{L}_{\text{electroweak}} = \mathcal{L}_{\text{gauge}} + \mathcal{L}_{\text{fermions}} + \mathcal{L}_{\text{Higgs}} + \mathcal{L}_{\text{Yukawa}}. \quad (13)$$

325 The first term can be written as follows

$$\mathcal{L}_{\text{gauge}} = -\frac{1}{4}W^{a\mu\nu}W^a_{\mu\nu} - \frac{1}{4}B^{\mu\nu}B^{\mu\nu} \quad (14)$$

326 where the a indices are numbered 1 through 3 and indicate the genera-
 327 tors of $SU(2)$ which are written

$$W^a_{\mu\nu} = \partial_\mu W^a_\nu - \partial_\nu W^a_\mu + g_2 \epsilon_{abc} W^b_\mu W^c_\nu \quad (15)$$

328 The gauge portion of the Lagrangian then generates interaction terms
 329 of between the gauge fields, which when rewritten in terms of the mass-
 330 eigenstate basis, generates interactions between three gauge bosons, like
 331 the ones in [Figure 5](#), as well as interactions between four gauge bosons.

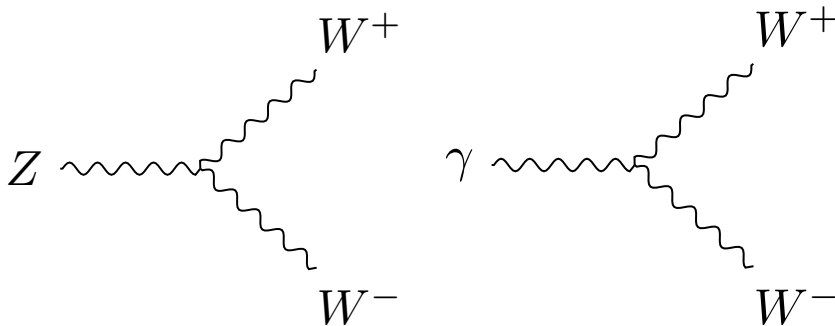


Figure 5: Feynman diagrams of trilinear gauge couplings in the [SM](#).

332 The fermion portion of the Lagrangian is written as

$$\begin{aligned} \mathcal{L}_{fermion} = & -\frac{1}{2}\bar{L}_m D \not{D} L_m - \frac{1}{2}\bar{Q}_m D \not{D} Q_m \\ & -\frac{1}{2}\bar{U}_m D \not{D} U_m - \frac{1}{2}\bar{D}_m D \not{D} D_m \\ & -\frac{1}{2}\bar{E}_m D \not{D} E_m \end{aligned} \quad (16)$$

333 where L is the left-handed lepton doublet, Q is the left-handed quark
 334 doublet, U is the right-handed singlet for up-type quarks, D is the same for
 335 down-type quarks, and E is the right-handed singlet for electrons, muons
 336 and taus. Each of these fields has an implicit index running from 1 to 3
 337 to represent the three generations. The covariant derivative in each term
 338 includes terms including all the gauge fields the fermion is charged under.
 339 Unlike the other forces, the weak force treats left- and right-handed
 340 fermion fields differently; it only interacts with the left-handed fields, so
 341 only the first two terms' covariant derivatives include W terms. The first
 342 term in this Lagrangian, for example, produces weak interactions depicted
 343 in [Figure 6](#). The Z bosons, because they represent a mixing between the
 344 W and B fields, can interact with right-handed leptons and quarks, but
 345 do so with different strengths than left-handed particles.

346 No right-handed term appears for the neutrino field, because only left-
 347 handed neutrinos and right-handed anti-neutrinos have been observed.
 348 However, because neutrinos have non-zero mass, their chirality can change
 349 with frame boosts, which complicates any claim that right-handed neutrinos
 350 do not exist [3]. It is possible that neutrinos are their own antiparticle,
 351 making the right-handed anti-neutrino the solution to this problem. It's
 352 also possible that very massive right-handed neutrinos do exist, and sim-
 353 ply haven't been discovered yet.

354 The remaining two terms of the electroweak Lagrangian are related to
 355 the Higgs field, which is the source of electroweak symmetry breaking.

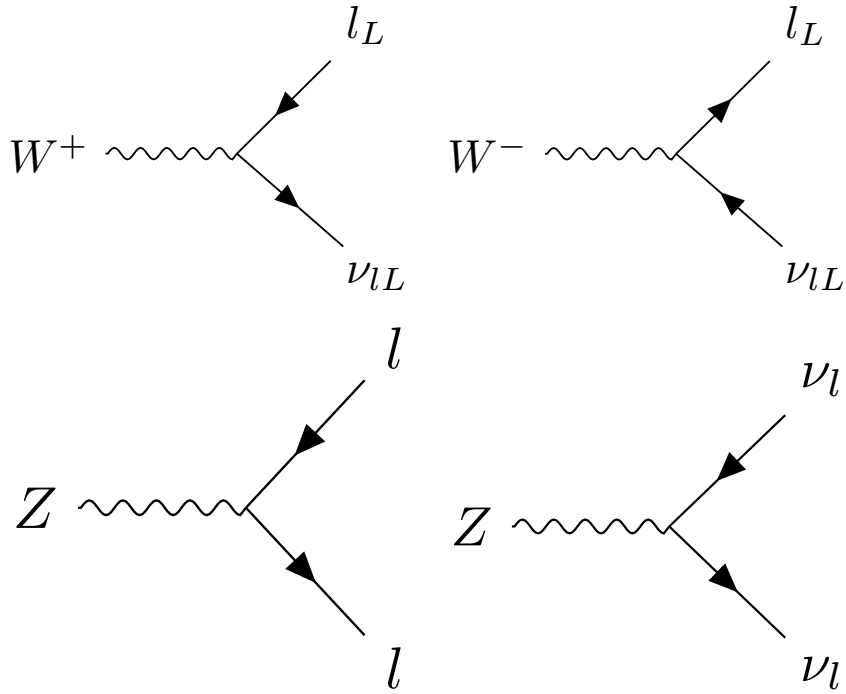


Figure 6: Feynman diagrams of weak couplings to leptons in the SM.

356 2.1.2.4 The Higgs Mechanism

357 The Higgs mechanism presents a way to generate a mass term for the
 358 electroweak gauge bosons. It is a scalar field, with a Lagrangian

$$\mathcal{L}_{Higgs} = \frac{1}{2}(\partial_\mu\phi)^*(\partial^\mu\phi) + \frac{1}{2}\mu^2\phi^*\phi - \frac{1}{4}\lambda^4(\phi^*\phi)^2 \quad (17)$$

359 where ϕ is a complex scalar field, $\phi = \phi_1 + i\phi_2$. This looks very similar to
 360 a standard scalar field Lagrangian, but the signs on the mass and interac-
 361 tion terms are reversed, implying an imaginary mass term. However, this
 362 isn't a good interpretation of the Lagrangian, because it differs from all
 363 previously considered Lagrangians in one important way: its ground state
 364 does not occur at $\phi = 0$. Because quantum field theory is perturbative, its
 365 validity only holds when expanded around a ground state, which, when
 366 calculated for this Higgs Lagrangian, must satisfy

$$\phi_1^2 + \phi_2^2 = \frac{\mu^2}{\lambda^4}. \quad (18)$$

367 The original Lagrangian can then be rewritten in terms of a field $v +$
 368 $H(x)$ centered around the ground state with energy called the vacuum
 369 expectation value defined as.

$$v = \frac{\mu}{\lambda^2}. \quad (19)$$

This rewriting produces a Lagrangian with a non-imaginary mass. However, in an effect called *spontaneous symmetry breaking*, the original $SO(2)$ rotational symmetry of the Lagrangian is lost, resulting only in a $U(1)$ rotational symmetry; the Lagrangian is invariant under a phase transformation.

As in [Section 2.1.2.1](#), it is possible to make the Lagrangian invariant under a local $U(1)$ transformation, $\phi \rightarrow e^{i\theta(x)}\phi$ by adding a massless gauge field A^μ and using the covariant derivative. Due to the many cross terms from the non-zero ground state, terms for the mass of one of the scalar bosons as well as the gauge field appear, leaving only one massless scalar boson. This massless boson, it turns out, can be completely removed from the theory via local $U(1)$ transformations, ultimately producing a theory with one massive scalar (the Higgs) and a massive gauge field (W).

The Higgs interaction with the weak gauge bosons also creates couplings between the particles, which can be seen in [Figure 7](#). There are also Higgs self-interaction terms included in the Lagrangian, producing vertices describing 3- and 4-Higgs interactions.

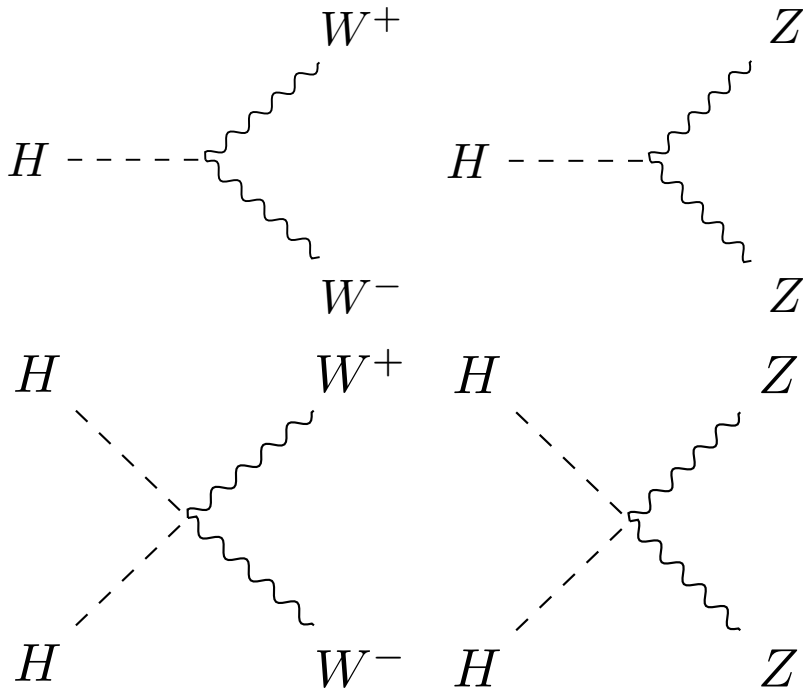


[Figure 7](#): Feynman diagrams demonstrating Higgs couplings to the weak gauge bosons in the [SM](#).

The remaining piece of the Lagrangian, \mathcal{L}_{Yukawa} describes the Higgs field's interactions with the fermions of the [SM](#), and can be written as

$$\mathcal{L}_{Yukawa} = -\Gamma_{mn}^e \bar{L}_m \phi E_n - \Gamma_{mn}^u \bar{Q}_m \phi U_n - \Gamma_{mn}^d \bar{Q}_m \phi D_n + h.c. \quad (20)$$

where *h.c.* is the hermitian conjugate term, and the Γ matrices are indexed by generation, and, when diagonalized, are proportional to the

391 masses of the fermions. The Higgs field's vacuum expectation value pro-
 392 duces terms that look like fermion mass terms. Additionally, terms that
 393 couple the fermions to the Higgs field are produced, with each fermion's
 394 coupling proportional to its mass, according to

$$g_f = \sqrt{2} \frac{m_f}{v} \quad (21)$$

395 where m_f is the mass of the fermion. Feynman diagrams for lepton and
 396 quark terms can be seen in [Figure 8](#).

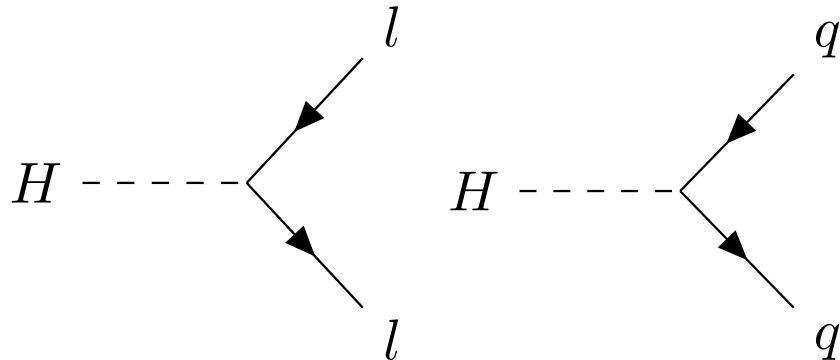


Figure 8: Feynman diagrams showing Higgs couplings to fermions in the [SM](#).

397 2.1.3 Phenomenology of Proton-Proton Collisions

398 As discussed in [Chapter 3](#), the [LHC](#) collides bunches of high-energy pro-
 399 tons, and the interactions of these protons' constituent quarks produce the
 400 wide array of particles seen in the ATLAS detector. The [LHC](#) typically cites
 401 its energy in terms of \sqrt{s} , the center of mass energy of protons in the two
 402 colliding beams, which in Run 2 is 13 TeV. However, because the proton is
 403 not fundamental, this energy is divided among many particles that make
 404 up the proton.

405 To first order, a proton consists of three quarks: two up quarks and one
 406 down quark, held together by gluons. However, a real quantum mechani-
 407 cal system is much more chaotic; in addition to these three quarks, called
 408 *valence* quarks, there are many others popping into and out of existence.
 409 These additional quarks are called *sea* quarks and can also carry fractions
 410 of the proton's energy.

411 The particles inside the proton can have a wide range of energies de-
 412 pending on the internal dynamics at the moment of the collision. These
 413 cannot be predicted exactly, but probabilistic models called Parton Distri-
 414 bution Functions ([PDFs](#)) describe the likelihood of any given configuration.
 415 These functions are determined using data from hard scattering experi-
 416 ments and give probabilistic estimates for how often a given type of parti-
 417 cle appears with a fraction x of the total proton energy, as seen in [Figure 9](#).

418 A classical proton model would suggest that each valence quark carries
 419 about one-third of the total proton energy. In practice, they each typically

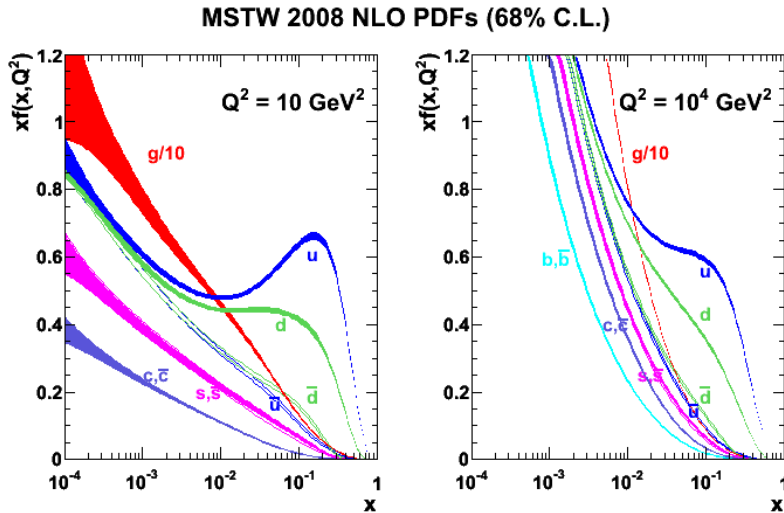


Figure 9: 2008 MSTW PDFs for various particle types given as a function of x and Q^2 , the square of the parton-parton momentum transfer. [15]

account for less than a third of the total energy, with the remaining energy divided among the many sea quarks and gluons. Thus, in a proton-proton collision, the initial particles rarely have more than a third of the beam energy, and often have a much lower energy resulting from the interaction of sea quarks.

These PDFs are used at the LHC to calculate the probability for a given process to occur, or its *cross-section*. The cross-section for a process to occur with a two-proton initial state is given by

$$\sigma(P_1, P_2 \rightarrow X) = \sum_{i,j} \int_0^1 dx_1 dx_2 f_i(x_1, Q^2) f_j(x_2, Q^2) \hat{\sigma}(x_1 P_1, x_2 P_2, Q^2) \quad (22)$$

where i and j are indices representing the partons within proton 1 and 2 respectively, $x_{i,j}$ gives these partons' momentum fraction, and $f_{i,j}$ gives their PDFs. $\hat{\sigma}$ gives the cross-section for a process going from partons to X , also referred to as the *matrix element*, and Q^2 gives the energy scale of this hard scattering of partons.

Matrix elements, in an ideal world, would include every possible Feynman diagram that describe the initial partons producing a given final state. In practice, the calculation of these diagrams can become very complicated when more and more loops are allowed. The simplest calculations, which include diagrams without any loops, are referred to as Leading Order (LO), while calculations including diagrams with one loop are called Next to Leading Order (NLO), and additional Ns can be added to describe more complex calculations.

Figure 10 shows cross-sections for many SM processes as a function of energy, demonstrating how processes involving high-mass objects have increasingly large cross-sections as the energy of the collider increases. In the analysis discussed in Part iv, the most important SM backgrounds are from

445 top quarks, Z bosons, and diboson processes (ZZ , WW , and WZ). Though
 446 Z boson production has the highest cross-section of those processes, it con-
 447 tributes the least to the background of the search because of the specific
 448 requirements made on events designed to reduce SM backgrounds. Details
 449 on these backgrounds and how they can appear as signal-like events are
 450 given in Chapter 7.

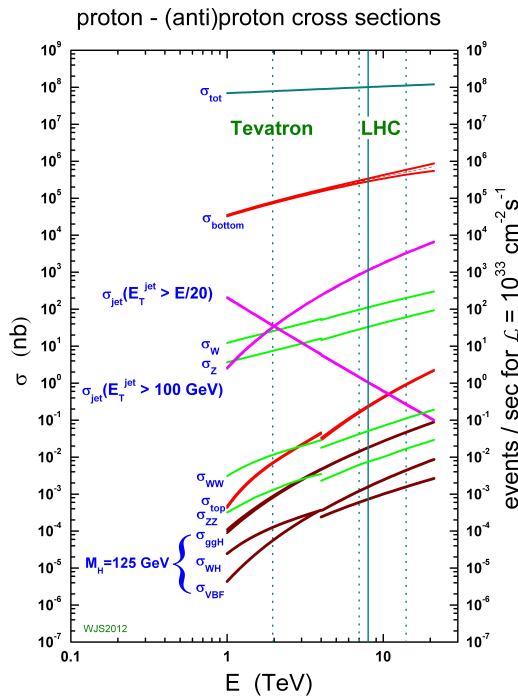


Figure 10: Cross-sections for many SM processes at the Tevatron and LHC [16].

451 2.1.3.1 Production of Jets in the ATLAS Detector

452 For most particles, the output of the hard scattering process is similar to
 453 the objects observed by a detector; electrons, photons, and muons emerg-
 454 ing from final states are all observed as they pass through sensitive ma-
 455 terials. There are exceptions: particles can radiate energy as they travel
 456 through the detector and photons can convert into electron-positron pairs,
 457 but in most cases, these final state particles can be directly observed. For
 458 color-charged particles, however, this is not the case.

459 As discussed in Section 2.1.2.2, quarks and gluons are strongly charged,
 460 and the coupling constant of the strong force increases asymptotically at
 461 large distance scales. As a consequence, colored particles undergo a pro-
 462 cess called *fragmentation*. Rather than continuing to propagate in a colored
 463 state, it is energetically preferable for high energy quarks and gluons pro-
 464 duced in hard scatterings to radiate additional colored particles, which can
 465 then be used to form colorless bound states. First, a process called *parton*
 466 *showering* occurs, in which many new colored particles are radiated from
 467 the original, creating a conic spray of particles along the original particle's

468 trajectory. This process repeats until the particles' energies reach the scale
 469 of hadronic masses, about 1 GeV. Next, these particles *hadronize*, forming
 470 composite particles that can propagate without interacting strongly.

471 The resulting spray of hadrons is called a *jet*, and it is jets, rather than in-
 472 dividual quarks or gluons, that are observed by particle detectors. Group-
 473 ing these particles into a jet is a non-trivial process, and is discussed in
 474 [Section 5.4](#).

475 Jets don't always come directly from the hard scattering process; colli-
 476 sions in the [LHC](#) often contain additional jets resulting from *initial and final*
 477 *state radiation*. In these processes, either the initial partons radiate energy
 478 (typically in the form of a gluon) or the products of the hard scattering
 479 process radiate additional colored particles before fragmentation occurs.

480 2.1.4 Problems in the Standard Model

481 Although the [SM](#) is a self-consistent theory that describes to great accuracy
 482 all of the particles and forces it includes, it does have certain shortcomings.
 483 The most glaring is the omission of gravity. Though the force is well un-
 484 derstood at large scales via the theory of General Relativity, no satisfying
 485 quantum description of gravity has been accepted, much less proven. The
 486 Planck scale, the energy scale at which gravitational interactions become
 487 large enough that no sound theory can ignore gravity, is at about 10^{19}
 488 GeV, 16 orders of magnitude above the electroweak scale, so the exclusion
 489 of gravity from the [SM](#) is unlikely to directly affect [LHC](#) physics.

490 Another clear omission of the [SM](#) is Dark Matter ([DM](#)), so named for its
 491 lack of electromagnetic interactions. This type of matter was first identi-
 492 fied in 1933 through the observation of galactic rotation curves [17]. The
 493 speed of rotation indicated both that there was more mass in the system
 494 than could be accounted for by observations made directly of the galaxy,
 495 and that this additional matter was distributed in a halo, not a disk like the
 496 typical luminous matter. This effect can be seen in [Figure 11](#), which demon-
 497 strates that the observed galactic density as a function of radius does not
 498 match the expected density from the luminous galactic disk. Since then, ev-
 499 idence for [DM](#) has been observed in colliding clusters [18], measurements
 500 of the cosmic microwave background [19], and in many more rotational
 501 curves, but the particles that form [DM](#) have never been directly detected
 502 or seen at a particle accelerator. As a consequence, very few details are
 503 known about the nature of this matter, only its density throughout the
 504 universe and that it does not interact strongly or electromagnetically.

505 Beyond the omissions of gravity and [DM](#), there are several aesthetic prob-
 506 lems with the [SM](#) - ones that could have no solution, but seem to suggest
 507 that the current [SM](#) are missing some pieces. The first is the sheer number
 508 of parameters in the [SM](#). There are 26 independent parameters determin-
 509 ing the mass of the particles and all the couplings between them. Besides
 510 the rough grouping of fermions into generations, there seems to be no or-
 511 der to masses of particles, and no way to predict many of the masses or
 512 couplings.

DISTRIBUTION OF DARK MATTER IN NGC 3198

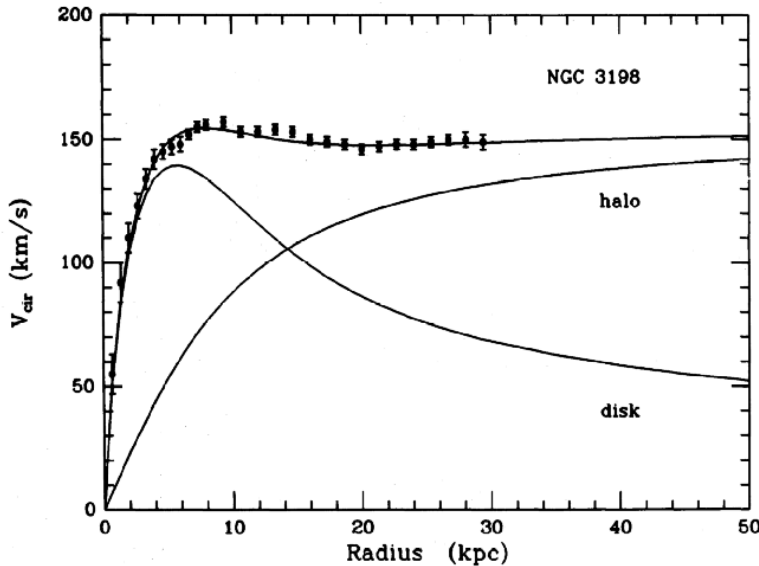


Figure 11: Galactic rotation curve of velocity as a function of radius in NGC 3198. Included is the observed data, as well as the expected velocity distribution from a disk-shaped galaxy corresponding to the expected density from electromagnetic observations. Another curve corresponding to a halo-shaped matter distribution is superimposed, and the halo and disk are summed and fit to the data. [20]

513 In the past, large numbers of seemingly unrelated parameters have indicated that a theory has a more fundamental form at shorter distance scales.
 514 The large number of elements, it turned out, could be explained by different groupings of three particles, the proton, neutron, and electron. Later,
 515 the menagerie of hadrons became so large that a similar re-imagining of
 516 what was fundamental took place, and the theory of quarks gave an order
 517 to the many mesons and baryons [21]. This pattern leaves physicists
 518 suspicious of any theory with too many particles and free parameters, sug-
 519 gesting that perhaps, at a higher energy, there is a simpler model that can
 520 unify many of the seemingly disparate elements of the SM.

521 In addition, some of these seemingly independent parameters have sus-
 522 picious symmetry. The Higgs mass, for example, has been measured to be
 523 125.7 ± 0.4 GeV[13]. This mass is the sum of the bare mass, the one that ap-
 524 pears in the Lagrangian, and quantum corrections from interactions with
 525 other particles, which are proportional to the square of the particles' mass.
 526 Since new physics must exist at the Planck scale to account for gravity,
 527 these corrections could be up to 35 orders of magnitude larger than the
 528 Higgs mass. Though the bare mass could theoretically cancel out this mas-
 529 sive correction, these parameters should be independent, and the odds
 530 that they would be precisely the same to 35 places are very, very small.
 531 This near-exact canceling is often called *fine-tuning*, an undesirable trait in
 532 a theory which suggests that some more fundamental symmetry has been
 533

Names	sparticles	particles	$SU(3)_C, SU(2)_L, U(1)_Y$
squarks, quarks	Q	$(\tilde{u}_L \tilde{d}_L)$	$(u_L d_L)$
	\tilde{u}	\tilde{u}_R^*	u_R^\dagger
	\tilde{d}	\tilde{d}_R^*	d_R^\dagger
sleptons, leptons	L	$(\tilde{\nu} \tilde{e}_L)$	(νe_L)
	\tilde{e}	\tilde{e}_R^*	e_R^\dagger
Higgs, higgsinos	H_u	$(\tilde{H}_u^+ \tilde{H}_u^0)$	$(H_u^+ H_u^0)$
	H_d	$(\tilde{H}_d^0 \tilde{H}_d^-)$	$(H_d^0 H_d^-)$
gluino, gluon	\tilde{g}	g	$(8, 1, 0)$
winos, W bosons	$\tilde{W}^\pm \tilde{W}^0$	$W^\pm W^0$	$(1, 3, 0)$
bino, B boson	\tilde{B}^0	B^0	$(1, 1, 0)$

Table 1: Supermultiplets of supersymmetric and SM particles. Sfermions, on the first five rows, are all spin-0. Higgsinos and gauginos are all spin-1/2. Three sets of each fermion's supermultiplet exist, one for each generation. [25]

missed. A *natural* solution, one free of this fine-tuning, is sought to resolve this SM problem.

2.2 SUPERSYMMETRY

Supersymmetry (SUSY) was proposed and developed in the 1970s to give solutions to many of these SM shortcomings [22–24]. The theory works by introducing a fermionic symmetry to the SM, in addition to the usual spacetime symmetries of translations, rotations, and changes of Lorentz frame. The combination of the usual spacetime with this fermionic dimension is called a *superspace*. Rotations in this dimension result in a particle's spin changing by 1/2, turning a spin-1/2 fermion into a spin-0 particle, for example. As a consequence, this symmetry requires the existence of many new particles - a bosonic *sfermion* for each fermion of the SM and a fermionic *gaugino* for each of the gauge bosons. These superpartners of SM particles should have identical quantum numbers to the original particle, except for their spins. Table 1 shows the SM particles and their superpartners.

If the theory is symmetric under these fermionic rotations, these particle-sparticle pairs can be described by a single *superfield*, which simultaneously describes the behavior of both SM and SUSY particles in the superspace. However, this completely symmetric behavior is untenable given basic observations of matter in the universe. For example, if there were a *selectron* (the superpartner of the electron, \tilde{e}), with identical mass to the electron, it would have been detected long ago. In fact, such a particle would fundamentally change atomic structure, with the bosonic selectrons capable of piling into the ground state of an atom, and removing all the

560 interesting valence-shell interactions of electrons that determine molecular
 561 structure. Thus, if SUSY does exist, the symmetry must be broken, so that
 562 the superpartners have much higher masses than the original SM particles.

563 **2.2.1 The Minimal Supersymmetric Standard Model**

564 The Minimal Supersymmetric Standard Model (MSSM) was designed to be
 565 the simplest supersymmetric extension of the SM that remains self consistent,
 566 and it results in the particles seen in Table 1[25]. The formulation
 567 of the MSSM begins by introducing a second Higgs doublet to account for
 568 the different masses of the sparticles. As with the SM Higgs, electroweak
 569 symmetry breaking results in the loss of degrees of freedom, and only
 570 five of the original eight states remain, the lightest of which, h^0 , can be
 571 interpreted as the SM Higgs already discovered. There are two remaining
 572 neutral states, A^0 and H^0 , as well as two charged Higgses, H^\pm .

573 The neutral Higgs states mix with the neutral gauge bosons, while the
 574 charged Higgs states mix with the charged gauge bosons, producing a
 575 series of states labeled only by their charge and the order of their masses.
 576 The neutral states, collectively called the neutralinos, are identified from
 577 lightest to heaviest, $\tilde{\chi}_1^0, \tilde{\chi}_2^0, \tilde{\chi}_3^0$, and $\tilde{\chi}_4^0$. The charged states, referred to as
 578 charginos, are similarly called $\tilde{\chi}_1^\pm$ and $\tilde{\chi}_2^\pm$.

579 The MSSM introduces many new interactions between SM particles and
 580 sparticles. Though these don't represent all possible interactions, a general
 581 rule is that any SM vertex can have two interacting particles replaced
 582 with their sparticle equivalents, and this vertex will be part of the MSSM.
 583 Figure 12 gives two examples of such vertices.

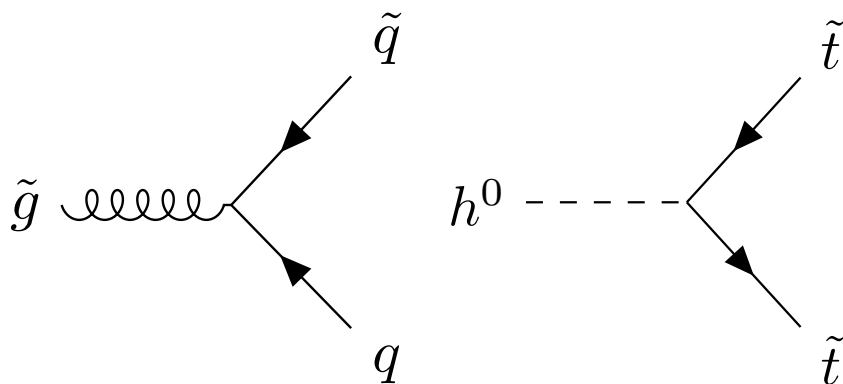


Figure 12: Two example vertices allowed by the MSSM.

584 In addition to these interactions, there are several terms that appear in
 585 the MSSM Lagrangian that violate the B and L conservation observed in
 586 the SM. In fact, these terms violate $B - L$, which, unlike B and L conser-
 587 vation individually, does not have even small violations in the SM. These
 588 superpotential terms appear as follows

$$W_{\Delta L=1} = \frac{1}{2} \lambda^{ijk} L_i L_j \bar{e}_k + \lambda'^{ijk} L_i Q_j \bar{d}_k + \mu'^i L_i H_u \quad (23)$$

$$W_{\Delta B=1} = \frac{1}{2} \lambda''^{ijk} \bar{u}_i \bar{d}_j \bar{d}_k. \quad (24)$$

Because there are very strong limits on non-conservation of $B - L$ from proton decay experiments, these terms present a challenge for the [MSSM](#). It would be possible, of course, to simply tune the λ parameters to be small enough to fit within experimental constraints, but these terms can also be eliminated by introducing a new conserved quantity, R -parity. It is defined by

$$P_R = -1^{3(B-L)+2s} \quad (25)$$

where s is the spin of the particle. Requiring that all terms in the Lagrangian have a multiplicative P_R of 1 excludes the terms in [Equation 24](#), removing the interactions that would lead to proton decay. All [SM](#) particles are R -parity even, while the sparticles are R -parity odd, so the conservation of R -parity can translate into a conservation of number of particles and sparticles. As a consequence, massive sparticles typically decay through a chain of lighter sparticles, emitting [SM](#) particles along the way.

2.2.2 Solutions to Standard Model Problems

Perhaps the most compelling consequence of [SUSY](#) comes from R -parity, which, through the formation of a new quantum number unique to sparticles, requires the Lightest Supersymmetric Particle ([LSP](#)) to be stable. This stable particle, if it is not electromagnetically charged charged, provides an excellent candidate [DM](#) particle. The lightest neutralino, for example, is a viable [DM](#) candidate because it does not interact electromagnetically or strongly, a constraint required due to measurements of the relic density of [DM](#) in the universe. An interaction cross-section higher than what's expected for weak interactions would have led the [DM](#) particle and its anti-particle to annihilate at lower densities, leaving a much smaller amount of [DM](#) in the universe than what is observed today [[26](#)].

Many believe that a complete [SM](#) should include a unification of the three forces, as electromagnetism and the weak force have already been unified. This requires that at some higher energy, the coupling constants of all three forces merge. However, in the [SM](#), the coupling constants come close to aligning, but don't perfectly cross. With the addition of [MSSM](#) particles with masses at the TeV scale, the alignment is near perfect, as shown in [Figure 13](#). This may be a mathematical coincidence, but it's very compelling to those physicists who believe that *grand unified theory* must exist.

[SUSY](#) also has the potential to solve the naturalness problem in the [SM](#). In the [SM](#), the massive amounts of fine tuning are required to cancel the

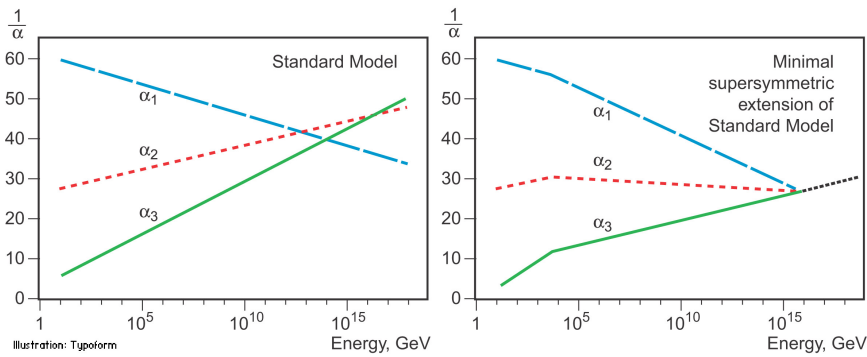


Figure 13: Running of the strong, weak, and electromagnetic coupling constants for the SM (left) and MSSM (right). [27]

quadratic corrections to the Higgs mass that result from loops involving, most importantly, the top quark. In the MSSM, an similar loop involving the stop quark (the vertex for which is depicted in Figure 12) contributes to the Higgs mass with the opposite sign, making it possible to naturally cancel the corrections without fine tuning. However, the larger the mass difference between the top quark and stop quark, the larger the remaining correction when the two terms cancel. Consequentially, to preserve a reasonable degree of naturalness (and here the definition of “reasonable” is subject to some debate), the stop quark should appear at masses not too much larger than the top’s, at approximately the TeV scale.

This naturalness mass limit, as well as the unification of couplings, make the argument for searching for SUSY at the LHC particularly compelling, as the LHC is the first collider capable of producing particles at the TeV scale. As new exclusions on SUSY are set, the remaining phase space becomes slightly less natural. But there is no shortage new SUSY models with unexcluded parameters, which are continually proposed as new limits are created.

2.2.3 Simplified Models of Supersymmetry

There are many different theorized models of SUSY, with different mechanisms for breaking the symmetry. The MSSM has 120 free parameters, with complex interactions that determine the mass hierarchy and interaction rates of the sparticles. From an experimental point of view, the details of these theories and the exact way the hierarchies are generated are less relevant to a search than their outputs.

Simplified models, which are typically inspired by more complete theories, are used to tune the observables of a model more directly. These models each consist of one production and decay diagram, with the masses and branching ratios of the particles free to be tuned directly. In a more complete theory, it is instead necessary to modify more fundamental parameters like the symmetry breaking scale. A change like this impacts the properties of all the sparticles, but the details of its impact are model dependent. The simplified models allow for relatively model independent

interpretations that can be reinterpreted in the context of a more complete SUSY theory [28].

In the analysis presented in Part iv, a simplified model is used which produces the decay depicted in Figure 14 with a 100% branching ratio. This decay chain begins with the pair production of gluinos, which decay via a pair of quarks to the second lightest neutralino, which then decay via a Z boson to the lightest neutralino. Only events in which the Z boson decays to pairs of electrons or muons are considered, with all-hadronic final states left to other searches [29]. The quarks emitted in the gluon decay are allowed to have flavors u , d , c , and s , each with a 25% probability. A similar model involving squark pair production is also considered, with the same breakdown of flavors. In this simplified model, the lightest neutralino is the LSP, and is stable.

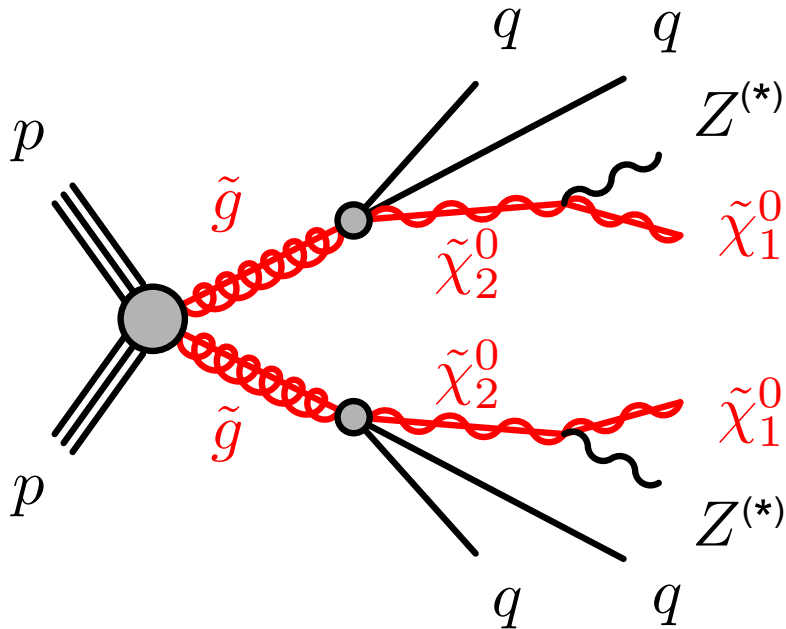


Figure 14: Feynman diagram of the decay considered in the simplified models used in the analysis presented in Part iv.

Using this simplified model, the masses of the particles can be set directly. This is very helpful for the generation of MC, discussed in Section 2.3, because a grid of different mass values of the important sparticles involved in the decay can be generated. Cross-sections calculations are performed for each point on these grids [30]. This grid allows analyzers to make predictions of likely signals, and to exclude the simplified models as a function of the mass of the sparticles in the case that no discrepancies between predictions and observations are seen.

2.2.3.1 Context and Motivation

This channel is well motivated from a theoretical perspective. Production of strongly charged sparticles, shown in Figure 15, is hypothesized to oc-

cur at much larger rates than the production of other particles, due to the difference in coupling constants. The specific decay considered in these simplified models does not have the largest branching ratio of all possible decays; even considering only changes to the SM decays involved, a $Z \rightarrow qq$ decay is roughly seven times more likely than $Z \rightarrow ll$. However, processes with higher branching ratios, like those producing an all-jet final state, often have much higher SM backgrounds, making them difficult to identify, even if they occur more frequently. This final state balances SM backgrounds and branching ratios, and when compared to other searches performed by the ATLAS collaboration, has competitive expected sensitivity to SUSY [31].

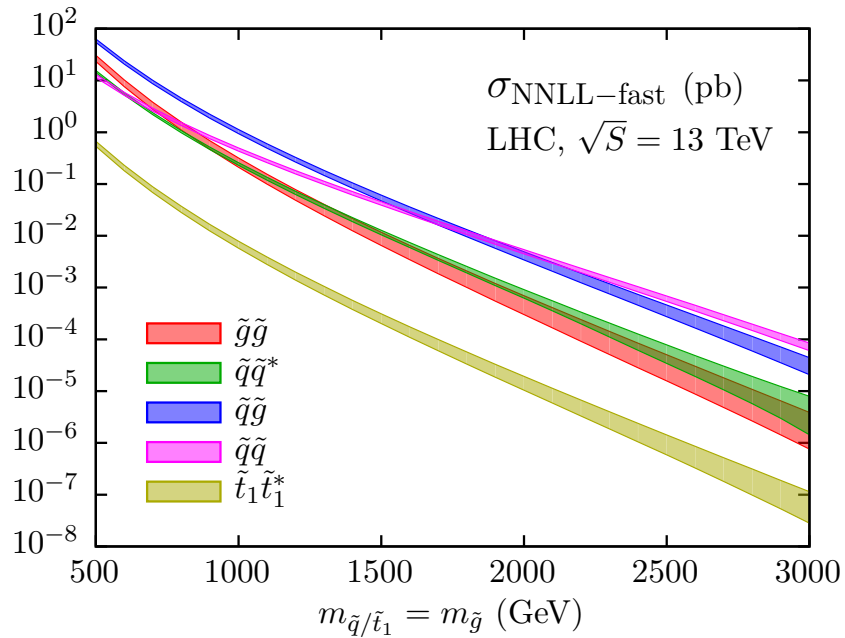


Figure 15: 13 TeV production cross-sections for sparticles, as a function of sparticle mass [32].

Processes similar to the one described by Figure 14 have been the target of previous LHC searches. Both CMS and ATLAS performed searches for SUSY in the two lepton channel with the 8 TeV data collected in 2012. The ATLAS search saw a 3σ excess, shown in Figure 16 [1]. The CMS search saw no excess in a similarly motivated signal region, albeit with different kinematic cuts than ATLAS's, following up on a 7 TeV search that saw no excess [33, 34].

Both searches also identified events with two leptons that weren't consistent with an on-shell Z decay, and in this region, an excess with a local significance of 2.4σ was observed by CMS, shown in Figure 17. No excess was observed by the ATLAS collaboration in a signal region with identical kinematic cuts [1].

These two excesses generated significant interest in the two lepton channel, and both CMS and ATLAS produced preliminary results in December 2015 with the first 3.2 fb^{-1} of 13 TeV data. ATLAS again reported an excess

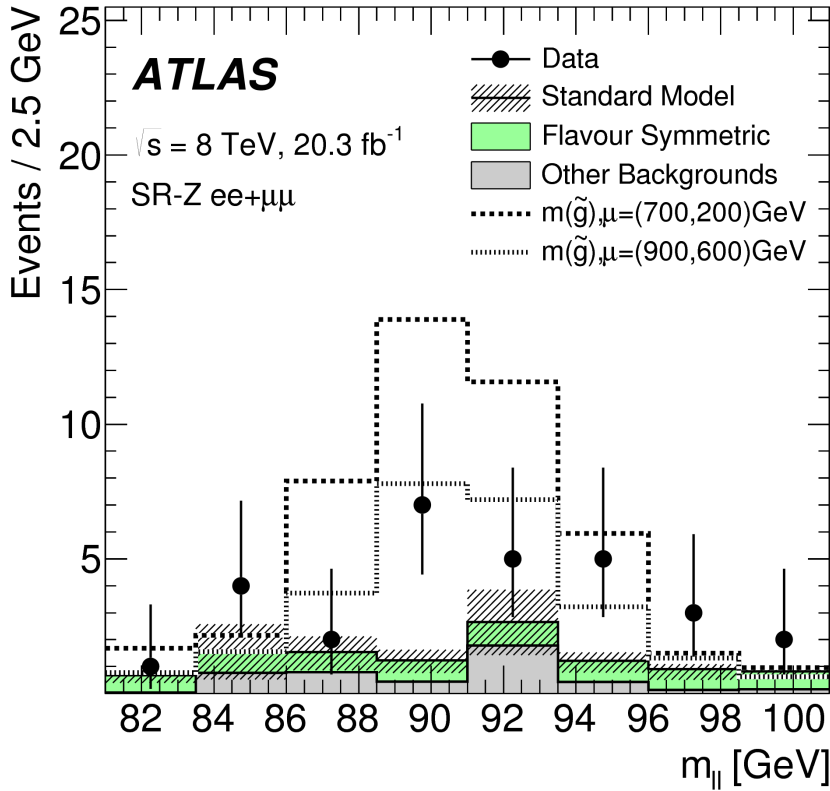


Figure 16: Results of an 8 TeV search performed by the ATLAS collaboration in a signal region targeting events like those in Figure 14. The events in the signal region are displayed as a function of m_{ll} , the invariant mass of the event's leading leptons. The SM backgrounds are shown with their full uncertainties based on data-driven background estimations, and two signals are superimposed on the distribution. The observed data-points are higher than the expected background, with a total excess of 3.0σ [1].

on the Z mass peak [2], shown in Figure 18, while CMS saw no excesses [35]. An all-hadronic ATLAS SUSY search released in 2016 which was sensitive to the same models also saw no significant excess [29].

2.3 MONTE CARLO EVENT GENERATION

The complex events of the LHC are difficult to model, but modeling them is crucial to analyzers' understanding of SM backgrounds and potential signals. To simplify the modeling process, particle interactions are broken down into very small steps, each with associated probabilities of various outcomes. This modeling method is called Monte Carlo simulation (MC), and, at the LHC it is broken into several larger steps which are each handled by different software.

The first step, discussed in Section 2.1.3, is to determine the energies of the initial particles in a collision, which are provided by several different PDF sets. These distributions come from experimental measurements,

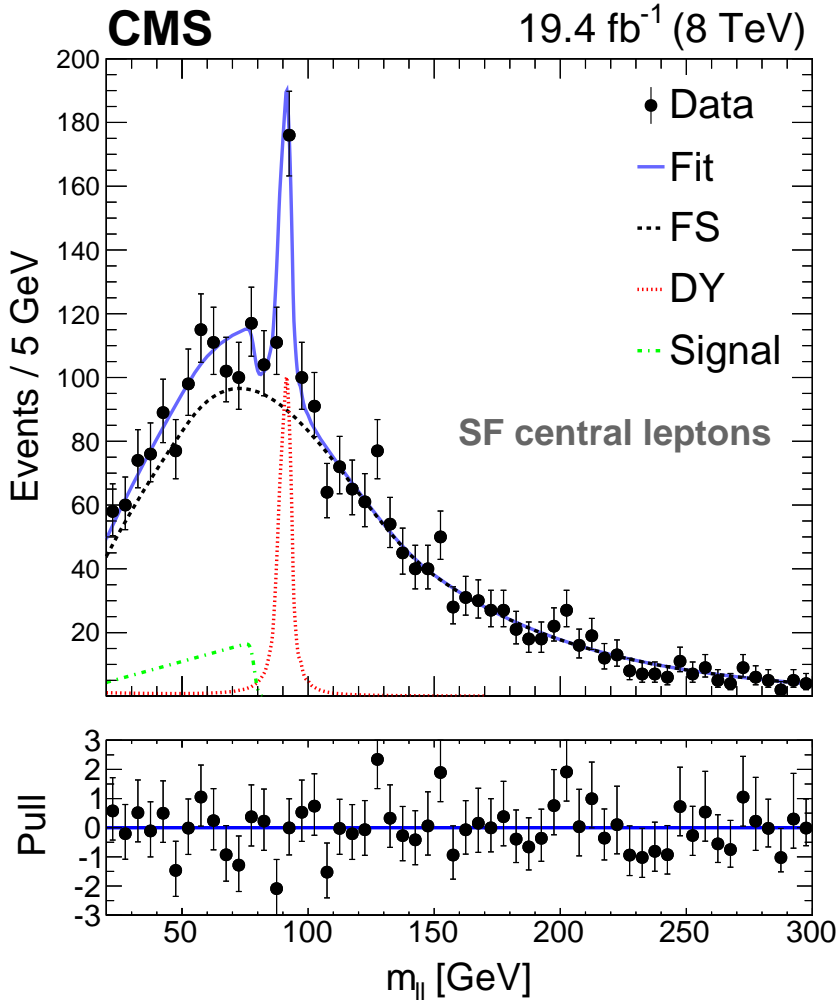


Figure 17: Results of an 8 TeV search performed by the CMS collaboration in a signal region including a broad range of $m_{\ell\ell}$. A 2.4σ local excess is seen in the low $m_{\ell\ell}$ region, and no excess of events is seen in the region with $m_{\ell\ell}$ consistent with an on-shell Z boson. The data is fit based on a data driven estimate of the flavor symmetric background (FS) and the Drell-Yan background (DY), with an additional component for the signal [34].

though there is some variation between different sets. Three different sets are used in this analysis: NNPDF2.3LO [36] and NLO CT10 [37] for background and signal processes, and MSTW 2008 [15] for pile-up events, discussed more in Section 3.4.

With the initial states of the constituents of the protons described by these probabilistic models, the next step is to model the hard scattering process resulting from the interaction of two of these particles. This is accomplished by a generator, which calculates the cross-sections of the Feynman diagrams of a given process. In particular, these generators typically produce matrix elements, which describe the probability to go from an initial to final state via a hard scattering, including the kinematic properties of the final state. The generator uses these matrix elements to assign

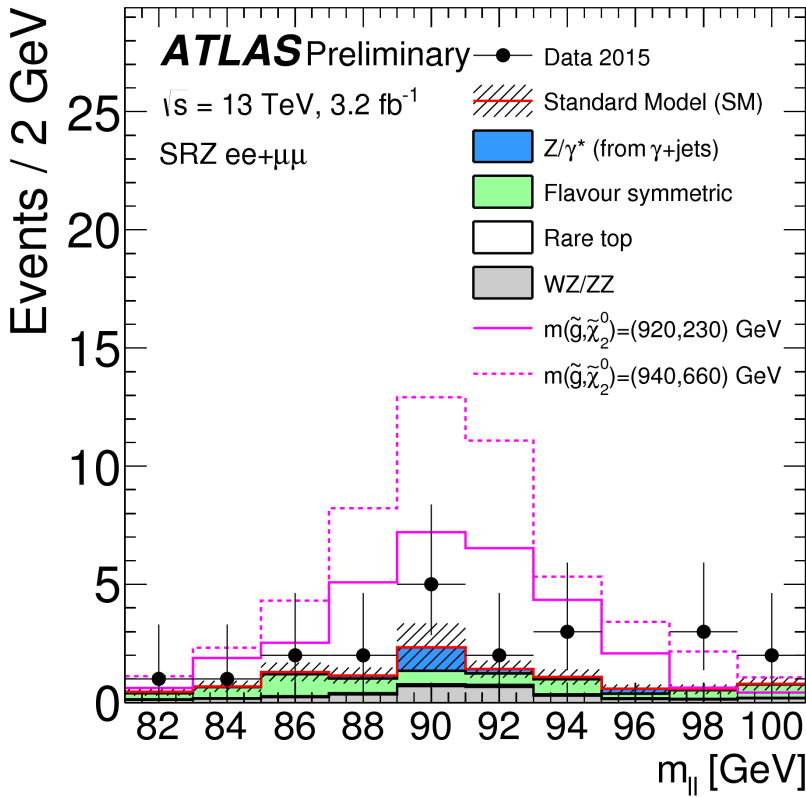


Figure 18: Preliminary results from a 13 TeV search targeting the same signal region as Figure 16, performed on 3.2 fb^{-1} of 2015 data. The events in the signal region are displayed as a function of $m_{\ell\ell}$, the invariant mass of the event's leading leptons. Flavor symmetric and Z/γ^* + jets backgrounds are taken from data-driven methods, while the other backgrounds are taken from MC. They are compared to the data, which shows a 2.2σ excess of events. Distributions from two signal points are superimposed [2].

one of these hard scattering final states to each event. These hard scattering outputs are then passed to the next step, where parton showering, hadronization, and final and initial state radiation can occur.

Because these matrix elements must be calculated for each event's specific kinematic properties, it can be very computationally intensive, especially when the calculations are performed at very high order. To save computational time, matrix elements are sometimes calculated at a lower order, and later, the total cross-section for a given process can be calculated at a higher order and used to scale the overall number of events generated for the process. These calculations can also be tuned, varying parameters in the generation to create outputs that most closely match experimental data.

Examples of generators include MADGRAPH5_AMC@NLO [38], POWHEG Box [39–41], and SHERPA [42]. Each has different strengths and is used to describe processes that best match those strengths. POWHEG Box, for example, cannot perform its own parton showering, and must be inter-

faced with another generator, typically PYTHIA [43], in order to describe any physics processes beyond the hard scattering, which can cause discontinuities in its predictions for large numbers of partons. However, it can calculate matrix elements at NLO, giving it an advantage in calculating some complex processes. SHERPA performs its own parton showering, but in most cases calculates its matrix elements at LO. The main advantage MADGRAPH5_AMC@NLO, which must also be interfaced with another generator perform parton showering, is its simple user interface. This makes it popular for producing SUSY signal samples, which must be done by each analysis team searching for a different SUSY process.

Once the final state particles of the hard interaction and showering have been calculated, the pile-up of the LHC (described in Section 3.4) must be accounted for. Events called *minimum bias* are generated to match the overall production of the LHC collisions, with no preselection. These events are overlaid on the original hard scatter to produce a more realistic representation of the many simultaneous interactions observed in the ATLAS detector.

This collection of particles must then be translated into signals in the detector. Their trajectories in the magnetic fields of the detector, their interactions in each layer, and the way these interactions deposit charge in each subdetector are modeled in software called GEANT4 [44]. In this software, every piece of the ATLAS detector is modeled, including the magnetic field and the many different materials. Particles then follow trajectories through the simulated detector and interact with the different materials based on several preprogrammed options for each material. For example a photon traveling through a material could continue along its trajectory, convert into a positron-electron pair, or deposit energy. As it crosses into a new material, a new set of options opens up for interactions. The particle is tracked until all of its energy is lost or it exits the geometry of the simulation.

The model of the detector used for this process is iteratively perfected by comparing data to MC. Figure 19 shows an example of a discrepancy between the simulation and observed data in the number of secondary vertices in a pixel module, which should correspond to the amount of material in the area. Observations of discrepancies like this can be used to correct the materials in the simulation.

Custom ATLAS code converts the energy deposited in active sensors into signals that resemble the expected detector response. These responses are typically very complicated with many parameters, and are frequently iterated on to best match the data. Electronic noise must also be added to correctly approximate the operating conditions of the detector. Additional alterations to this signal translation, including dead sensors and misalignments of the detector, can also be added at this stage.

Once the simulated particles have been converted into detector signals, the same reconstruction software used on data can be used on the MC, converting the detector signals back into particle interpretations. This reconstruction process is described in Chapter 5. The original information

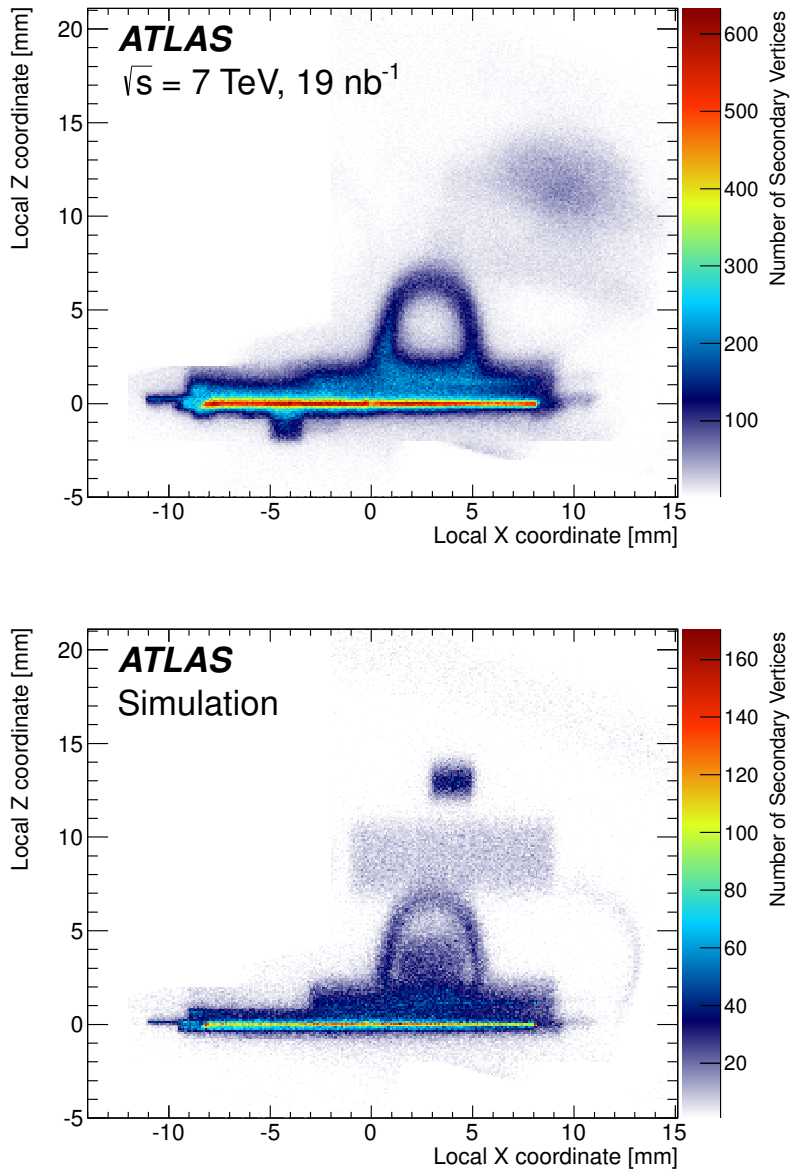


Figure 19: Number of secondary vertices in a module in the first layer of the pixel detector in data (top) and MC (bottom). There are more events in the data than the MC [45].

796 about the particles from the generator, referred to as *truth* information, is
 797 also kept, and can be compared to the reconstruction output to study its
 798 efficacy.

Part III

THE EXPERIMENT

801
802
803
804
805
806

This section describes the LHC and the ATLAS detector, which collectively provide the physical environment and the data collection for the analysis discussed in Part iv. Reconstruction of events in the ATLAS detector is also explained, with an emphasis on the reconstruction of tracks in the innermost part of the detector.

3

807

808 THE LARGE HADRON COLLIDER

809 The LHC is unique in the world, producing proton-proton collisions at en-
810 ergies an order of magnitude higher than any accelerator before [46]. It
811 provides unique environments at its collision points where massive, unsta-
812 ble particles can exist for an instant, then decay to the ordinary material of
813 the universe. It is the goal of the ATLAS experiment to identify these short-
814 lived particles, but the LHC's work of producing them is equally complex.

815 The LHC sits in a 26.7 km circular tunnel that straddles the French-Swiss
816 border outside of Geneva, originally built in 1989 for the Large Electron-
817 Positron (LEP) collider [47]. In the LHC, two beams of protons are accel-
818 erated to 6.5 TeV, then focused and collided at four points around the
819 ring, which can be seen in Figure 20. These points are each encased by
820 particle detectors, which can examine the outputs of the collisions, and
821 have different strengths and goals. The two multipurpose detectors are AT-
822 LAS and CMS, which have very complex detectors aimed and measuring
823 as many SM particles as possible and discovering new processes [48, 49].
824 Large Hadron Collider beauty (LHCb) examines processes related to the b
825 quark [50]. Meanwhile, A Large Ion Collider Experiment (ALICE) focuses
826 on special runs of the LHC which collide lead ions instead of protons, and
827 seeks to understand the high energy densities resulting from the collisions
828 of such massive, complex particles [51].

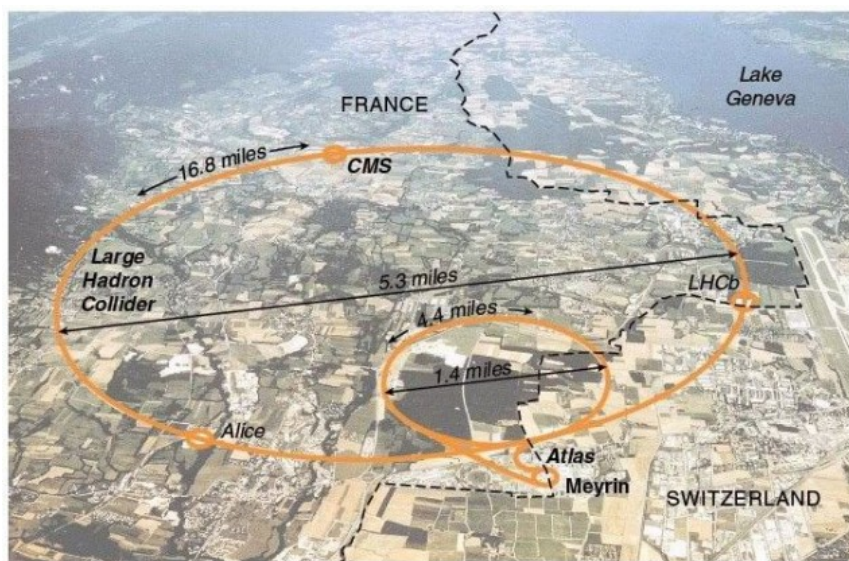


Figure 20: The LHC main collider ring and pre-accelerator SPS overlaid on a map of Switzerland and France, with the four main LHC experiments identified.

829 3.1 THE INJECTOR COMPLEX

830 The goal of the LHC is to provide high luminosity proton-proton collisions
 831 at 13 TeV. To achieve this, it must be capable of rapidly accelerating large
 832 numbers of protons and holding them at a constant energy, and organizing
 833 them into bunches which can be focused and collided at precise points
 834 and times. To do this, a complex system of pre-accelerators is required, as
 835 well as a precisely engineered system of magnets within the LHC. The full
 836 system of pre-accelerators is shown in Figure 21.

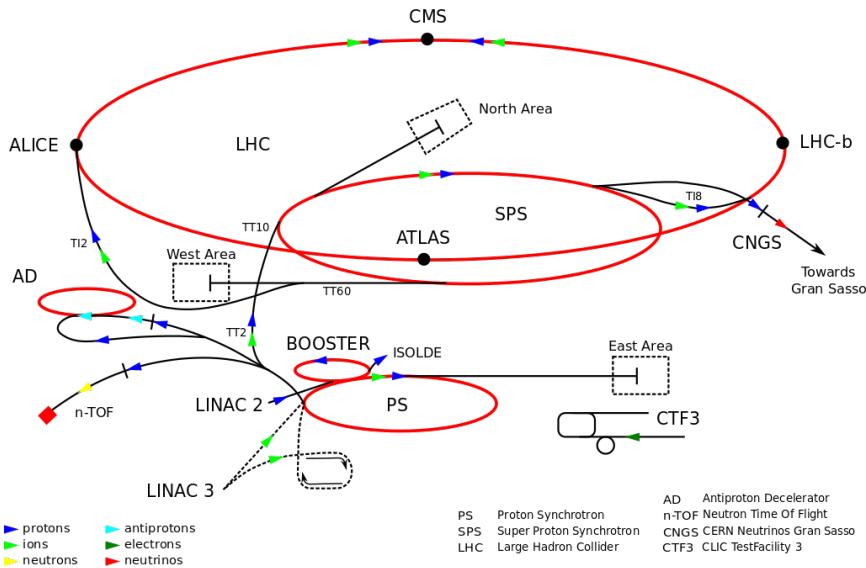


Figure 21: The pre-accelerators of the LHC.

837 The chain begins with when hydrogen gas is stripped of its electrons
 838 and injected in short pulses into Linac2, a linear accelerator which uses
 839 Radiofrequency (RF) cavities, which use alternating positive and negative
 840 electric fields to simultaneously push and pull particles forward through
 841 the accelerator. This RF behavoir keeps the bunches of protons resulting
 842 from the original pulses separated, beginning the formation of the bunch
 843 structure used for collisions. Quadropole magnets along the accelerator
 844 keep the beam focused. By the end of the accelerator, protons have reached
 845 50 MeV.

846 The proton beam is then injected into the Proton Synchrotron Booster
 847 (PSB), the first circular accelerator in the pre-accelerator chain. It increases
 848 its magnetic field as the protons increase in speed, ultimately accelerating
 849 them to 1.4 GeV.

850 At this point the proton beam moves on to the PS, a 600 m long circular
 851 accelerator that consists of 277 electromagnets that accelerate the protons
 852 up to 25 GeV, and 100 additional dipole magnets to bend the beam.

853 The last accelerator before injection into the LHC is the SPS, a 7 km long
 854 ring which, long before the LHC tunnel was built, was responsible for the
 855 discovery of the W and Z bosons. The SPS accelerates particles up to 450
 856 GeV before they are launched into the LHC.

Proton bunches are structured for ease of acceleration, with distinct features resulting from each of the pre-accelerators. The PS produces 72 bunches separated by 25 ns, which are injected into the SPS, as seen in Figure 22. However, as the magnetic field directing these protons out of the PS loop is turned on, there must be a gap in the bunch structure. Without this gap, called the injection kicker rise time, the changing magnetic field would direct particles out of the accelerator and produce high amounts of unsafe radiation around the PS. A similar gap in bunch structure is required for the injection from the SPS to the LHC. The injection process is repeated until the LHC is completely filled with around 2000 bunches, which takes about three minutes.

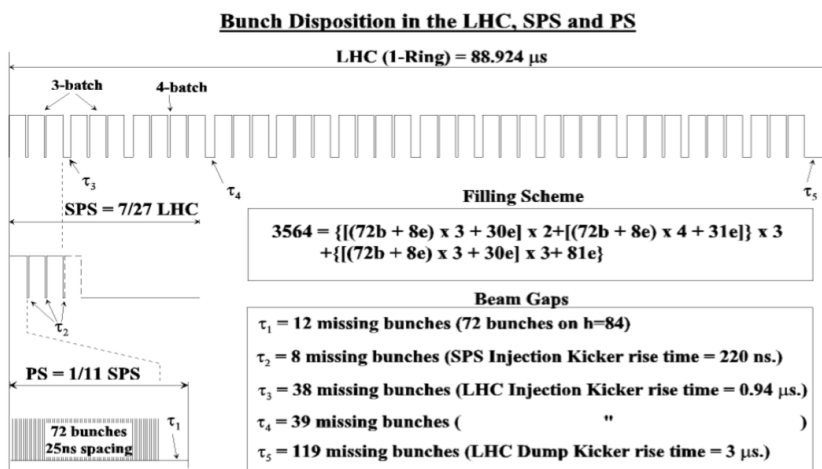


Figure 22: Bunch structure in the PS, SPS, and LHC.

3.2 OPERATION OF THE LARGE HADRON COLLIDER

The LHC consists of eight straight sections each connected by an arc. In each straight section, RF cavities accelerate protons, ultimately bringing them up to 6.5 GeV. Between these straight sections, 8.4 T dipole magnets bend the beams to maintain the approximately circular path. However, because the LHC is a proton-proton collider as opposed to a proton-antiproton collider, the two counter-rotating beams must be housed in separate rings and be accelerated separately. To achieve this, twin-bore superconducting magnets, one example of which can be seen in Figure 23, surround the two rings and accelerate them both. Quadropole magnets are used at the four collision points to focus the beams, which cross at an interaction point at the center of a detector. In total there are 1232 main dipole magnets over 5000 additional magnets, which are all superconducting and kept below their critical temperatures by liquid helium cooling.

When first injected into the LHC, the protons must be accelerated over many turns through the machine, with the magnetic field from the dipoles increasing with each pass to apply more force with which to bend the beam. Once the protons have reached a maximum energy, a process called

LHC DIPOLE : STANDARD CROSS-SECTION

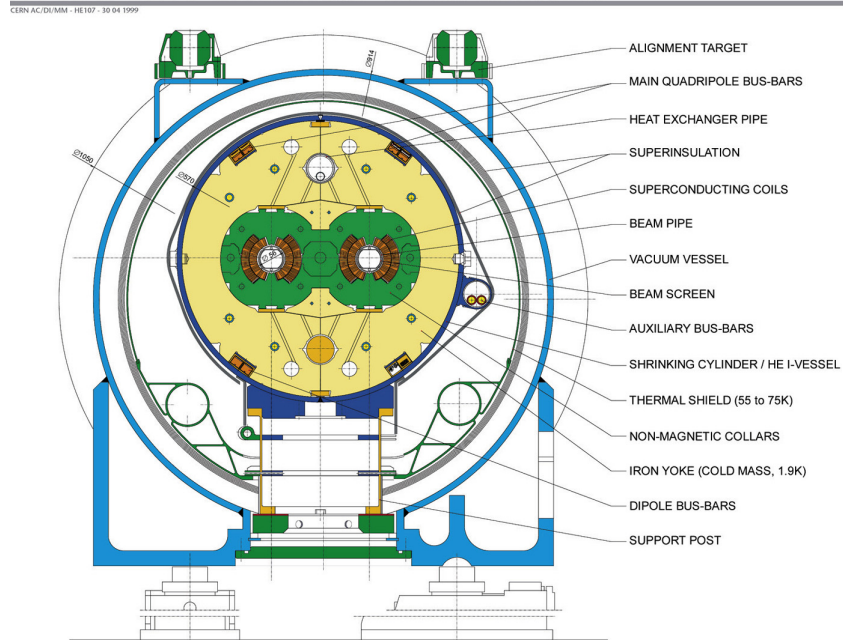


Figure 23: Cross-section of a cryodipole magnet in the LHC.

“squeezing” occurs, in which the total transverse area of the beam is reduced and bunches are elongated slightly. The shape produced by this process determines the “beam spot” for the ATLAS detector, the measurement of the area in which collisions occur within the detector. As shown in Figure 24, the collisions all occur very close together in the $x - y$ plane, but have a long spread in the z direction¹.

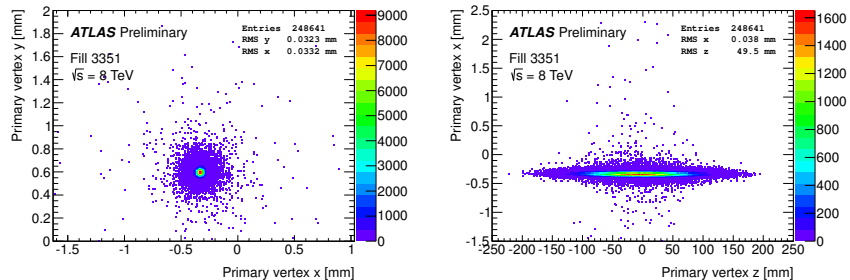


Figure 24: Beam spot in the ATLAS detector for one run in 2015. Distributions show only the highest p_T vertex per event. Left is the $x - y$ distribution of vertices, while the right plot shows the $x - z$ distribution.

Once the beams are at a stable energy and have been squeezed, the LHC indicates that it is physics-ready to the experiments around the ring, and, after some additional checks by each experiment, data-taking can begin. As collisions occur, the beam is depleted, and when it is sufficiently depleted to require a new fill, or if any instability occurs, the beam is dumped into a cavern filled with steel and concrete, which absorbs the energy.

¹ The coordinate system used here is discussed in Section 4.1.

899 3.3 LUMINOSITY

900 The goal of the collisions provided by the LHC is to produce SM and BSM
 901 particles, which can be observed by the detectors. How frequently a given
 902 process could occur was a crucial consideration in its design. The number
 903 of events of a given type is given by

$$N_{event} = L\sigma_{event} \quad (26)$$

904 where L is the luminosity delivered by the LHC and σ_{event} is the cross-
 905 section of the process in question. These cross-sections vary over many or-
 906 ders of magnitude for different processes, as shown in Figure 10, a plot of
 907 many different SM cross-sections. As a consequence, a very large amount
 908 of luminosity is required to produce the more rare events, and to have
 909 enough statistical power to differentiate them from other much more com-
 910 mon events.

911 The instantaneous luminosity at the LHC is given by

$$L = \frac{N_b^2 n_b f_{rev} \gamma_r}{4\pi \epsilon_n \beta^*} F \quad (27)$$

912 where N_b is the number of protons per bunch ($\sim 10^{11}$), n_b is the number
 913 of bunches in each beam ($\sim 10^3$), f_{rev} is the number of times per second
 914 that the beam travels around the ring, γ_r is the relativistic gamma factor,
 915 ϵ_n is the normalized transverse beam emittance, and β^* is the β -function
 916 at the collision point, which describes the transverse displacement of par-
 917 ticles in the beam. F gives the reduction factor due to the geometry of the
 918 beam crossings, and is given by

$$F = \left(1 + \left(\frac{\theta_c \sigma_z}{2\sigma^*}\right)^2\right)^{-1/2} \quad (28)$$

919 where θ_c is the crossing angle of the beams, σ_z is the RMS of the bunch
 920 length in the z direction, and σ^* is the same in the transverse direction.

921 As the proton beams circulate and collide, N_b decreases, producing a
 922 falling instantaneous luminosity, as seen in a Run 1 example in Figure 25.
 923 In Run 2, peak instantaneous luminosity was brought up to $10^{34} \text{ cm}^{-2}\text{s}^{-1}$.
 924 This high instantaneous luminosity and consistent running resulted in
 925 much faster data collection than in Run 1, which is depicted in Figure 26.

926 3.4 PILE-UP IN PROTON-PROTON COLLISIONS

927 One consequence of the high instantaneous luminosity is “pile-up”, or
 928 multiple simultaneously interactions. Because each bunch has on order
 929 100 billion protons, it is very likely that multiple protons will collide in
 930 the same bunch crossing. In fact, the average number of simultaneous
 931 interactions in 13 TeV data, shown in Figure 27, is about twenty.

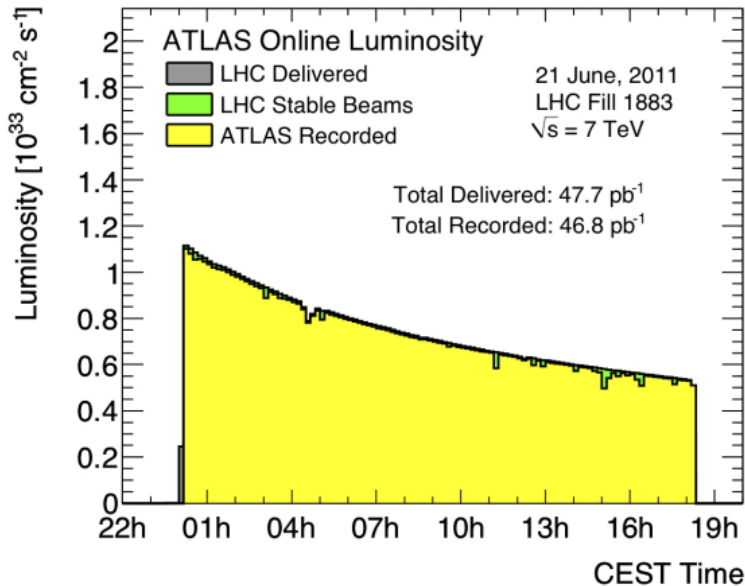


Figure 25: Instantaneous luminosity of one fill of 7 TeV data in 2011.

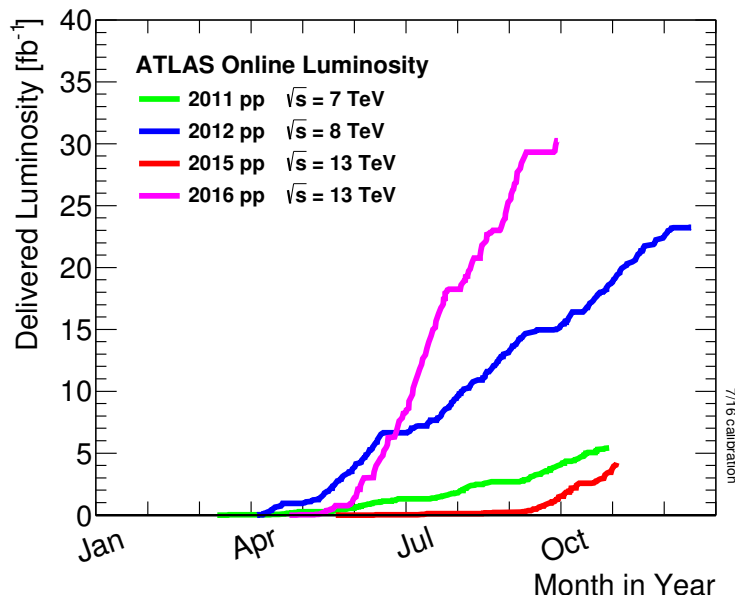


Figure 26: ATLAS luminosity for Run 1 and Run 2, as of September 2016.

932 Pile-up can be a difficult challenge for the ATLAS collaboration because
 933 it typically results in additional jets in an event, and can increase SM back-
 934 grounds for analyses seeking to identify events with jets. It can also add
 935 to the overall hadronic energy of an event, and that energy can be mis-
 936 assigned to other objects. Fortunately, it is typically possible to resolve the
 937 different vertices that each proton-proton collision makes, and so pile-up
 938 jets can be identified and rejected.

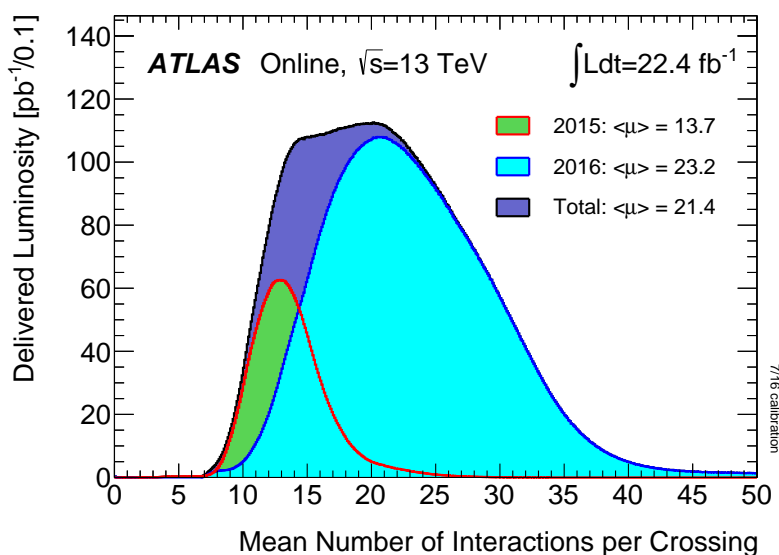


Figure 27: Average number of interactions per crossing shown for 2015 and 2016 separately, as well as the sum of the two years.

939

940 THE ATLAS DETECTOR

941 The ATLAS detector circumscribes the LHC’s beam pipe, enclosing the col-
 942 lision point with a series of particle detecting layers, aimed at making as
 943 many measurements of the particles leaving the collision point as possible.
 944 Its goal is to get a precise measurement of all the stable or semi-stable par-
 945 ticles flying from proton-proton collisions at its center, allowing analyzers
 946 to fully reconstruct the kinematics of the underlying processes.

947 The ATLAS detector is the largest detector of its kind, measuring 44
 948 m in length and 25 m in height, as seen in Figure 28. The size is mainly
 949 determined by the constraints of the MS, discussed in Section 4.4, which is
 950 the largest and outermost subsystem. The MS is submerged in a spatially
 951 varying magnetic field provided by three toroidal magnets, while the ID
 952 (Section 4.2) is encased by a superconducting solenoid, which provides a
 953 uniform 2 T field throughout its volume [48].

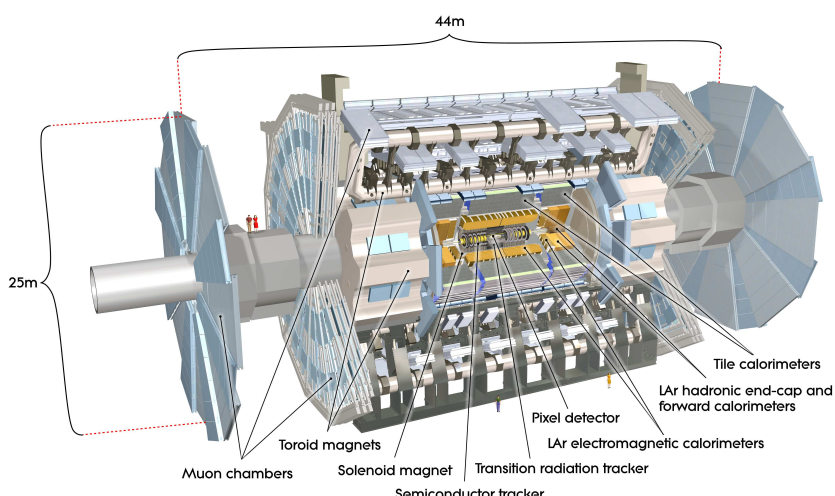


Figure 28: Diagram of the ATLAS detector, with subsystems and magnets identified.

954 4.1 COORDINATE SYSTEM USED IN THE ATLAS DETECTOR

955 The ATLAS detector is centered around the $p - p$ collision point, and is
 956 built radially out from the beam pipe, maintaining as much rotational
 957 symmetry around the beam pipe as possible. It is also symmetric in the
 958 forward-backward directions. A coordinate system using the collision point
 959 as the origin is used, with the beam line defining the z -axis. The positive
 960 x direction is defined as pointing to the center of the LHC ring, while the
 961 positive y direction points upwards. For ease of reference, the side of the

962 detector in the positive- z direction is referred to as the A side, and the
963 other side is referred to as the C side.

964 Because of the cylindrical design of the detector, angular coordinates are
965 often used. The azimuthal angle ϕ defines the angle around the beam pipe
966 and the polar angle θ defines the angle from the beam axis (z). However, a
967 transformation of the polar angle called pseudorapidity (η) is used more
968 often, and is defined as

$$\eta = -\ln[\tan \frac{\theta}{2}]. \quad (29)$$

969 η is used because the particle distribution from LHC collisions is roughly
970 uniform in this variable. Building on this definition, angular distance be-
971 tween objects is typically defined as

$$\Delta R = \sqrt{\Delta\eta^2 + \Delta\phi^2}. \quad (30)$$

972 Often variables are defined purely in the transverse plane, which is in-
973 dicated by a subscripted T , as in p_T , which gives an object's transverse
974 momentum.

975 4.2 THE INNER DETECTOR

976 The Inner Detector (**ID**) is responsible for the production of tracks, esti-
977 mates of the paths charged particles take as they travel through the detec-
978 tor. Collisions in the detector can produce about 1000 particles, so identi-
979 fying and differentiating all the tracks resulting from a collision is both a
980 hardware and a computational challenge.

981 The **ID** consists of three separate subdetectors, each of which has mul-
982 tiple layers capable of producing an electrical signal, called a *hit*, when a
983 charged particle travels through its active material. ATLAS tracking soft-
984 ware considers all these hits and forms tracks, with the goal of minimizing
985 fake tracks due to random noise and maximizing the efficiency of identi-
986 fying a real particle. Some details of this procedure are discussed in [Chapter 6](#). The full **ID** can be seen in [Figure 29](#), while a schematic in [Figure 30](#)
987 shows more detail on the placement of each layer.
988

989 4.2.1 *The Pixel Detector*

990 The pixel detector lies closest to the beam pipe of the LHC, and has four lay-
991 ers comprising 92 million pixels. There are three standard layers, referred
992 to as Layers 0-2 (L0, L1, L2), and an additional layer added for the 2015
993 data-taking, called the Insertable B-Layer (**IBL**).

994 4.2.1.1 *The Original Pixel Detector*

995 The Pixel Detector consists of high-precision silicon chip pixel modules,
996 with 1744 in total, and each module is made up of 16 sensors each with

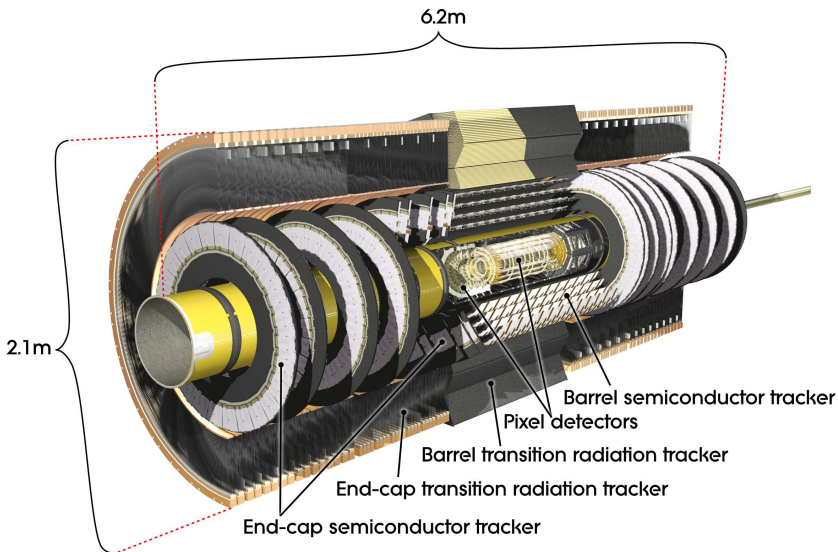


Figure 29: Diagram of the ATLAS Inner Detector, containing the Pixel, SCT, and TRT subsystems.

997 its own read-out system. Each sensor is identical, containing 47232 pixels,
 998 which are typically each $50 \times 400 \mu\text{m}^2$, though pixels at the edges of the
 999 sensors are slightly longer, at $50 \times 600 \mu\text{m}^2$.

1000 As shown in Figure 30, the central η region (barrel) is covered by three
 1001 concentric cylindrical layers of sensors, while the higher η region (end-cap)
 1002 is covered by a series of three disks positioned in the $x - y$ plane. Together,
 1003 they give complete coverage out to $|\eta| = 2.5$, and a particle coming from
 1004 the collision point will typically produce hits in three layers.

1005 The sensors are n-type silicon wafers with a voltage applied, and a pass-
 1006 ing charged particle produces thousands of electron-hole pairs inside the
 1007 material, which drift in the electric field towards the mounted read-out
 1008 system. A hit occurs when the resulting current becomes large enough to
 1009 pass a threshold designed to suppress noise. A larger total charge deposit
 1010 will result in the signal remaining over the threshold for a longer period
 1011 of time. The initial timing of the hit, and the Time Over Threshold (ToT)
 1012 are both recorded. This measurement is spatially accurate in the barrel
 1013 (endcap) to $10 \mu\text{m}$ in the $R - \phi$ direction and $115 \mu\text{m}$ in the $z (R)$ direction.

1014 4.2.1.2 Addition of the IBL

1015 In 2014, the IBL was added to the pixel detector. This layer sits on top
 1016 of the beam pipe, inside barrel Lo, providing a measurement of particles
 1017 only about 3 cm away from the interaction point. Its addition provides
 1018 greater precision for all track measurements, but it is especially useful for
 1019 the detection of B mesons, whose non-trivial lifetimes lead to secondary
 1020 vertices in ATLAS events. The location of the IBL gives a measurement
 1021 closer to these secondary vertices, and its increased pixel density increases
 1022 the probability that these vertices can be resolved.

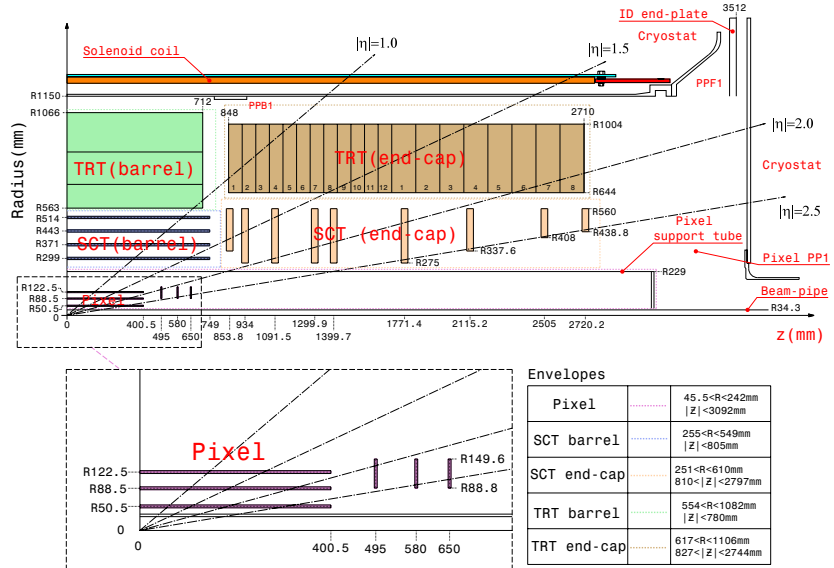


Figure 30: Diagram of one-quarter of the ATLAS Inner Detector in the $R - z$ plane, with lines drawn to indicate various η locations.

1023 4.2.2 The Silicon Microstrip Tracker

1024 The Silicon Microstrip Tracker (**SCT**) employs a similar technology to the
 1025 Pixel Detector, with 15912 sensors and 6.3 million readout channels. Its
 1026 difference from the Pixel Detector is in the readout, which is performed
 1027 by a series of 12 cm long strips with a width of $80\text{ }\mu\text{m}$. These layers are
 1028 paired, placed on top of one another at a small (40 mrad) angle to allow for
 1029 position determination in both directions, giving 4 spatial measurements
 1030 for each particle passing through the **SCT**. In the barrel, these strips run
 1031 parallel to the beam pipe, while in the endcap, they are arranged radially.
 1032 These strips have a resolution in the barrel (endcap) of $17\text{ }\mu\text{m}$ in the $R - \phi$
 1033 direction and $580\text{ }\mu\text{m}$ in the z (R) direction.

1034 4.2.3 The Transition Radiation Tracker

1035 The Transition Radiation Tracker (**TRT**) uses 4 mm diameter gas-filled tubes,
 1036 each with a high voltage wire suspended along the center of the tube. The
 1037 tubes run the length of the barrel, with a separate wire in the positive and
 1038 negative z direction. In the endcap, the tubes are arranged radially. In total,
 1039 there are about 351,000 readout channels in the **TRT**. This detector makes
 1040 measurements only in the $R - \phi$ direction, where the resolution of each
 1041 measurement is $130\text{ }\mu\text{m}$, and coverage extends to $|\eta| = 2.0$. Each particle
 1042 typically creates about 36 hits as it passes through the **TRT**.

1043 Particles passing through the gas mixture of the **TRT** ionize the gas, pro-
 1044 ducing electrons which drift towards the wire due to a potential difference
 1045 applied between it and the tube. The **TRT** also responds to low-energy trans-
 1046 sition radiation photons, which produce a much larger signal than charged

1047 particles passing through the detector. Because of this strong difference in
 1048 signals, hits from the [TRT](#) are used to help differentiate between electrons
 1049 and photons in the detector.

1050 4.3 THE CALORIMETERS

1051 Unlike the tracking detectors, which aim to take measurements of a parti-
 1052 cle with minimal alterations of its trajectory, the calorimeters measure the
 1053 energy of objects by stopping them entirely. The calorimeters, which can be
 1054 seen in [Figure 31](#), provide coverage out to $|\eta| < 4.9$. High granularity elec-
 1055 tronagnetic measurements are made within $|\eta| < 2.5$ to complement the
 1056 [ID](#)'s tracking capability. In this range, high p_T electrons and photons have
 1057 nearly straight tracks, making momentum measurement through track cur-
 1058 vature difficult, leaving the calorimeter as the primary energy measure-
 1059 ment. The hadronic calorimeters, as well as the higher $|\eta|$ electromag-
 1060 netic calorimeters, have a coarser granularity.

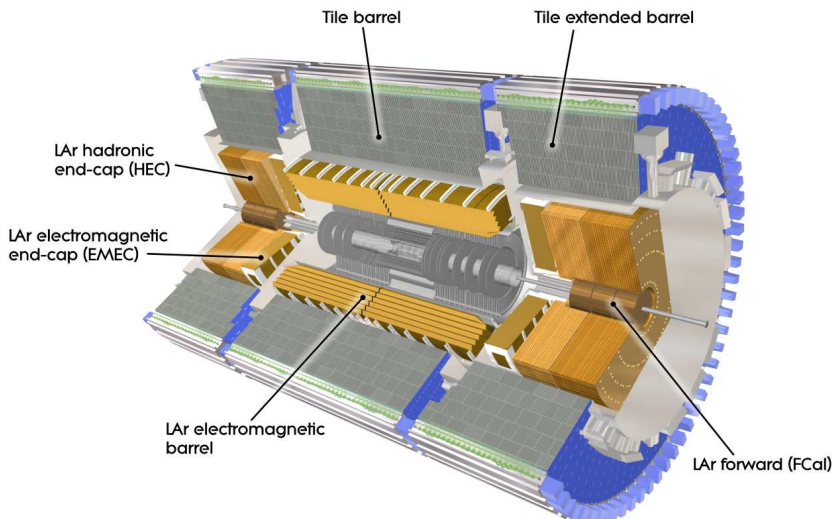


Figure 31: The calorimeter system of the ATLAS detector.

1061 Besides measuring the energy of passing particles, another task of the
 1062 calorimeter system is to limit punch-through to the [MS](#), described in [Sec-](#)
 1063 [tion 4.4](#). All other particles must be fully stopped by the calorimeters to
 1064 allow for clean signals from muons, and to measure the total energy of the
 1065 particle. This requirement sets a minimum number of interaction lengths
 1066 for each of the calorimeters.

1067 **THE LAR ELECTROMAGNETIC CALORIMETER** uses liquid argon as its
 1068 active detector medium alternating with layers of lead acting as the ab-
 1069 sorber. The layers are shaped like accordions, which allows for complete
 1070 coverage with multiple layers of active material, three in central η ($0 <$
 1071 $|\eta| < 2.5$) and two at higher η ($2.5 < |\eta| < 3.2$). [Figure 32](#) shows the layout
 1072 of a central η module, including this accordion-like layering. At $|\eta| < 1.8$,

1073 an instrumented liquid argon presampler provides a measurement of en-
 1074 ergy lost prior to reaching the calorimeters. The total energy resolution for
 1075 this detector is about 10%.

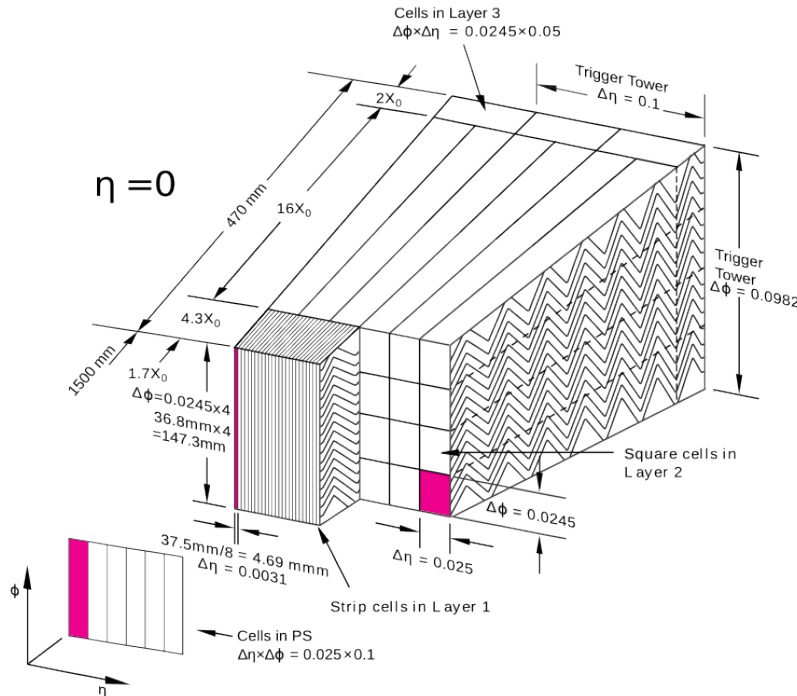


Figure 32: Layout of the LAr calorimeter module at central η [48].

1076 **THE TILE CALORIMETER** is a hadronic calorimeter which surrounds
 1077 the LAr Calorimeter. It uses layers of steel as its absorber with scintillating
 1078 tiles as the active material between them, which are read out by photomul-
 1079 tiplier tubes. The Tile Calorimeter covers $|\eta| < 1.7$ with a typical energy
 1080 resolution of about 50%.

1081 **THE LAR HADRONIC ENDCAP CALORIMETER** covers the hadronic calorime-
 1082 try for higher η . It uses liquid argon active material and copper plate
 1083 absorbers, resulting in an energy resolution of approximately 50%. This
 1084 calorimeter covers $1.5 < |\eta| < 3.2$, overlapping with the hadronic calorime-
 1085 ters in either direction of its η range.

1086 **THE FCAL** or forward calorimeter provides electromagnetic and hadronic
 1087 coverage at very high η ($3.1 < |\eta| < 4.9$). This calorimeter also uses liquid
 1088 argon as its active material, and uses copper-tungsten as the absorber. Its
 1089 energy resolution is about 100%.

1090 4.4 THE MUON SPECTROMETER

1091 The Muon Spectrometer ([MS](#)) measures charged particles that penetrate the
 1092 calorimeter system. Because the calorimeters are designed to completely

absorb electrons, photons, and hadrons, the [MS](#) mainly detects muons, which pass through the calorimeter with very little loss of energy. The goal of the [MS](#) is to give a high-precision measurement of these muons, and also to be able to quickly identify events with muons for the sake of triggering, discussed in [Section 4.6](#). The layout of the [MS](#) can be seen in Figures 33 and 34. Muons can be measured for all $|\eta| < 2.7$, and they can be triggered on for $|\eta| < 2.4$. The entire system is about 24 m tall and 40 m long.

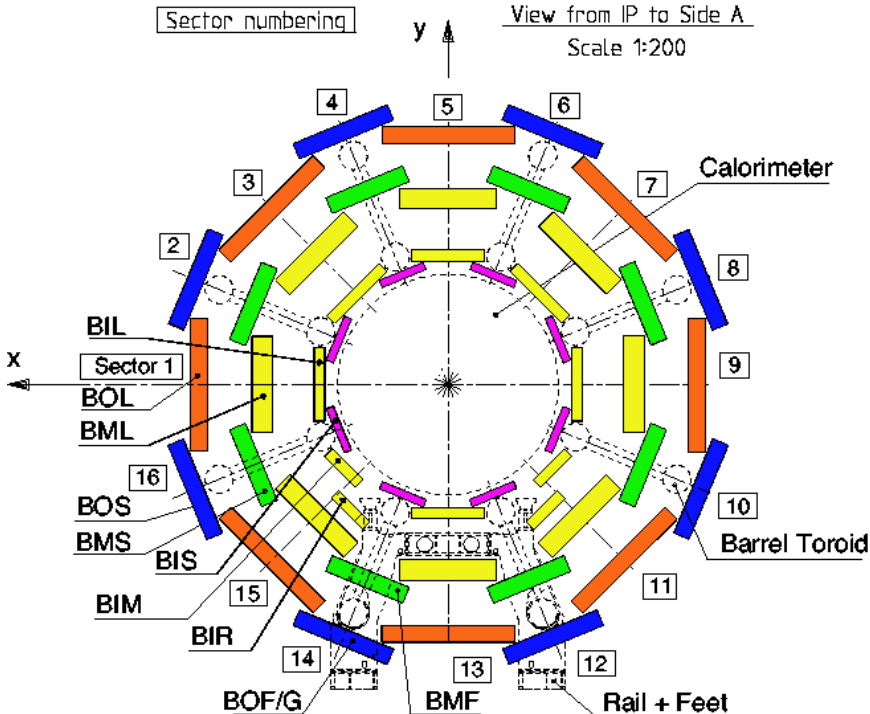


Figure 33: An x - y view of the [MS](#). In it, the three barrel layers are visible, as well as the overlapping, differently sized chambers. The outer layer of the [MS](#) is about 20m in diameter.

To achieve these goals, the [MS](#) has several subsystems. The system responsible for precision measurement is called the Monitored Drift Tubes ([MDTs](#)). This subdetector consists of chambers of three to eight layers of tubes, with three layers of chambers covering both the barrel and end-cap regions. In the barrel, these chambers are arranged in layers concentric cylinders with small overlaps between adjacent chambers. The chambers are oriented such that the drift tubes are parallel to the beam line. In the endcap, the chambers form disks with drift tubes approximately aligned in the R direction.

The tubes each contain an Ar/CO₂ gas mixture and a single high voltage wire which runs at its center along its length. Charged particles excite the gas as they pass through it, producing electrons which drift towards the high voltage wire. The resulting electric signal is read out, and the magnitude and timing of the signals are both used to differentiate particle traces from noise.

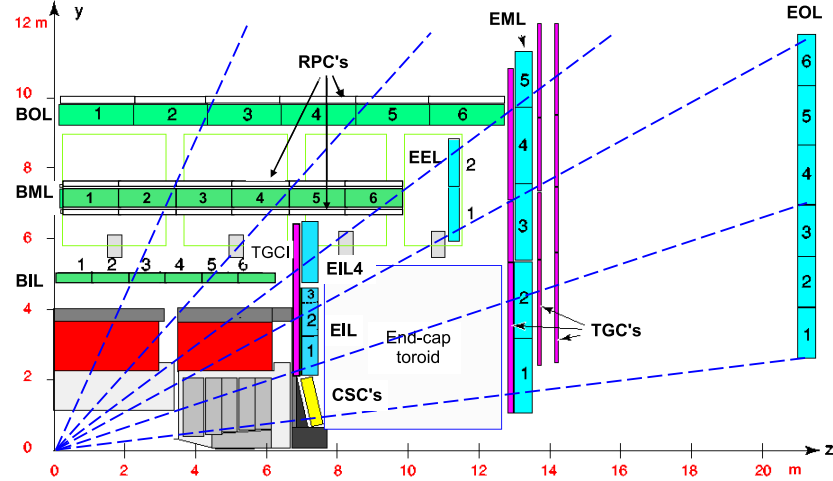


Figure 34: An r - z view of the MS. The three layers of the barrel and endcap MS are visible, and all muons at $|\eta|<2.7$ should traverse three detectors, assuming they propagate in an approximately straight line from the interaction point.

Though very effective at giving a precise measurement, the MDTs have two shortcomings. The first is that the measurement is only precise in the direction perpendicular to the tubes; in the direction parallel to them, the resolution is not much better than the length of the drift tube, which are typically several meters long. The resolution in the perpendicular direction is about $35\ \mu\text{m}$ with the combined measurement of all the tubes in a chamber. The second major shortcoming is that the MDTs are slow, with a maximum drift time of about 700 ns.

The slow drift time means that muons from sequential collisions can appear in the same event, and that the signals from the MDTs are received too late to be used for triggering. To solve the former problem, another detector called the Cathode-Strip Chambers (CSCs) is used in high-rate regions of the MS. This detector consists of multi-wire proportional chambers which have cathode strips on either side of the anode in orthogonal directions, providing a $40\ \mu\text{m}$ resolution in one direction and 5mm resolution in the other. Their drift times are much shorter than those of the MDTs, at about 40 ns. They are placed in the forward region of the detector ($2<|\eta|<2.7$) where the incident particle rates are highest.

To achieve responses fast enough to be used for triggering, Resistive Plate Chambers (RPCs) and Thin Gap Chambers (TGCs) are used. These chambers both take less than 25 ns to produce a signal. The RPCs are used in the barrel and are made up of two high-resistance plastic plates with a gas mixture under an electric field between them. Passing particles ionize this gas, and the resulting signal is read out via metallic strips mounted to the plastic plates. The TGCs used in the endcap are a form of multi-wire proportional chambers, like the CSCs. Unlike the CSCs, the cathode is placed extremely close to the wires, speeding up its operation.

1143 The massive **MS** is subject to deformations due to gravity and the mag-
 1144 netic field. To achieve a high precision alignment, these deformations are
 1145 constantly monitored in each **MDT** chamber with a set of four optical align-
 1146 ment rays, which give alignment information at the precision of $<30\ \mu\text{m}$.
 1147 In addition, a sag-adjustment system can use this information to re-align
 1148 any wires that droop under gravity's pull. Lastly, the **MS** can be aligned
 1149 using the tracks made from hits it measures, discussed more in [Section 5.3](#).

1150 4.5 THE MAGNET SYSTEM

1151 The ATLAS magnet system consists of four superconducting magnets: an
 1152 inner solenoid, a barrel toroid, and two endcap toroids. Collectively, they
 1153 are 22m in diameter and 26m long, and their basic layout can be seen in
 1154 [Figure 35](#).

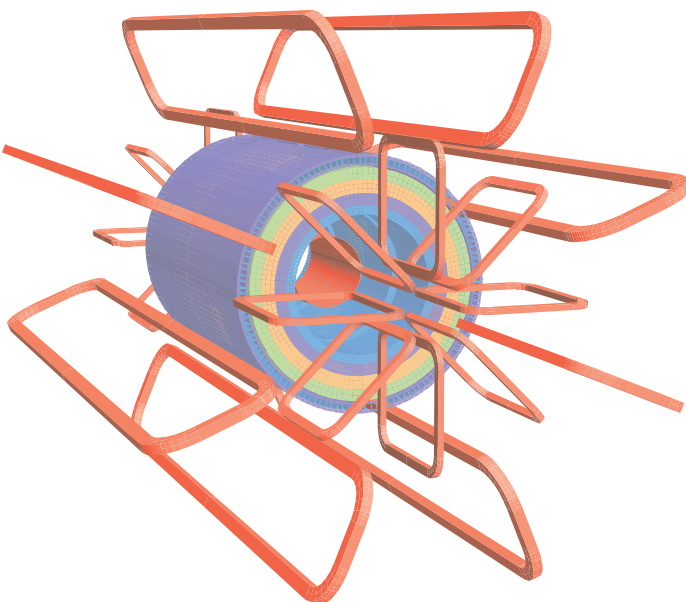


Figure 35: The magnet system of the ATLAS detector. The inner cylinder shows the solenoid which gives a uniform magnetic field in the **ID**. Outside of that are the barrel and endcap toroids, which provide a non-uniform magnetic field for the **MS**.

1155 The solenoid is inside the calorimeter volume and provides a uniform
 1156 2T magnetic field for particles traveling through the **ID**. This axial field
 1157 causes the trajectories of charged particles to bend in the $x - y$ plane, and
 1158 measurements of the curvature of these trajectories give the most accurate
 1159 p_{T} measurement for many particles according to the equation

$$p_{\text{T}} = qB\rho \quad (31)$$

1160 where q is the charge of the particle, B is the magnetic field in the z
 1161 direction, and ρ is the radius of curvature.

Because the solenoid is placed between the tracking system and the calorimeter, it is important that it interfere minimally with particles in order to allow the calorimeter to measure their full energies. The solenoid is placed inside the same vacuum chamber as the LAr calorimeter and is made of Al-stabilized NbTi superconductor with aluminum casing, giving it a total thickness of about 0.66 radiation lengths.

The barrel toroid is outside the calorimeters and provides the magnetic field for the barrel [MS](#), which varies from 0.2–2.5T. The endcap toroids have a magnetic field range of 0.2–3.5T. All three toroid magnets are made with Al-stabilized Nb/Ti/Cu superconducting coils supported by Al-alloy struts.

The magnets are cooled with liquid helium, and take up to a month to be brought down to operating temperatures. All magnets have cold masses surrounding them to absorb heat in the event of a quench.

The B -field resulting from this magnet system can be seen in [Figure 36](#). The plot on top demonstrates the relatively constant field rate within the barrel which drops steeply at $|z|=2$. The bottom plot shows the field integral in the [MDTs](#) as a function of $|\eta|$, demonstrating the good coverage out to $|\eta|<2.6$ excluding a transition region between the barrel and endcap, where the field changes rapidly, making precise p_T construction difficult.

4.6 THE TRIGGER SYSTEM AND DATA ACQUISITION

The [LHC](#) provides proton bunch crossings every 25 ns, and each of these events contains about one MB of data, corresponding to 40 TB/s, a completely unmanageable amount of data. In addition to this concern, many of ATLAS’s subdetectors like the pixel detector and [MDTs](#) take much longer than 25 ns to read out, making keeping up with the bunch crossing rate impossible. To reduce the total data read out and allow for selective reading out of the slower detectors, a triggering system is used.

The trigger system uses fast detectors to get a coarse picture of an event’s topology, which is then compared to a trigger menu, which lists the types of events that are interesting enough to keep. Overall, the trigger system reduces the 40 million events a second to about 1000 to be fully read out from the ATLAS detector.

This filtering of events is done in two steps: the [L₁](#) trigger is implemented in hardware and reduces the initial 40MHz to 100kHz, while the [HLT](#) is implemented in software, further reducing the rate to 1kHz [[52](#)]. The [L₁](#) trigger uses coarse granularity information from the fast read-out subdetectors: the calorimeters, the [RPCs](#) and [TGCs](#).

The coarse grained calorimeter information used for the [L₁](#) trigger decision is referred to as L₁ Calorimeter Trigger ([L₁Calo](#)) and uses information from all calorimeter systems. [L₁Calo](#) is responsible for all triggers excluding muons, meaning it must be capable of identifying a large number of different objects and event topologies, including high- p_T objects, E_T^{miss} , and large amounts of hadronic energy. The trigger can also identify isolated

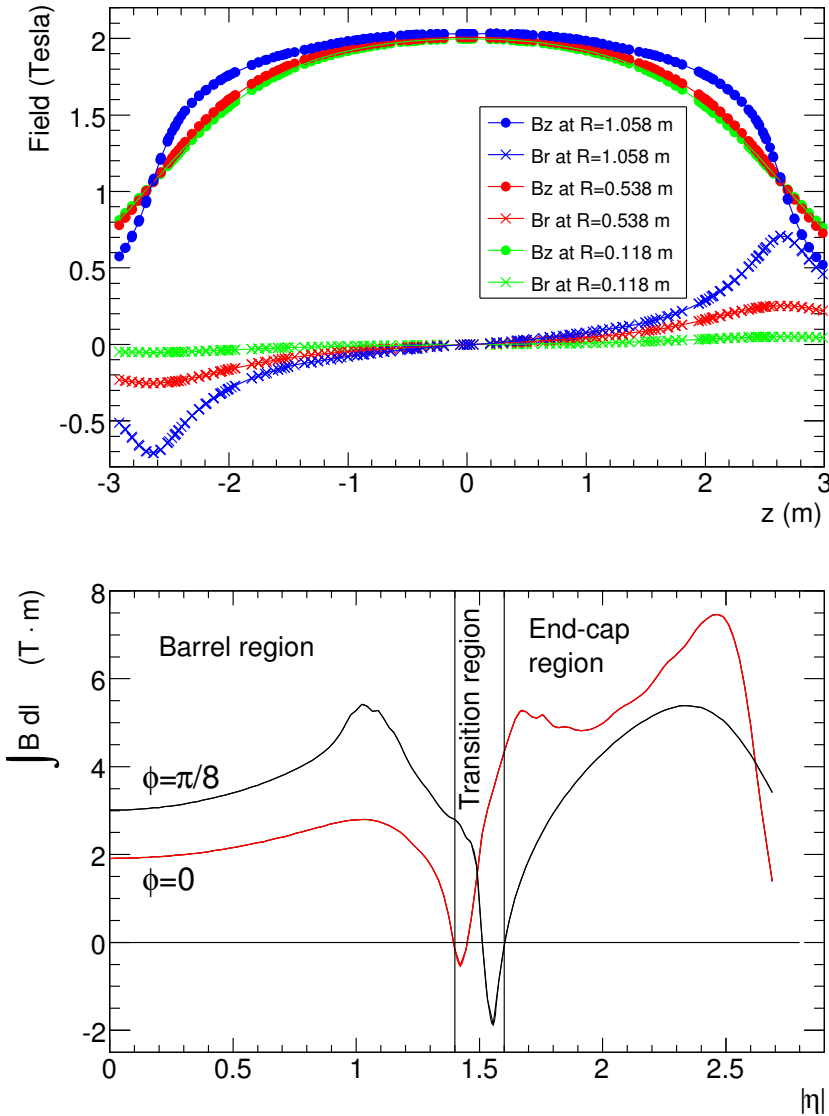


Figure 36: Plots of the magnetic field within the ATLAS detector. Top is the field (broken into its R and z components) as a function of z for several different values of R . Bottom is the field integral through the MDTs as a function of $|\eta|$ for two different ϕ values.

1206 objects, objects with very few calorimeter deposits from other objects near
 1207 them.

1208 For muon triggers, the trigger algorithm looks for patterns of hits from
 1209 the RPC and TGC that are consistent with high- p_T muons with origins at
 1210 the interaction point.

1211 An example of the L1 trigger rates for different types of events can be
 1212 seen in Figure 37 for one run in July 2016. The common features to all rates
 1213 are due to LHC luminosity changes, deadtimes due to detector inefficiency,
 1214 and adjustment of prescales to optimize trigger bandwidth.

1215 All of this information is analyzed by the Central Trigger Processor
 1216 (CTP), which uses a trigger menu identifying all types of events to be kept

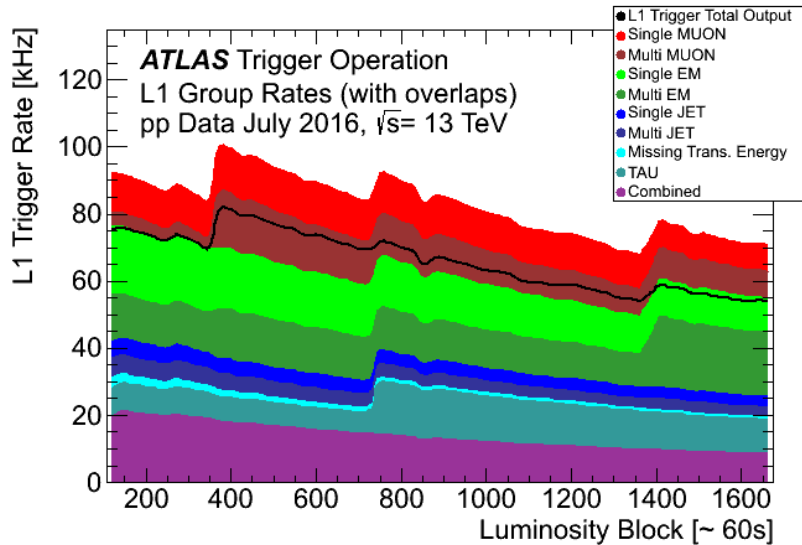


Figure 37: L_1 trigger rates for a run in July 2016 as a function of luminosity block, an approximately 60-second long period of data-taking. The total rate is lower than the combined stack because of overlapping triggers.

to return a trigger decision. The event must be processed in about 2.5 μs so that the remaining event information not yet read out is still available on the subdetectors when the trigger decision is made. This decision is passed to the Trigger Timing and Control (TTC), which communicates with all subdetectors. Upon receiving a L_1 trigger, the subdetectors read out all the information they've stored about the event and place it on their Read Out Boards (ROBs).

The HLT takes the data from particular Region of Interests (RoIs), areas containing interesting objects that caused the L_1 trigger, and analyzes this much more complete picture of the region to decide whether or not the event is still interesting enough to keep. This process has its own trigger menu with dedicated L_1 seeds for each item. HLT triggers typically have slightly higher thresholds than their corresponding L_1 triggers to ensure that events that would pass the HLT requirements are very likely to have passed the L_1 requirements. Figure 38 shows the HLT rates for the same run in July. In addition to the event types seen in Figure 37, the HLT can also identify events with b -jets, differentiate between electrons and photons, and identify events interesting for B-physics.

Events passing the HLT trigger are written to disk to be analyzed. An example of the total trigger efficiency for single electron triggers is shown in Figure 39. Trigger efficiencies can be taken directly from MC, and are measured in data via a method called tag-and-probe, the main principles of which are discussed in Section 10.3.

Events types that occur very frequently, such that it would require too much of the total trigger bandwidth to record all events passing a given threshold, are prescaled. Events passing these triggers are only recorded a

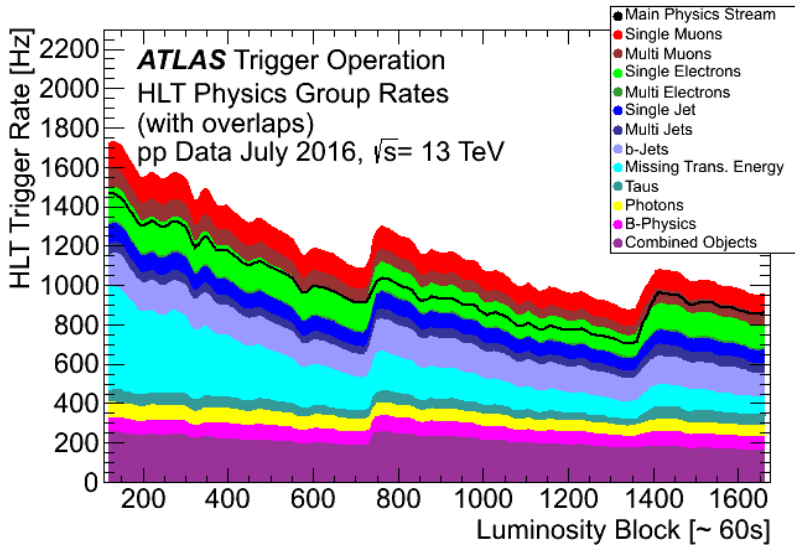


Figure 38: HLT trigger rates for a run in July 2016 as a function of luminosity block, an approximately 60-second long period of data-taking. The total rate is lower than the combined stack because of overlapping triggers.

fraction of the time, and these prescaling rates are used to adjust the final data to account for the limited rate. For example, the lowest unprescaled single electron trigger in 2016 data-taking required an electron with 60 GeV p_T . A trigger requiring electrons with only 10 GeV p_T also exists, but is prescaled by approximately a factor of ten.

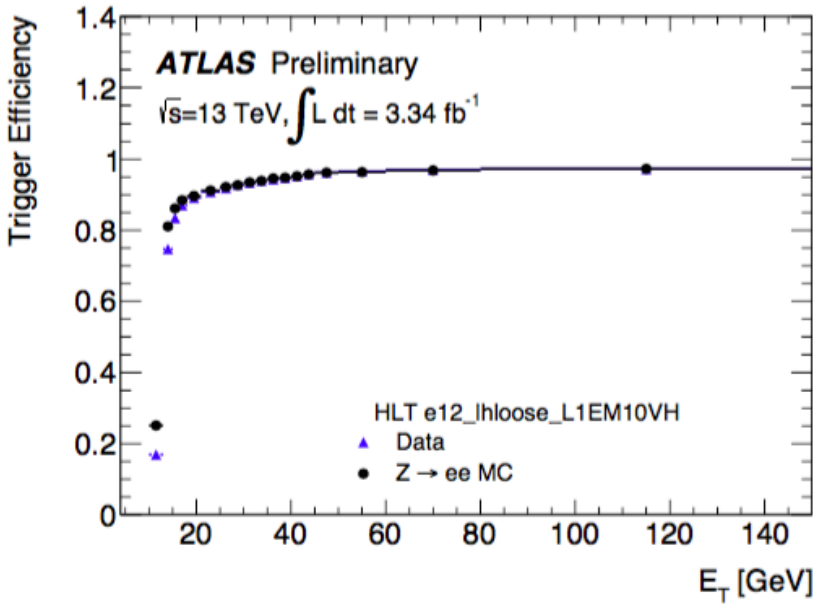


Figure 39: Trigger efficiencies as a function of E_T for data and MC. Efficiencies are given for offline selected loose electrons.

1248

1249 OBJECT RECONSTRUCTION IN THE ATLAS DETECTOR

1250 Object reconstruction is the computationally intensive process of interpreting
1251 the signals from the approximately 100 million read-out channels of
1252 the ATLAS detector into a collection of particles and jets, the objects with
1253 which physics analysis can be performed. This process is complicated, and
1254 requires dedicated working groups in the ATLAS experiment that optimi-
1255 ze the understanding of each type of object. These groups must all col-
1256 laborate to provide a full picture of the events in the detector. For each
1257 object type, candidate objects are reconstructed, and then an identification
1258 step is performed, which chooses which candidates will be used at the
1259 analysis level, based on a series of quality requirements.

1260 5.1 ELECTRONS

1261 Electrons are reconstructed through a combination of [ID](#) and calorimeter
1262 measurements. They travel through the tracking system, leaving charge de-
1263 posits in each layer, then are absorbed by the electromagnetic calorimeter.
1264 These two measurements work in conjunction to deliver high resolution
1265 measurements of electron momentum from low- p_T , where track curvature
1266 gives the most reliable measure of the electron's energy, to high- p_T , where
1267 the tracks are almost perfectly straight, but the calorimeter can still pro-
1268 vide a reliable measurement.

1269 In the central region ($|\eta| < 2.47$) of the ATLAS detector, electron recon-
1270 struction begins with the identification of energy deposits in the electro-
1271 magnetic calorimeter. The calorimeter clusters are seeded by sliding longi-
1272 tudinal windows, which are measured in units of 0.025 in η and ϕ . 3×5
1273 unit windows are used, which require at least 2.5 GeV in the window to
1274 form a seed [53].

1275 These clusters are matched to [ID](#) tracks by extrapolating each track to the
1276 middle layer of the calorimeter and identifying nearby clusters. If there are
1277 multiple tracks associated with a given cluster, tracks with silicon hits are
1278 preferentially chosen, and then the track with the smallest ΔR to the center
1279 of the cluster is selected. If a matching track is found, it is used to deter-
1280 mine the likely direction of bremsstrahlung radiation in the calorimeter,
1281 and maximum distance to match a track to a cluster is expanded in the ϕ
1282 direction to account for this radiation. If no track is found, the cluster is
1283 rejected.

1284 The calorimeter clusters are then rebuilt in larger windows, 3×7 in the
1285 barrel and 5×5 in the end-caps. An estimate of the energy is made by sum-
1286 ming the measured calorimeter energy with estimates of the energy lost
1287 before the electron reached the calorimeter, energy outside of the cluster
1288 window, and energy not fully deposited in the calorimeter. These estimates

1289 are made with parametrized functions determined from a combination of
 1290 **MC** and measurements of energy loss determined with the presampler.

1291 The momentum of a central electron is determined through a combina-
 1292 tion of the calorimeter and track measurements of the electron, while its η
 1293 and ϕ are taken from the track at its vertex.

1294 In the forward region, where no tracking is available, electron energy is
 1295 determined more roughly. Calorimeter cells are formed into variable-sized
 1296 clusters in regions of significant energy deposition, and the center of the
 1297 cluster is used to determine angular coordinates of the electron. However,
 1298 because these electrons have worse resolution in both their position and
 1299 energy, they are often rejected by analyses that depend on well-measured
 1300 objects.

1301 These reconstructed electron candidates' quality are then assessed based
 1302 on an algorithm that uses multivariate analysis to assign a likelihood that
 1303 a candidate is a true electron based on input from just under twenty differ-
 1304 ent variables. These include track quality, hadronic leakage, cluster shape,
 1305 and transition radiation, incorporating information from as many subde-
 1306 tectors as possible in its determination of the candidate's quality. Each
 1307 variable is assigned a probability distribution function for true electrons
 1308 and background processes, and they are collectively used to provide a
 1309 *likelihood* value which can be cut on.

1310 Three levels of identification, **Loose**, **Medium**, and **Tight**, are defined with
 1311 different likelihood cuts, with electron candidates passing tighter identifi-
 1312 cation levels always a subset of looser electrons. [Figure 40](#) gives the effi-
 1313 ciencies at each of these working points both for true electrons and for
 1314 hadrons, which can be misidentified as electrons. Tighter working points
 1315 have worse efficiencies, but lower misidentification rates for hadrons as
 1316 well as photons.

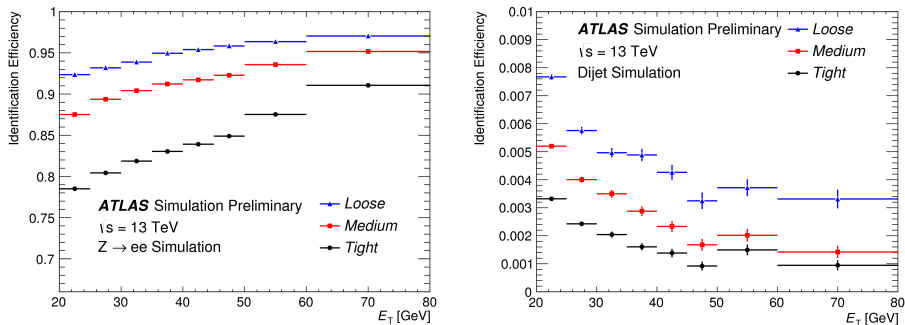


Figure 40: Identification efficiencies from **MC** samples for **Loose**, **Medium**, and **Tight** working points. Left is the efficiency for identification of true electrons taken from $Z \rightarrow ee$ **MC**, and right is the efficiency for mis-
 identification of jets as electrons taken from dijet **MC** [54].

1317 **MC** efficiencies can be compared to efficiencies measured in data using
 1318 the tag-and-probe method, to obtain a *scale factor*, a correction factor ap-
 1319 plied to **MC** to better emulate the rates at which electrons are reconstructed
 1320 and identified in data. [Figure 41](#) shows a comparison of the combined re-

construction and identification efficiencies in data and MC, with the resulting scalefactors also displayed as the ratio.

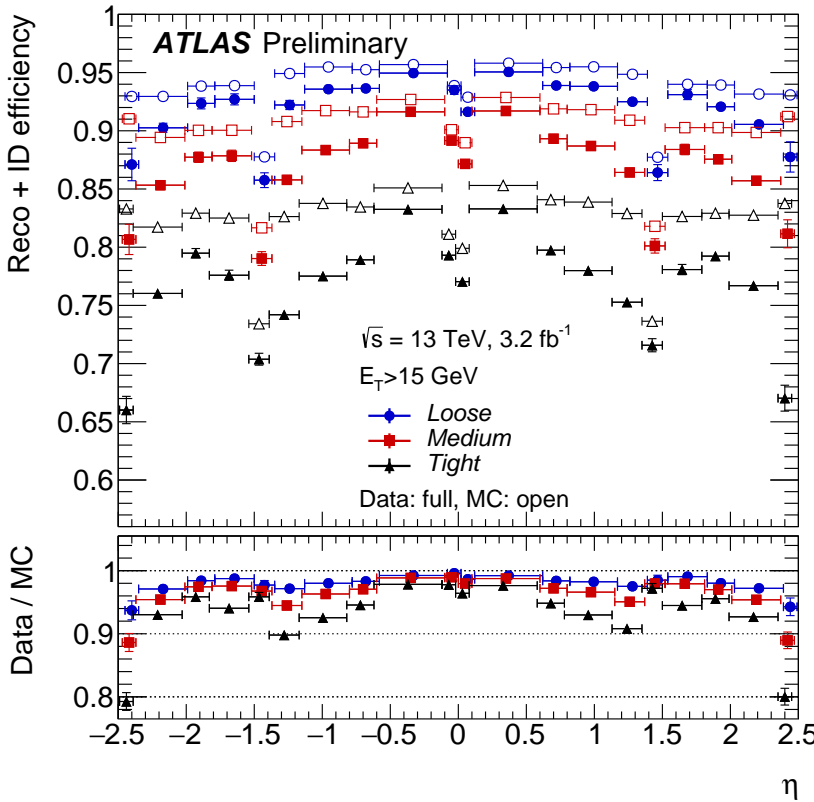


Figure 41: Combined electron reconstruction and identification efficiencies measured as a function of η for data (using the tag-and-probe method on $Z \rightarrow ee$ events) and $Z \rightarrow ee$ MC. Distributions include all electrons with $E_T > 15 \text{ GeV}$. [54].

Electrons can also have *isolation* requirements, cuts on nearby calorimeter activity or tracks. Isolation variables are primarily used to reject non-prompt leptons, leptons which aren't produced by the initial hard scattering of the $p - p$ collision. These can be produced by heavy flavor hadron decays and converted photons, as well as misidentified hadrons. Cuts are made on the amount of nearby calorimetric energy and sum of the p_T of any nearby tracks relative to the electron's energy, forming a series of working points. Fixed cut working points, which specify the relative fraction to cut on, can be used, but efficiency targeted working points are more popular. These include Tight and Loose working points, which operate at 95 and 98% efficiency respectively, and working points that target higher efficiencies at higher electron p_T , Gradient and GradientLoose. These working points each have 99% efficiency for electrons with $p_T > 60 \text{ GeV}$, but 90 and 95% efficiencies at 25 GeV.

1337 5.2 PHOTONS

1338 The reconstruction of photons is performed in parallel to electron recon-
 1339 struction. Seed clustering is performed, and tracks are matched to these
 1340 clusters, as in the case of the electron reconstruction described in [Sec-
 1341 tion 5.1](#).

1342 Photons can be converted to electron-positron pairs in the [ID](#), leaving
 1343 a pair of tracks, or they can pass through without conversion, leaving no
 1344 tracks behind. As a consequence, calorimeter clusters resulting from pho-
 1345 tons can have no tracks associated with them, two tracks, or one track, in
 1346 the case that one of the conversion tracks is not reconstructed. The recon-
 1347 struction software attempts to identify all these scenarios and differentiate
 1348 these clusters from electron and hadron deposits [55].

1349 Two-track clusters are required to consist of two oppositely charged
 1350 tracks that emerge from a conversion vertex running parallel to one an-
 1351 other. A likelihood that these tracks are from electrons is determined using
 1352 the high threshold hits in the [TRT](#), and quality requirements are made on
 1353 the tracks using this likelihood. For tracks with silicon hits, a loose like-
 1354 lihood requirement of 10% is made, while tracks without silicon hits are
 1355 required to have at least 80% likelihood. The tracks are then fit to deter-
 1356 mine the conversion vertex, and quality cuts are made, such as requiring
 1357 that conversion vertices within the silicon volume correspond to tracks
 1358 with silicon hits.

1359 Single track clusters occur most often from conversions in the outermost
 1360 layers of the [ID](#), and are more difficult to reconstruct. Tracks are typically
 1361 lost because an electron or positron resulting from the conversion has a p_T
 1362 too low to be reconstructed, or because the two tracks are so close together
 1363 that they're identified as a single track. The single track is required to have
 1364 at least a 95% electron likelihood from [TRT](#) hits, and must not have a hit in
 1365 the innermost layer of the pixel detector. The conversion vertex is defined
 1366 as the first hit of the single track.

1367 The tracks associated with these conversion vertices are extrapolated to
 1368 the calorimeter and matched to cluster, except in the case that there are two
 1369 tracks that differ substantially in their p_T measurements, in which case the
 1370 position of the conversion vertex is used for extrapolation to the calorime-
 1371 ter, assuming a straight-line trajectory. If multiple vertices are matched to
 1372 a single cluster, preference is given to vertices with double tracks, silicon
 1373 hits, and finally to tracks closest to the interaction point.

1374 Any cluster with neither a conversion vertex or a track associated with
 1375 it is identified as an unconverted photon. Clusters associated with both
 1376 electrons and photons are assigned to one or the other based on their
 1377 properties. Clusters are preferentially identified as photons in the case that
 1378 they are matched to a conversion vertex in which at least one track is
 1379 associated with both the vertex and the cluster, or if the associated tracks
 1380 have a p_T smaller than the cluster's p_T . E/p , the ratio of the cluster and
 1381 track energy measurements, can also be used to differentiate electrons and

1382 photons. Electron candidates are instead reconstructed as photons if they
 1383 have $E/p > 10$ or if the track matched to the electron has p_T below 2 GeV.

1384 Photon energy is determined in a 3×5 (3×7) window for unconverted
 1385 (converted) photons in the barrel, where the window is expanded to com-
 1386 pensate for the increased spread of energy from the conversion products.
 1387 In the endcap, the 5×5 window is used in all cases. Like the electrons,
 1388 the calibration of the photon's energy accounts for energy loss before the
 1389 calorimeter, as well as energy deposited outside the cell and beyond the
 1390 electromagnetic calorimeter.

1391 Photon identification is performed in the range $|\eta| < 2.37$ using a se-
 1392 ries of cuts on the shape of the shower in the electromagnetic calorime-
 1393 ter, as well as the amount of additional energy deposited in the hadronic
 1394 calorimeter. Photons in the the so called *crack* region of the calorime-
 1395 ter ($1.37 < |\eta| < 1.52$), where a discontinuity prevents accurate assess-
 1396 ment of photon energy, are rejected. The photon identification has only
 1397 one working point, called **Tight**, which has an identification efficiency
 1398 of 53–64% (47–61%) for unconverted (converted) photons with $E_T = 10$
 1399 GeV and 88–92% (96–98%) for photons with $E_T \geq 100$ GeV [56]. Effici-
 1400 cies as a function of p_T measured in the 2016 data and compared to **MC**
 1401 can be seen in Figure 42.

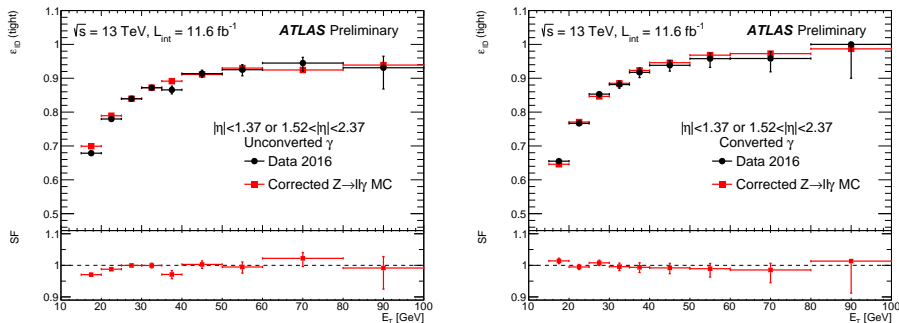


Figure 42: Comparison of Tight identification efficiency measurements from data and $Z \rightarrow \ell\ell\gamma$ MC for unconverted (left) and converted (right) photons, with an inclusive η selection. The bottom of each figure shows the ratio of data and MC efficiencies. [57].

1402 Photon isolation, like electron isolation, can be determined as the com-
 1403 bination of nearby calorimeter deposits and tracks. Fixed cuts on the iso-
 1404 lation as a fraction of photon energy is typically used. A working point
 1405 called **FixedCutTight** reconstructs the amount of calorimeter energy (ex-
 1406 cluding that of the photon) in a cone of $\Delta R = 0.4$ around the photon and
 1407 the amount of energy from the sum of track p_T in a cone of $\Delta R = 0.2$,
 1408 including only tracks associated with the primary vertex. Defined relative
 1409 to the photon's p_T , this working point includes photons with calorimetric
 1410 isolation less than $0.022 p_T + 2.45$ GeV and track isolation less than $0.05 p_T$
 1411 [58].

1412 5.3 MUONS

1413 Muon reconstruction is performed independently in the **ID** and the **MS**,
 1414 then the two measurements are combined when consistent tracks are found
 1415 in each system [59]. The **ID** reconstruction is performed using the tracking
 1416 mechanism over the $|\eta| < 2.5$ range. As with electrons, hits in the layers
 1417 of the **ID** are fit to tracks, a process described in more detail in [Chapter 6](#).

1418 The **MS** track reconstruction is performed in the $|\eta| < 2.7$ range and
 1419 begins with a search in each muon chamber for patterns of hits consistent
 1420 with a track, called *segments*. The **MDT** chamber hits are fit to a straight line,
 1421 and nearby **RPC** and **TGC** chambers provide the coordinate orthogonal to
 1422 the magnetic curvature for these hits. Segments are also built in the **CSC**,
 1423 where they are required to be loosely consistent with a track originating
 1424 from the interaction point.

1425 These segments are then fit together, starting from the middle layers
 1426 of the **MS**, with track quality requirements on the resulting combinations
 1427 based on the χ^2 of the fits. Tracks must have at least two segments, except
 1428 in the transition region between the barrel and endcap, where a single high
 1429 quality segment can qualify as a track. Segments are allowed to be shared
 1430 between multiple tracks in the initial reconstruction, but after the combi-
 1431 nation, tracks with shared segments and low quality fits are removed.

1432 These **MS** tracks are then combined with measurements from other parts
 1433 of the ATLAS detector. The best quality muons are combined muons,
 1434 which have **ID** and **MS** tracks associated to them, the hits of which are re-fit
 1435 to form a combined track. **MS** hits can be added or removed at this stage
 1436 based on their consistency with the new track. Other types of muons exist,
 1437 including extrapolated muons, which have only **MS** tracks that are con-
 1438 sistent with the interaction point, calorimeter-tagged muons, which com-
 1439 bine an **ID** track with a calorimeter deposit consistent with a muon, and
 1440 segment-tagged muons, which combine an **ID** track with a segment in the
 1441 **MS**. Muons with shared **ID** tracks are not allowed, with preference given
 1442 to combined muons, then calorimeter-tagged muons, and lastly segment-
 1443 tagged muons.

1444 There are four muon identification working points for muons: **Loose**,
 1445 **Medium**, **Tight**, and **High- p_T** . These working points all have different effi-
 1446 ciencies for the identification of muons, balanced against the mis-identification
 1447 of hadrons. One of the key variables for their discrimination is q/p signif-
 1448 icance, which quantifies the consistency between the **ID** and **MS** mea-
 1449 surements of momentum. The χ^2 of the combined fit is also an important
 1450 discriminator.

1451 The **Loose**, **Medium**, and **Tight** efficiencies are inclusive, with all **Tight**
 1452 muons passing the **Medium** requirements, and **Medium** muons passing the
 1453 **Loose** requirements. The **Loose** requirement includes all types of recon-
 1454 structed muons, but allows muons without **MS** tracks only in the $\eta < 0.1$
 1455 range where there is a gap in the **MS** coverage to accomodate cabling
 1456 for the calorimeter system. The **Medium** working point includes only com-
 1457 bined and extrapolated muons, and is the default for most ATLAS analy-

ses. Extrapolated muons are allowed only outside the **ID** tracking system ($|\eta| > 2.5$), a region often excluded by analyses because of the decreased efficiency and larger p_T resolution of these muons. For the combined muons, at least three hits in at least two **MDT** layers are required (except in the $\eta < 0.1$ region) and a q/p significance cut is made to reduce backgrounds. Even with the reduced requirements at low η , there is a drop in efficiency in this region, as shown in Figure 43. The Tight working point additionally cuts on χ^2 and makes further requirements on the consistency between **ID** and **MS** p_T measurements.

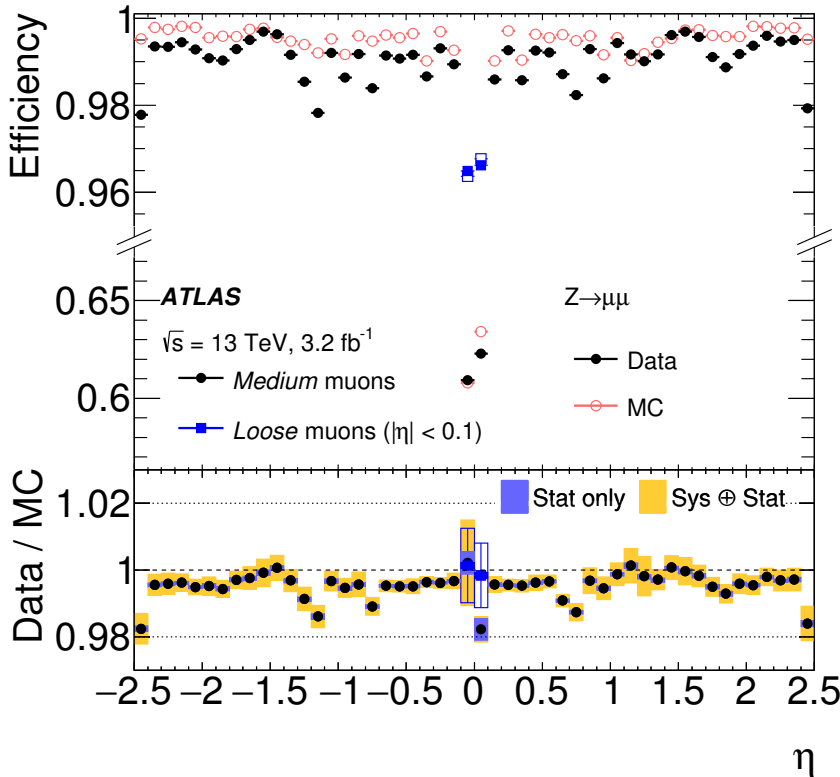


Figure 43: Muon reconstruction efficiency for the Medium and (for small $|\eta|$) Loose working points measured with $Z \rightarrow \mu\mu$ events in data using the tag-and-probe method and in MC as a function of η . The ratio between the two is shown at the bottom. [59]

The High- p_T working point is designed to minimize the resolution for high- p_T muons, at the cost of lower efficiencies. Muons passing the High- p_T requirements must have at least three **MDT** hits in three layers, which decreases efficiency but gives greatly improved p_T resolution. In addition, some regions of the **MS** with poor alignment are vetoed to cut down on mismeasurement. Compared to the default working point these muons have much lower efficiency: 78% (90%) for High- p_T muons compared to 96% (96%) for Medium in the p_T range of 4-20 GeV (20-100 GeV). The efficiency as a function of η for this working point can be seen in Figure 44, where the efficiency loss due to the of vetoing of some chambers is especially apparent. Mismodeling of the alignment and the specificity of the

momentum resolution cuts cause a large discrepancy between data and MC efficiencies, resulting in scale factors that differ from unity by as much as 10%.

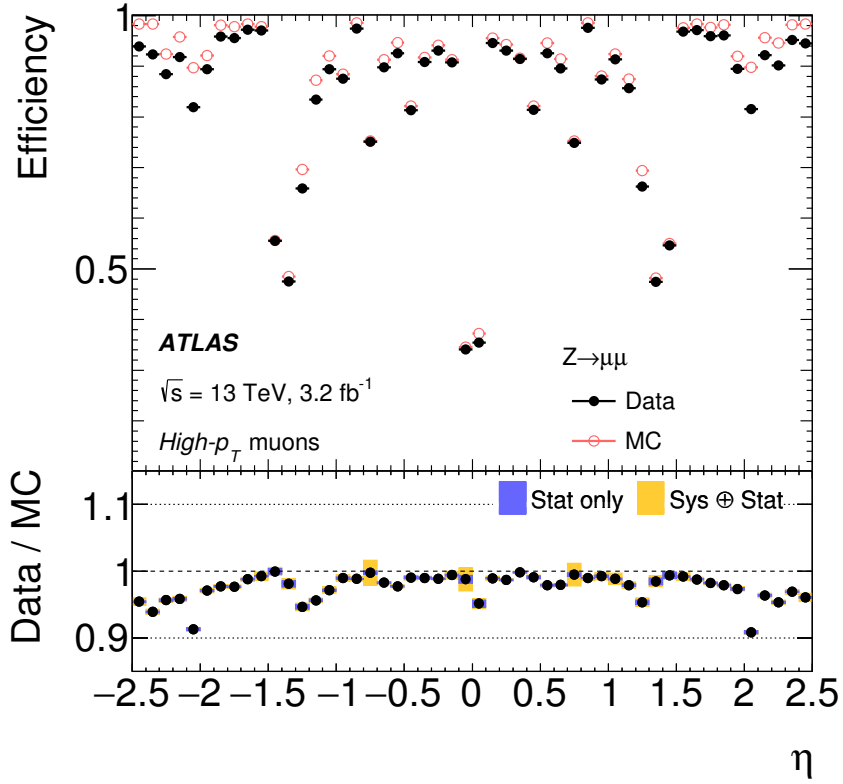


Figure 44: Muon reconstruction efficiency for the High- p_T working point measured with $Z \rightarrow \mu\mu$ events in data using the tag-and-probe method and in MC as a function of η . The ratio between the two is shown at the bottom. [59]

The most common isolation selection for muons is designed in the same way as the electron isolation, and also called GradientLoose. It is constructed such that muons with p_T of 25 GeV have an efficiency of 95%, and muons with p_T of 60 GeV have an efficiency of 99%.

5.4 JETS

Jets are the most complicated objects to reconstruct in the ATLAS detector because each jet is an assembly of many hadronic particles. In contrast to a lepton, whose reconstructed energy can easily be compared to its true energy from simulation, even a jet's true energy is ambiguous, and is dependent on the choice of the jet's definition. The standard jet reconstruction algorithm used in the ATLAS experiment is called anti- k_t [60].

This algorithm begins with clusters in the calorimeter defined by topologically connected cells with energy deposits significantly higher than the noise background. These clusters can be defined in multiple ways, but

1495 there are two collections used most commonly for analysis. One uses cluster
 1496 energies calibrated for electromagnetic showers ([EM](#)), and another uses
 1497 clusters calibrated to hadronic showers. The second uses a method called
 1498 Local Cluster Weighting ([LCW](#)), which first determines the extent to which
 1499 the cluster is electromagnetic or hadronic based on the energy density and
 1500 the shower depth, then applies a calibration accordingly for each cluster.

1501 To reconstruct jets, a set of clusters is chosen and the anti- k_t algorithm
 1502 is then applied, beginning with the highest energy cluster and grouping it
 1503 with nearby clusters according to the distance measure

$$d_{ij} = \min(k_{ti}^{-2}, k_{tj}^{-2}) \frac{\Delta_{ij}^2}{R^2} \quad (32)$$

1504 where R is the algorithm's radius parameter, typically set to 0.4, Δ gives
 1505 the angular separation of the two clusters, and k_t is the transverse mo-
 1506 mentum associated with the cluster. The jet is defined by clusters grouped
 1507 within the cone radius, then the axis of the jet is reassessed. This process
 1508 is iterated upon until a stable jet is produced. The inverse dependence on
 1509 the k_t of the cluster produces jets with energetic cores and softer edges,
 1510 which matches the expectation from a hadronic shower. In addition it is
 1511 infrared and collinear safe, with neither soft emission or collinear particles
 1512 altering the reconstruction of the jet.

1513 A series of calibrations are then applied to these jets. The first is to cor-
 1514 rect for additional hadronic energy due to pile-up. [Figure 45](#) demonstrates
 1515 the impact of pile-up on the energy density of an event, and this overall
 1516 change in energy density can affect the amount of stray energy associated
 1517 with reconstructed jets. To remove this dependence, a correction is taken
 1518 from [MC](#) and parametrized in terms p_T , η , and the number of primary ver-
 1519 tices in the event, as well as the average number of vertices, which makes
 1520 correction for out-of-time pile-up possible. Next, jets are corrected to have
 1521 their origin at the primary vertex instead of the center of the ATLAS de-
 1522 tector. After that, the jets are corrected based on η dependent Jet Energy
 1523 Scale ([JES](#)) factors derived from [MC](#). [Figure 46](#) shows the energy response,
 1524 the inverse of these factors, for [EM](#) jets. Lastly, an observed bias in the η
 1525 measurement of jets is accounted for.

1526 In addition to correcting for additional energy due to pile-up, it is neces-
 1527 sary to reject reconstructed jets that come from pile-up vertices. To accom-
 1528 plish this, a multivariate algorithm called [JVT](#) was created which builds
 1529 upon an older method, [JVF](#) [62]. The original method vetoed jets by sum-
 1530 ming the total p_T of associated tracks and assessing the fraction of that p_T
 1531 that came from tracks associated with the event's primary vertex. This frac-
 1532 tion decreases with higher pile-up, making the construction of an explicit
 1533 cut difficult in varying pile-up conditions. [JVT](#) improved on the method
 1534 by producing a pile-up corrected [JVF](#)-like variable and including it in the
 1535 inputs of the tagger with other variables measuring the fraction of jet en-
 1536 ergy that can be associated with the primary vertex. [Figure 47](#) shows the
 1537 efficiency and fake rate for the two methods, demonstrating [JVT](#)'s superior
 1538 stability across events with different numbers of pile-up vertices.

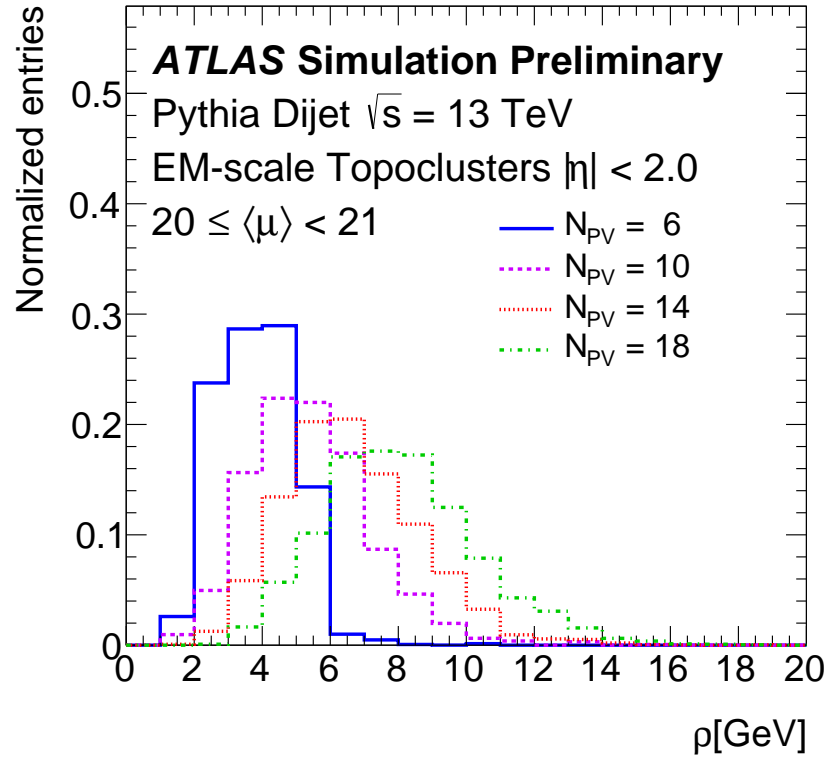


Figure 45: Distribution of event p_T density, ρ , taken from MC dijets for different numbers of primary vertices. [61]

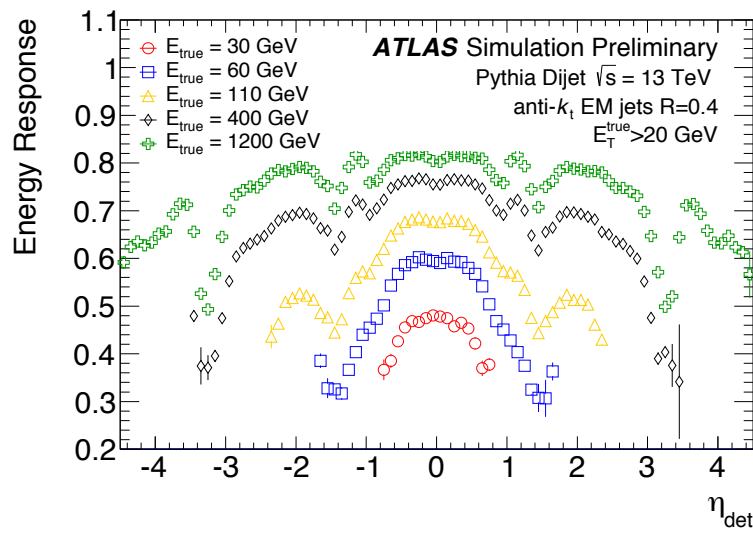


Figure 46: Energy response as a function of energy and η for EM jets in dijet MC. [61]

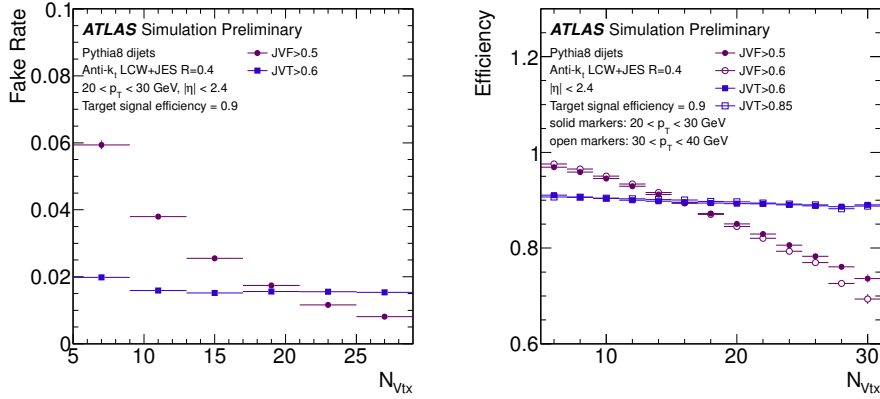


Figure 47: Dijet MC distributions of the number of pile-up jets passing the JVT and JVf cuts (left) and the efficiency for jets from the primary vertex (right) as a function of number of primary vertices in the event [62].

1539 It is possible to differentiate jets resulting from b -hadron decays from
 1540 other jets due to the non-negligible lifetimes of the hadrons. Many BSM
 1541 processes preferentially produce b quarks, as does any process involving
 1542 top quarks, so this identification can be useful for targeting specific decays
 1543 in many analyses. Multivariate techniques are used to identify secondary
 1544 vertices using the ID [63]. In ATLAS, separate algorithms are used to iden-
 1545 tify jets with tracks with significantly non-zero impact parameters, tracks
 1546 that reconstruct a secondary vertex, and tracks that can be identified with
 1547 a chain of vertices beginning with the primary vertex. This information
 1548 is fed into a boosted decision tree called MV2c20, which outputs a dis-
 1549 criminant shown in Figure 48. Using this discriminant, a working point is
 1550 chosen such that b -jets can be identified with a 70% efficiency, with mis-
 1551 identification rates at around 12% for c -jets and 0.2% for light-flavor jets.

1552 5.5 OVERLAP REMOVAL

1553 Because most of these reconstruction methods are run independently, it
 1554 is common for energy deposits and tracks to be shared between jets and
 1555 particles of different types. To account for this, a process called Overlap
 1556 Removal (OR) is used, which iteratively removes overlapping objects. The
 1557 process is performed at the *baseline* level, a set of loose selections on ob-
 1558 jects which are later further refined to create the *signal* objects used in
 1559 analysis. Each analysis defines these levels according to its needs; the spe-
 1560 cific requirements made for the analysis described in Part iv are outlined
 1561 in Chapter 8.

1562 The first step in the OR process is to remove reconstructed jets that ap-
 1563 pear to be due to calorimetric deposits from an electron. To accomplish
 1564 this, any baseline jet within $\Delta R = 0.2$ from a baseline electron is removed.
 1565 A caveat is added due to the frequent production of leptons in the decay
 1566 of heavy-flavor jets; if the jet is b -tagged, the electron will be removed in-
 1567 stead. After these electrons and jets have been removed, a new search is

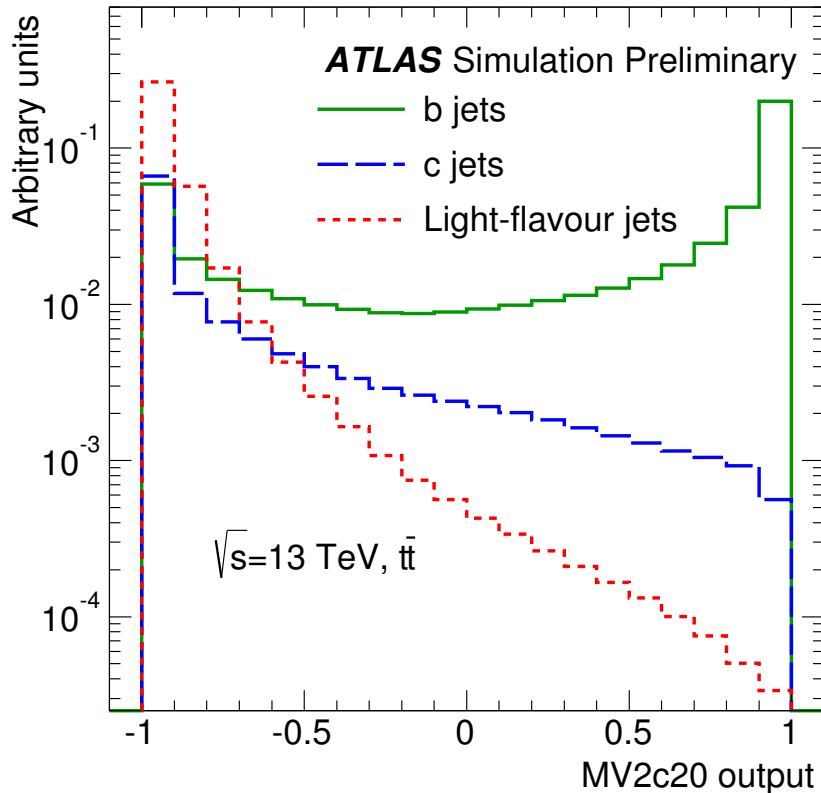


Figure 48: Distribution of MV2c20 output for b -jets, c -jets, and light-flavor jets in $t\bar{t}$ MC [63].

1568 done for jets and electrons within $\Delta R = 0.4$ of one another. In this iteration,
 1569 the electron is removed, again to reduce backgrounds from heavy-flavor
 1570 decays.

1571 Next, the muon-jet OR is applied, which is very similar to that of the
 1572 electron. Any jet within $\Delta R = 0.2$ of a muon is removed, unless the jet is
 1573 b -tagged, in which case the muon is removed due to the likelihood that it
 1574 resulted due to a heavy-flavor decay. The muon-jet OR then differs from the
 1575 electron's in that a p_T -based ΔR cut is used in the last step. Muons within
 1576 $\Delta R < \min(0.04 + (10 \text{ GeV})/p_T, 0.4)$ of a jet are removed, with the shrink-
 1577 ing cone for high- p_T muons designed to improve efficiency for energetic
 1578 muons that produce significant calorimeter deposits, while still rejecting
 1579 the heavy-flavor muons that are typically lower p_T .

1580 The next step is to remove electrons resulting from muon bremsstrahlung.
 1581 Any remaining electron within $\Delta R = 0.1$ of a muon is removed from the
 1582 event.

1583 Lastly, overlap between photons and both jets and electrons is consid-
 1584 ered. Baseline photons within $\Delta R = 0.4$ of an electron are removed, as are
 1585 jets within $\Delta R = 0.4$ of a remaining photon.

1586 5.6 MISSING TRANSVERSE MOMENTUM

1587 Missing transverse momentum ($\mathbf{p}_T^{\text{miss}}$, with magnitude E_T^{miss}), is the neg-
 1588 ative vector sum of p_T measured in an event. Because colliding parti-
 1589 cles have no initial transverse momentum, the true value of this quan-
 1590 tity should be zero unless a particle escapes the detector without being
 1591 measured, as neutrinos do. In practice, the reconstructed E_T^{miss} can also be
 1592 non-zero due to mismeasurement. E_T^{miss} reconstruction is perhaps the most
 1593 complex because it depends on all other object reconstructions performed
 1594 in the ATLAS detector.

1595 E_T^{miss} components are calculated independently for each type of base-
 1596 line object reconstructed, as well as for a soft term, which accounts for
 1597 low- p_T radiation [64]. This component comprises the energy observed by
 1598 the ATLAS detector but not associated with a baseline object, and can be
 1599 calculated based either based on calorimeter or track measurements. While
 1600 the Calorimeter Soft Term (CST) is very sensitive to pile-up, the Track Soft
 1601 Term (TST) is much more robust, as it can exclude tracks emanating from
 1602 pile-up vertices. Tracks associated with any reconstructed object are also
 1603 removed. Figure 49 shows the TST resolution's dependence on number of
 1604 primary vertices, which is considerably more stable than CST. Because of
 1605 this improved performance, using TST to reconstruct E_T^{miss} is now the stan-
 1606 dard for ATLAS analyses.

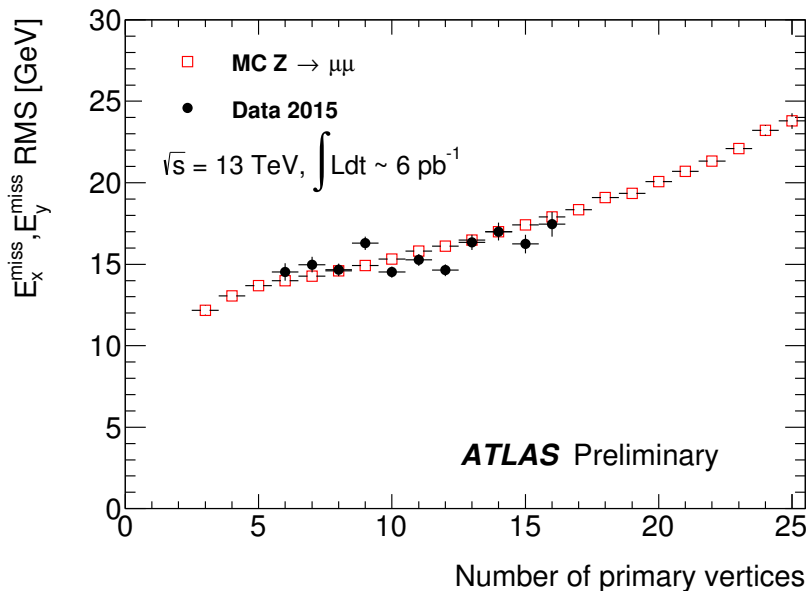


Figure 49: Distributions of the resolution of the x and y components of TST E_T^{miss} in $Z \rightarrow \mu\mu$ events in data and MC [65].

1607 Figure 50 shows the the E_T^{miss} resulting from muons, jets, and the soft
 1608 term in $Z \rightarrow \mu\mu$ events. These events very rarely have any true E_T^{miss} , so
 1609 these distributions primarily demonstrate how mismeasurement of vari-
 1610 ous objects contributes to the E_T^{miss} term. Though the soft term falls off
 1611 very quickly, rarely producing events with more than 50 GeV of E_T^{miss} , both

- ₁₆₁₂ the jet and muon distributions have longer tails, producing more events
₁₆₁₃ with higher E_T^{miss} .
₁₆₁₄ The jet and muon distributions both have significant high tails, while
₁₆₁₅ the soft term falls off much more quickly.

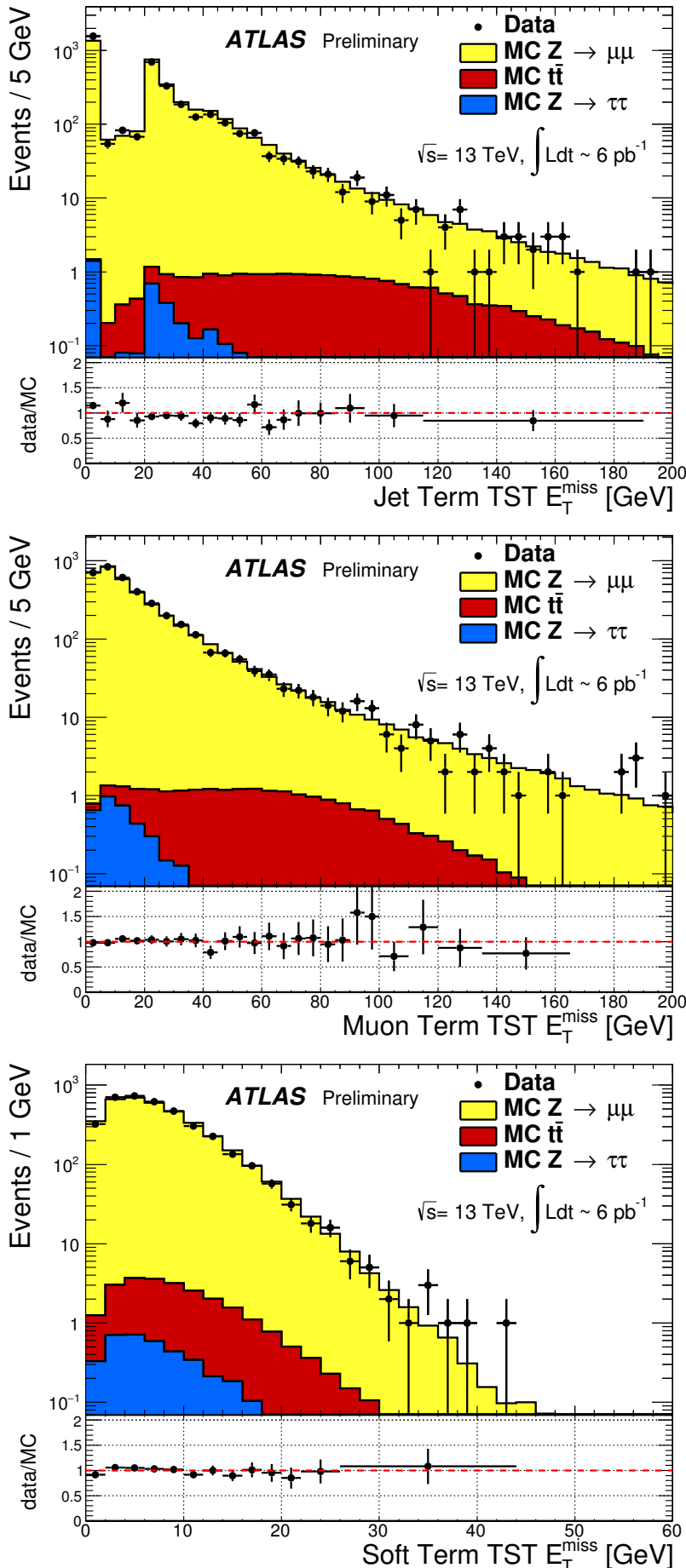


Figure 50: Distributions of the jet term (top left), muon term (top right), and TST (bottom) E_T^{miss} in $Z \rightarrow \mu\mu$ events in data and MC. In the jet term distribution, the feature at zero is due to events with no jets, and the spike at 20 GeV corresponds to the minimum jet p_T considered for the analysis [65].

1616

1617 APPLICATION OF A NEURAL NETWORK TO PIXEL 1618 CLUSTERING

1619 6.1 CLUSTERING IN THE PIXEL DETECTOR

1620 Creating tracks from individual hits in the Inner Detector is one of most
 1621 computationally challenging parts of the reconstruction of ATLAS events.
 1622 Each event typically contains thousands of hits in the pixel detector alone,
 1623 which must be combined into one coherent picture of which particles tra-
 1624 versed the detector, and how they moved and lost energy as they traveled.
 1625 A typical particle deposits charge in several pixels per layer, forming a se-
 1626 ries of clusters which can be connected together to form a track. This track
 1627 can in turn be used to measure the charge, momentum, and trajectory of
 1628 the particle.

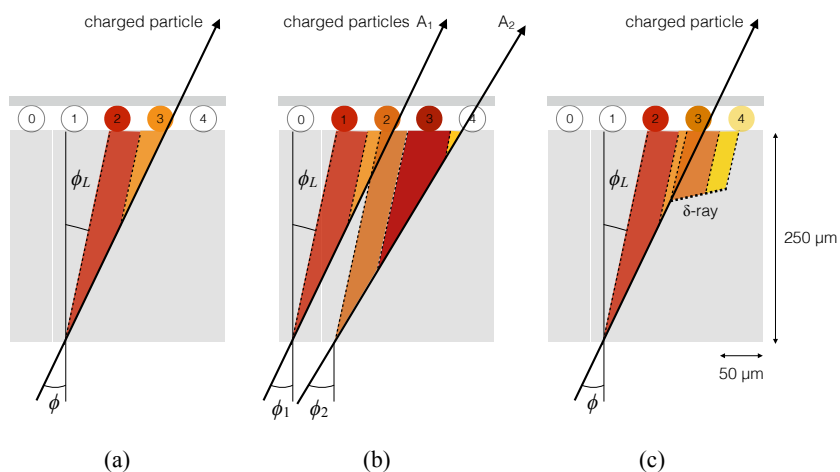


Figure 51: A few possible types of clusters in the Pixel Detector. (a) shows a single particle passing through a layer of the detector, (b) shows two particles passing through the detector, creating a single merged cluster, and (c) shows a single particle emitting a δ -ray as it passes through the detector [66].

1629 The process of going from clusters to track is relatively simple in an
 1630 isolated environment in which one particle travels cleanly through all the
 1631 layers, but can be complicated by multiple close-by tracks and by a single
 1632 particle's emission of low energy particles, called δ -rays. In these cases, it
 1633 can be hard to tell how many particles were involved in creating a clus-
 1634 ter, and where exactly each of those particles passed through the layer. A
 1635 few examples of particle interactions with the pixel sensor can be seen in
[Figure 51](#).

1637 Clusters are initially made by a process called Connected Component
 1638 Analysis ([CCA](#)). In this process, pixels in a given layer are grouped together
 1639 if they share any edge or corner. The position of the resulting cluster is
 1640 defined by local x and y coordinates, which describe its position and size
 1641 within the pixel module on which it appears. Determining the position
 1642 of the particle that formed that cluster is less straightforward, and has
 1643 recently been updated from a charge interpolation method to a method
 1644 using a [NN](#).

1645 6.1.1 Charge Interpolation Method

1646 A typical cluster contains a few pixel hits spanning in the x and y direc-
 1647 tions, each with its own measurement of charge deposition, or [ToT](#). In the
 1648 charge interpolation method, these individual hits are combined to make
 1649 one estimation of the position a single particle which passed through them,
 1650 using the following equation:

$$x_{cluster} = x_{center} + \Delta_x(\phi, N_{row}) \cdot \left[\Omega_x - \frac{1}{2} \right] \quad (33)$$

$$x_{cluster} = x_{center} + \Delta_x(\phi, N_{row}) \cdot \left[\Omega_x - \frac{1}{2} \right] \quad (34)$$

1651 where $\Omega_{x(y)}$ is defined by

$$\Omega_{x(y)} = \frac{q_{last\ row(col)}}{q_{first\ row(col)} + q_{last\ row(col)}} \quad (35)$$

1652 and q represents the [ToT](#) of a given pixel, and $\Delta_{x(y)}$ is a function derived
 1653 from either data or [MC](#) and produces an output related to the projected
 1654 length of the particles track on the pixel sensor and is measured as a func-
 1655 tion of ϕ , the incident angle of a particle on the sensor, and $N_{row(col)}$, the
 1656 number of pixels in the x and y direction.

1657 In a simple case, such as (a) of [Figure 51](#), this method works quite effec-
 1658 tively. However, in cases like (b), it has no ability distinguish two-particle
 1659 from one-particle clusters, and can only assign a cluster center between the
 1660 two particles' locations, despite that intermediate pixel having the lowest
 1661 [ToT](#). Furthermore, because this method can't differentiate two-particle clus-
 1662 ters, the tracking software can't use that information to preferentially al-
 1663 low multiple tracks to share two-particle clusters. Allowing tracks to share
 1664 clusters indiscriminately in dense track environments creates fake tracks
 1665 from the many possible cluster combinations, so this cannot be broadly
 1666 permitted. In cases like (c), the δ -ray will bias the measurement of the
 1667 particle's position in whichever direction it is emitted.

1668 6.1.2 Improving Measurement with Neural Networks

1669 To address these problems, a series of [NNs](#) were created [66]. The first esti-
 1670 mates the number of particles in a given cluster, the second estimates their

1671 positions within the cluster, and the third assesses the uncertainty of the
 1672 position measurement. They are referred to, respectively, as the “Number”,
 1673 “Position”, and “Error” NNs.

1674 These NNs are taken from the AGILEPack library [67], and trained using
 1675 simulated ATLAS MC. Each NN is given the following inputs:

- 1676 • a 7×7 grid of cluster ToT information¹
- 1677 • a 7-element vector containing the y -size of the pixels in the grid²
- 1678 • the layer of the pixel detector that the cluster was observed in
- 1679 • a variable indicating whether the cluster is located in the barrel or
 1680 endcap
- 1681 • θ and ϕ variables projecting the incident angles of the particle on the
 1682 sensor³
- 1683 • the pixel module’s η index, a label assigned to each module that
 1684 differentiates modules based on their η position

1685 After the Number NN predicts a number of particles associated with the
 1686 cluster, required to be between 1 and 3, the same inputs are fed to one of
 1687 three Position NNs based on the determined number of particles, which
 1688 then outputs the x and y positions of each of the particles. Then, the same
 1689 inputs combined with the output of the Position NN are fed into one of
 1690 three Error NNs (also distinguished by number of particles), which outputs
 1691 an uncertainty for each of the position predictions made. An example of
 1692 the output of this process can be seen in Figure 52, where the improved
 1693 position resolution from the ability to identify a multi-particle cluster is
 1694 evident.

1695 The particle location predictions from the NNs are then handed to the
 1696 tracking software, which now can use these multiple particle position es-
 1697 timations as independent hits to be fit. As a result, tracks in dense envi-
 1698 ronments have fewer clusters shared between multiple tracks, and their
 1699 trajectories are known to a greater degree of precision.

1700 6.2 IMPACT OF THE NEURAL NETWORK

1701 The NN was first applied to 7 TeV data, where it improved position res-
 1702 olution for particles in small and large clusters. Figure 53 shows the im-
 1703 provement from the addition of the NN in x resolution in different cluster

¹ Clusters spanning more than seven pixels in either direction are rare, but when they occur they are rejected, and the original charge interpolation estimate of a single particle’s position is kept.

² The pixel detector contains some long pixels at the edges of modules, and this is intended to help the NN identify these cases.

³ If the NN is applied before tracking is performed, these angles project to the nominal interaction point, and if tracking has already been performed, the angles are taken from the track fit to the cluster.

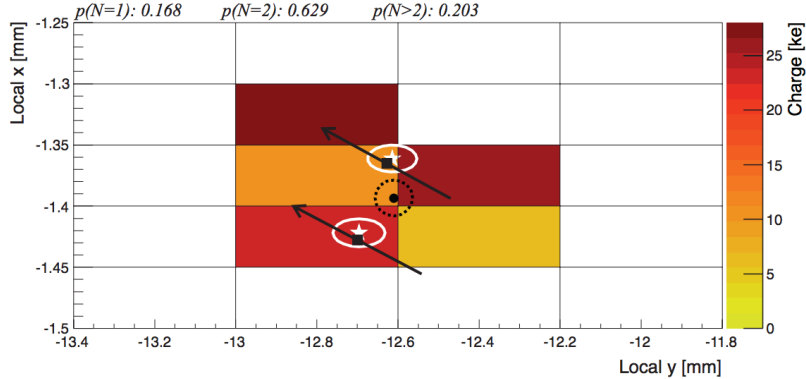


Figure 52: One example of a two-particle cluster and its truth information compared with the output of the NNs. The boxes represent pixels, with a color scale indicating ToT. At top, the $p(N = i)$ values give the output of the Number NN, the probabilities that the cluster contains 1, 2, and 3 particles. Given the highest probability is for $N = 2$, the other NNs predict the position and errors of the two particles (in white). The black arrows and squares represent the truth information from the cluster, and the black dot and dotted line show the position measurement for the un-split cluster [66].

1704 sizes. The improvement from charge interpolation clustering is particu-
 1705 larly evident in the 4-pixel case, where the double peaked structure of the
 1706 interpolation method has been completely removed with the NN.

1707 6.2.1 The Neural Network in 13 TeV Data

1708 In Run 2, the tracking algorithm is first run on the CCA clusters with posi-
 1709 tions determined via charge interpolation, where it constructs tracks with
 1710 loose quality requirements. In this step, the tracking algorithm allows
 1711 shared clusters, clusters used in multiple track fits [68]. The NN is then
 1712 used to identify which clusters are likely to have had multiple particles
 1713 pass through them, and to estimate the positions of those particles. In the
 1714 case that the cluster is determined to have resulted only from one particle,
 1715 tracks that share that cluster are penalized. In general, tracks with more
 1716 than two shared clusters are rejected.

1717 Because the NN is trained only with MC simulations, any mismodeling of
 1718 the way charge is deposited in the ATLAS detector could cause the NN to
 1719 perform in an unexpected way when applied to data. The potential impact
 1720 of this mismodeling was investigated with 13 TeV MC [69]. The goal of
 1721 these studies was to determine which variables the NN's predictions were
 1722 most sensitive to, and whether it was likely that these variables could be
 1723 mismodeled enough to produce unexpected results in data.

1724 One example of a variable capable of significantly altering the NN out-
 1725 puts was the overall charge scale. To study its impact, the ToT of all pixels
 1726 in a cluster were scaled up and down, and the resulting outputs of the
 1727 NN were compared, as shown in Figure 54. In this case, the likelihood to

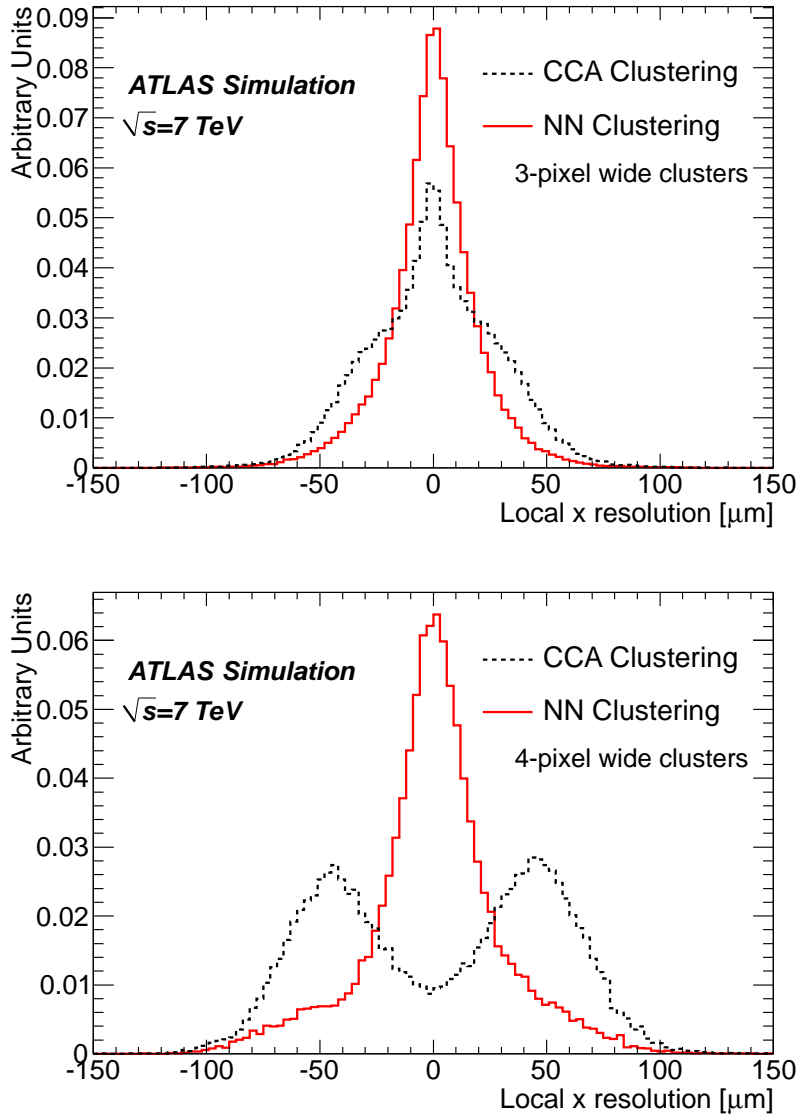


Figure 53: x resolutions for clusters with 3 (top) and 4 (bottom) pixels in the x direction in 7 TeV data for CCA (using only charge interpolation to determine position) and NN clustering taken from MC [66].

misidentify multi-particle clusters and single particle clusters depended significantly on this scaling. However, experts on the simulation of this scale agree that it's unlikely to be mismodeled by more than 10%, so very extreme effects from a difference between data and MC are unlikely. Overall, it was found that variations on the cluster charge produced a significant impact on predictions, while all other variations, such as incidence angle variation and spatial smearing of charge, had a minimal effect.

In addition to studies on the impact of alterations of individual simulation variables, studies directly comparing the NN output in data and MC were performed. Figure 55 shows a comparison of how often the NN identifies different types of clusters in data and MC. Each figure is made using by selecting pairs of collimated tracks that share a common cluster on a given

₁₇₄₀ layer, then calculating the fraction of those clusters that are determined by
₁₇₄₁ the **NN** to be single or multi-particle clusters. This fraction is plotted as a
₁₇₄₂ function of the distance between the two tracks in the cluster's layer. Very
₁₇₄₃ good agreement is seen between the two samples, demonstrating that the
₁₇₄₄ **MC**-trained **NN** performs similarly on both **MC** and data.

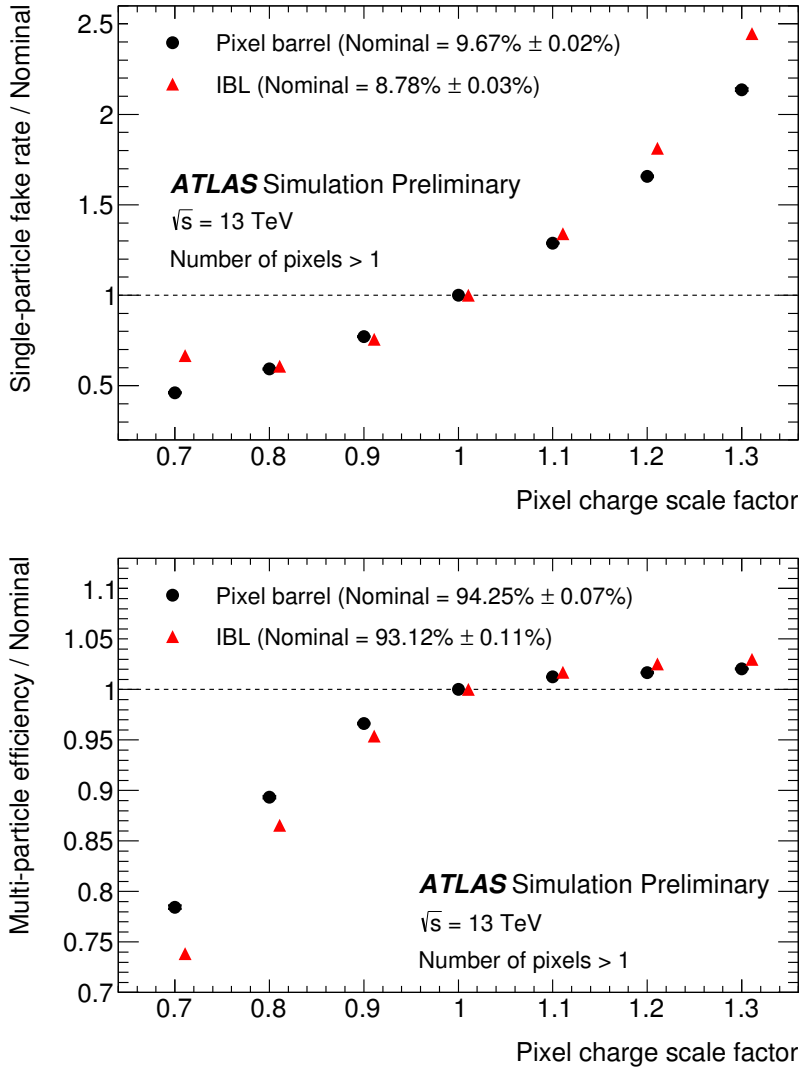


Figure 54: Performance of the pixel neural network used to identify clusters created by multiple charged particles, as a function of constant coherent scaling of the charge in each pixel in the cluster. The top figure shows the rate at which the neural network wrongly identifies clusters with one generated particle as clusters with multiple particles. The bottom figure shows the rate at which the neural network correctly identifies clusters generated by multiple particles as such.

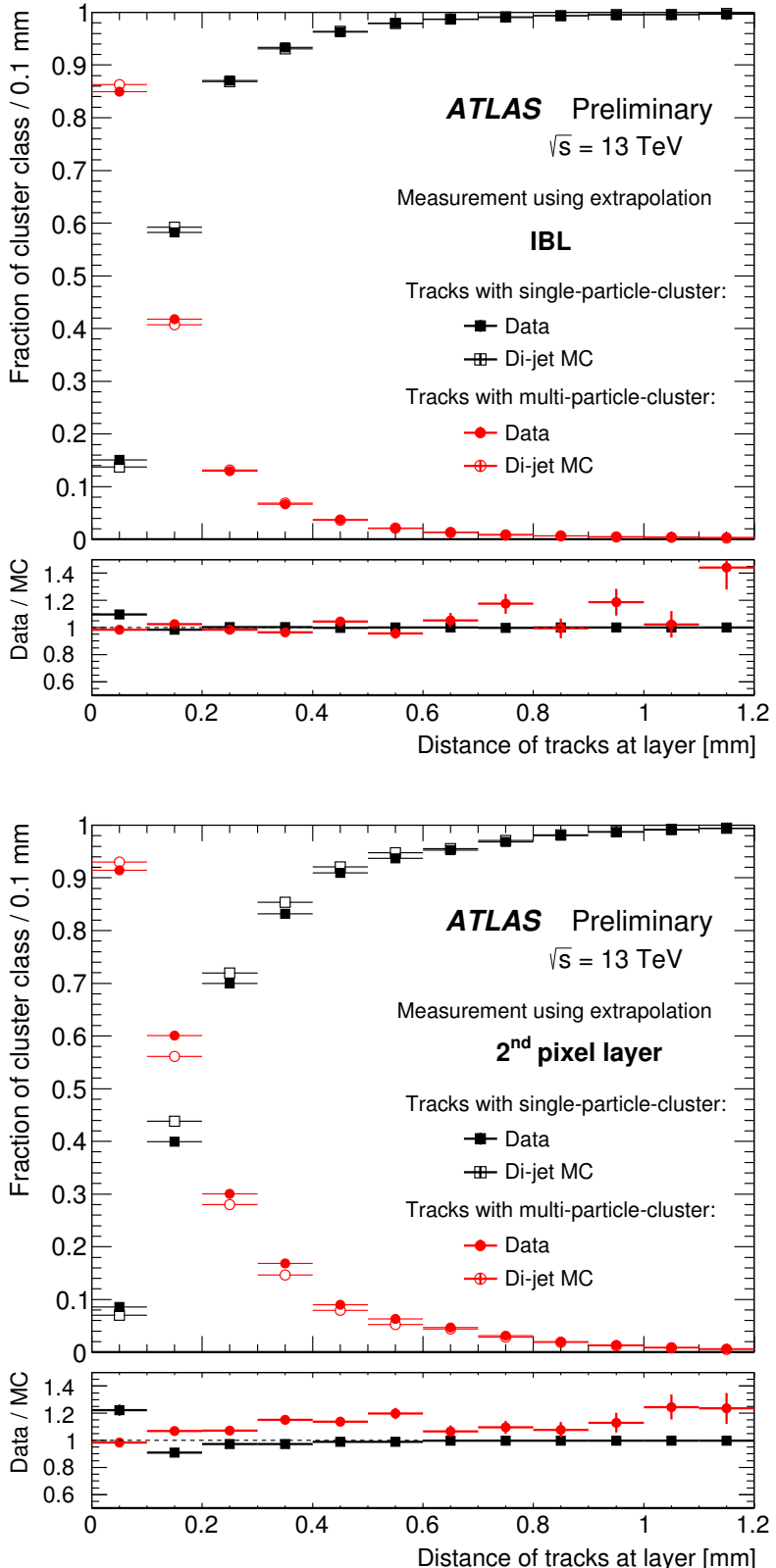


Figure 55: Fraction of cluster classes as a function of the distance between tracks for IBL (top) and 2nd pixel layer (bottom).

1745

Part IV

1746

SEARCHING FOR SUPERSYMMETRY

1747

This section describes an analysis of the ATLAS data carried out by the author and her analysis team. The analysis was performed on events from $p - p$ collisions provided by the LHC at $\sqrt{s}=13$ TeV. It searches for events like those described in [Section 2.2.3](#), which contain a Z boson decaying to leptons, jets, and missing transverse energy. The selection of a signal region in which to search for these events, background estimates, systematic uncertainty estimates, results, and interpretations are all discussed.

1748

1749

1750

1751

1752

1753

1754

1755

1756

1757 BACKGROUND PROCESSES

1758 This analysis is fundamentally a search for Supersymmetry ([SUSY](#)) in events
 1759 with two leptons whose invariant mass is consistent with a Z boson. Ad-
 1760 ditional event selections are made to reduce Standard Model ([SM](#)) pro-
 1761 cesses relative to potential [SUSY](#) processes, defined by simplified models
 1762 discussed in [Section 2.2.3](#). [SUSY](#) events typically have large amounts of
 1763 E_T^{miss} , H_T (the scalar sum of the p_T of all jets and the leading two leptons
 1764 in an event), and many jets. All of these features can help isolate these
 1765 events from backgrounds. To understand what cuts would optimize the
 1766 sensitivity of the search, it is essential to first understand what these [SM](#)
 1767 backgrounds are.

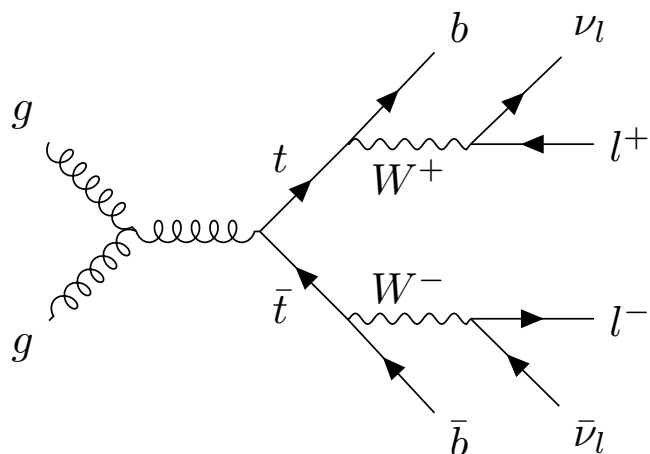


Figure 56: An example Feynman diagram of $t\bar{t}$ production and decay.

1768 TOP-ANTITOP ($t\bar{t}$) production is the largest background for this search.
 1769 [Figure 56](#) shows an example of this process, which results in many jets, lep-
 1770 tons, and neutrinos, which are seen in the detector as E_T^{miss} . Thus, $t\bar{t}$ events
 1771 naturally have high E_T^{miss} and H_T , jets, and leptons from two different W
 1772 boson decays, which may coincidentally form an invariant mass consistent
 1773 with a Z boson. These events are very difficult to separate from potential
 1774 signals, though keeping the mass window small and requiring E_T^{miss} and
 1775 H_T above the typical values for $t\bar{t}$ events helps reduce this background.

1776 DIBOSON (VV) production is the next leading background. These events
 1777 can contain real Z bosons and will peak on-Z like a signal. In addition, in
 1778 events like [Figure 57](#), an additional W boson can decay to another lepton
 1779 and a neutrino, providing E_T^{miss} . The pictured process can occur with asso-
 1780 ciated jets, but at reduced rates, so adding a jet requirement to the signal
 1781 region helps reduce these events. If the W boson in this diagram instead

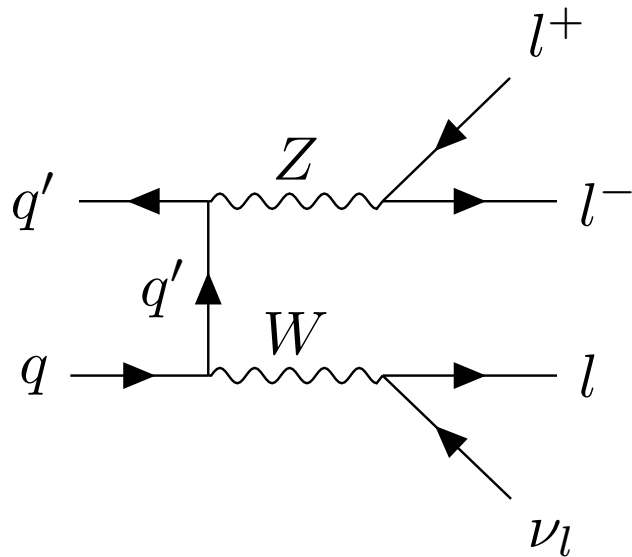


Figure 57: An example Feynman diagram of the production and decay of a WZ event.

1782 decayed to two jets, there would be no true E_T^{miss} from a neutrino, so a
 1783 E_T^{miss} cut in conjunction with a jet cut is very effective in reducing the total
 1784 diboson background. A veto on a third lepton could also be used to reduce
 1785 this background, but, depending on the signal model considered, this veto
 1786 can also decrease signal acceptance, so it is not used in this analysis.

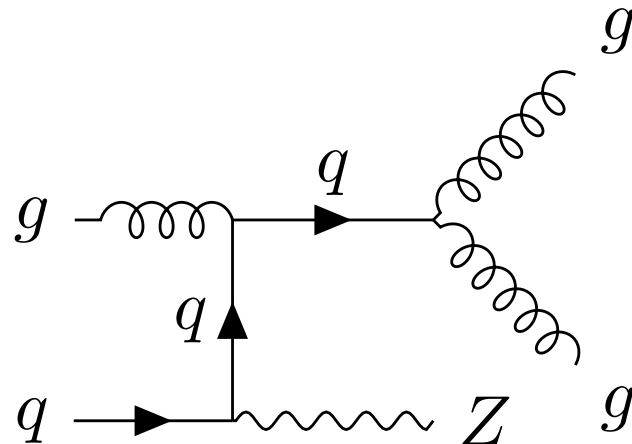


Figure 58: An example Feynman diagram of the production and decay of a $Z/\gamma^* + \text{jets}$ event.

1787 $Z/\gamma^* + \text{jets}$ processes are very common but, as shown in Figure 58,
 1788 don't produce any true E_T^{miss} . A high H_T cut helps reduce this background,
 1789 but this process often occurs with associated jets, producing many events
 1790 with large amounts of hadronic activity. E_T^{miss} is the most powerful variable
 1791 to reduce this background, because though events with mismeasured jets

1792 or leptons can fake E_T^{miss} , mismeasurements drastic enough to produce
 1793 hundreds of GeV of E_T^{miss} are rare.

1794 Other processes can contribute to the Standard Model background at
 1795 lower rates. Processes similar to $Z/\gamma^* + \text{jets}$ but with a W boson instead of
 1796 a Z have real E_T^{miss} from leptonic W decays, but only one lepton. However,
 1797 a fake or non-prompt lepton can cause these events to look very similar to
 1798 simulated signals. Additionally, there are rare processes such as $t\bar{t}$ produc-
 1799 tion in association with bosons that will also be difficult to separate from
 1800 signal processes.

1801 7.1 DATA AND MONTE CARLO SAMPLES

1802 This analysis uses data collected by the ATLAS detector from $p - p$ colli-
 1803 sions at a center-of-mass energy of 13 TeV in 2015 and 2016, corresponding
 1804 to a total luminosity of 14.7 fb^{-1} . The data collected using a combination
 1805 of unprescaled single and dilepton triggers, discussed in greater detail in
 1806 [Chapter 9](#). In addition, photon events are collected for use in a control
 1807 region using both prescaled and unprescaled triggers, with the lowest trig-
 1808 ger threshold at 20 GeV.

1809 MC samples are generated for each background process that appears
 1810 in the signal and validation regions. [Table 2](#) details the method used to
 1811 produce each sample, and more information can be found in [Section 2.3](#).
 1812 These simulated background events, in conjunction with the simulated
 1813 signal discussed in [Section 2.2.3](#), are used to determine approximate sensi-
 1814 tivities of the search and optimize signal regions and amount of data used.
 1815 The background MC also provides a valuable cross-check for many of the
 1816 data-driven background estimates discussed in [Chapter 10](#), and in some
 1817 cases, provides the primary estimate of the background.

Table 2: Simulated background event samples used in this analysis with the corresponding matrix element and parton shower generators, cross-section order in α_s used to normalise the event yield, underlying-event tune and PDF set.

Physics process	Generator	Parton Shower	Cross section	Tune	PDF set
$t\bar{t} + W$ and $t\bar{t} + Z$ [70, 71]	MG5_AMC@NLO	Pythia 8.186	NLO [72, 73]	A14	NNPDF23LO
$t\bar{t} + WW$ [70]	MG5_AMC@NLO	Pythia 8.186	LO [38]	A14	NNPDF23LO
$t\bar{t}$ [74]	PowHEG Box v2 r3026	Pythia 6.428	NNLO+NNLL [75, 76]	PERUGIA2012	NULO CT10
Single-top (Wt) [74]	PowHEG Box v2 r2856	Pythia 6.428	Approx. NNLO [77]	PERUGIA2012	NULO CT10
WW , WZ and ZZ [78]	SHERPA 2.1.1	SHERPA 2.1.1	NLO [79, 80]	SHERPA default	NULO CT10
$Z/\gamma^*(\rightarrow \ell\ell) + \text{jets}$ [81]	SHERPA 2.1.1	SHERPA 2.1.1	NNLO [82, 83]	SHERPA default	NULO CT10
$\gamma + \text{jets}$	SHERPA 2.1.1	SHERPA 2.1.1	LO [42]	SHERPA default	NULO CT10
$V(=W, Z)\gamma$ signal	SHERPA 2.1.1	SHERPA 2.1.1	LO [42]	SHERPA default	NULO CT10
	MG5_AMC@NLO	Pythia 8.186	NULO	A14	NNPDF23LO

1818

1819 OBJECT IDENTIFICATION AND SELECTION

1820 This section describes the identification and selection of objects in the
 1821 events of this analysis. Objects are first required to pass *baseline* selections,
 1822 which are used for Overlap Removal ([OR](#)) and the calculation of E_T^{miss} ,
 1823 then have tighter *signal* selections applied, which define the objects consid-
 1824 ered in the final analysis of events. Definitions are presented for electrons,
 1825 muons, and jets, which are all required in the Signal Region ([SR](#)) of the
 1826 analysis, as well as photons, which are used in background estimation.
 1827 This section refers to quality definitions described in [Chapter 5](#).

1828 8.1 ELECTRONS

1829 Electrons are reconstructed using the Egamma algorithm discussed in [Sec-](#)
 1830 [tion 5.1](#). All electrons are required to be within $|\eta| < 2.47$, to ensure that all
 1831 tracks are consistently within the tracking capability of the [ID](#). Baseline lep-
 1832 tons are required to have $p_T > 10 \text{ GeV}$ and pass the [LHLoose](#) quality stan-
 1833 dard. Signal leptons are further required to be of [LHMedium](#) quality with
 1834 [GradientLoose](#) isolation, and must have $p_T > 25 \text{ GeV}$. Additional cuts on
 1835 impact parameter are made for electrons with the goal of identifying only
 1836 electrons coming from the primary vertex of the event, the vertex with the
 1837 highest associated p_T . These requirements, and all the other requirements
 1838 made on the electrons can be seen in [Table 3](#).

Cut	Value/description
Baseline Electron	
Acceptance	$p_T > 10 \text{ GeV}, \eta^{\text{clust}} < 2.47$
Quality	Loose
Signal Electron	
Acceptance	$p_T > 25 \text{ GeV}, \eta^{\text{clust}} < 2.47$
Quality	Medium
Isolation	GradientLoose
Impact parameter	$ z_0 \sin \theta < 0.5 \text{ mm}$ $ d_0 / \sigma_{d_0} < 5$

Table 3: Summary of the electron selection criteria. The signal selection require-
 ments are applied on top of the baseline selection.

1839 With these requirements, the ATLAS detector is 95% efficient at identify-
 1840 ing electrons with $p_T > 25 \text{ GeV}$, which rises to 99% at $p_T > 60 \text{ GeV}$ [[84](#)]. Scale
 1841 factors are applied to correct [MC](#) to match data efficiencies. These efficien-

1842 cies are measured as a function of p_T and η , and include both electron
 1843 identification efficiencies and trigger efficiencies.

1844 8.2 MUONS

1845 Muons are reconstructed according to the process discussed in [Section 5.3](#).
 1846 Baseline muons are required to have $p_T > 10$ GeV and $|\eta| < 2.5$, including
 1847 muons that can be tracked both by the [ID](#) and the [MS](#), and must pass a
 1848 Medium quality cut. Signal muons are additionally required to have $p_T >$
 1849 25 GeV, and to have [GradientLoose](#) isolation. As with the electrons, quality
 1850 cuts are made to ensure that the muon is consistent with coming from
 1851 a decay from the event's primary vertex. Additionally, the muon must
 1852 not be flagged [isBadMuon](#), which reduces the number of events with very
 1853 inconsistent [ID](#) and [MS](#) tracks. The full set of requirements can be seen in
 1854 [Table 4](#).

Cut	Value/description
Baseline Muon	
Acceptance	$p_T > 10$ GeV, $ \eta < 2.5$
Quality	Medium
Signal Muon	
Acceptance	$p_T > 25$ GeV, $ \eta < 2.5$
Quality	Medium
Isolation	GradientLoose
Impact parameter	$ z_0 \sin \theta < 0.5$ mm $ d_0/\sigma_{d_0} < 3$
isBadMuon	MCP isBadMuon Flag

Table 4: Summary of the muon selection criteria. The signal selection requirements are applied on top of the baseline selection.

1855 Muons with $p_T > 25$ GeV are identified with a 95% efficiency, which
 1856 rises to 99% for muons with $p_T > 80$ GeV[85]. Including trigger and iso-
 1857 lation requirements, these efficiencies drop to about 80% for muons with
 1858 $p_T > 25$ GeV and 90% for muons with $p_T > 200$ GeV. This drop is largely
 1859 the consequence of incomplete η coverage of the [RPCs](#), discussed in [Sec-](#)
 1860 [tion 5.3](#). Scalefactors to correct the [MC](#) identification efficiencies according
 1861 to data are used.

1862 8.3 JETS

1863 Jets are reconstructed according to [Section 5.4](#), with baseline jets using the
 1864 [AntiKt4EMTopo](#) algorithm, with a minimum p_T of 20 GeV and $|\eta| < 2.8$.
 1865 Signal jets increase this p_T requirement to 40 GeV and decrease their ac-

1866 ceptance to $|\eta| < 2.5$. JVT requirements are enforced to reduce the number
1867 of jets from pile-up. The full set of requirements can be seen in [Table 5](#).

Cut	Value/description
Baseline jet	
Collection	AntiKt4EMTopo
Acceptance	$p_T > 20 \text{ GeV}$, $ \eta < 2.8$
Signal jet	
Acceptance	$p_T > 30 \text{ GeV}$, $ \eta < 2.5$
JVT	$ \text{JVT} > 0.59$ for jets with $p_T < 60 \text{ GeV}$ and $ \eta < 2.4$
Signal b -jet	
b -tagger Algorithm	MV2c20
Efficiency	77 %
Acceptance	$p_T > 30 \text{ GeV}$, $ \eta < 2.5$
JVT	$ \text{JVT} > 0.59$ for jets with $p_T < 60 \text{ GeV}$ and $ \eta < 2.4$

Table 5: Summary of the jet and b -jet selection criteria. The signal selection requirements are applied on top of the baseline requirements.

1868 Though no b -jets are required in the SR of this analysis, some Control
1869 Regions (CRs) use b -enhanced and b -vetoed regions to determine the im-
1870 pact of heavy flavor. These b -jets are identified using the MV2c20 algorithm
1871 at a 77% efficient working point, and are only identified for $|\eta| < 2.5$.

1872 8.4 PHOTONS

1873 Photons are used to estimate the $Z/\gamma^* + \text{jets}$ background in this analy-
1874 sis, and they are reconstructed according to [Section 5.2](#). Baseline and sig-
1875 nal photons are nearly identical. Each must pass a tight selection with
1876 FixedCutTight isolation and have $p_T > 25 \text{ GeV}$ as well as $|\eta| < 2.37$. Sig-
1877 nal photons with $1.37 < |\eta| < 1.6$ are rejected due to an discontinuity
1878 in the calorimeter which results in very large energy resolutions in this
1879 region. The full selection requirements can be seen in [Table 6](#).

Cut	Value/description
Baseline Photon	
Acceptance	$p_T > 25 \text{ GeV}, \eta < 2.37$
Quality	tight
Signal Photon	
Acceptance	$p_T > 25 \text{ GeV}, \eta < 2.37$ rejecting $1.37 < \eta < 1.6$
Quality	tight
Isolation	FixedCutTight

Table 6: Summary of the photon selection criteria.

1880

1881 EVENT SELECTION

1882 The goal of this analysis is to identify events resembling [Figure 14](#) in col-
 1883 lisions in the ATLAS detector. In order to do this, a Signal Region ([SR](#)) is
 1884 defined with the goal of maximizing the identification efficiency of signal-
 1885 like events while minimizing [SM](#) backgrounds. However, because this anal-
 1886 ysis reinvestigates an excess of events seen in Run 1 with the ATLAS de-
 1887 tector, the signal region was frozen and could not be reoptimized for the
 1888 new, higher energy data in Run 2. The [SR](#), called *SRZ*, was predetermined,
 1889 including events with two opposite-sign, same-flavor leptons that recon-
 1890 struct a mass, $m_{\ell\ell}$, close to that of the Z boson, with the additional require-
 1891 ment of two jets, $E_T^{\text{miss}} > 225 \text{ GeV}$, and H_T of at least 600 GeV. Additionally,
 1892 a cut on $\Delta\phi(\text{jet}_{12}, p_T^{\text{miss}})$ was made in order to reduce the number of events
 1893 with high E_T^{miss} due to mismeasurement of one of the leading two jets.

1894 Though this [SR](#) was fixed, the methods used to estimate its expected [SM](#)
 1895 backgrounds were not. A set of Control Regions ([CRs](#)) and Validation Re-
 1896 gions ([VRs](#)) were chosen to make these estimations possible. [CRs](#) are regions
 1897 in which the collected data can be used to make an estimate of an expected
 1898 background in the [SR](#), while [VRs](#) are used to confirm the efficacy of these
 1899 methods. Both [CRs](#) and [VRs](#) are designed to minimize contamination from
 1900 the [BSM](#) process being searched for. This is desirable because signal con-
 1901 tamination in a [CR](#) can lead to an overestimate of the [SM](#) background in
 1902 the [SR](#), disguising a genuine signal as background. Contamination in a [VR](#),
 1903 where background estimates are being validated, can make it appear that
 1904 the [SM](#) background is not well described by an estimate, causing analyzers
 1905 to adjust the method to account for the difference, and again, disguising
 1906 the effect of the same signal in the [SR](#).

1907 The strategy for estimating the [FS](#) backgrounds, for example, depends
 1908 on a series of [CRs](#) and [VRs](#) depicted in [Figure 59](#). One estimate, the fla-
 1909 vor symmetry method, takes data from CR-FS, a different-flavor region with
 1910 slightly wider $m_{\ell\ell}$ bounds than the [SR](#), and uses these events to predict
 1911 the contribution of flavor symmetric processes to SRZ. An independent
 1912 method called a sideband fit uses a control region CRT to measure the
 1913 flavor symmetric events outside of the Z mass window, and uses [MC](#) to
 1914 extrapolate inside the Z mass window to SRZ. Then, both methods are
 1915 validated at lower E_T^{miss} with an otherwise identical series of regions, with
 1916 VRS corresponding to SRZ, VRT corresponding to CRT, and VR-FS corre-
 1917 sponding to CR-FS.

1918 Each background estimation requires its own set of these regions, and
 1919 the full list of regions used in this analysis can be seen in [Table 7](#). In ad-
 1920 dition to the Flavor Symmetric ([FS](#)) regions described above, there is one
 1921 more [CR](#), CR- γ , which is a photon region used to predict the number of
 1922 $Z/\gamma^* + \text{jets}$ events, a process described in [Section 10.2](#). Additional [VRs](#),

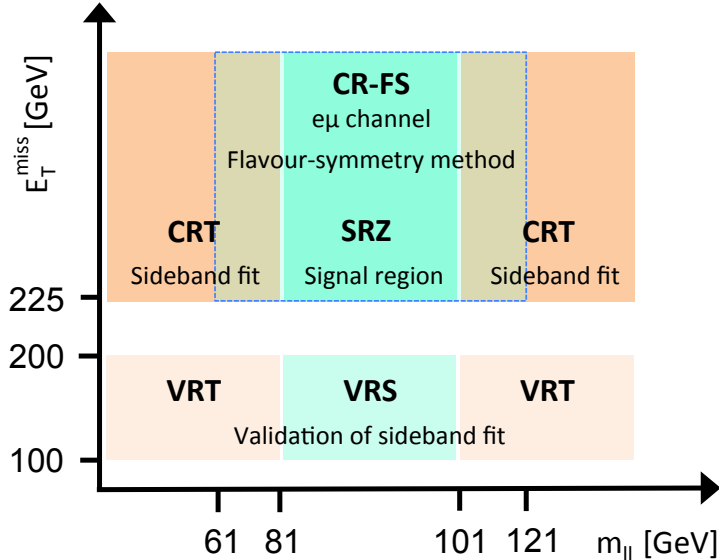


Figure 59: Schematic diagrams of the control, validation and signal regions for the on-shell Z (top) and edge (bottom) searches. For the on-shell Z search the various regions are shown in the $m_{\ell\ell} - E_T^{\text{miss}}$ plane, whereas in the case of the edge search the signal and validation regions are depicted in the $H_T - E_T^{\text{miss}}$ plane.

1923 VR-ZZ, VR-WZ, and VR-3L, are introduced in order to validate the back-
 1924 grounds taken directly from MC. There are several additional regions used,
 1925 for example, in the estimation of the fakes and $Z/\gamma^* + \text{jets}$ backgrounds,
 1926 that are defined in their respective sections.

1927 **9.1 TRIGGER STRATEGY**

1928 In order to collect data for the analysis, triggers must be chosen that pro-
 1929 vide good efficiency in each of the SR, VR, and CRs. This analysis primarily
 1930 depends on triggers on leptons, which are required in nearly every region.
 1931 To simplify the application of trigger scalefactors, which correct MC yields
 1932 for a given trigger to match the data efficiencies, events are broken down
 1933 into a series of kinematic ranges, each with a designated trigger. These
 1934 regions can be seen in Table 8.

1935 In kinematic regions where single lepton triggers are fully efficient, they
 1936 are preferentially used. In lower- p_T ranges, dilepton triggers are used, tar-
 1937 geting either ee , $\mu\mu$, or $e\mu$ events. Electron triggers are selected over muon
 1938 triggers when possible because they have higher efficiencies in most cases.

1939 In CR- γ , there are no leptons, so an alternate trigger strategy must be
 1940 used. Section 10.2.1 describes this triggering scheme, which includes a
 1941 combination of prescaled and unprescaled photon triggers to allow for the
 1942 collection of low- p_T $\gamma + \text{jets}$ events.

Table 7: Overview of all signal, control and validation regions used in the on-shell Z search. More details are given in the text. The flavour combination of the dilepton pair is denoted as either “SF” for same-flavour or “DF” for different flavour. All regions require at least two leptons, unless otherwise indicated. In the case of CR γ , VR-WZ, VR-ZZ, and VR-3L the number of leptons, rather than a specific flavour configuration, is indicated. The main requirements that distinguish the control and validation regions from the signal region are indicated in bold. Most of the kinematic quantities used to define these regions are discussed in the text. The quantity $m_T(\ell_3, E_T^{\text{miss}})$ indicates the transverse mass formed by the E_T^{miss} and the lepton which is not assigned to either of the Z-decay leptons.

On-shell Z regions	E_T^{miss} [GeV]	H_T [GeV]	n_{jets}	$m_{\ell\ell}$ [GeV]	SF/DF	$\Delta\phi(\text{jet}_{12}, p_T^{\text{miss}})$	$m_T(\ell_3, E_T^{\text{miss}})$ [GeV]	$n_{\text{b-jets}}$
Signal region								
SRZ	> 225	> 600	≥ 2	$81 < m_{\ell\ell} < 101$	SF	> 0.4	—	—
Control regions								
CRZ	< 60	> 600	≥ 2	$81 < m_{\ell\ell} < 101$	SF	> 0.4	—	—
CR-FS	> 225	> 600	≥ 2	61 < $m_{\ell\ell}$ < 121	DF	> 0.4	—	—
CRT	> 225	> 600	≥ 2	> 40 , $m_{\ell\ell} \notin [81, 101]$	SF	> 0.4	—	—
CR γ	—	> 600	≥ 2	—	$0\ell, 1\gamma$	—	—	—
Validation regions								
VRZ	< 225	> 600	≥ 2	$81 < m_{\ell\ell} < 101$	SF	> 0.4	—	—
VRT	100–200	> 600	≥ 2	> 40 , $m_{\ell\ell} \notin [81, 101]$	SF	> 0.4	—	—
VRS	100–200	> 600	≥ 2	$81 < m_{\ell\ell} < 101$	SF	> 0.4	—	—
VR-FS	100–200	> 600	≥ 2	61 < $m_{\ell\ell}$ < 121	DF	> 0.4	—	—
VR-WZ	100–200	—	—	—	3 ℓ	—	< 100	0
VR-ZZ	< 100	—	—	—	4 ℓ	—	—	0
VR-3L	60–100	> 200	≥ 2	$81 < m_{\ell\ell} < 101$	3 ℓ	> 0.4	—	—

Lepton p_T	Trigger in 2015	Trigger in 2016
Di-electron channel		
$p_T(e_1) > 65 \text{ GeV}$	HLT_e60_lhmedium	HLT_e60_lhmedium_nod0
$p_T(e_1) \leq 65 \text{ GeV}$	HLT_2e17_lhloose	HLT_2e17_lhvloose_nod0
Di-muon channel		
$p_T(\mu_1) > 52.5 \text{ GeV}$	HLT_mu50	HLT_mu50
$p_T(\mu_1) \leq 52.5 \text{ GeV}$	HLT_mu24_mu8noL1	HLT_2mu14_nomucomb
Electron-muon channel		
$p_T(e) > 65 \text{ GeV}$	HLT_e60_lhmedium	HLT_e60_lhmedium_nod0
$p_T(e) \leq 65 \text{ GeV}$ and $p_T(\mu) > 52.5 \text{ GeV}$	HLT_mu50	HLT_mu50
$p_T(e) \leq 65 \text{ GeV}$ and $p_T(\mu) \leq 52.5 \text{ GeV}$ and $p_T(e) < p_T(\mu)$	HLT_e7_lhmedium_mu24	HLT_e7_lhmedium_nod0_mu24
$p_T(e) \leq 65 \text{ GeV}$ and $p_T(\mu) \leq 52.5 \text{ GeV}$ and $p_T(\mu) < p_T(e)$	HLT_e17_lhloose_mu14	HLT_e17_lhloose_nod0_mu14

Table 8: Lepton trigger requirements used for the analysis in different regions of lepton- p_T phase space.

1943 9.2 SIGNAL EFFICIENCY AND CONTAMINATION

1944 Using the simplified models discussed in [Section 2.2.3](#), the contributions
 1945 of potential signals in these regions can be studied. In the [SR](#), the goal
 1946 is to include as much of the potential signal as possible, while excluding
 1947 as much [SM](#) background as possible. [Figure 60](#) shows the acceptance and
 1948 efficiency for the simplified models at different mass points. Acceptance
 1949 is defined as the fraction of signal events that produce signatures that
 1950 kinematically match the [SR](#), while the efficiency is the fraction of these
 1951 events expected to be correctly identified by the ATLAS detector.

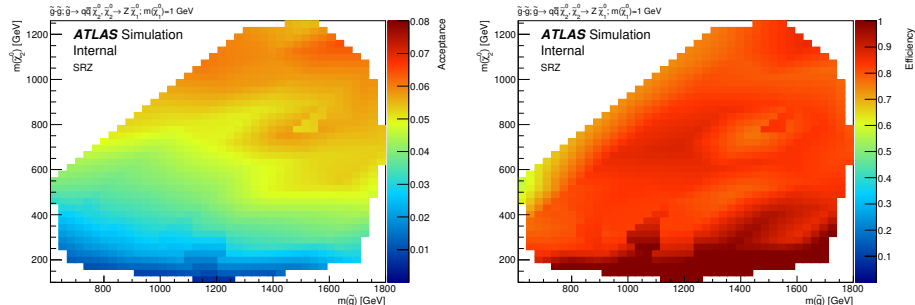


Figure 60: Signal region acceptance (left) and efficiency (right) in SRZ for the simplified model with gluino pair production with $\tilde{\chi}_2^0$ decays to $\tilde{\chi}_1^0$ and an on-shell Z boson with 1GeV neutralino LSP. Acceptance is calculated by applying the signal-region kinematic requirements to truth objects in [MC](#), which do not suffer from identification inefficiencies or measurement resolutions.

1952 A similar test is done for the main [CRs](#) and [VRs](#) which estimates their sus-
 1953 ceptibility to signal contamination. Figures [61](#) and [62](#) show the fraction of
 1954 events in these regions expected to come from signal for different points
 1955 on the simplified model's mass grid. Contamination is highest in VRS, at

1956 low $m_{\tilde{g}}$. However, past analyses have already excluded most models with
 1957 $m_{\tilde{g}} < 800$ GeV, so these regions are not important targets for this search
 1958 [1].

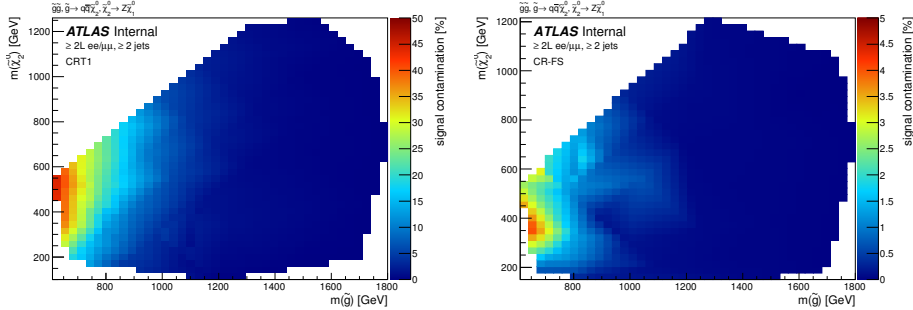


Figure 61: Expected signal contamination in CRT (left) and CR-FS (right) for the signal model with gluino pair production, where the gluinos decay to quarks and a neutralino, with the neutralino subsequently decaying to a Z boson and a 1GeV neutralino LSP.

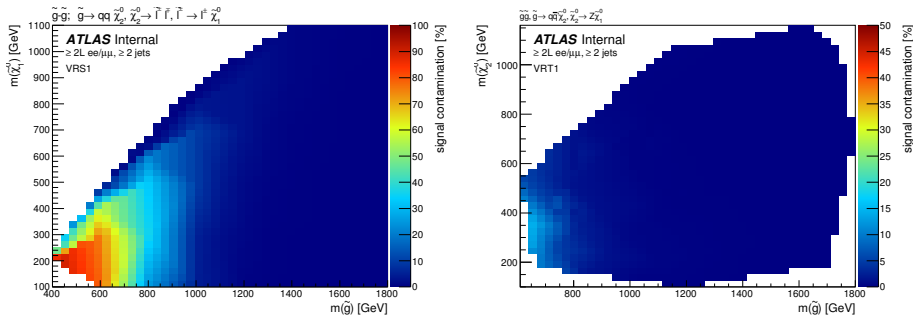


Figure 62: Expected signal contamination in VRS (left) and VRT (right) for the signal model with gluino pair production, where the gluinos decay to quarks and a neutralino, with the neutralino subsequently decaying to a Z boson and a 1GeV neutralino LSP.

1959

1960 BACKGROUND ESTIMATION

1961 This analysis requires two leptons that reconstruct to a Z mass, jets, E_T^{miss} ,
 1962 and H_T . Any standard model processes that produce this signature will
 1963 appear as a background to the search. The most important task of the
 1964 analysis is to identify and estimate these backgrounds, so that any excess
 1965 of events appearing on top of the standard model background can be iden-
 1966 tified. The main backgrounds for this analysis are described in [Chapter 7](#).
 1967 The largest background is from flavor symmetric processes, with smaller
 1968 contributions coming from diboson processes, $Z/\gamma^* + \text{jets}$, rare top pro-
 1969 cesses, and fake and non-prompt leptons.

1970 10.1 FLAVOR SYMMETRIC PROCESSES

1971 Flavor Symmetric ([FS](#)) backgrounds include any processes that produce
 1972 pairs of leptons with uncorrelated flavor in the final state. In this analysis,
 1973 the largest contribution comes from $t\bar{t}$, with additional events from pro-
 1974 cesses like WW and $Z \rightarrow \tau\tau$. In these processes, each lepton comes from
 1975 a different decay. Unlike a $Z \rightarrow \ell\ell$ decay then, these leptons' flavors are
 1976 completely independent.

1977 10.1.1 *Flavor Symmetry Method*

1978 As a consequence of the independence of the lepton flavors, any [FS](#) process
 1979 should produce ee , $\mu\mu$, and $e\mu$ events in a 1:1:2 ratio. This ratio is taken
 1980 advantage of in the flavor symmetry method by measuring $e\mu$ events in
 1981 data and using them to predict the contribution of these processes in the
 1982 ee and $\mu\mu$ channels. [1]

1983 To estimate the number of events in SRZ, a control region called CR-FS is
 1984 used. Both regions are defined in [Table 7](#). CR-FS is very similar to SRZ with
 1985 two changes: it requires different-flavor leptons instead of the same-flavor
 1986 leptons required by SRZ, and the $m_{\ell\ell}$ range it covers has been expanded
 1987 by a factor of three, now ranging from 61 to 121 GeV. The expansion of the
 1988 $m_{\ell\ell}$ window is done to increase the number of events in the control region,
 1989 thus lowering the statistical uncertainty of the prediction¹.

1990 This control region is expected to be about 95% pure in [FS](#) processes,
 1991 with most of the remaining events coming from fake or non-prompt lep-

¹ Though this statistical uncertainty is no longer dominant for the analysis, the method was developed for a smaller dataset for which this expansion dramatically decreased the total uncertainty on the background prediction. [86] Because of previous excesses seen, the signal region was not reoptimized for the larger dataset used in this search, but in future iterations of this analysis, the signal region will likely have tighter cuts, making this decreased statistical uncertainty significant once again.

tons. The **FS** portion is made up primarily of $t\bar{t}$ ($\sim 80\%$), with additional contributions from Wt ($\sim 10\%$), WW ($\sim 10\%$), and $< 1\% Z \rightarrow \tau\tau$.

After the number of data events are measured in CR-FS, correction factors are applied to account for trigger efficiencies, selection efficiencies, the $m_{\ell\ell}$ expansion, and the purity of the control region. Combining these factors, the estimate for number of events in the ee and $\mu\mu$ channels is as follows:

$$N_{ee}^{\text{est}} = \frac{1}{2} \cdot f_{\text{FS}} \cdot f_{Z\text{-mass}} \cdot \sum_{i=1}^{N_{e\mu}^{\text{data}}} k_e(p_T^\mu, \eta^\mu) \cdot \alpha(p_T^{\ell_1}, \eta^{\ell_1}), \quad (36)$$

$$N_{\mu\mu}^{\text{est}} = \frac{1}{2} \cdot f_{\text{FS}} \cdot f_{Z\text{-mass}} \cdot \sum_{i=1}^{N_{e\mu}^{\text{data}}} k_\mu(p_T^e, \eta^e) \cdot \alpha(p_T^{\ell_1}, \eta^{\ell_1}), \quad (37)$$

where $N_{e\mu}^{\text{data}}$ is the number of data events observed in CR-FS, f_{FS} is the **FS** purity in CR-FS, $f_{Z\text{-mass}}$ is the fraction of events in the widened $m_{\ell\ell}$ range expected to be in the on- Z range (taken from $t\bar{t}$ MC), $k_e(p_T, \eta)$ and $k_\mu(p_T, \eta)$ are relative selection efficiencies for electrons and muons, calculated in bins of p_T and η of the lepton to be replaced, and $\alpha(p_T, \eta)$ accounts for the different trigger efficiencies for events in each channel, binned based on the kinematics of the leading lepton. These k and α factors are calculated from data in an inclusive on- Z selection ($81 < m_{\ell\ell}/\text{GeV} < 101$, ≥ 2 jets), according to:

$$k_e(p_T, \eta) = \sqrt{\frac{N_{ee}^{\text{meas}}}{N_{\mu\mu}^{\text{meas}}}} \quad (38)$$

$$k_\mu(p_T, \eta) = \sqrt{\frac{N_{\mu\mu}^{\text{meas}}}{N_{ee}^{\text{meas}}}} \quad (39)$$

$$\alpha(p_T, \eta) = \frac{\sqrt{\epsilon_{ee}^{\text{trig}}(p_T, \eta) \times \epsilon_{\mu\mu}^{\text{trig}}(p_T, \eta)}}{\epsilon_{e\mu}^{\text{trig}}(p_T, \eta)} \quad (40)$$

where $\epsilon_{ee/\mu\mu}^{\text{trig}}$ is the trigger efficiency² and $N_{ee/\mu\mu}^{\text{meas}}$ is the number of $ee/\mu\mu$ events in the inclusive on- Z region described above. Here $k_e(p_T, \eta) = 1/k_\mu(p_T, \eta)$, and this k factor is calculated separately for leading and sub-leading leptons, and the appropriate k value is selected based on which of the leptons is to be replaced.

Electron, muon, and trigger efficiencies are all quite close to one, and as a consequence, these correction factors are typically within 10% of unity, except in the region $|\eta| < 0.1$ where, because of the lack of coverage of the muon spectrometer, they are up to 50% from unity.

² This efficiency is defined by taking all events in the inclusive on- Z selection mentioned above and determining the fraction that passes the relevant trigger requirement defined by [Table 8](#). Because the offline selection made on these events already has some trigger dependence, this calculation of efficiency could be slightly biased. This effect is considered in [Section 11.1.1](#), and the uncertainty applied to the estimate as a result is described.

Region	ee prediction	$\mu\mu$ prediction	combined prediction
SRZ	16.50 ± 2.11	16.67 ± 2.04	33.16 ± 3.94
VRS	49.70 ± 4.61	49.60 ± 4.56	99.31 ± 8.47

Table 9: Yields in signal and validation regions for the flavor symmetric background. Errors include statistical uncertainty, uncertainty from MC closure, uncertainty from the k and α factors, uncertainty due to deriving triggers efficiencies from a DAOD, and uncertainty on the MC shape used to correct for the $m_{\ell\ell}$ expansion.

2017 The estimate is corrected for contamination of non-**FS** backgrounds in
 2018 CR-**FS**. A scaling factor is determined by subtracting these backgrounds
 2019 from the number of $e\mu$ events measured in CR-**FS**, then determining the
 2020 fraction of the original data events that this pure-**FS** number represents.
 2021 The estimate for the non-**FS** backgrounds is taken from **MC** for all processes
 2022 except fakes, which are predicted from data using the matrix method de-
 2023 scribed in [Section 10.3](#).

2024 A prediction is made both for the signal region, SRZ, and the lower- E_T^{miss}
 2025 validation region, VRS. This process is performed separately for the two
 2026 data taking periods, 2015 and 2016, because of the changing triggers and
 2027 conditions. The results are then summed together, as shown in [Table 9](#).
 2028 The uncertainties in this table are discussed in [Section 11.1.1](#).

2029 10.1.2 Sideband Fit Method

2030 As a crosscheck to the flavor symmetry method, a **MC**-based method is
 2031 used. This method is called a *sideband fit*, and it begins with a **MC** estimate
 2032 of the signal region across an $m_{\ell\ell}$ range that includes all values above 40
 2033 GeV. This region, excluding the on-Z range that makes up the **SR**, is used
 2034 as a control region, defined as CRT in [Table 7](#).

2035 The total data yield is measured in CRT, and the **MC** is fit to match this
 2036 yield with one normalization factor which scales the overall $t\bar{t}$ background.
 2037 As mentioned in the previous section, $t\bar{t}$ is the dominant **FS** background,
 2038 making up about 80% of the total events. All other backgrounds contribut-
 2039 ing to this control region are constrained by their uncertainties, which are
 2040 used as nuisance parameters in the fit. The normalization factor from this
 2041 fit is then applied to the $t\bar{t}$ **MC** yield in the **SR**, and combined with the **MC**
 2042 predictions of the other **FS** processes in the **SR** to give a final estimate of
 2043 this background. The results of the fit can be seen in [Table 10](#).

2044 The method is repeated in VRS to validate the method. The normal-
 2045 ization factors, listed in [Table 11](#), are significantly different for the two
 2046 regions. This is expected because there is a known problem in which the
 2047 $t\bar{t}$ **MC** over-predicts the high- E_T^{miss} tail. This effect can be seen in a data-**MC**
 2048 comparison in [Figure 63](#). This is likely due to a mismodeling of the top
 2049 quark p_T distribution, which does not match the spectrum seen in data [87,

BACKGROUND ESTIMATION

channel	$ee/\mu\mu$ CRT	$ee/\mu\mu$ SRZ	ee SRZ	$ee/\mu\mu$ SRZ
Observed events	273	60	35	25
Fitted bkg events	272.76 ± 16.88	49.33 ± 8.04	27.09 ± 4.73	22.70 ± 3.80
Fitted flavour symmetry events	236.96 ± 21.66	28.96 ± 7.47	16.41 ± 4.33	12.55 ± 3.29
Fitted WZ/ZZ events	4.03 ± 1.13	14.27 ± 4.45	7.81 ± 2.45	6.46 ± 2.07
Fitted SHERPA Z/γ^* + jets events	1.95 ± 0.14	0.00 ± 0.00	0.00 ± 0.00	0.00 ± 0.00
Data-driven Z/γ^* + jets (γ + jets) events	0.00 ± 0.00	3.10 ± 2.25	$1.02^{+1.25}_{-1.02}$	2.08 ± 1.38
Fitted rare top events	4.04 ± 1.04	2.90 ± 0.76	1.39 ± 0.38	1.50 ± 0.40
Data-driven fake lepton events	25.78 ± 14.26	$0.10^{+0.18}_{-0.10}$	0.46 ± 0.45	0.10 ± 0.01
MC exp. SM events	366.71	61.01	33.73	27.74
MC exp. flavour symmetry events	331.32	40.72	23.09	17.63
MC exp. WZ/ZZ events	4.02	14.20	7.77	6.43
MC exp. SHERPA Z/γ^* + jets events	1.94	0.00	0.00	0.00
Data-driven exp. Z/γ^* + jets (γ + jets) events	0.00	3.10	1.02	2.08
MC exp. rare top events	4.04	2.89	1.39	1.50
Data-driven exp. fake lepton events	25.39	0.10	0.46	0.10

Table 10: Background fit results from the sideband fit method. The $t\bar{t}$ MC's normalization is taken as a free parameter in the fit to data in CRT, then that normalization factor is applied in SRZ. The results are shown here both divided between the ee and $\mu\mu$ channels and summed together. All other backgrounds are taken from MC in CRT, while in SRZ, the Z/γ^* + jets contribution is taken from the γ + jets method. The uncertainties quoted include both statistical and systematic components.

2050 88]. However, this method corrects for this mismodeling by performing fits
 2051 in regions very kinematically similar to the signal region.

Fit region	$t\bar{t}$ normalization
CRT	0.64 ± 0.18
VRT	0.80 ± 0.09

Table 11: Summary of the $t\bar{t}$ normalization factors calculated by the sideband fit to CRT and VRT for the 2015+2016 data.

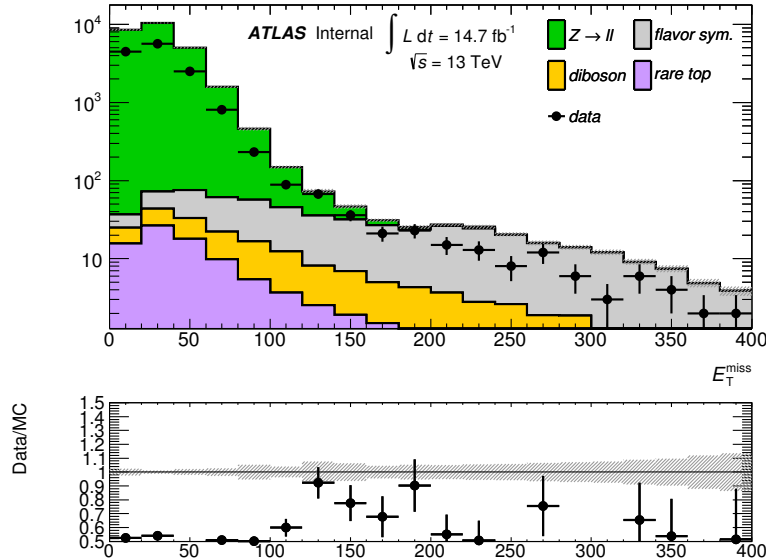


Figure 63: Comparison of data and MC in a selection like SRZ, without the E_T^{miss} cut.

2052 This method is extremely effective as a crosscheck because it uses a com-
 2053 pletely independent dataset from the flavor symmetry method, and the
 2054 two methods have very little overlap in dependence on MC. They produce
 2055 consistent results in both SRZ and VRS, as shown in Table 12.

2056 10.2 Z/γ^* + JETS BACKGROUND

2057 The Z/γ^* + jets background is mainly produced by a process called Drell-
 2058 Yan in which annihilating quark/anti-quark pairs produce a Z boson or
 2059 a virtual photon. These bosons then decay to two leptons, which, in the
 2060 case of the Z boson, naturally appear in the Z -mass window. The bo-
 2061 son typically recoils off a hadronic system, which can satisfy the jet and
 2062 H_T requirement in SRZ. However, this process rarely produces real E_T^{miss}
 2063 (though occasionally neutrinos do appear in its hadronic decays), so most
 2064 events with large amounts of E_T^{miss} are the result of extreme mismeasure-
 2065 ment. Because SRZ cuts on the very high E_T^{miss} tails of a Z distribution, a
 2066 small change in the assumptions about jet resolution or energy scale in MC

Region	Flavour-symmetry	Sideband fit
SRZ	33 ± 4	29 ± 7
VR-S	99 ± 8	92 ± 25

Table 12: Comparison of FS background predictions from the nominal method, the flavor symmetry method, and the cross-check, the sideband fit method. Uncertainties include statistical and systematic uncertainties in both cases.

2067 can drastically change the prediction, and a low $Z/\gamma^* + \text{jets}$ prediction
 2068 can result in a signal-like peak appearing in the final result.

2069 Because of this volatility in the MC prediction in these high E_T^{miss} tails, a
 2070 data-driven method is used to estimate this background. The method uses
 2071 $\gamma + \text{jets}$ events which, like the $Z/\gamma^* + \text{jets}$ events, contain one boson recoil-
 2072 ing against a hadronic system. These $\gamma + \text{jets}$ events are then corrected for
 2073 the kinematic differences between γ and Z s [33, 89]. The sample of $\gamma + \text{jets}$
 2074 events is taken from CR- γ , defined in Table 7. This region is similar to the
 2075 SRZ selection without the E_T^{miss} requirement, but it vetoes events with lep-
 2076 tons and requires at least one photon. Additionally, the $\Delta\phi(\text{jet}_{12}, p_T^{\text{miss}})$ cut
 2077 in SRZ, which is designed to reduce the background from mismeasured
 2078 jets, is removed for this region because of its unpredictability at very low
 2079 values of E_T^{miss} , when the angle of the E_T^{miss} is much less meaningful.

2080 Despite their similarities, there are many theoretical differences between
 2081 γ and Z events. The massive Z boson recoils differently against a jet system
 2082 than the massless photon. Another consequence of its masslessness is that
 2083 photons cannot appear in decays with no jets because such a decay would
 2084 always violate conservation of energy in some frame. As a consequence,
 2085 many kinematic variables have different shapes between the two samples.
 2086 Figure 64 shows a MC comparison of boson p_T between γ and Z events,
 2087 demonstrating the shape differences between the two processes.

2088 The most significant experimental difference between Z and γ events
 2089 is that Z bosons rapidly decay, in the case of this analysis, to two leptons,
 2090 which are then be observed by the ATLAS detector. In contrast, the photon
 2091 is stable, and can be directly detected by ATLAS. This means that the re-
 2092 constructed Z boson and the directly observed photon have very different
 2093 energy resolutions, which can result in different amounts of E_T^{miss} in the
 2094 two events.

2095 Ultimately, the goal of this method is to predict the E_T^{miss} distribution of
 2096 the $Z+\text{jets}$ background. These differences between $Z+\text{jet}$ and $\gamma+\text{jet}$ events
 2097 can be broken down into two categories: differences which affect the jet
 2098 energy and measurement, and differences which affect the boson energy
 2099 and measurement. The differences in the hadronic system are simpler, and
 2100 mostly consist of different numbers and energies of jets between the two
 2101 samples, which can be accounted for via reweighting in a variable that's
 2102 representative of the total energy scale of the event. The differences in the

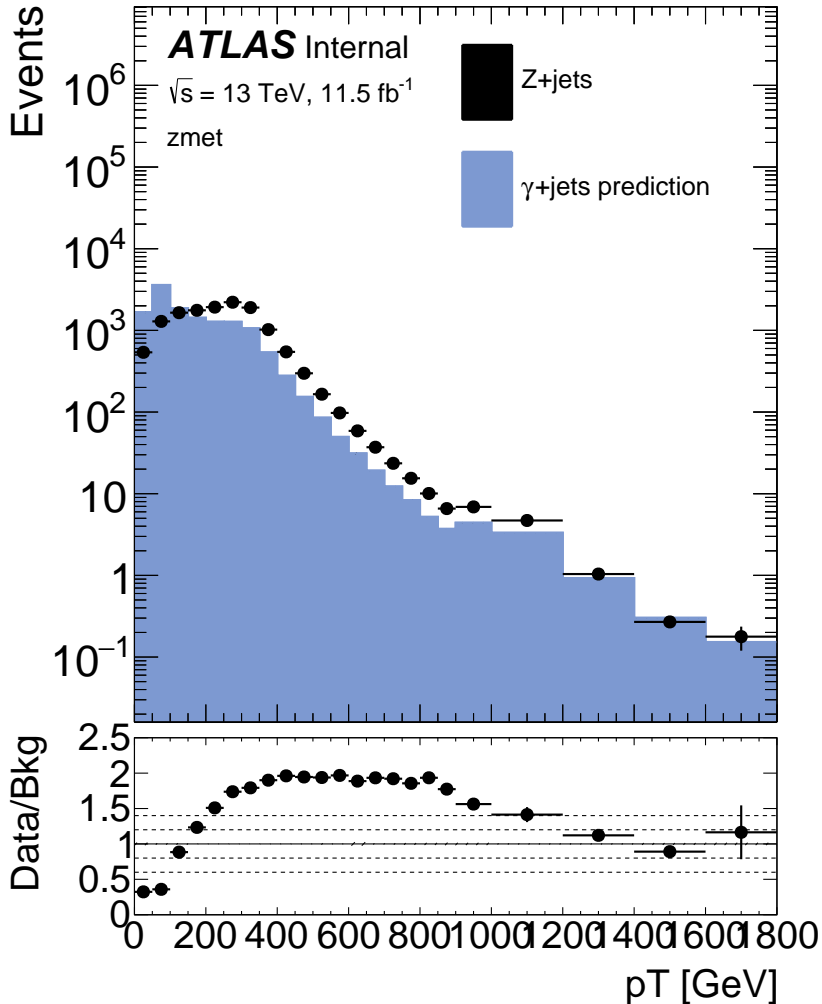


Figure 64: MC comparison of boson p_T in a selection of photon and $Z \rightarrow \ell\ell$ events with $H_T > 600$ GeV.

bosons are more complex, and require the application of smearing functions based on the different observed objects. Together these corrections allow for complete modeling of the $Z/\gamma^* + \text{jets}$ E_T^{miss} spectrum with $\gamma+\text{jet}$ events.

10.2.1 Photon and Z Event Selection

The baseline photon events come from an inclusive CR with no E_T^{miss} cut, a lepton veto, and the requirement of at least one photon, which is called CR- γ and defined in Table 7³. This selection is very pure in $\gamma+\text{jet}$ events, but some $V\gamma$ events are also included, which can include real E_T^{miss} . These backgrounds are subtracted off at the end off the estimation procedure.

³ This region includes an H_T cut, which requires the translation of photon p_T into an equivalent di-lepton p_T scalar sum. This process is described in Section 10.2.4.

2113 The triggering scheme for these events is more complicated than in other
 2114 regions because the lowest unprescaled photon trigger requires a photon
 2115 p_T of at least 120 (140) GeV in 2015 (2016) datataking, but the method re-
 2116 quires events with much lower p_T to predict the full Z -boson p_T spectrum.
 2117 To accomplish this, the lower- p_T photons are broken down into small p_T
 2118 ranges with a different prescaled trigger required in each range, listed in
 2119 [Table 13](#). The events in each selection are then weighted by the prescale
 2120 value of the trigger used to reconstruct a smooth p_T spectrum.

p_T Range [GeV]	Trigger Name
2015 Data-Taking	
$37 < p_T < 45$	HLT_g35_loose_L1EM15
$45 < p_T < 50$	HLT_g40_loose_L1EM15
$50 < p_T < 55$	HLT_g45_loose_L1EM15
$55 < p_T < 125$	HLT_g50_loose_L1EM15
$p_T > 125$	HLT_g120_loose_L1EM15
2016 Data-Taking	
$25 < p_T < 30$	HLT_g20_loose_L1EM12
$30 < p_T < 40$	HLT_g25_loose_L1EM12
$40 < p_T < 45$	HLT_g35_loose_L1EM12
$45 < p_T < 50$	HLT_g40_loose_L1EM12
$50 < p_T < 55$	HLT_g45_loose_L1EM12
$55 < p_T < 65$	HLT_g50_loose_L1EM12
$65 < p_T < 75$	HLT_g60_loose_L1EM12
$75 < p_T < 85$	HLT_g70_loose_L1EM12
$85 < p_T < 105$	HLT_g80_loose_L1EM12
$105 < p_T < 145$	HLT_g100_loose_L1EM12
$p_T > 145$	HLT_g140_loose_L1EM12

Table 13: List of triggers used to collect photon events in 2015 and 2016 data-taking.

2121 These γ events can then be compared to baseline $Z \rightarrow \ell\ell$ events with
 2122 a similar selection. These events have the same dilepton requirements as
 2123 SRZ, without the $m_{\ell\ell}$ cut. They also have no E_T^{miss} cut, but like the photons,
 2124 are required to have $H_T > 600$ GeV as in SRZ.

2125 10.2.2 Smearing of Photon Events

2126 While Z +jet events are measured as a pair of leptons recoiling against
 2127 a hadronic system, γ +jet events are measured only as one object recoil-
 2128 ing against jets. In addition, detector resolution is different for electrons,

muons, and photons. The impact of these differences must be corrected for in $\gamma+\text{jet}$ events in order for them to accurately predict the $E_{\text{T}}^{\text{miss}}$ distribution of the Zs. Luckily, in most cases, the resolution of the photon's p_{T} is better than the Z boson's, so the photon events can be smeared to emulate the Zs.

To isolate mismeasurement of boson p_{T} , this method uses $E_{T,\parallel}^{\text{miss}}$, the $E_{\text{T}}^{\text{miss}}$ projection on an axis defined by the momentum of the boson. Figure 65 shows the $E_{T,\parallel}^{\text{miss}}$ distribution in MC for the two samples, and demonstrates the discrepancies between them. The core of the photon distribution is somewhat similar to the $Z \rightarrow ee$ distribution because, in the high- p_{T} limit, measurements of both photons and electrons are primarily taken from the electromagnetic calorimeter and should have similar resolutions. For muons, which rely only on tracks to determine p_{T} , the resolution becomes very large at high p_{T} values where the tracks are nearly straight. As a consequence, the resolutions for photon and $Z \rightarrow \mu\mu$ events are very different.

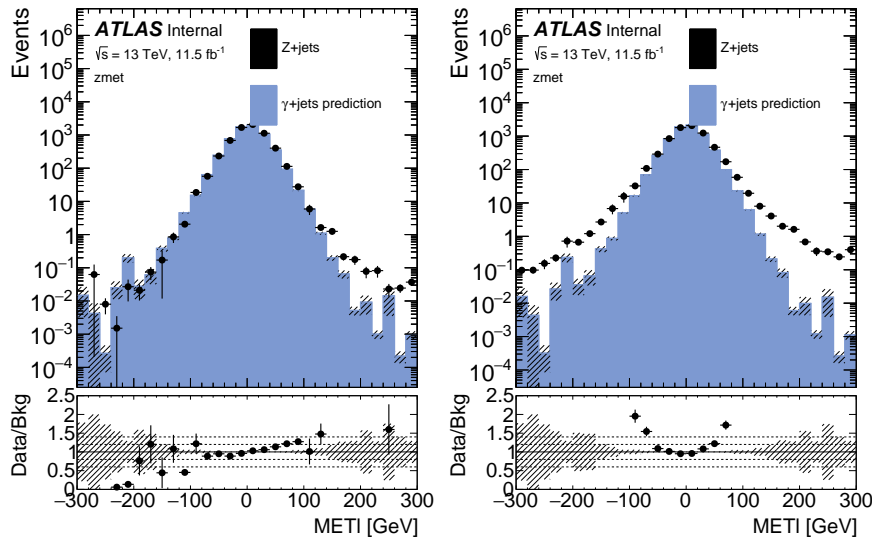


Figure 65: $E_{T,\parallel}^{\text{miss}}$ distributions in MC for $Z+\text{jets}$ ee (left) and $\mu\mu$ (right) channels compared to $\gamma + \text{jets}$ in an inclusive region with $H_{\text{T}} > 600$ GeV.

A function to smear photon events is derived from the deconvolution of the photon and lepton response functions, taken from 1-jet CRs with no H_{T} cut, which are otherwise identical to the baseline Z and γ selections. This region is chosen because it is orthogonal to the SR, so the resolution can be obtained from data as well as MC. In these regions, events are binned in boson p_{T} , and in each bin, a $E_{T,\parallel}^{\text{miss}}$ distribution is made. The smearing function is derived for each bin via the deconvolution of the $Z/\gamma^* + \text{jets}$ and $\gamma + \text{jets}$ distributions.

Next, for each photon event, the smearing function matching the event's photon p_{T} is sampled, yielding a smearing factor Δp_{T} . The photon's p_{T} is then adjusted according to

$$p_{\text{T}}^{\gamma'} = p_{\text{T}}^{\gamma} + \Delta p_{\text{T}} \quad (41)$$

and the corresponding change in E_T^{miss} is made,

$$E_{T,\parallel}^{\text{miss}'} = E_{T,\parallel}^{\text{miss}} - \Delta p_T. \quad (42)$$

The nominal smearing function is taken from MC in order to remove contamination from other backgrounds, and the resulting $E_{T,\parallel}^{\text{miss}}$ distributions can be seen in Figure 66. Though there is a small amount of oversmearing in the negative tail, the improvement in agreement between the distributions is clear.

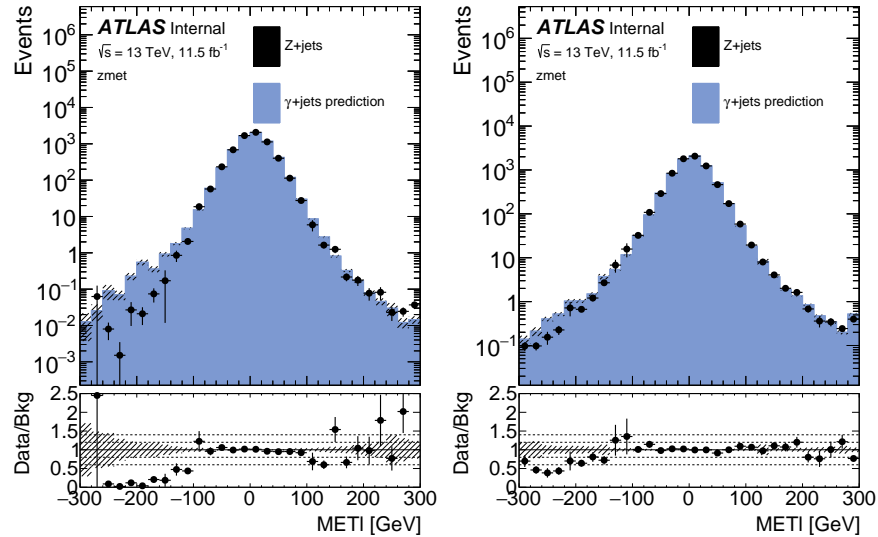


Figure 66: $E_{T,\parallel}^{\text{miss}}$ distributions in MC for Z+jets ee (left) and $\mu\mu$ (right) channels compared to $\gamma + \text{jets}$ in an inclusive region with $H_T > 600 \text{ GeV}$ after the smearing procedure has been performed. These distributions have also been p_T reweighted, as described in Section 10.2.3.

10.2.3 p_T Reweighting of Photon Events

Next, the photon events are reweighted to match the boson p_T of the Z events. This is accomplished by making histograms of boson p_T for γ and Z events, similar to that in Figure 64, and with binning identical to that used in Section 10.2.2. Photons are binned based on their smeared p_T determined in the previous step. A reweighting factor $f(p_T)$ is then calculated in each bin, according to

$$f(x) = \frac{N_{Z/\gamma^*+\text{jets}}(x)}{N_{\gamma+\text{jets}}(x)} \quad (43)$$

in MC, and in data according to

$$f(x) = \frac{N_{\text{data}}(x) - N_{t\bar{t}}(x) - N_{VV}(x)}{N_{\gamma+\text{jets data}}(x)} \quad (44)$$

where the contamination from other backgrounds is taken from MC and subtracted from the Z selection. The resulting reweighting factors can be seen in Figure 67 and are calculated independently for ee and $\mu\mu$ events.

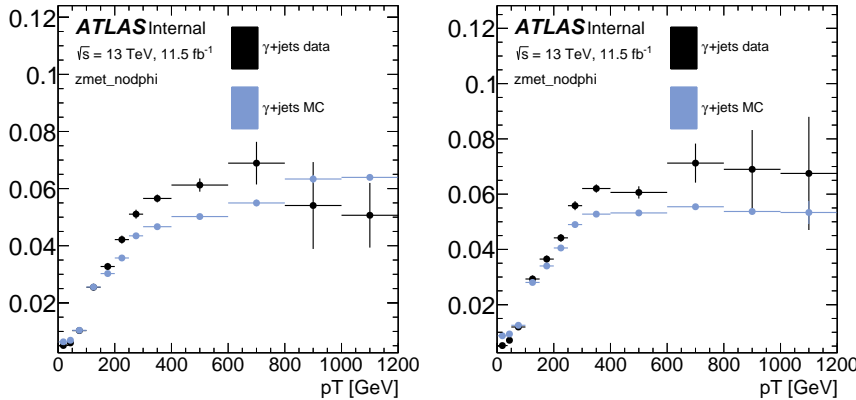


Figure 67: Photon reweighting factors for the ee (left) and $\mu\mu$ (right) channels derived from data and MC.

This reweighting, though it is performed on the boson p_T , primarily serves to produce more similar jet distributions between the γ and Z samples. Because, excluding E_T^{miss} contributions, the boson p_T must match the energy of the jet system off which it recoils, these two variables are closely tied. Once the two samples have similar amounts of hadronic energy, the E_T^{miss} contribution from mismeasurement of jet energy should also be similar.

Together, the boson smearing and p_T reweighting produce a E_T^{miss} spectrum in the modified photon events that closely match that of the Z events. Figures 68 and 69 show the comparison of the E_T^{miss} distributions before any alteration, with only p_T reweighting, and after the smearing and reweighting, demonstrating the impact of each step. Once the E_T^{miss} distribution is well described, the $\Delta\phi(\text{jet}_{12}, p_T^{\text{miss}})$ can be applied.

10.2.4 Determining H_T and $m_{\ell\ell}$

One complication thus far ignored is that CR- γ has no leptons, but some quantities that define the SR require them, namely H_T (which includes the p_T of the two leading leptons) and $m_{\ell\ell}$. Both of these variables are determined by creating histograms binned in the boson p_T and sampling.

In the case of H_T , distributions of the scalar sum of the p_T of the leading leptons are made for each Z p_T bin. A sampled value from the distribution is then added to the H_T of the jets in a photon event to produce the final estimate. This sampling is done before any reweighting is performed because the H_T is needed to make the preselection for the reweighting process. However, the smearing is performed inclusively in H_T , so this procedure can be performed using the smeared photon p_T to choose the distribution to sample.

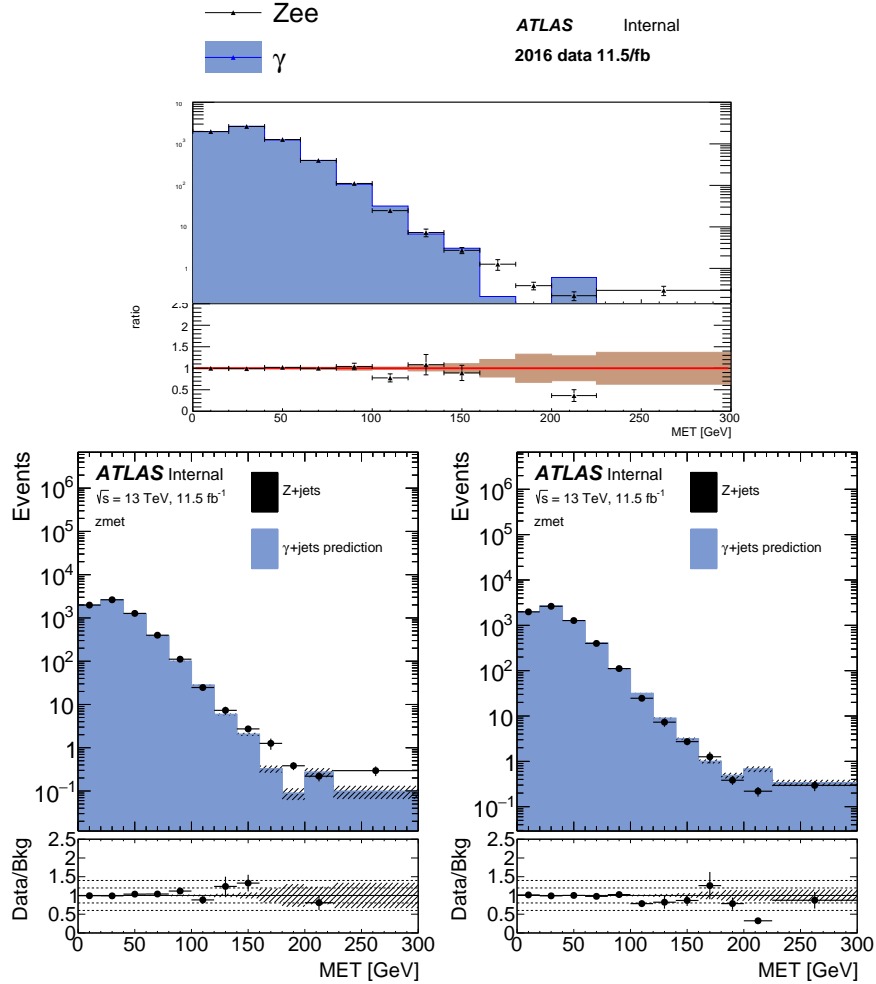


Figure 68: E_T^{miss} distribution comparing MC distributions of photon and Z events before any smearing is applied (top), with only p_T reweighting applied (bottom left), and after p_T reweighting and smearing have both been applied (bottom right) in the ee channel of 2016 data.

2198 The $m_{\ell\ell}$ determination is done after both the smearing and reweighting,
2199 and is tied closely to the smearing step. Mismeasurements in lepton p_T
2200 can create E_T^{miss} in a $Z/\gamma^* + \text{jets}$ event, but the same event is likely to mi-
2201 grate off the Z $m_{\ell\ell}$ window due to the mismeasured lepton. Thus it is very
2202 important that the two effects be carefully correlated in the manipulated
2203 photon events. To achieve this, MC Z events from the 1-jet CR described in
2204 Section 10.2.2 are used to make two-dimensional distributions of $m_{\ell\ell}$ as
2205 a function of the difference between reconstructed and true Z p_T for the
2206 ee and $\mu\mu$ channels. A photon event then uses the Δp_T assigned to it dur-
2207 ing the smearing process to index the distribution, and an $m_{\ell\ell}$ value is
2208 sampled from the corresponding bin ⁴

⁴ Ideally this Δp_T would also include the difference between the true and reconstructed p_T of the photon events, but this information is of course not accessible in data. Luckily, in the events in the final SR this value is typically negligible compared to the Δp_T from smearing, so the impact is small.

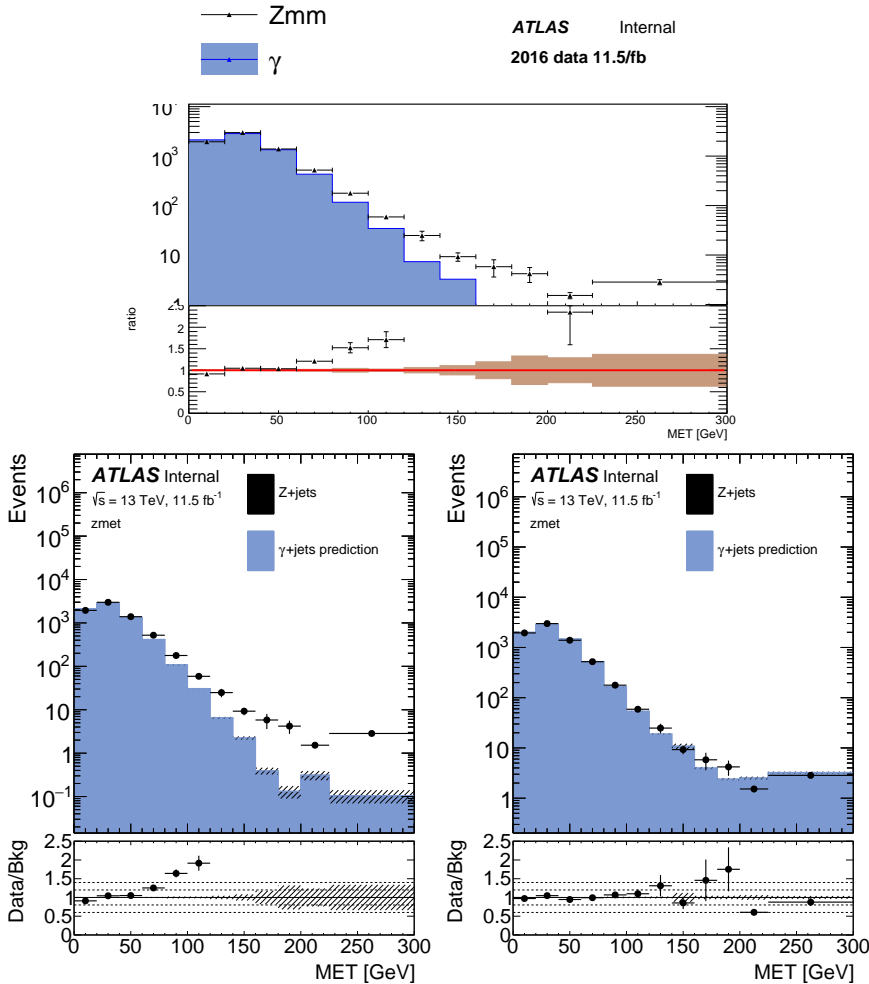


Figure 69: E_T^{miss} distribution comparing MC distributions of photon and Z events before any smearing is applied (top), with only p_T reweighting applied (bottom left), and after p_T reweighting and smearing have both been applied (bottom right) in the $\mu\mu$ channel of 2016 data.

2209 To test the soundness of this procedure, it is repeated purely in MC, and
 2210 the results of the MC prediction and the data prediction are compared to
 2211 the $m_{\ell\ell}$ distribution in $Z/\gamma^* + \text{jets}$ MC in Figure 70. After the $m_{\ell\ell}$ distribution
 2212 has been emulated, a cut requiring that the photon events be “on the
 2213 Z mass peak” can be required.

2214 10.2.5 Subtraction of $V\gamma$ Events

2215 At high E_T^{miss} , where the signal region lies, contamination of CR- γ with
 2216 $V\gamma$ events becomes significant, as shown in Figure 71. These events must
 2217 be subtracted from the $\gamma + \text{jets}$ prediction because, once the photons are
 2218 corrected to approximate Z s, they essentially provide a (not very accurate)
 2219 prediction of diboson events, which are already accounted for in another
 2220 background estimate.

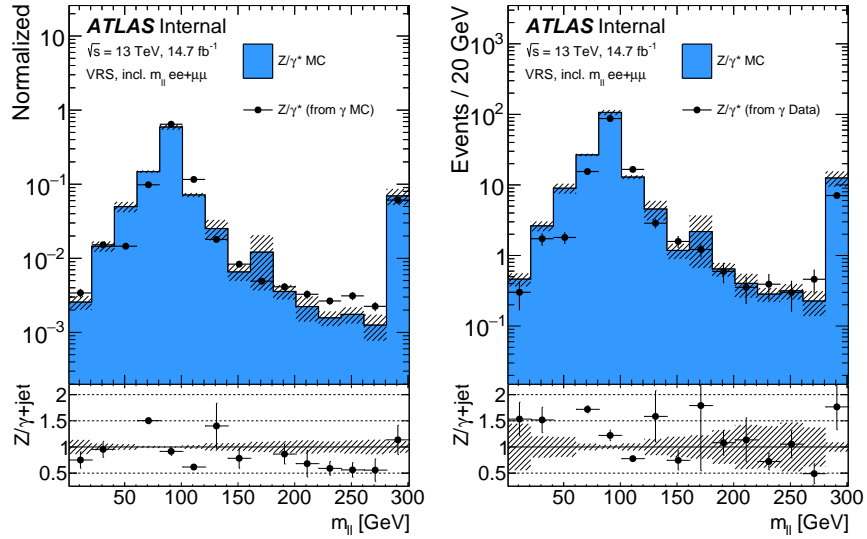


Figure 70: Z/γ^* + jets MC $m_{\ell\ell}$ distribution compared to the prediction from γ + jets method performed on MC (left) and the prediction from γ + jets method performed on data (right).

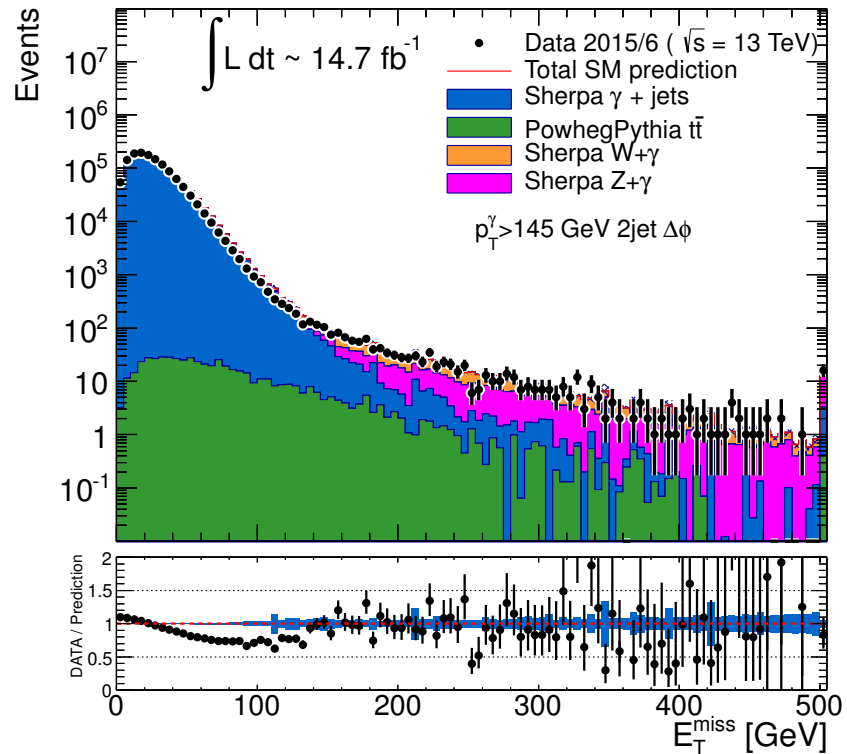
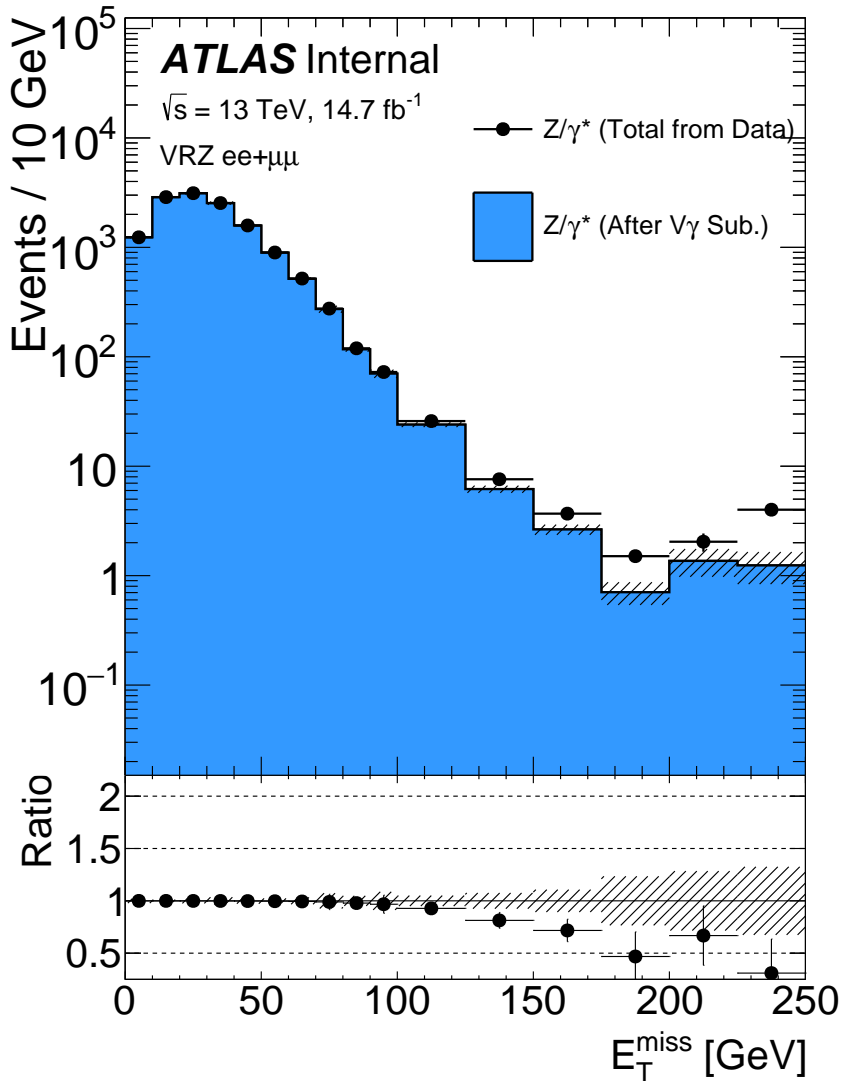


Figure 71: Comparison of data and MC in CR- γ without any H_T cut, including the contributions from various $V\gamma$ processes.

This subtraction accomplished by performing the γ + jets method on $V\gamma$ MC to approximate these backgrounds' contribution to the final E_T^{miss} distribution. This contribution is then subtracted from the γ + jets prediction,

the impact of which can be seen in [Figure 72](#). As expected, the impact is greatest at high E_T^{miss} where these backgrounds are most significant.



[Figure 72](#): Total $\gamma + \text{jets}$ data prediction in SRZ (excluding the E_T^{miss} cut) and the prediction after the $V\gamma$ subtraction.

10.2.6 Validation in Data

The $\gamma + \text{jets}$ jets method is validated in a region called VRZ, defined in [Table 7](#), which is similar to SRZ, but with an inverted E_T^{miss} cut. [Figure 73](#) shows the low- E_T^{miss} portion of this VR where the $Z/\gamma^* + \text{jets}$ background is dominant. Here, the three data-driven background estimates, as well as the remaining [MC](#) backgrounds are stacked and compared to the data yield in this region, demonstrating excellent agreement across a wide E_T^{miss} range.

An additional check can be made in VRZ by removing the $\Delta\phi(\text{jet}_{12}, \mathbf{p}_T^{\text{miss}})$ intended to suppress the $Z/\gamma^* + \text{jets}$ background from jet mismeasurement.

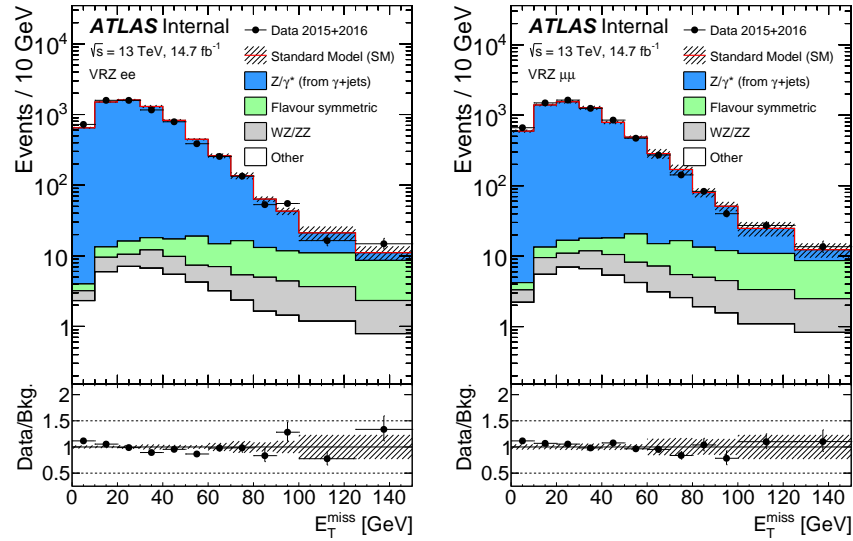


Figure 73: E_T^{miss} distribution in VRZ ee (left) and $\mu\mu$ (right) with total data yield compared to the sum of the prediction from the $\gamma + \text{jets}$ method, the prediction from the flavor symmetry method, the prediction from the fake background estimation (included under “other”), and the remaining backgrounds taken from MC.

2236 Figure 74 shows the distribution of this variable in VRZ, and demonstrates
 2237 that, even at low values where the $Z/\gamma^* + \text{jets}$ background is dominant,
 2238 the $\gamma + \text{jets}$ method models it accurately.

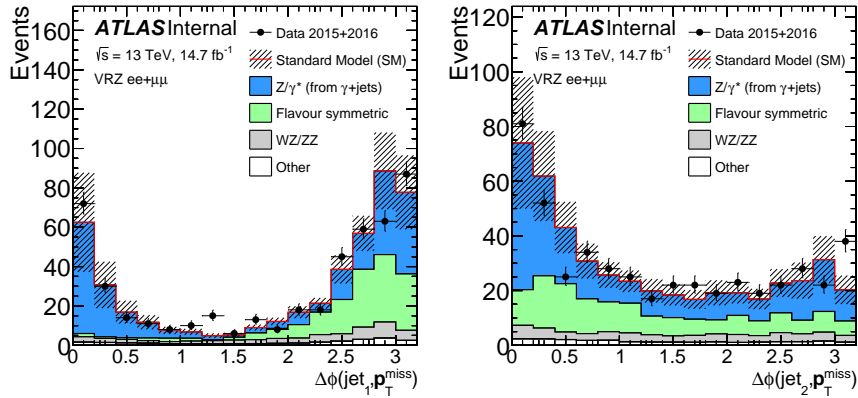


Figure 74: $\Delta\phi(\text{jet}, p_T^{\text{miss}})$ distribution for the leading jet (left) and the subleading jet (right). The comparison is performed in VRZ with the cut on $\Delta\phi(\text{jet}_{12}, p_T^{\text{miss}})$ removed. The total data yield is compared to the sum of the prediction from the $\gamma + \text{jets}$ method, the prediction from the flavor symmetry method, the prediction from the fake background estimation (included under “other”), and the remaining backgrounds taken from MC.

2239 10.3 FAKE AND NON-PROMPT LEPTONS

2240 The *fakes* background consists of processes that produce only one lepton,
 2241 but whose events are otherwise kinematically similar to the [SR](#). These pro-
 2242 cesses include semileptonic $t\bar{t}$, W -jets, and single top processes. Though
 2243 these processes typically only produce one lepton, they can be recon-
 2244 structed with two leptons due to a hadron being misidentified as a lepton
 2245 or due to a real non-prompt lepton resulting from photon conversions or
 2246 B -hadron decays. As with the $Z/\gamma^* + \text{jets}$ background, it is very difficult
 2247 to predict with [MC](#) because the flaws in reconstruction are typically less
 2248 well described by the models used in [MC](#) production than the successes.
 2249 Nonetheless, a rough estimate can be made of this background by using
 2250 [MC](#), which indicates that the number of fake events in SRZ is consistent
 2251 with zero.

2252 Despite the small predicted contribution in the [SR](#), a data-driven method
 2253 called the *matrix method* is employed to estimate these fake events [90]. This
 2254 method is also used to estimate the fakes contribution to other control and
 2255 validation regions where their impact is more significant.

2256 In the matrix method, the quality requirements for signal leptons are
 2257 loosened to give a selection of baseline leptons (see [Table 3](#) and [Table 4](#)),
 2258 which consist of a higher fraction of fake leptons. In each [CR](#), [VR](#), or [SR](#), the
 2259 remaining kinematic selections are made on the baseline leptons, and the
 2260 number of leptons in the region which pass the signal lepton requirements
 2261 (N_{pass}) and the number which fail (N_{fail}) are measured. For a 1-lepton
 2262 selection, these quantities can be used to predict the number of fake events
 2263 that pass the selection according to:

$$N_{\text{pass}}^{\text{fake}} = \frac{N_{\text{fail}} - (1/\epsilon^{\text{real}} - 1) \times N_{\text{pass}}}{1/\epsilon^{\text{fake}} - 1/\epsilon^{\text{real}}}. \quad (45)$$

2264 The efficiencies ϵ^{real} and ϵ^{fake} give the relative identification efficiency
 2265 from baseline to signal for genuine, prompt leptons and fake and non-
 2266 prompt leptons, respectively. For a 2-lepton selection, the principle is the
 2267 same, but the equation is more complicated, requiring a four-by-four ma-
 2268 trix to account for possible combinations of real and fake leptons.

2269 To calculate ϵ^{real} , the tag-and-probe method is performed a selection of
 2270 $Z \rightarrow \ell\ell$ data events, CR-real, described in [Table 14](#). In this method, one *tag*
 2271 lepton passing a signal selection is required, as is another *probe* lepton pass-
 2272 ing a baseline requirement. Distributions in $m_{\ell\ell}$ for events with a tag and
 2273 a passing probe and events with a tag and a failing probe are produced
 2274 and fit, and the efficiency is computed using the ratio acquired from the
 2275 fit. A comparison of data and [MC](#) in CR-real can be seen in [Figure 75](#).

2276 The fake efficiency, ϵ^{fake} , is determined using the tag-and-probe method
 2277 in CR-fake, also described in [Table 14](#). This region is different from all
 2278 other regions considered in this analysis because it requires same-sign lep-
 2279 tons. Very few processes genuinely produce two same-sign leptons, so this
 2280 region is enhanced in fake leptons. An upper limit on $E_{\text{T}}^{\text{miss}}$ is placed on

Fakes regions	E_T^{miss} [GeV]	H_T [GeV]	n_{jets}	$m_{\ell\ell}$ [GeV]	SF/DF	OS/SS	n_{ℓ}
CR-real	–	> 200	≥ 2	81–101	2ℓ SF	OS	2
CR-fake	< 125	–	–	> 12	2ℓ SF/DF	SS	≥ 2

Table 14: Control regions used to measure efficiencies of real and fake leptons. The flavour combination of the dilepton pair is denoted as either “SF” for same-flavour or “DF” for different flavour. The charge combination of the leading lepton pairs are given as “SS” for same-sign or “OS” for opposite-sign.

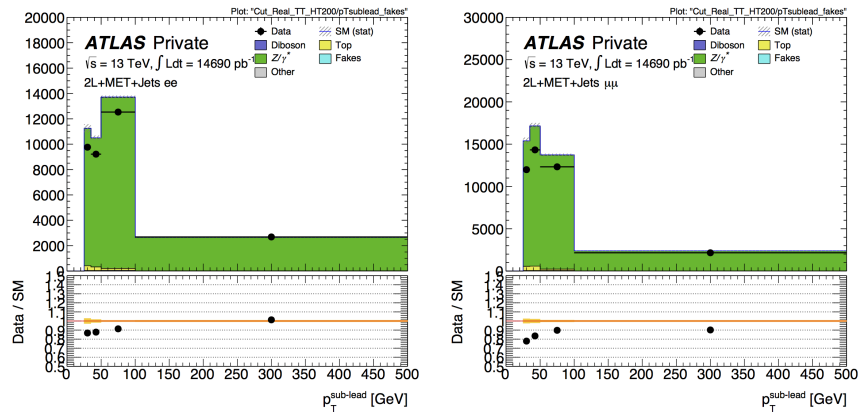


Figure 75: Sub-leading lepton p_T for ee (left) and $\mu\mu$ (right) events in the tight-tight region used to measure the real-lepton efficiency for 2016.

2281 CR-fake to limit the possible contamination from BSM processes. According
 2282 to MC, real, prompt leptons make up about 7% (11%) of the baseline
 2283 electron (muon) sample and about 10% (61%) of the signal electron (muon)
 2284 sample in this region. These real lepton backgrounds are subtracted from
 2285 the CR-fake yields when calculating the efficiencies. Figure 76 shows a
 2286 comparison of data and MC in this region.

2287 This method is validated in a fakes-rich validation region with a same-
 2288 sign lepton requirement, $E_T^{\text{miss}} \geq 50\text{GeV}$, ≥ 2 jets, and a veto on $m_{\ell\ell}$ on
 2289 the Z-mass peak for same flavor channels. The results of this validation
 2290 can be seen in Figure 77. With the systematic uncertainties, discussed in
 2291 Section 11.1.3, the prediction agrees well with the data across a wide range
 2292 of $m_{\ell\ell}$ values.

2293 10.4 DIBOSON AND RARE TOP PROCESSES

2294 The remaining backgrounds are diboson processes (excluding WW, which
 2295 is included in the FS background) and rare top processes. Dibosons events

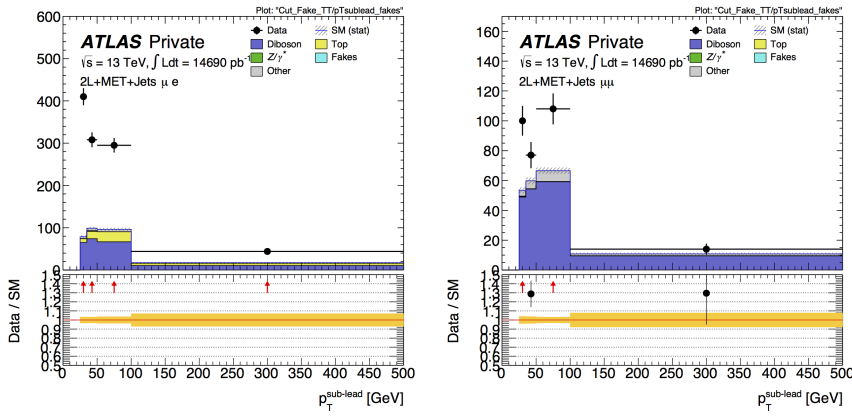


Figure 76: Sub-leading lepton p_T for μe (left) and $\mu \mu$ (right) events in the tight-tight region used to measure the fake-lepton efficiency for 2016.

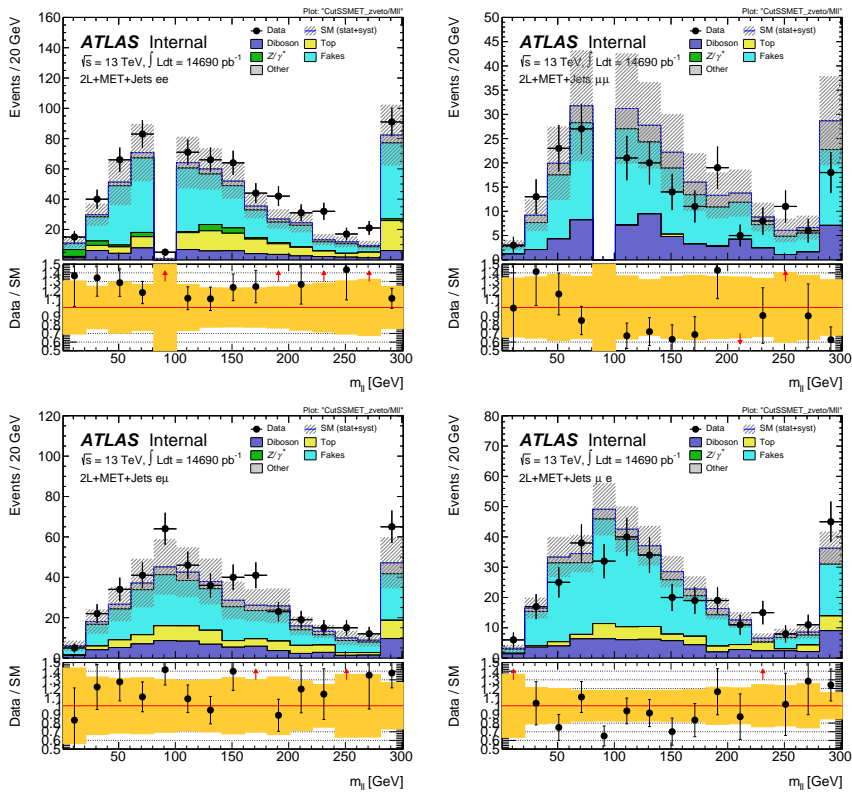


Figure 77: Same sign validation regions in the ee (top left), $\mu\mu$ (top right), $e\mu$ (bottom left) and μe (bottom right) channels combining 2015+2016 data. Uncertainty bands include both statistical and systematic uncertainties.

make up about 30% of the events in SRZ, while rare top process contributions are much smaller. Both are taken directly from MC, with validation regions to confirm the accuracy of the prediction. These regions are described in Table 7, and target different parts of these backgrounds. VR-ZZ is a four-lepton selection designed to select a very pure sample of ZZ events. VR-WZ requires three leptons and makes specific cuts on m_T , the

transverse mass, and E_T^{miss} in order to select mostly $WZ \rightarrow ll\nu\nu$ events. VR-3L is similar to VR-S, but loosens the H_T and E_T^{miss} cuts and requires at least three leptons. This region is designed to target any ≥ 3 -lepton process in a region as kinematically close to SRZ as possible while still maintaining enough events to validate. The makeups of these multilepton validation regions, as well as VRS, are shown in [Table 15](#).

	VR-S	VR-WZ	VR-ZZ	VR-3L
Observed events	236	698	132	32
Total expected background	224 ± 41	613 ± 66	139 ± 25	35 ± 10
Flavour-symmetric	99 ± 8	-	-	-
WZ/ZZ events	27 ± 13	573 ± 66	139 ± 25	25 ± 10
Rare top events	11 ± 3	14 ± 3	0.44 ± 0.11	9.1 ± 2.3
$Z/\gamma^* + \text{jets}$ events	84 ± 37	-	-	-
Fake lepton events	4 ± 4	26 ± 6	-	0.6 ± 0.3

[Table 15](#): Yields in validation regions. In VRS, data-driven background estimates are used for $Z/\gamma^* + \text{jets}$, fakes, and [FS](#) processes. All other backgrounds are taken from [MC](#), including all backgrounds in the multi-lepton [VRS](#). Uncertainties include statistical and systematic components.

To confirm that the kinematics are well modeled in the diboson validation regions, distributions of boson mass and p_T are shown in [MC](#) and data. Figures [78](#) and [79](#) show these distributions for VR-WZ, and [Figure 80](#) shows these distributions for VR-ZZ.

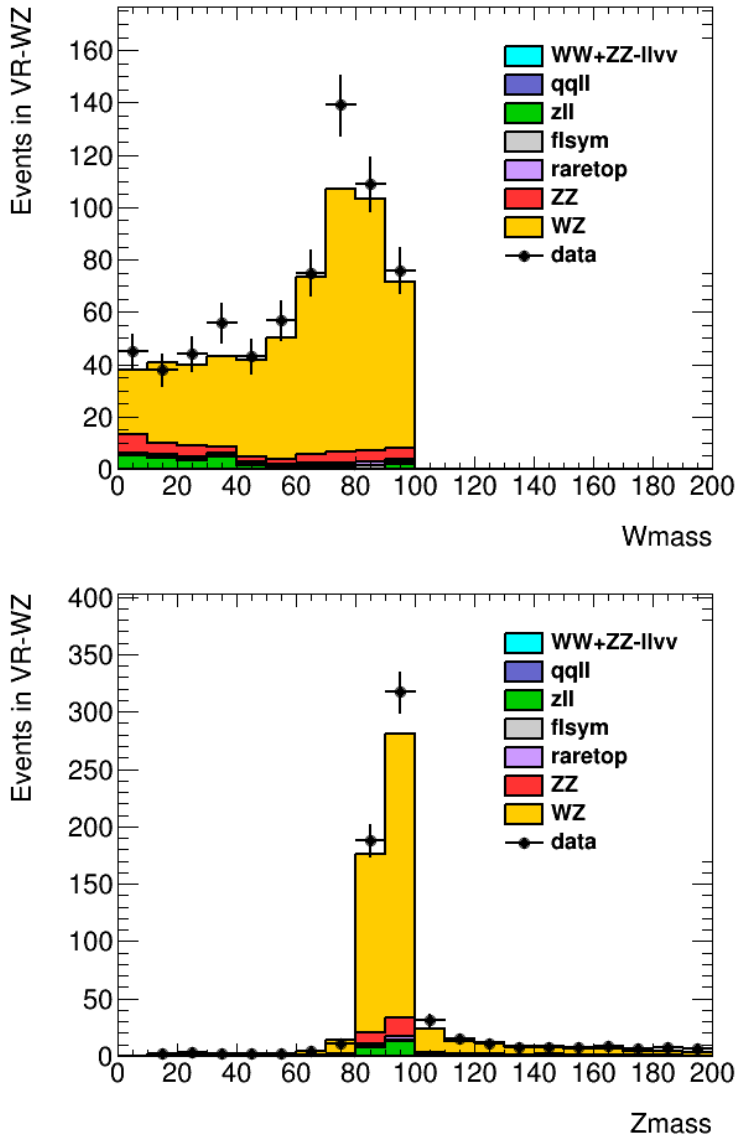


Figure 78: Distribtuions of data and MC in VR-WZ. Reconstructed transverse mass of the W (top) and mass of the Z (bottom).

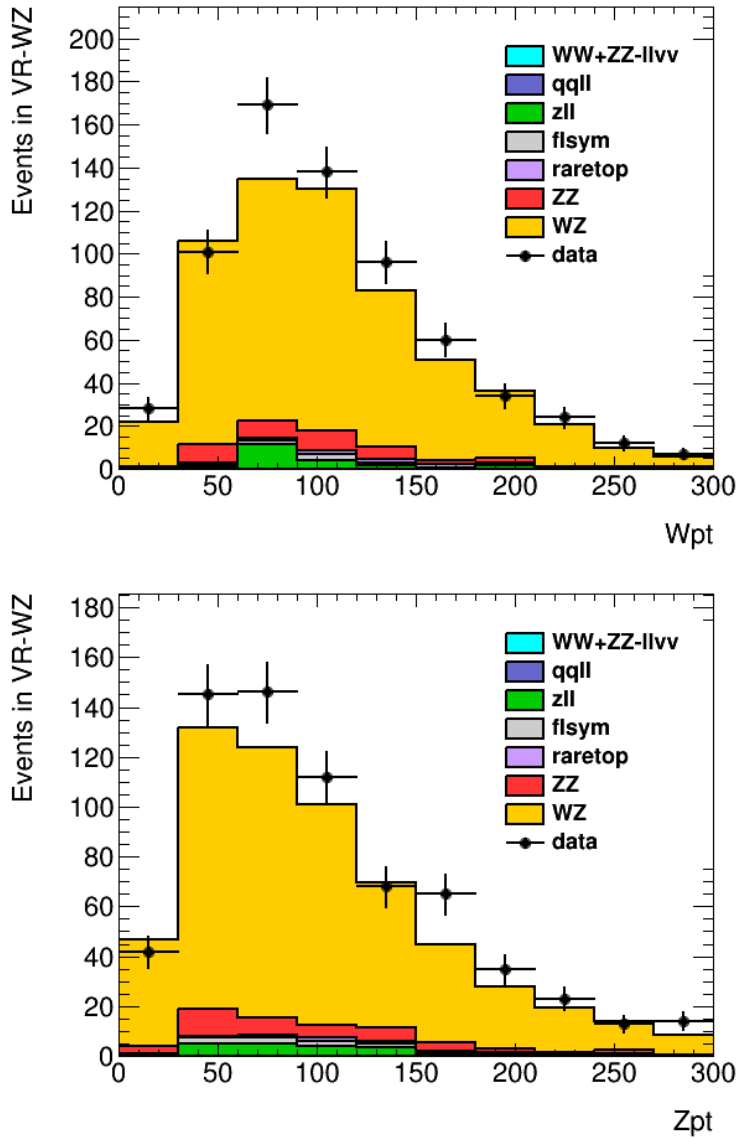


Figure 79: Distributions of data and MC in VR-WZ. p_T of the W (top) and Z (bottom).

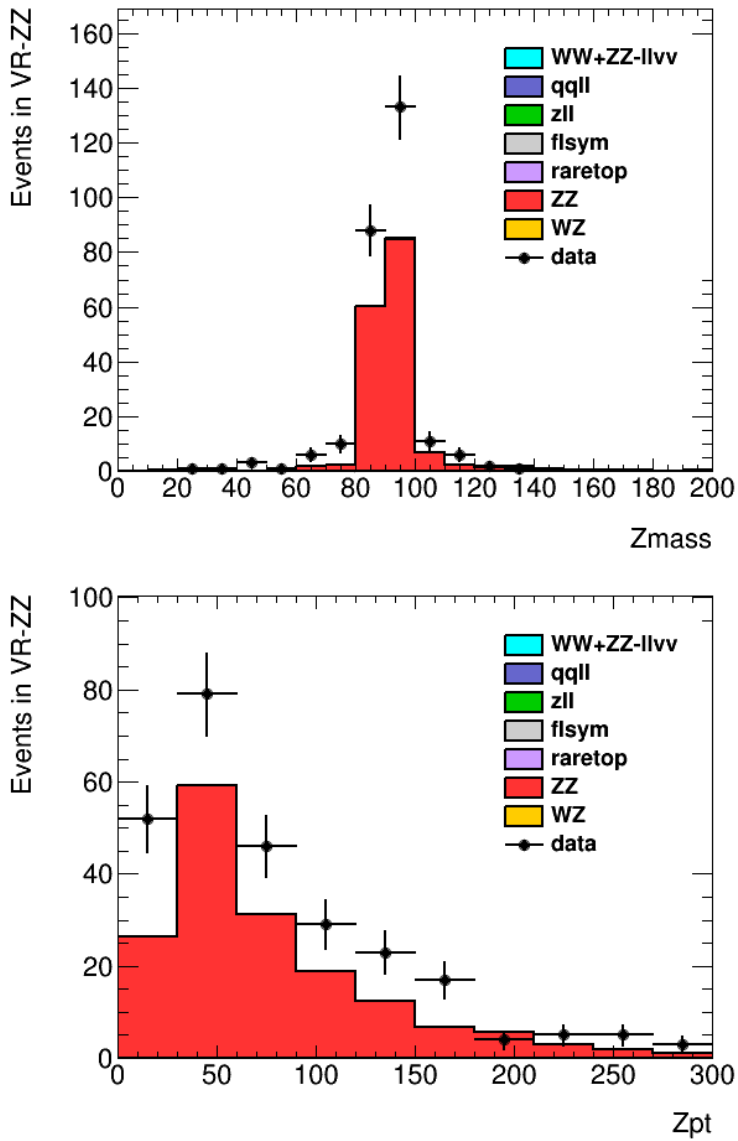


Figure 8o: Distributions in VR-WZ. On the top, mass of the Z bosons in the event, and on the bottom, p_T of the Z bosons.

2312

2313 SYSTEMATIC UNCERTAINTIES

2314 11.1 UNCERTAINTIES ON DATA-DRIVEN BACKGROUNDS

2315 11.1.1 *Uncertainties on the Flavor Symmetry Method*

2316 The flavor symmetry method is a data driven method that makes its esti-
 2317 mate primarily on based events populating an [SR-like CR](#) in the different-
 2318 flavor channel. The statistical uncertainty on these events makes up the
 2319 dominant uncertainty on the method. To reduce this uncertainty, the $m_{\ell\ell}$ range
 2320 on the [CR](#) is expanded, approximately tripling the number of events in [CR-FS](#). The statistical uncertainty is reduced by this expansion, though it is
 2321 still significantly higher than any of the other systematic uncertainties on
 2322 this method, as seen in [Table 16](#). Also included in the statistical uncertainty
 2323 column is the uncertainty on the number of non-[FS](#) events in [CR-FS](#), which
 2324 is used to scale the prediction to account for contamination in the [CR](#).

Reg.	Ch.	Pred.	Uncertainties					
			stat. clos.	MC and α	k and α	dAOD usage	$m_{\ell\ell}$ shape	total
SRZ	ee	16.50	1.82	0.88	0.53	0.12	0.22	2.11
	$\mu\mu$	16.67	1.83	0.79	0.33	0.11	0.23	2.04
	$ee+\mu\mu$	33.16	3.66	1.07	0.86	0.23	0.45	3.94
VRS	ee	49.70	3.21	2.34	2.20	0.34	0.75	4.61
	$\mu\mu$	49.60	3.14	2.88	1.40	0.31	0.75	4.56
	$ee+\mu\mu$	99.31	6.34	4.00	3.60	0.65	1.49	8.47

Table 16: Uncertainties in the on-Z signal and validation regions. Nominal predictions are given with statistical uncertainty (including uncertainty from subtracted backgrounds), MC Closure uncertainty, uncertainty on the prediction from varying k and α by their statistical uncertainties, comparing the efficiencies from AODs to that of DAOs, and on the $m_{\ell\ell}$ widening, which includes MC statistics and a data/MC comparison in a loosened region.

2326 The next largest contribution to the uncertainty comes from [MC](#) closure
 2327 tests, which are used to determine how effective the method is in its predic-
 2328 tion. If, for example, using weights derived from an inclusive selection at
 2329 high E_T^{miss} lead to a bias, the closure test would indicate that and an appro-
 2330 priate uncertainty could be placed on the estimate based on the difference
 2331 between the [MC](#) prediction and the prediction from the flavor symmetry
 2332 method.

2333 In this test, the entire **FS** procedure is performed on $t\bar{t}$ **MC**, including a
 2334 recalculation of weighting factors α and k . The prediction from $e\mu$ events
 2335 in **MC** is compared to the **MC** ee and $\mu\mu$ events, as seen in [Figure 81](#). The dif-
 2336 ference between the two predictions is then summed in quadrature with
 2337 the statistical uncertainty on each prediction to give the total closure un-
 2338 certainty seen in [Table 16](#). In these closure tests, all predictions agree within
 2339 the statistical uncertainty, so the largest contributor to the resulting error
 2340 is **MC** statistics.

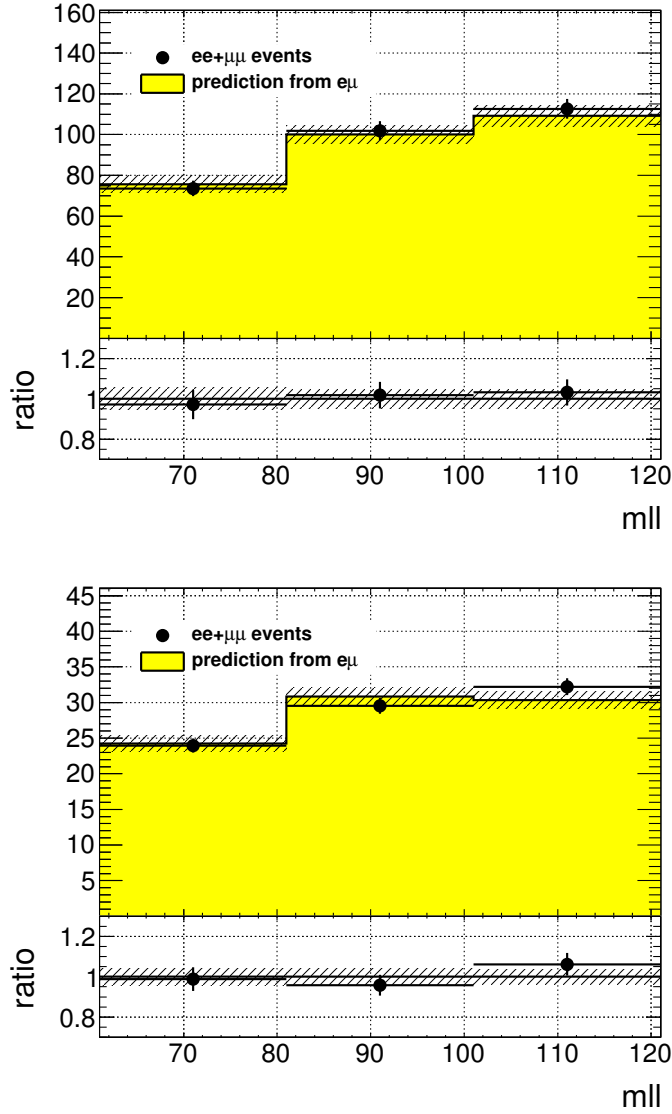


Figure 81: **MC** closure plots of VRS (top) and SRZ (bottom). The number of events from **MC** (black points) is compared to the number of events predicted from the flavor symmetry method (yellow histogram). The comparison is performed before the expanded m_{ll} window is used to predict the on-Z bin, but because the shape is taken from the same **MC**, the result is identical.

2341 A small uncertainty is added based on the statistical uncertainty on the
 2342 k and α factors derived from data. These factors are measured in many dif-
 2343 ferent bins (see, for example, the different measurements of k in Figure 82),
 2344 and as a consequence, some bins can have very large statistical uncertain-
 2345 ties. To assess the uncertainty on the total estimate, each measurement
 2346 of these factors is varied by its uncertainty in order to produce the max-
 2347 imum and minimum possible prediction. The differences with respect to
 2348 the nominal prediction are used to create a symmetrized error, which is
 2349 included in Table 16.

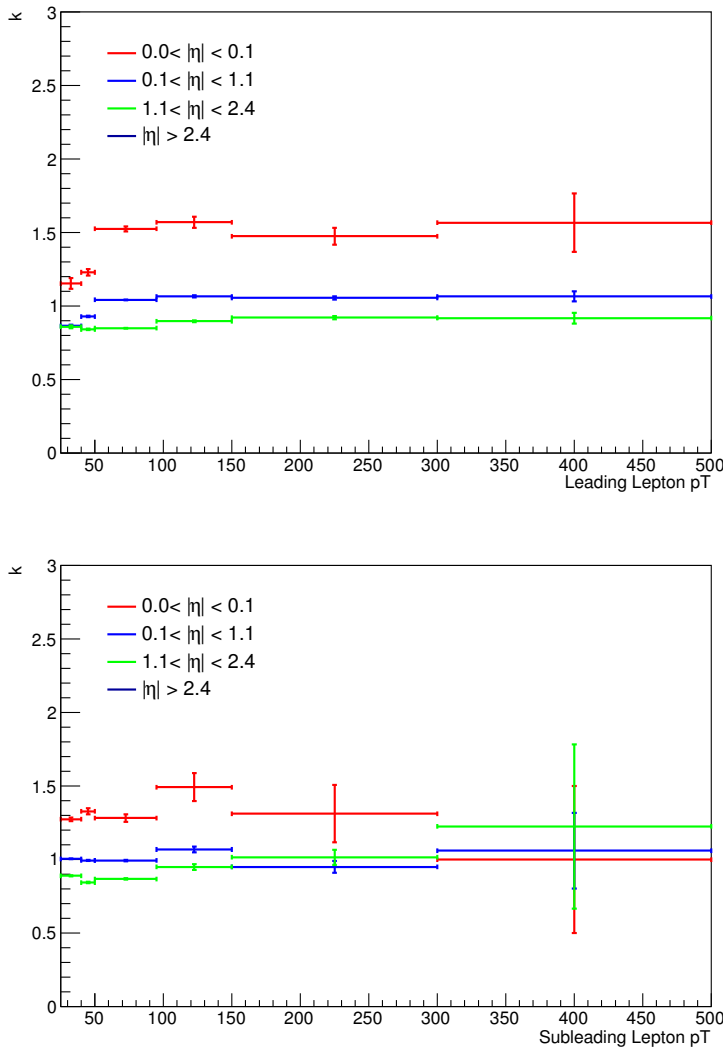


Figure 82: Measurements of k , the ratio of electron to muon events, in bins of p_T and η . On the top is the measurements indexed by the leading lepton, while the measurements indexed by the subleading lepton are on the bottom. These efficiencies are for the 2016 dataset.

2350 The next uncertainty considers a potential bias in the way the α factors
 2351 are calculated. Because they are derived from data, there is already trigger
 2352 dependence in data collection; only events passing a trigger are stored.

Additional trigger dependence is created by the data format used for analysis. ATLAS data and MC are stored in a format called Analysis Object Data (AOD), but smaller, slimmer versions of these datasets, called derived AODs (dAODs) are used for analysis. These dAODs are designed with specific analyses in mind, filtering on the triggers and objects required by the analyses. As a consequence, in the dAOD used in this analysis, there are explicit requirements that lepton or E_T^{miss} triggers are passed in order for events to be included.

As a consequence, the trigger efficiencies ϵ^{trig} used in Equation 40 to define α do not consider all possible data events. The ϵ^{trig} factor is calculated for each trigger using events passing the kinematic selection for that trigger, outlined in Section 9.1. The efficiency factor is then measured according to the equation

$$\epsilon^{\text{trig}} = \frac{N_{\text{trig}}}{N_{\text{all}}} \quad (46)$$

where N_{trig} is the number of events passing the trigger in the kinematic selection and N_{all} is all events in the selection. The latter measurement is the one subject to this bias, as it contains only the events that pass at least one trigger required for inclusion in the dAOD. As a consequence of these missing events, the ϵ^{trig} values will be artificially high. However, because the ratio of trigger efficiencies for the different channels is the only quantity needed for this analysis, the missing events will only bias the prediction if the different channels are differently impacted by the trigger preselection.

Calculating the flavor symmetry method's dependence on these biases requires the use of MC. With a generated MC sample, there is no trigger dependence, so an unskimmed sample can be compared to a typical skimmed MC dAOD to identify the effect of the skimming. Figure 83 shows a comparison of the α factors calculated for different bins in E_T^{miss} from the nominal source, data, as well as these two MC sources. A E_T^{miss} dependence would be the most likely bias between the two MC-derived α factors because E_T^{miss} triggers are the only triggers besides lepton triggers that will allow an event to be accepted into the dAOD used by this analysis. Though there is some difference between the data-derived α and those taken from MC, it is clear from this plot that there is very little dependence on the choice of an unskimmed or skimmed sample. The calculation of the uncertainty is performed by repeating the flavor symmetric method in MC with each of the two α factors and using the difference between the estimates as a symmetric error.

The last uncertainty relates to the main MC dependence of the method - the $m_{\ell\ell}$ shape of the FS background. A correction factor is taken from MC in order to account for the $m_{\ell\ell}$ widening, and the accuracy of that factor must be checked. Its shape is compared to that of data in region similar to VR-FS, but with an H_T cut lowered to 300 GeV to increase statistics. The difference between the fraction of events on the Z-mass peak in data and MC in this region is taken as a systematic uncertainty. To confirm that using

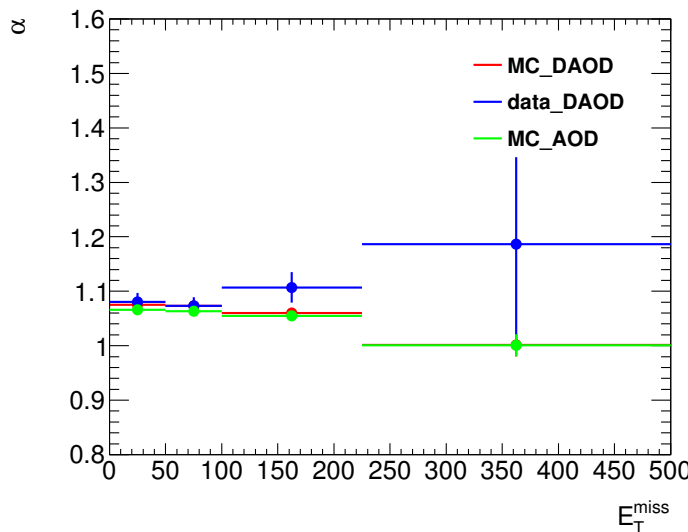


Figure 83: α , the trigger efficiency ratio, calculated as a function of E_T^{miss} from three different sources: data (blue), the usual skimmed $t\bar{t}$ MC (red), and an unskimmed $t\bar{t}$ MC (green).

2397 this lowered H_T cut still gives a valid answer, the fractions are compared
 2398 as a function of H_T in Figure 84. In these plots, especially in the higher-
 2399 statistics 2016 plot, it is clear both that the data and MC agree very well
 2400 and that there is no strong H_T dependence.

2401 All the uncertainties are calculated independently for the two datasets,
 2402 then added together. Statistical uncertainties, including the MC closure sta-
 2403 tistical uncertainties and the k and α uncertainties, are added in quadrature
 2404 between the two years. Uncertainties that are more likely to be correlated,
 2405 such as the difference between the two estimates in MC closure and the
 2406 dependence on using a dAOD to calculate trigger efficiencies, are added
 2407 linearly. The total uncertainty is about 12% of the nominal prediction in
 2408 SRZ and about 9% in VRS.

2409 11.1.2 Uncertainties on the $\gamma + \text{jets}$ Method

2410 One of the largest sources of uncertainty on the $\gamma + \text{jets}$ method is derived
 2411 by comparing the results from reweighting in different variables. Though
 2412 boson p_T is used as the nominal reweighting variable, the differences in
 2413 the kinematics of γ and Z events also impact number of jets, H_T , and E_T
 2414 (which includes the mass of the boson). The $\gamma + \text{jets}$ method is repeated
 2415 using each of these variables to reweight, and their E_T^{miss} distributions are
 2416 shown in Figure 85. The maximum difference from the nominal prediction
 2417 is symmetrized and used as an uncertainty on the method.

2418 Another uncertainty is applied to estimate the validity of using MC in a
 2419 1-jet CR to determine the smearing functions. Smearing functions are made
 2420 using data from the same 1-jet region and using MC in a ≥ 2 -jet region
 2421 otherwise identical to the 1-jet CR. These distributions are also shown in
 2422 Figure 85, and like the alternate reweighting distributions, are used to find

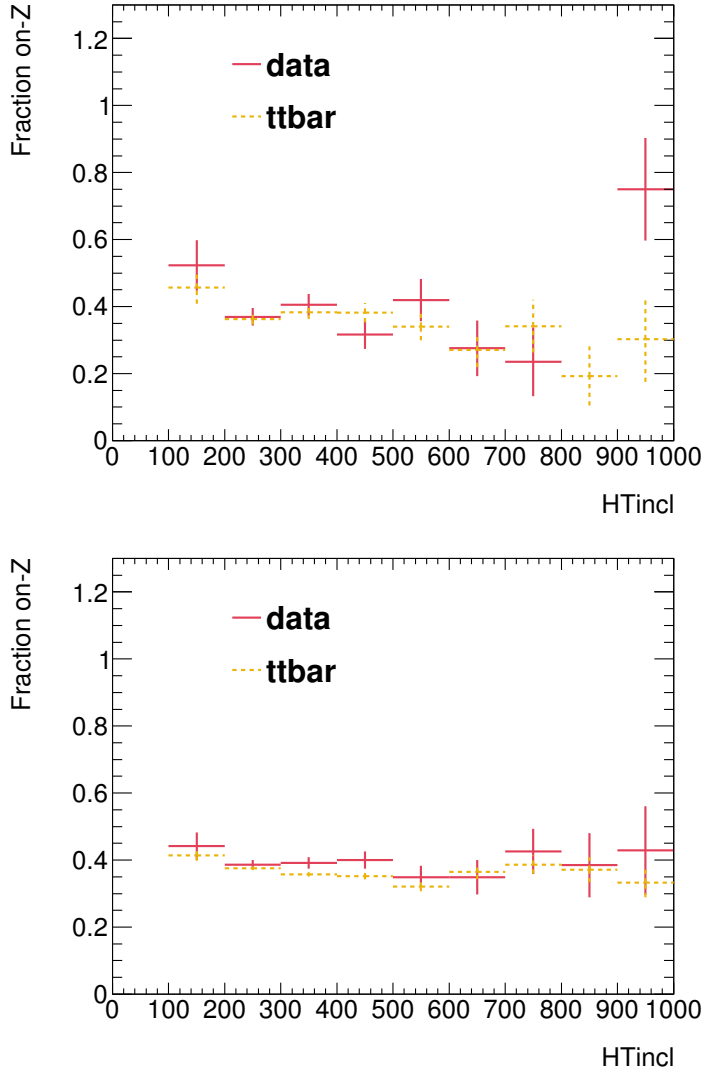


Figure 84: Plots of the fraction of on-Z events with a VR-FS-like selection as a function of H_T . The top figure shows 2015 data and MC while the bottom figure shows the same for 2016.

2423 a maximum difference from the nominal prediction which is translated
2424 into a symmetric error.

2425 As in the flavor symmetric method, the full procedure is carried out on
2426 MC in order to test MC closure, including a recalculation of any weights
2427 that are typically derived from data. The resulting comparison between
2428 $Z/\gamma^* + \text{jets}$ MC and the $\gamma + \text{jets}$ method performed on MC can be seen
2429 in Figure 86. The final non-closure uncertainty is taken from VRS, where
2430 larger numbers of events give a clearer picture of the success of the method
2431 than in SRZ. In this region, the statistical uncertainty on the prediction is
2432 compared to the non-closure, and the larger of the two is used as the final
2433 uncertainty.

2434 The uncertainty on the $V\gamma$ contamination in CR- γ is also considered.
2435 An uncertainty on the MC prediction is made based on comparison of data

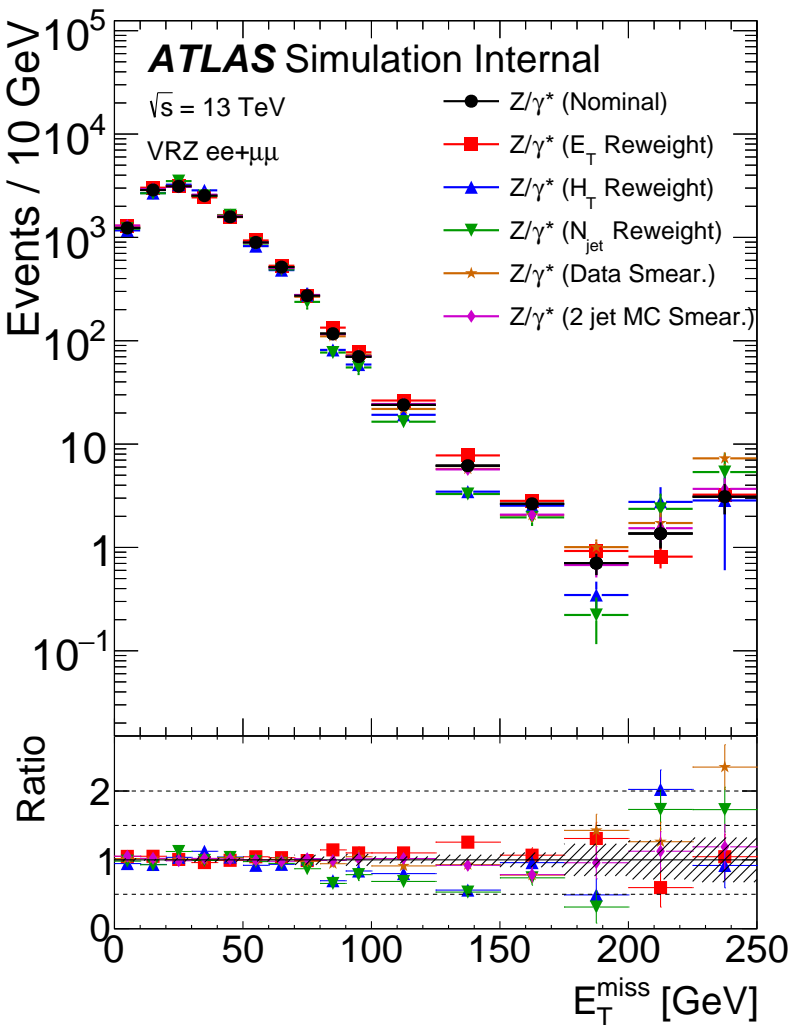


Figure 85: E_T^{miss} distributions for $\gamma + \text{jets}$ predictions using different reweighting variables, as well as distributions with the nominal reweighting but with smearing functions taken from data and from MC in a ≥ 2 -jet region.

and MC in a $W + \text{jets}$ VR, shown in Figure 87. This VR is similar to CR- γ , but instead of vetoing events with leptons, requires at least one well-isolated lepton with a p_T over 25 GeV. At E_T^{miss} values over 100 GeV, region is about 90% pure in $W\gamma$ processes. The MC agrees well with data in this region, even at very high E_T^{miss} , so an uncertainty of 16% based primarily on statistical uncertainty in this VR is placed on the $V\gamma$ MC. This uncertainty is propagated to the final result through the subtraction procedure.

An uncertainty on the $m_{\ell\ell}$ shape is determined using MC closure as well. The comparison of $m_{\ell\ell}$ shapes in $Z/\gamma^* + \text{jets}$ MC and the $\gamma + \text{jets}$ method applied to MC is shown in Figure 70. As with the main MC closure test, the maximum of the statistical uncertainty and the non-closure is taken as the final uncertainty on this background.

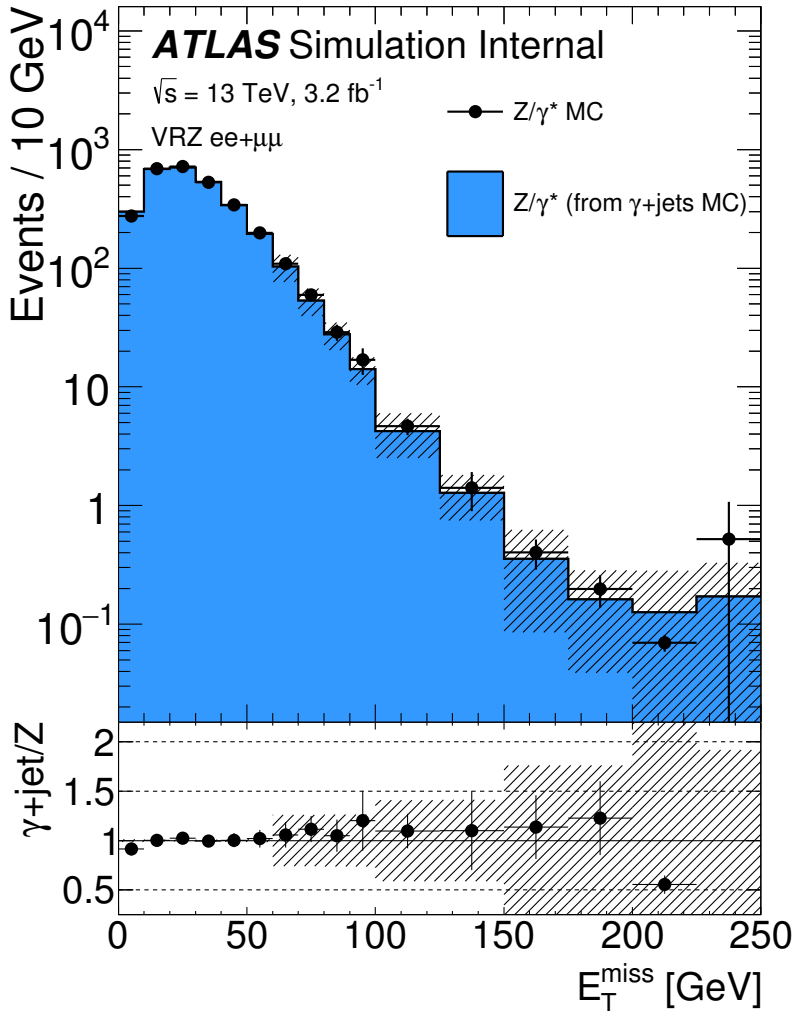


Figure 86: MC closure of the $\gamma + \text{jets}$ method as a function of E_T^{miss} comparing the MC prediction of the Z background with the $\gamma + \text{jets}$ MC. The uncertainty band includes both statistical and reweighting uncertainties.

2448 One last uncertainty based on the statistical uncertainty on the number
2449 of $\gamma + \text{jets}$ data events used for this method is also included. The full
2450 breakdown of uncertainty in SRZ can be seen in Table 17.

2451 11.1.3 Uncertainties on the Fakes Background

2452 Systematic uncertainties on the fakes background are derived from a se-
2453 ries of variations on the nominal method. Variations include scaling the
2454 real and fake efficiencies up and down by their statistical uncertainties,
2455 scaling the prompt lepton contamination in CR-fake up and down by 20%,
2456 and by requiring and vetoing b -tagged jets in CR-fake to determine the
2457 dependence on heavy flavor. Statistical uncertainties can also be large in
2458 regions with small numbers of events in the baseline selection, such
2459 as SRZ. In other regions, the b -tagging dependence provides the largest

Ch.	Pred.	Uncertainties (%)						
		$V\gamma$ sub.	MC clos.	$m_{\ell\ell}$ shape	re- weight	smear	stat.	total
ee	1.02	53.0	21.0	19.0	100.0	65.0	56.0	145.0
$\mu\mu$	2.08	27.0	14.0	23.0	30.0	59.0	40.0	86.0
$ee+\mu\mu$	3.1	36.0	16.0	22.0	43.0	60.0	33.0	92.0

Table 17: Uncertainty breakdown for the $\gamma + \text{jets}$ method in SRZ. Uncertainties considered are the impact of MC uncertainty on $V\gamma$ backgrounds, MC closure, uncertainty on $m_{\ell\ell}$ shape (also determined via MC closure), reweighting uncertainties, smearing uncertainties, and statistical uncertainty on the $\gamma + \text{jets}$ events used in the method.

uncertainty. The full breakdown of uncertainties for the most important regions are listed in Table 18.

Variation	SRZ	CRT	CRFS	VRFS	VRS	VRT
Nominal	0.10 ± 1.61	25.39 ± 5.35	3.73 ± 2.19	10.53 ± 3.56	3.64 ± 3.20	80.06 ± 9.80
EL F Up	0.15	30.23	3.96	10.93	3.56	92.46
EL F Down	0.06	21.80	3.52	10.18	3.54	70.07
EL R Up	0.25	26.17	3.92	11.10	4.13	82.57
EL R Down	-0.07	24.51	3.52	9.92	3.10	77.24
MU F Up	-0.20	32.48	4.77	16.41	5.25	86.48
MU F Down	0.29	20.17	2.91	7.04	2.87	70.12
MU R Up	0.13	25.67	3.78	10.66	3.81	81.18
MU R Down	0.05	25.04	3.67	10.38	3.44	78.72
Total Sys	+0.26 -0.35	+8.64 -6.39	+1.08 -0.87	+5.92 -3.56	+1.70 -0.97	+14.24 -14.42
Total Sys (%)	+261.05 -354.72	+34.01 -25.19	+29.05 -23.23	+56.22 -33.85	+46.57 -26.60	+17.78 -18.02
Real Cont. Up	0.23	20.97	3.06	8.08	3.15	68.79
Real Cont. Down	-0.01	29.67	4.38	12.95	4.16	90.23
b-jet	0.31	40.44	5.28	8.98	5.63	120.50
no b-jet	0.16	23.44	3.08	11.38	3.97	70.55
Total Sys	+0.25 -0.11	+15.65 -4.83	+1.69 -0.93	+2.56 -2.90	+2.09 -0.49	+41.71 -14.74
Total Sys (%)	+260.46 -109.06	+61.66 -19.02	+45.30 -24.85	+24.32 -27.58	+57.31 -13.35	+52.10 -18.42

Table 18: Systematic uncertainties on the fake-lepton background for on-Z regions for 2015+2016 yields. The nominal yield includes statistical uncertainty from the baseline selection in a given region. The following rows indicate the results of varying the real and fake lepton efficiencies up and down by their statistical uncertainty. Real cont. gives an uncertainty on the contamination of real leptons in the fake lepton efficiency. b-jet and no b-jet indicate the impact of requiring or vetoing b-tagged jets in the regions used to measure the fake efficiency.

11.2 THEORETICAL AND EXPERIMENTAL UNCERTAINTIES

Experimental uncertainties cover any detector effect or LHC condition that may not be modeled precisely correctly in MC. For each uncertainty, a standard prescription from the ATLAS experiment is followed. Uncertainties are included on the following parameters:

- 2467 • Luminosity (2.9%) [91, 92]
- 2468 • Jet energy scale [61]
- 2469 • Jet energy resolution [61]
- 2470 • Jet vertex tagging
- 2471 • Heavy flavor tagging
- 2472 • E_T^{miss} soft term [64]
- 2473 • e/μ momentum scale
- 2474 • e/μ trigger, reconstruction, and identification efficiencies
- 2475 • Pile-up

2476 These uncertainties are applied to all MC samples used in the analysis.
 2477 This includes signal models, diboson and rare top samples for the nominal
 2478 estimate, and all backgrounds taken from MC in the sideband fit.

2479 Theoretical uncertainties include cross-section uncertainties, scale uncer-
 2480 tainties, and PDF uncertainties. For the diboson samples, the scale uncer-
 2481 tainties, given in Table 19 are calculated by varying each scale up and
 2482 down by a factor of two. These are combined with a 6% cross-section un-
 2483 certainty and a generator uncertainty obtained by comparing PowHEG and
 2484 SHERPA MC yields in a given region. This generator uncertainty, shown in
 2485 Table 20, is dominant in most regions. Rare top processes are given a 13%
 2486 PDF and scale variation uncertainty [38] and a 22% cross section uncer-
 2487 tainty [71–73].

2488 Signal models have both the central value and uncertainty on cross-
 2489 sections taken from an envelope of predictions using different scales and
 2490 PDF sets [93]. The signal processes are calculated at Next-to-Leading-Logarithmic
 2491 Accuracy (NLO+NLL); they are initially calculated at NLO in the strong
 2492 coupling constant, with additional terms from next-to-leading-logarithmic
 2493 resummation of soft gluon emission [94–98].

2494 11.3 IMPACT OF UNCERTAINTIES ON THE SIGNAL REGION

2495 The breakdown of each major uncertainty’s contribution to the total un-
 2496 certainty in SRZ is shown in Table 21. The dominant uncertainty is the
 2497 diboson generator uncertainty, followed by the statistical uncertainty from
 2498 the FS background. Uncertainties smaller than 1% are not shown in the
 2499 table.

$VV \rightarrow ll\nu\nu$ Samples							
	SRZ	VRS	CRT	VRT	VRWZ	VRZZ	VR ₃ L
resummation	0.07	0.03	0.01	0.02	0.00	0.00	0.00
renormalization	0.13	0.17	0.16	0.22	0.00	0.00	0.00
factorization	0.01	0.01	0.01	0.03	0.00	0.00	0.00
total	0.15	0.17	0.16	0.22	0.00	0.00	0.00
$WZ \rightarrow lll\nu$ Samples							
	SRZ	VRS	CRT	VRT	VRWZ	VRZZ	VR ₃ L
resummation	0.07	0.05	0.13	0.08	0.02	0.00	0.01
renormalization	0.26	0.20	0.28	0.21	0.07	0.00	0.18
factorization	0.04	0.04	0.02	0.06	0.01	0.00	0.02
total	0.28	0.21	0.31	0.23	0.07	0.00	0.18
$ZZ \rightarrow llll$ Samples							
	SRZ	VRS	CRT	VRT	VRWZ	VRZZ	VR ₃ L
resummation	0.27	1.07	0.01	0.01	0.06	0.01	0.53
renormalization	0.28	0.26	0.30	0.60	0.07	0.04	0.14
factorization	0.27	0.25	0.30	0.58	0.13	0.02	0.16
total	0.48	1.13	0.43	0.84	0.16	0.05	0.57

Table 19: Fractional uncertainties of dibosons in signal and validation regions from Sherpa scale variations.

Region	Sherpa Events/fb ⁻¹	Sherpa Events	Powheg Events/fb ⁻¹	Powheg Events	% Difference
WZ Samples					
SRZ+VRZ	5.219	76.722	3.286	48.300	37.046
CRT+VRT	1.060	15.583	0.742	10.913	29.970
WW/ZZ Samples					
SRZ+VRZ	1.921	28.244	0.685	10.070	71.424
CRT+VRT	6.281	92.332	3.142	46.188	55.474

Table 20: Comparison of yields in on-Z and off-Z regions in Sherpa and Powheg diboson MC at 14.7 fb⁻¹.

Source	Relative systematic uncertainty [%]
SRZ	
Total systematic uncertainty	17
WZ/ZZ generator uncertainty	13
Flavour symmetry (statistical)	7
WZ/ZZ scale uncertainty	6
$Z/\gamma^* + \text{jets}$ (systematic)	4
Flavour symmetry (systematic)	3
$Z/\gamma^* + \text{jets}$ (statistical)	2
Fake-leptons	1

Table 21: Overview of the dominant sources of systematic uncertainty on the total background estimate in the signal regions. The values shown are relative to the total background estimate, shown in %.

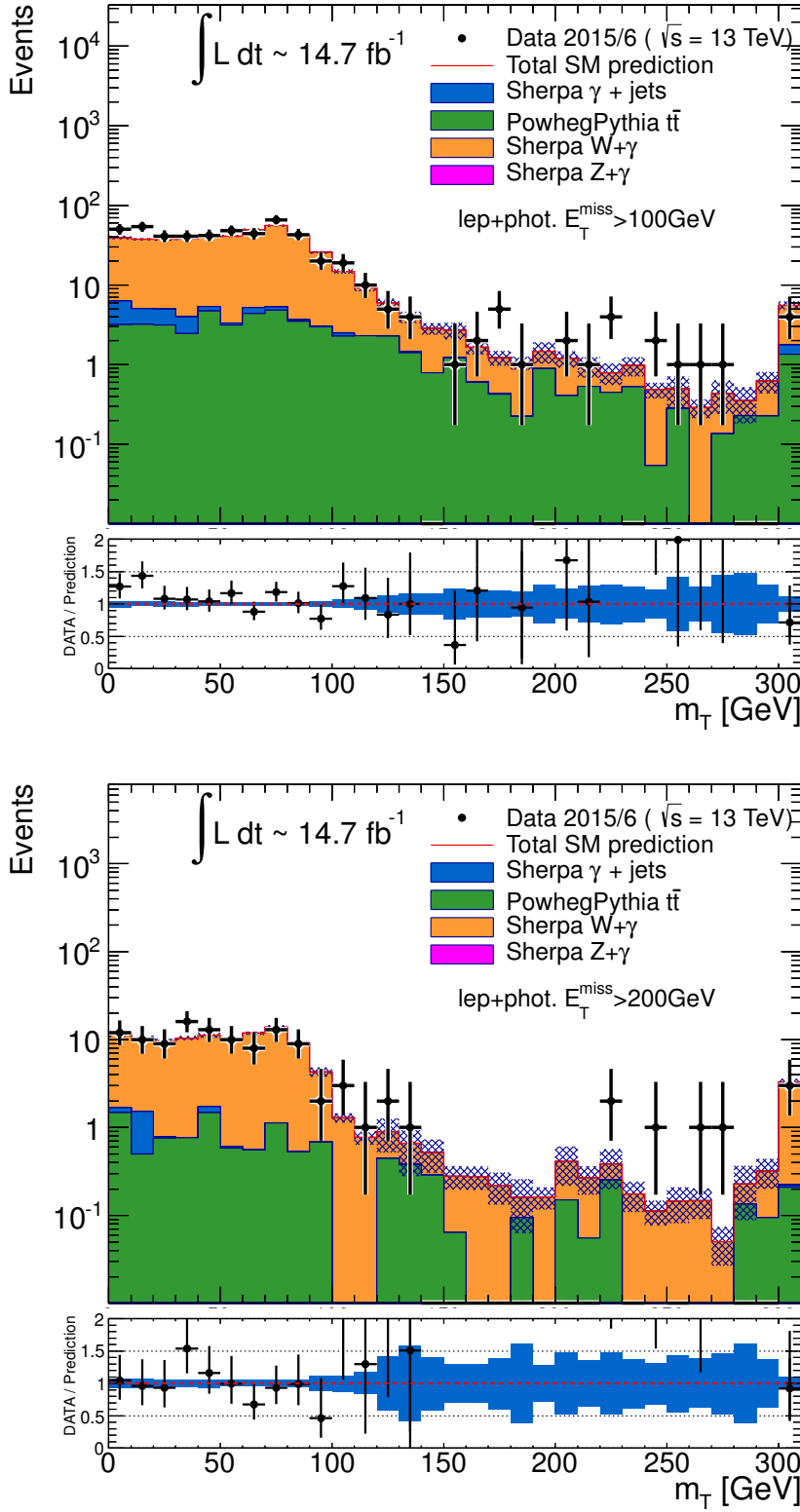


Figure 87: Distributions of $m_T(\ell, E_T^{\text{miss}})$, the transverse mass of the lepton and the E_T^{miss} in a VR designed to target $W\gamma$ processes. Top is the distribution with a E_T^{miss} cut at 100 GeV, and bottom is the same distribution with a E_T^{miss} cut of 200 GeV.

2500

2501 RESULTS

2502 The results of the search can be seen in [Table 22](#), which displays the ex-
 2503 pected and observed numbers of events in SRZ, both divided by channel
 2504 and inclusively. The predictions and uncertainties for each background are
 2505 shown, though many of these uncertainties are correlated between back-
 2506 grounds, so the final uncertainty does not correspond to a simple addition
 2507 in quadrature of each error. A total of sixty events are observed, with 53.5 ± 9.3
 2508 events expected. [Figure 88](#) shows the expected and observed results
 2509 visually for the **SR** as well as three **VRs**, all designed to verify the accuracy
 2510 of the backgrounds taken from **MC**. Excellent agreement is seen in all cases,
 2511 with the largest deviation at about 1σ .

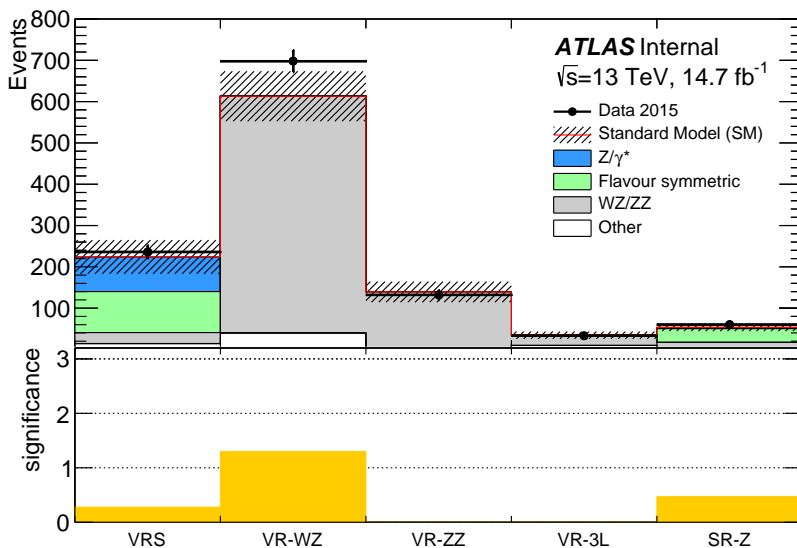


Figure 88: Comparison of background predictions and data yields in four validation regions, as well as the signal region. Definitions of all regions can be found in [Table 7](#), with both rare top and fake backgrounds grouped together under the “other” label. The uncertainty band includes all statistical and systematic uncertainties. Below is a panel of the one-sided statistical significances of the deviations between the predicted and observed quantities for each region.

2512 [Table 22](#) also shows several statistical interpretations of the results. The
 2513 discovery p -value for zero signal strength, which gives the probability that
 2514 the observed events are compatible with a **SM**-only hypothesis, is given as
 2515 0.32. The significance is listed as 0.47σ , which is a reinterpretation of the p -
 2516 value into a gaussian significance. This p -value is one-sided; when the data
 2517 yield is less than expected the p -value is set to 0.5, and the significance is
 2518 set to 0. S^{95} , the upper limit on the number of signal events that could be

Table 22: Number of events expected and observed in the ee , $\mu\mu$, and combined channels. Expected predictions include all systematic and statistical uncertainties discussed in Chapter 11. Also shown is the discovery p -value for zero signal strength ($p(s = 0)$) [99], Gaussian significance, 95% CL observed and expected upper limits on the number of signal events (S^{95}), and the corresponding observed upper limit on the visible cross section ($\langle\epsilon\sigma\rangle_{\text{obs}}^{95}$).

	SRZ	SRZ ee	SRZ $\mu\mu$
Observed events			
	60	35	25
Total expected background events	53.5 ± 9.3	27.1 ± 5.1	26.8 ± 4.4
Flavour-symmetric ($t\bar{t}$, Wt , WW and $Z \rightarrow \tau\tau$) events	33.2 ± 3.9	16.5 ± 2.1	16.7 ± 2.0
Z/γ^* + jets events	3.1 ± 2.8	$1.0^{+1.3}_{-1.0}$	2.1 ± 1.4
WZ/ZZ events	14.2 ± 7.7	7.8 ± 4.3	6.4 ± 3.5
Rare top events	2.9 ± 0.8	1.4 ± 0.4	1.5 ± 0.4
Fake-lepton events	$0.1^{+0.8}_{-0.1}$	$0.5^{+0.7}_{-0.5}$	$0^{+0.2}_{-0.2}$
$p(s = 0)$	0.32	0.15	0.5
Significance (σ)	0.47	1.00	0
Observed (Expected) S^{95}	$28.2 (24.5^{+8.9}_{-6.7})$	$22.0 (15.8^{+6.5}_{-4.5})$	$12.9 (14.0^{+5.7}_{-3.9})$
$\langle\epsilon\sigma\rangle_{\text{obs}}^{95}$ [fb]	1.9	1.5	0.88

in the SR at a 95% CL, is determined both for the expected and observed number of events. This limit is also reinterpreted based on the integrated luminosity used in the search to produce an upper limit on the visible cross-section of signal events, $\langle\epsilon\sigma\rangle_{\text{obs}}^{95}$.

The predictions in SRZ, combined with the MC shapes, are used to produce plots in a broader $m_{\ell\ell}$ range, seen in Figure 89. These plots are useful demonstrations of efficacy of the background estimation methods, showing the well-modeled $Z/\gamma^* + \text{jets}$ shape in the same-flavor region, and in the different-flavor region, demonstrating that there are no extreme fluctuations within the region used to predict the flavor symmetric background.

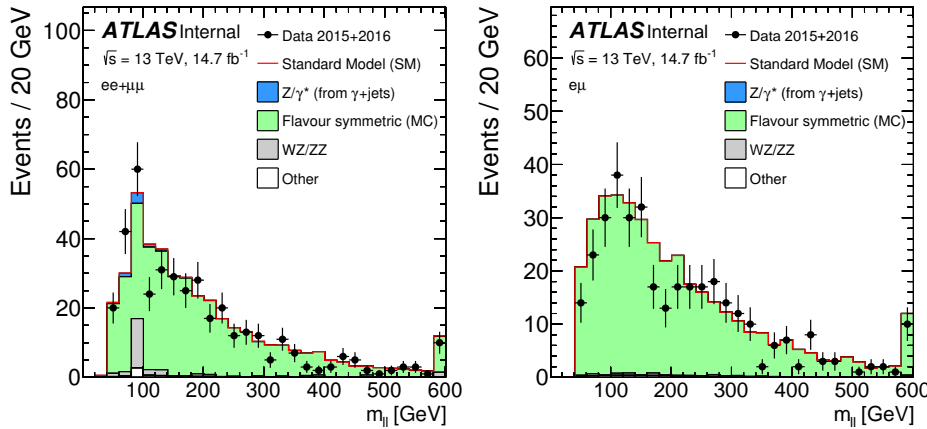


Figure 89: Comparisons as a function of $m_{\ell\ell}$ of background predictions with observed data in an SRZ-like region, with the $m_{\ell\ell}$ cut removed. Left is the same-flavor channel, where all background shapes are taken from MC and scaled to their SRZ predictions, except for the $Z/\gamma^* + \text{jets}$ background, which is taken entirely from the data-driven background. Right is the different-flavor channel, in which the backgrounds are taken directly from MC, except for $t\bar{t}$, which is scaled to match the total data yield.

Focusing in on the SR itself, comparisons of background predictions, observed events, and signal models can be made as a function of key variables for the analysis. Figure 90 shows several of these. The first two figures focus on the features of the SR events' leading leptons; they give the mass and p_T of a hypothetical parent particle reconstructed from the leptons. In the case of events with a real Z boson, these variables simply give that boson's mass at p_T . The next two figures show distributions in the two most important variables used to differentiate signal from background, E_T^{miss} and H_T . In this analysis, where the frozen SR resulted in cuts on these quantities that are lower than those that would be chosen based on a new optimization, these plots show that, even in more sensitive regions, no large excess above the SM background is seen. The last pair of figures relates to the jets in the event, showing the total number of jets and the total number of b -jets in the SR events. The b -jet quantity is not explicitly cut on in the analysis because the fraction of b -jets produced is extremely model dependent. However, an excess at high b -jet

2545 multiplicity would suggest a BSM process. In each of these distributions,
 2546 the observed distributions match the background predictions very well,
 2547 and no evidence for any of the superimposed signal models is seen.

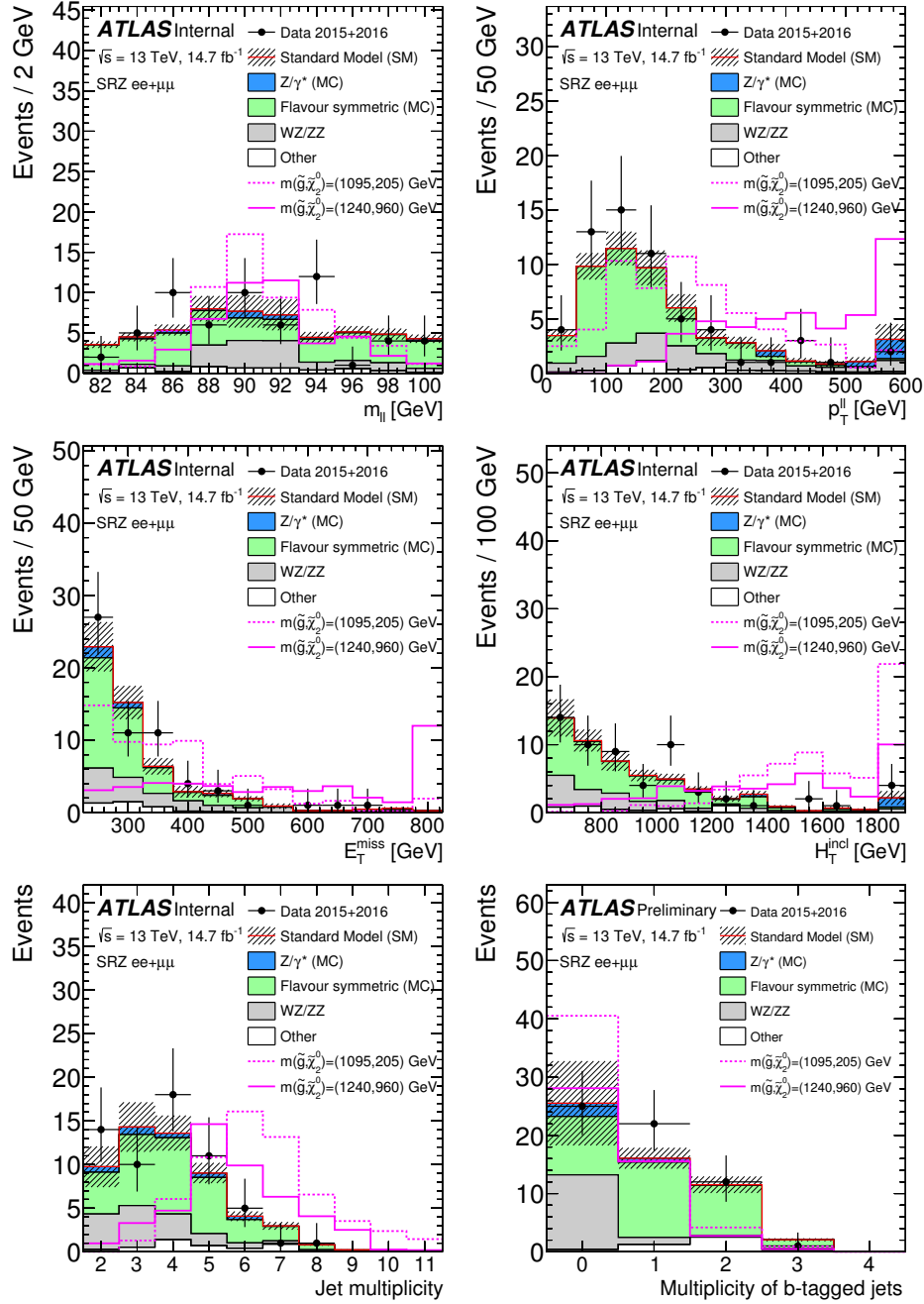


Figure 90: Distributions of observed data, background predictions, and simulated signals are shown in SRZ as a function of $m_{\ell\ell}$, $p_T^{\ell\ell}$, E_T^{miss} , H_T , number of jets, and number of b -jets. The two example signals have $(m(\tilde{g}), m(\tilde{\chi}_2^0)) = (1095, 205) \text{ GeV}$. All background shapes are taken from MC, and in the case of flavor symmetric and $Z/\gamma^* + \text{jets}$ backgrounds, their yields are scaled to match the data-driven predictions. Uncertainties include statistical and systematic components.

2548 Comparisons of the observed and expected yield are also made as a
2549 function of $\Delta\phi(\text{jet}_{12}, p_T^{\text{miss}})$, shown in [Figure 91](#). Here, results are shown
2550 in a region similar to SRZ with the cut on this variable removed, showing
2551 the efficacy of the background prediction in a region enhanced in $Z/\gamma^* +$
2552 jets events. Again, excellent agreement is seen between the background
2553 prediction and observed data.

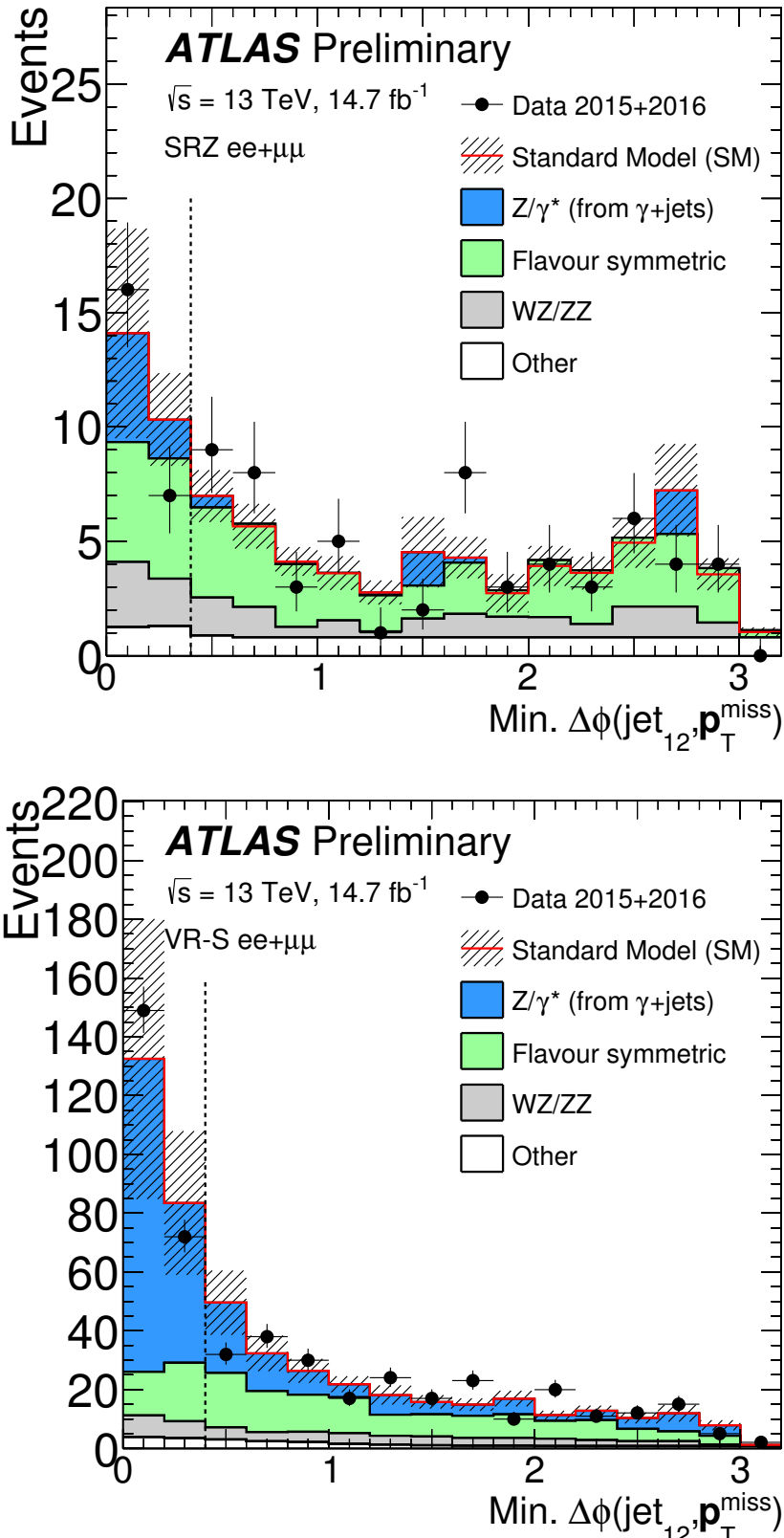


Figure 91: Comparisons as a function of $\Delta\phi(\text{jet}_{12}, \mathbf{p}_T^{\text{miss}})$ of background predictions with observed data in an SRZ-like (left) and VRS-like (right) region, with the $\Delta\phi(\text{jet}_{12}, \mathbf{p}_T^{\text{miss}})$ cut removed. All background shapes are taken from MC and scaled to their SRZ predictions, except for the Z/ γ^* + jets background, which is taken entirely from the data-driven background.

2554

2555 INTERPRETATIONS

2556 Using the simplified models discussed in [Section 2.2.3](#), these results can be
 2557 interpreted into exclusions of theories based on the masses of the particles
 2558 involved. Of course, these exclusions include all the assumptions of the
 2559 models used, so they shouldn't be interpreted to mean that no theory
 2560 with a given set of particle masses can possibly exist, but they do provide
 2561 a helpful guideline for targeting future searches and comparing results
 2562 from different analyses.

2563 Limits are determined using a program called HistFitter [99], designed
 2564 within the ATLAS experiment, which builds upon the capabilities of ROOT
 2565 [100], RooStats [101], and HistFactory [102] to combine the uncertainties
 2566 of the various background predictions, including their correlations, and
 2567 produce cross-section limits at 95% CL using the CL_S prescription [103,
 2568 104]. In this prescription, a likelihood is constructed based on the expected
 2569 signal and background contributions to the SR. Nuisance parameters are
 2570 created based on the statistical and systematic uncertainties for each data-
 2571 driven background, as well as for each systematic applied to the MC-driven
 2572 background estimates. The fit uses Gaussian models for nuisance param-
 2573 eters for all signal and background uncertainties, except for the statistical
 2574 uncertainty on data- and MC-driven background estimates, which are in-
 2575 terpreted as Poissonian. Experimental uncertainties are considered fully
 2576 correlated across the signal and background MC-based estimates.

2577 A fit is performed, leaving a signal strength parameter (μ) free, to max-
 2578 imize the likelihood, and subsequent fits are preformed to at discrete μ
 2579 values to determine the relative likelihood of each value. Using this rela-
 2580 tive likelihood, the probability of a background-only hypothesis, p_b , can be
 2581 determined by setting $\mu = 0$, as well as the probability of a signal + back-
 2582 ground hypothesis p_{s+b} with any non-zero signal strength, but nominally
 2583 with $\mu = 1$. The confidence limit is constructed as a ratio

$$CL_S = \frac{p_{s+b}}{1 - p_b}. \quad (47)$$

2584 Then, if CL_S falls below 5%, the signal + background hypothesis can be
 2585 excluded at 95%. Expected exclusion limits are constructed by assuming
 2586 the observed data precisely matches the prediction, and 1σ uncertainty
 2587 bands are formed by varying the nuisance parameters away from their fit-
 2588 ted values to produce a change in the likelihood. The observed limit uses
 2589 the actual observation of data in the SR to set exclusion limits, so any excess
 2590 above the expected background will result in worse limits than expected,
 2591 and any deficit will result in better limits. This exclusion is typically dis-
 2592 played with error bands that represent a 1σ variation in the cross-section
 2593 of the signal models.

The simplified model discussed in Section 2.2.3, in which pair-produced gluinos decay via a $\tilde{\chi}_2^0$ to jets, a Z boson, and a $\tilde{\chi}_1^0$ LSP, is produced in two grids, which differ by their choice of the LSP mass. The first grid assumes a light LSP, fixing its mass to 1 GeV for all mass points, and is shown as a function of \tilde{g} and $\tilde{\chi}_2^0$. The second grid is defined as a function of \tilde{g} and $\tilde{\chi}_1^0$, and its varying LSP mass is defined relative to the $\tilde{\chi}_2^0$ mass by $m(\tilde{\chi}_1^0) = m(\tilde{\chi}_2^0) - 100$ GeV. Figure 92 shows the first of these grids, along with exclusions on a similar simplified model, which replaces the gluinos with squarks and uses the same mass scheme. The exclusion contours on the second grid is shown in Figure 93, as a function of $m(\tilde{g})$ and $m(\tilde{\chi}_1^0)$.

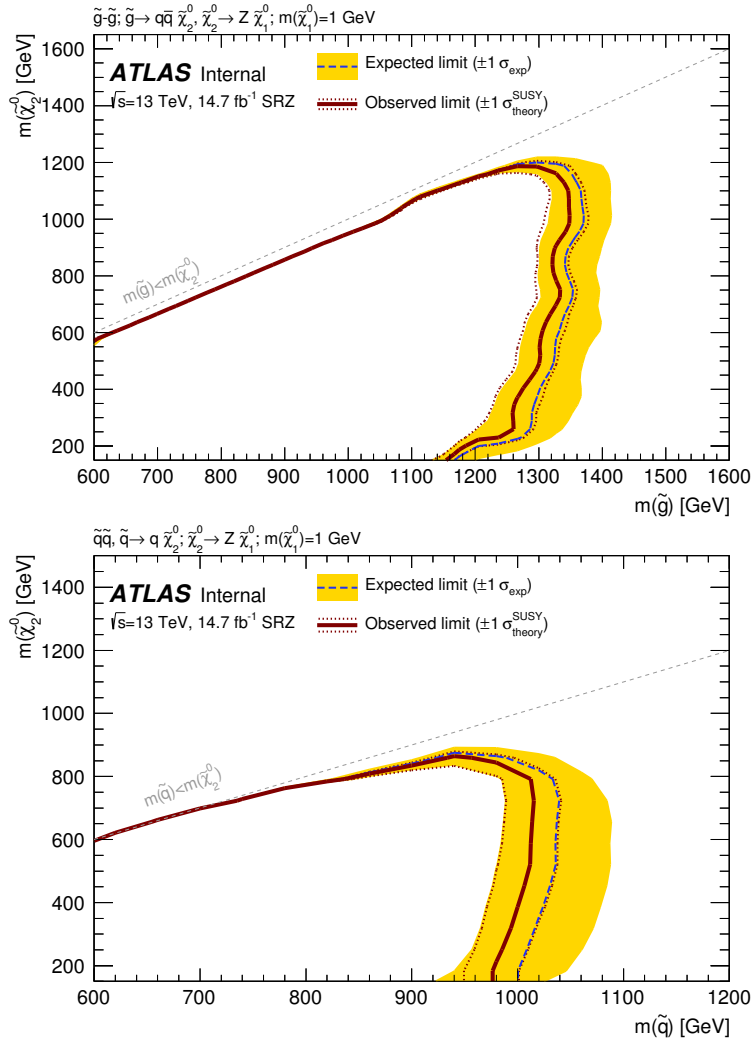


Figure 92: Expected and observed exclusion contours derived from the results in SRZ for the (top) $\tilde{g}-\tilde{\chi}_2^0$ on-shell grid and (bottom) $\tilde{q}-\tilde{\chi}_2^0$ on-shell grid. The dashed blue line indicates the expected limits at 95% CL and the yellow band shows the 1σ variation of the expected limit as a consequence of the uncertainties in the background prediction and the experimental uncertainties in the signal ($\pm 1\sigma_{\text{exp}}$). The observed limits are shown by the solid red line, with the dotted red lines indicating the variation resulting from changing the signal cross section within its uncertainty ($\pm 1\sigma_{\text{theory}}^{\text{SUSY}}$).

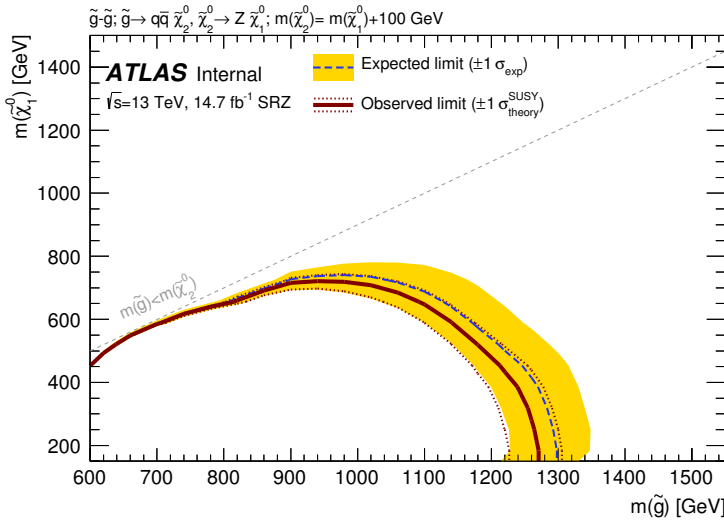


Figure 93: Expected and observed exclusion contours derived from the results in SRZ for the $\tilde{g}-\tilde{\chi}_1^0$ on-shell grid. The dashed blue line indicates the expected limits at 95% CL and the yellow band shows the 1σ variation of the expected limit as a consequence of the uncertainties in the background prediction and the experimental uncertainties in the signal ($\pm 1\sigma_{\text{exp}}$). The observed limits are shown by the solid red line, with the dotted red lines indicating the variation resulting from changing the signal cross section within its uncertainty ($\pm 1\sigma_{\text{theory}}^{\text{SUSY}}$).

2604 In general, the observed exclusions are slightly weaker than the expected
 2605 exclusions, due to a very small excess of events observed in SRZ. The
 2606 observed lower limit on $m(\tilde{g})$ is about 1.3 TeV for models with $m(\tilde{\chi}_2^0) = 500$
 2607 GeV for the $\tilde{g}-\tilde{\chi}_2^0$ grid. These improve significantly on the previous ATLAS
 2608 exclusion, which used different models for interpretation, but placed a
 2609 lower limit on $m(\tilde{g})$ at around 900 GeV for similar $m(\tilde{\chi}_2^0)$.

2610

Part V

2611

CONCLUSIONS

2612

2613

2614 CONCLUSIONS AND OUTLOOK

2615 After a series of moderate excesses observed by the ATLAS experiment
 2616 in events with a Z boson, jets, and E_T^{miss} , this analysis performed on 14.7
 2617 fb^{-1} of 13 TeV data sees excellent agreement between observations and
 2618 the background expectation. The resulting exclusion pushes the gluino
 2619 mass lower limit beyond 1 TeV, putting further constraints on possible
 2620 [SUSY](#) models. Along with the many other searches for [SUSY](#), this exclusion
 2621 limits the phase space available for natural [SUSY](#) models. However, [SUSY](#) is
 2622 adaptable; new theories stretching those bounds are continually proposed
 2623 as tighter experimental constraints are set, and there are always small gaps
 2624 in the exclusions where sparticles could hide.

2625 ATLAS's dataset for 2016 includes 36 fb^{-1} , more than twice the lumi-
 2626 nosity included in this search. Because no excess was seen in this analysis,
 2627 the next search in this channel will be able to re-optimize its signal re-
 2628 gions for this larger dataset. In fact, because the signal region has been
 2629 frozen since the 8 TeV search, this analysis's signal region hasn't ever been
 2630 re-optimized for the increased energy of the [LHC](#)'s collisions. A new sig-
 2631 nal region that increases E_T^{miss} and H_T requirements will allow for better
 2632 sensitivity to [SUSY](#) processes.

2633 In addition, the current signal region, in which 60 events were observed
 2634 with 14.7 fb^{-1} , will be populated enough to be subdivided based on event
 2635 features. The current search is agnostic to the number of b -jets in the event,
 2636 for example, but there are now enough events to separate this signal region
 2637 into complementary b -tagged and b -vetoed regions, allowing analyzers to
 2638 independently target models which produce b -jets and those that don't,
 2639 and in the latter case, to dramatically reduce the $t\bar{t}$ background. Signal
 2640 regions can also be binned in other model-dependent features, like number
 2641 of jets, and the E_T^{miss} and H_T requirements can be increased independently,
 2642 targeting different event topologies.

2643 The [LHC](#) will continue to run through 2018 with a possible increase to
 2644 $\sqrt{s} = 14 \text{ TeV}$, and will shut down for upgrades until 2021. Three more
 2645 years of data-taking at 14 TeV will follow, with approximately twice the
 2646 current luminosity, referred to as Run 3. After that, the [LHC](#) will shut down
 2647 again to prepare for the High Luminosity Large Hadron Collider ([HL-LHC](#)),
 2648 which will begin data-taking in 2026 at a luminosity approximately five
 2649 times the current rate. This run will result in roughly 3000 fb^{-1} , which
 2650 will allow for dramatically better sensitivity in [SUSY](#) searches. An example
 2651 can be seen in [Figure 94](#), which shows the potential exclusions on a simple
 2652 gluino pair-production model with decays via squarks to a [LSP](#), for the
 2653 approximate luminosities of Run 3 and the [HL-LHC](#).

2654 Searches like this one will surely be repeated with higher and higher
 2655 luminosities, the analyses increasing both in sensitivity and in complexity.

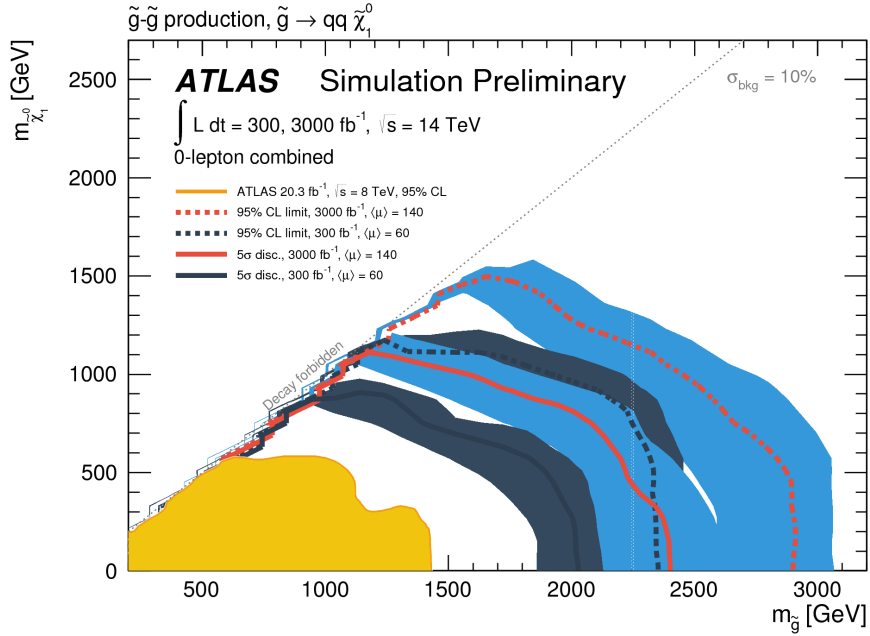


Figure 94: Expected 95% CL exclusion contours (dashed) and 5 σ discovery contours (solid) for $L_{int} = 300^{-1}$ (black) and 3000^{-1} (red) for gluino pair-production, with 1σ bands representing the uncertainty on the production cross-section. Superimposed is the observed 8 TeV exclusion for similar models. [105]

2656 Whether or not they uncover any hints of physics beyond the Standard
 2657 Model remains to be seen.

BIBLIOGRAPHY

- [1] ATLAS Collaboration. “Search for supersymmetry in events containing a same-flavour opposite-sign dilepton pair, jets, and large missing transverse momentum in $\sqrt{s} = 8$ TeV pp collisions with the ATLAS detector.” In: *Eur. Phys. J. C* 75 (2015), p. 318. doi: [10.1140/epjc/s10052-015-3518-2](https://doi.org/10.1140/epjc/s10052-015-3518-2). arXiv: [1503.03290 \[hep-ex\]](https://arxiv.org/abs/1503.03290).
- [2] ATLAS Collaboration. *A search for supersymmetry in events containing a leptonically decaying Z boson, jets and missing transverse momentum in $\sqrt{s} = 13$ TeV pp collisions with the ATLAS detector.* ATLAS-CONF-2015-082. 2015. URL: <http://cdsweb.cern.ch/record/2114854>.
- [3] C. P. Burgess and G. D. Moore. *The standard model: A primer.* Cambridge University Press, 2006. ISBN: 9780511254857, 9781107404267, 9780521860369.
- [4] S. L. Glashow. “Partial Symmetries of Weak Interactions.” In: *Nucl. Phys.* 22 (1961), pp. 579–588. doi: [10.1016/0029-5582\(61\)90469-2](https://doi.org/10.1016/0029-5582(61)90469-2).
- [5] Abdus Salam. “Renormalizability of Gauge Theories.” In: *Phys. Rev.* 127 (1 1962), pp. 331–334. doi: [10.1103/PhysRev.127.331](https://doi.org/10.1103/PhysRev.127.331). URL: <http://link.aps.org/doi/10.1103/PhysRev.127.331>.
- [6] Steven Weinberg. “A Model of Leptons.” In: *Phys. Rev. Lett.* 19 (21 1967), pp. 1264–1266. doi: [10.1103/PhysRevLett.19.1264](https://doi.org/10.1103/PhysRevLett.19.1264). URL: <http://link.aps.org/doi/10.1103/PhysRevLett.19.1264>.
- [7] D. Galbraith. *The Standard Model of the Standard Model.* 1997. URL: <http://davidgalbraith.org/portfolio/ux-standard-model-of-the-standard-model/>.
- [8] David J Griffiths. *Introduction to elementary particles; 2nd rev. version.* Physics textbook. New York, NY: Wiley, 2008. URL: <https://cds.cern.ch/record/111880>.
- [9] P. Hut and K. A. Olive. “A cosmological upper limit on the mass of heavy neutrinos.” In: *Physics Letters B* 87 (Oct. 1979), pp. 144–146. doi: [10.1016/0370-2693\(79\)90039-X](https://doi.org/10.1016/0370-2693(79)90039-X).
- [10] Huang, Qing-Guo, Wang, Ke, and Wang, Sai. “Constraints on the neutrino mass and mass hierarchy from cosmological observations.” In: *Eur. Phys. J. C* 76.9 (2016), p. 489. doi: [10.1140/epjc/s10052-016-4334-z](https://doi.org/10.1140/epjc/s10052-016-4334-z). URL: <http://dx.doi.org/10.1140/epjc/s10052-016-4334-z>.
- [11] The MEG Collaboration. “Search for the Lepton Flavour Violating Decay $\mu^+ \rightarrow e^+ \gamma$ with the Full Dataset of the MEG Experiment.” In: (2016). eprint: [arXiv:1605.05081](https://arxiv.org/abs/1605.05081).
- [12] LHCb collaboration. “Observation of $J/\Psi p$ resonances consistent with pentaquark states in $\Lambda_b^0 \rightarrow J/\Psi K^- p$ decays.” In: (2015). doi: [10.1103/PhysRevLett.115.072001](https://doi.org/10.1103/PhysRevLett.115.072001). eprint: [arXiv:1507.03414](https://arxiv.org/abs/1507.03414).

- [13] K. A. Olive et al. “Review of Particle Physics.” In: *Chin. Phys. C* 38 (2014), p. 090001. doi: [10.1088/1674-1137/38/9/090001](https://doi.org/10.1088/1674-1137/38/9/090001).
- [14] Johan Messchendorp. “Physics with Charmonium – A few recent highlights of BESIII.” In: *PoS Bormio2013* (2013), p. 043. arXiv: [1306.6611 \[hep-ex\]](https://arxiv.org/abs/1306.6611).
- [15] A. D. Martin, W. J. Stirling, R. S. Thorne, and G. Watt. “Parton distributions for the LHC.” In: (2009). doi: [10.1140/epjc/s10052-009-1072-5](https://doi.org/10.1140/epjc/s10052-009-1072-5). eprint: [arXiv:0901.0002](https://arxiv.org/abs/0901.0002).
- [16] W.J. Stirling. *proton-(anti)proton cross sections*. 2013. URL: <http://www.hep.ph.ic.ac.uk/~wstirlin/plots/plots.html>.
- [17] F. Zwicky. “Die Rotverschiebung von extragalaktischen Nebeln.” In: *Helvetica Physica Acta* 6 (1933), 110–127.
- [18] Douglas Clowe, Marusa Bradac, Anthony H. Gonzalez, Maxim Markevitch, Scott W. Randall, Christine Jones, and Dennis Zaritsky. “A direct empirical proof of the existence of dark matter.” In: (2006). doi: [10.1086/508162](https://doi.org/10.1086/508162). eprint: [arXiv:astro-ph/0608407](https://arxiv.org/abs/astro-ph/0608407).
- [19] G. Hinshaw et al. “Five-Year Wilkinson Microwave Anisotropy Probe (WMAP) Observations: Data Processing, Sky Maps, and Basic Results.” In: (2008). doi: [10.1088/0067-0049/180/2/225](https://doi.org/10.1088/0067-0049/180/2/225). eprint: [arXiv:0803.0732](https://arxiv.org/abs/0803.0732).
- [20] T. S. van Albada, J. N. Bahcall, K. Begeman, and R. Sancisi. “Distribution of dark matter in the spiral galaxy NGC 3198.” In: *The Astrophysical Journal* 295 (Aug. 1985), pp. 305–313. doi: [10.1086/163375](https://doi.org/10.1086/163375).
- [21] M. Gell-Mann. *THE EIGHTFOLD WAY: A THEORY OF STRONG INTERACTION SYMMETRY*. 1961. doi: [10.2172/4008239](https://doi.org/10.2172/4008239). URL: <http://www.osti.gov/scitech/servlets/purl/4008239>.
- [22] J. Wess and B. Zumino. “Supergauge transformations in four dimensions.” In: *Nuclear Physics B* 70.1 (1974), pp. 39–50. ISSN: 0550-3213. doi: [http://dx.doi.org/10.1016/0550-3213\(74\)90355-1](http://dx.doi.org/10.1016/0550-3213(74)90355-1). URL: <http://www.sciencedirect.com/science/article/pii/0550321374903551>.
- [23] J.-L. Gervais and B. Sakita. “Field theory interpretation of supergauges in dual models.” In: *Nuclear Physics B* 34 (1971), pp. 632–639. doi: [10.1016/0550-3213\(71\)90351-8](https://doi.org/10.1016/0550-3213(71)90351-8).
- [24] P. Ramond. “Dual Theory for Free Fermions.” In: *Physical Review D* 3 (1971), pp. 2415–2418. doi: [10.1103/PhysRevD.3.2415](https://doi.org/10.1103/PhysRevD.3.2415).
- [25] Stephen P. Martin. “A Supersymmetry primer.” In: (1997). [Adv. Ser. Direct. High Energy Phys. 18, 1 (1998)]. doi: [10.1142/9789812839657_0001](https://doi.org/10.1142/9789812839657_0001), [10.1142/9789814307505_0001](https://doi.org/10.1142/9789814307505_0001). arXiv: [hep-ph/9709356 \[hep-ph\]](https://arxiv.org/abs/hep-ph/9709356).
- [26] Craig J Copi, David N. Schramm, and Michael S. Turner. “Big-Bang Nucleosynthesis and the Baryon Density of the Universe.” In: (1994). doi: [10.1126/science.7809624](https://doi.org/10.1126/science.7809624). eprint: [arXiv:astro-ph/9407006](https://arxiv.org/abs/astro-ph/9407006).

- [27] NobelPrize.org. *The Nobel Prize in Physics 2004 - Popular Information*. 2016. URL: https://www.nobelprize.org/nobel_prizes/physics/laureates/2004/popular.html.
- [28] ATLAS Collaboration. “Dark matter interpretations of ATLAS searches for the electroweak production of supersymmetric particles in $\sqrt{s} = 8$ TeV proton-proton collisions.” In: (2016). doi: [10.1007/JHEP09\(2016\)175](https://doi.org/10.1007/JHEP09(2016)175). eprint: [arXiv:1608.00872](https://arxiv.org/abs/1608.00872).
- [29] The ATLAS collaboration. “Further searches for squarks and gluinos in final states with jets and missing transverse momentum at $\sqrt{s} = 13$ TeV with the ATLAS detector.” In: (2016).
- [30] W. Beenakker, S. Brensing, M. Krämer, A. Kulesza, E. Laenen, L. Motyka, and I. Niessen. “Squark and gluino hadroproduction.” In: (2011). doi: [10.1142/S0217751X11053560](https://doi.org/10.1142/S0217751X11053560). eprint: [arXiv:1105.1110](https://arxiv.org/abs/1105.1110).
- [31] ATLAS Collaboration. *ATLAS SUSY Searches - 95% CL Lower Limits*. <https://atlas.web.cern.ch/Atlas/GROUPS/PHYSICS/CombinedSummaryPlots/SUSY/ATLASsl> 2016.
- [32] Wim Beenakker, Christoph Borschensky, Michael Krämer, Anna Kulesza, and Eric Laenen. *NNLL-fast: predictions for coloured supersymmetric particle production at the LHC with threshold and Coulomb resummation*. 2016. eprint: [arXiv:1607.07741](https://arxiv.org/abs/1607.07741).
- [33] CMS Collaboration. “Search for physics beyond the standard model in events with a Z boson, jets, and missing transverse energy in pp collisions at $\sqrt{s} = 7$ TeV.” In: *Phys. Lett. B* 716 (2012), pp. 260–284. doi: [10.1016/j.physletb.2012.08.026](https://doi.org/10.1016/j.physletb.2012.08.026). arXiv: [1204.3774 \[hep-ex\]](https://arxiv.org/abs/1204.3774).
- [34] CMS Collaboration. “Search for physics beyond the standard model in events with two leptons, jets, and missing transverse momentum in pp collisions at $\sqrt{s} = 8$ TeV.” In: *JHEP* 04 (2015), p. 124. doi: [10.1007/JHEP04\(2015\)124](https://doi.org/10.1007/JHEP04(2015)124). arXiv: [1502.06031 \[hep-ex\]](https://arxiv.org/abs/1502.06031).
- [35] *Search for new physics in final states with two opposite-sign same-flavor leptons, jets and missing transverse momentum in pp collisions at sqrt(s)=13 TeV*. Tech. rep. CMS-PAS-SUS-15-011. Geneva: CERN, 2015. URL: <https://cds.cern.ch/record/2114811>.
- [36] Richard D. Ball et al. “Parton distributions with LHC data.” In: *Nucl. Phys.* B867 (2013), pp. 244–289. doi: [10.1016/j.nuclphysb.2012.10.003](https://doi.org/10.1016/j.nuclphysb.2012.10.003). arXiv: [1207.1303 \[hep-ph\]](https://arxiv.org/abs/1207.1303).
- [37] Hung-Liang Lai et al. “New parton distributions for collider physics.” In: *Phys. Rev. D* 82 (2010), p. 074024. doi: [10.1103/PhysRevD.82.074024](https://doi.org/10.1103/PhysRevD.82.074024). arXiv: [1007.2241 \[hep-ph\]](https://arxiv.org/abs/1007.2241).
- [38] J. Alwall, R. Frederix, S. Frixione, V. Hirschi, F. Maltoni, O. Matelaer, H. S. Shao, T. Stelzer, P. Torrielli, and M. Zaro. “The automated computation of tree-level and next-to-leading order differential cross sections, and their matching to parton shower simula-

- tions.” In: *JHEP* 07 (2014), p. 079. doi: [10.1007/JHEP07\(2014\)079](https://doi.org/10.1007/JHEP07(2014)079). arXiv: [1405.0301 \[hep-ph\]](https://arxiv.org/abs/1405.0301).
- [39] P. Nason. “A new method for combining NLO QCD with shower Monte Carlo algorithms.” In: *JHEP* 0411 (2004), p. 040. arXiv: [hep-ph/0409146 \[hep-ph\]](https://arxiv.org/abs/hep-ph/0409146).
- [40] S. Frixione, P. Nason, and C. Oleari. “Matching NLO QCD computations with parton shower simulations: the POWHEG method.” In: *JHEP* 0711 (2007), p. 070. arXiv: [0709.2092 \[hep-ph\]](https://arxiv.org/abs/0709.2092).
- [41] S. Alioli, P. Nason, C. Oleari, and E. Re. “A general framework for implementing NLO calculations in shower Monte Carlo programs: the POWHEG BOX.” In: *JHEP* 1006 (2010), p. 043. arXiv: [1002.2581 \[hep-ph\]](https://arxiv.org/abs/1002.2581).
- [42] T. Gleisberg et al. “Event generation with Sherpa 1.1.” In: *JHEP* 0902 (2009), p. 007. arXiv: [0811.4622 \[hep-ph\]](https://arxiv.org/abs/0811.4622).
- [43] T. Sjöstrand, S. Mrenna, and P. Skands. “PYTHIA 6.4 Physics and Manual.” In: *JHEP* 0605 (2006), p. 026. doi: [10.1088/1126-6708/2006/05/026](https://doi.org/10.1088/1126-6708/2006/05/026). arXiv: [hep-ph/0603175 \[hep-ph\]](https://arxiv.org/abs/hep-ph/0603175).
- [44] S. Agostinelli et al. “GEANT4: A simulation toolkit.” In: *Nucl. Instrum. Meth. A* 506 (2003), pp. 250–303. doi: [10.1016/S0168-9002\(03\)01368-8](https://doi.org/10.1016/S0168-9002(03)01368-8).
- [45] Morad Aaboud et al. “A measurement of material in the ATLAS tracker using secondary hadronic interactions in 7 TeV pp collisions.” In: (2016). arXiv: [1609.04305 \[hep-ex\]](https://arxiv.org/abs/1609.04305).
- [46] Lyndon Evans and Philip Bryant. “LHC Machine.” In: *Journal of Instrumentation* 3.08 (2008), So8001. URL: <http://stacks.iop.org/1748-0221/3/i=08/a=S08001>.
- [47] *LEP design report*. Copies shelved as reports in LEP, PS and SPS libraries. Geneva: CERN, 1984. URL: <https://cds.cern.ch/record/102083>.
- [48] ATLAS Collaboration. “The ATLAS Experiment at the CERN Large Hadron Collider.” In: *JINST* 3 (2008), So8003. doi: [10.1088/1748-0221/3/08/S08003](https://doi.org/10.1088/1748-0221/3/08/S08003).
- [49] The CMS Collaboration. “The CMS experiment at the CERN LHC.” In: *Journal of Instrumentation* 3.08 (2008), So8004. URL: <http://stacks.iop.org/1748-0221/3/i=08/a=S08004>.
- [50] The LHCb Collaboration. “The LHCb Detector at the LHC.” In: *Journal of Instrumentation* 3.08 (2008), So8005. URL: <http://stacks.iop.org/1748-0221/3/i=08/a=S08005>.
- [51] The ALICE Collaboration. “The ALICE experiment at the CERN LHC.” In: *Journal of Instrumentation* 3.08 (2008), So8002. URL: <http://stacks.iop.org/1748-0221/3/i=08/a=S08002>.
- [52] ATLAS Collaboration. *2015 start-up trigger menu and initial performance assessment of the ATLAS trigger using Run-2 data*. ATL-DAQ-PUB-2016-001. 2016. URL: [http://cds.cern.ch/record/2136007](https://cds.cern.ch/record/2136007).

- [53] “Electron performance measurements with the ATLAS detector using the 2010 LHC proton-proton collision data.” In: *Eur. Phys. J. C* 72 (2012), p. 1909. doi: [10.1140/epjc/s10052-012-1909-1](https://doi.org/10.1140/epjc/s10052-012-1909-1). arXiv: [1110.3174 \[hep-ex\]](https://arxiv.org/abs/1110.3174).
- [54] *Electron efficiency measurements with the ATLAS detector using the 2015 LHC proton-proton collision data.* Tech. rep. ATLAS-CONF-2016-024. Geneva: CERN, 2016. URL: <http://cds.cern.ch/record/2157687>.
- [55] ATLAS Collaboration. *Measurement of the photon identification efficiencies with the ATLAS detector using LHC Run-1 data.* 2016. eprint: [arXiv:1606.01813](https://arxiv.org/abs/1606.01813).
- [56] *Photon identification in 2015 ATLAS data.* Tech. rep. ATL-PHYS-PUB-2016-014. Geneva: CERN, 2016. URL: <https://cds.cern.ch/record/2203125>.
- [57] *Photon Identification Efficiencies using 2016 Data with radiative Z boson decays.* Tech. rep. EGAM-2016-003. Geneva: CERN, 2016. URL: <https://atlas.web.cern.ch/Atlas/GROUPS/PHYSICS/PLLOTS/EGAM-2016-003/index.html>.
- [58] *Official Isolation Working Points.* Geneva, 2016. URL: <https://twiki.cern.ch/twiki/bin/view/AtlasProtected/IsolationSelectionTool#Photons>.
- [59] ATLAS Collaboration. “Muon reconstruction performance of the ATLAS detector in proton–proton collision data at $\sqrt{s}=13$ TeV.” In: (2016). doi: [10.1140/epjc/s10052-016-4120-y](https://doi.org/10.1140/epjc/s10052-016-4120-y). eprint: [arXiv:1603.05598](https://arxiv.org/abs/1603.05598).
- [60] Matteo Cacciari, Gavin P. Salam, and Gregory Soyez. “The Anti-k(t) jet clustering algorithm.” In: *JHEP* 0804 (2008), p. 063. doi: [10.1088/1126-6708/2008/04/063](https://doi.org/10.1088/1126-6708/2008/04/063). arXiv: [0802.1189 \[hep-ph\]](https://arxiv.org/abs/0802.1189).
- [61] ATLAS Collaboration. *Jet Calibration and Systematic Uncertainties for Jets Reconstructed in the ATLAS Detector at $\sqrt{s} = 13$ TeV.* ATL-PHYS-PUB-2015-015. 2015. URL: <http://cds.cern.ch/record/2037613>.
- [62] ATLAS Collaboration. *Tagging and suppression of pileup jets with the ATLAS detector.* ATLAS-CONF-2014-018. 2014. URL: <http://cds.cern.ch/record/1700870>.
- [63] ATLAS Collaboration. *Expected performance of the ATLAS b-tagging in Run-2.* ATL-PHYS-PUB-2015-022. 2015. URL: <http://cdsweb.cern.ch/record/2037697>.
- [64] ATLAS Collaboration. *Expected performance of missing transverse momentum reconstruction for the ATLAS detector at $\sqrt{s} = 13$ TeV.* ATL-PHYS-PUB-2015-023. 2015. URL: <http://cds.cern.ch/record/2037700>.
- [65] ATLAS Collaboration. *Performance of missing transverse momentum reconstruction for the ATLAS detector in the first proton-proton collisions at $\sqrt{s} = 13$ TeV.* ATL-PHYS-PUB-2015-027. 2015. URL: <http://cds.cern.ch/record/2037904>.

- [66] ATLAS Collaboration. “A neural network clustering algorithm for the ATLAS silicon pixel detector.” In: *JINST* 9 (2014), P09009. doi: [10.1088/1748-0221/9/09/P09009](https://doi.org/10.1088/1748-0221/9/09/P09009). arXiv: [1406.7690 \[hep-ex\]](https://arxiv.org/abs/1406.7690).
- [67] Luke de Oliveira. *AGILEPack: Algorithms for Generalized Inference, Learning, and Extraction*. 2016. URL: <http://lukedeo.github.io/AGILEPack/>.
- [68] ATLAS Collaboration. *Measurement of performance of the pixel neural network clustering algorithm of the ATLAS experiment at $\sqrt{s} = 13$ TeV*. ATL-PHYS-PUB-2015-044. 2015. URL: <http://cdsweb.cern.ch/record/2054921>.
- [69] ATLAS Collaboration. *Robustness of the Artificial Neural Network Clustering Algorithm of the ATLAS experiment*. ATL-PHYS-PUB-2015-052. 2015. URL: <http://cdsweb.cern.ch/record/2116350>.
- [70] ATLAS Collaboration. *Modelling of the $t\bar{t}H$ and $t\bar{t}V$ ($V = W, Z$) processes for $\sqrt{s} = 13$ TeV ATLAS analyses*. ATL-PHYS-PUB-2016-005. 2016. URL: <http://cds.cern.ch/record/2120826>.
- [71] M. V. Garzelli, A. Kardos, C. G. Papadopoulos, and Z. Trocsanyi. “ $t\bar{t}W^{+-}$ and $t\bar{t}Z$ Hadroproduction at NLO accuracy in QCD with Parton Shower and Hadronization effects.” In: *JHEP* 11 (2012), p. 056. doi: [10.1007/JHEP11\(2012\)056](https://doi.org/10.1007/JHEP11(2012)056). arXiv: [1208.2665 \[hep-ph\]](https://arxiv.org/abs/1208.2665).
- [72] J. M. Campbell and R. K. Ellis. “ $t\bar{t}W$ production and decay at NLO.” In: *JHEP* 1207 (2012), p. 052. arXiv: [1204.5678 \[hep-ph\]](https://arxiv.org/abs/1204.5678).
- [73] A. Lazopoulos, T. McElmurry, K. Melnikov, and F. Petriello. “Next-to-leading order QCD corrections to $t\bar{t}Z$ production at the LHC.” In: *Phys. Lett. B* 666 (2008), p. 62. arXiv: [0804.2220 \[hep-ph\]](https://arxiv.org/abs/0804.2220).
- [74] ATLAS Collaboration. *Simulation of top quark production for the ATLAS experiment at $\sqrt{s} = 13$ TeV*. ATL-PHYS-PUB-2016-004. 2016. URL: <http://cds.cern.ch/record/2120417>.
- [75] M. Czakon, P. Fiedler, and A. Mitov. “Total Top-Quark Pair-Production Cross Section at Hadron Colliders Through $O(\alpha_s^4)$.” In: *Phys. Rev. Lett.* 110 (2013), p. 252004. arXiv: [1303.6254 \[hep-ph\]](https://arxiv.org/abs/1303.6254).
- [76] M. Czakon and A. Mitov. “Top++: A Program for the Calculation of the Top-Pair Cross-Section at Hadron Colliders.” In: *Comput. Phys. Commun.* 185 (2014), p. 2930. doi: [10.1016/j.cpc.2014.06.021](https://doi.org/10.1016/j.cpc.2014.06.021). arXiv: [1112.5675 \[hep-ph\]](https://arxiv.org/abs/1112.5675).
- [77] N. Kidonakis. “Two-loop soft anomalous dimensions for single top quark associated production with a W^- or H^- .” In: *Phys. Rev. D* 82 (2010), p. 054018. doi: [10.1103/PhysRevD.82.054018](https://doi.org/10.1103/PhysRevD.82.054018). arXiv: [1005.4451 \[hep-ph\]](https://arxiv.org/abs/1005.4451).
- [78] ATLAS Collaboration. *Multi-Boson Simulation for 13 TeV ATLAS Analyses*. ATL-PHYS-PUB-2016-002. 2016. URL: <http://cds.cern.ch/record/2119986>.

- [79] J. M. Campbell and R. K. Ellis. “An update on vector boson pair production at hadron colliders.” In: *Phys. Rev. D* 60 (1999), p. 113006. arXiv: [hep-ph/9905386 \[hep-ph\]](#).
- [80] J. M. Campbell, R. K. Ellis, and C. Williams. “Vector boson pair production at the LHC.” In: *JHEP* 1107 (2011), p. 018. arXiv: [1105.0020 \[hep-ph\]](#).
- [81] ATLAS Collaboration. *Monte Carlo Generators for the Production of a W or Z/ γ^* Boson in Association with Jets at ATLAS in Run 2*. ATL-PHYS-PUB-2016-003. 2016. URL: <http://cds.cern.ch/record/2120133>.
- [82] S. Catani, L. Cieri, G. Ferrera, D. de Florian, and M. Grazzini. “Vector boson production at hadron colliders: a fully exclusive QCD calculation at NNLO.” In: *Phys. Rev. Lett.* 103 (2009), p. 082001. arXiv: [0903.2120 \[hep-ph\]](#).
- [83] S. Catani and M. Grazzini. “An NNLO subtraction formalism in hadron collisions and its application to Higgs boson production at the LHC.” In: *Phys. Rev. Lett.* 98 (2007), p. 222002. arXiv: [hep-ph/0703012 \[hep-ph\]](#).
- [84] ATLAS Collaboration. *Electron efficiency measurements with the ATLAS detector using the 2012 LHC proton–proton collision data*. ATLAS-CONF-2014-032. 2014. URL: <http://cdsweb.cern.ch/record/1706245>.
- [85] ATLAS Collaboration. “Muon reconstruction performance of the ATLAS detector in proton–proton collision data at $\sqrt{s} = 13$ TeV.” In: *Eur. Phys. J. C* 76 (2016), p. 292. DOI: [10.1140/epjc/s10052-016-4120-y](https://doi.org/10.1140/epjc/s10052-016-4120-y). arXiv: [1603.05598 \[hep-ex\]](#).
- [86] ATLAS Collaboration. *Search for supersymmetry in final states with jets, missing transverse momentum and a Z boson at $\sqrt{s} = 8$ TeV with the ATLAS detector*. ATLAS-CONF-2012-152. 2012. URL: <http://cds.cern.ch/record/1493491>.
- [87] ATLAS Collaboration. “Measurement of the differential cross-section of highly boosted top quarks as a function of their transverse momentum in $\sqrt{s} = 8$ TeV proton-proton collisions using the ATLAS detector.” In: *Phys. Rev. D* 93.3 (2016), p. 032009. DOI: [10.1103/PhysRevD.93.032009](https://doi.org/10.1103/PhysRevD.93.032009). arXiv: [1510.03818 \[hep-ex\]](#).
- [88] CMS Collaboration. “Measurement of the integrated and differential t-tbar production cross sections for high-pt top quarks in pp collisions at $\sqrt{s} = 8$ TeV.” In: *Phys. Rev. D* (2016). Submitted. arXiv: [1605.00116 \[hep-ex\]](#).
- [89] ATLAS Collaboration. *Search for physics beyond the Standard Model in events with a Z boson and large missing transverse momentum using $\sqrt{s} = 7$ TeV pp collisions from the LHC with the ATLAS detector*. ATLAS-CONF-2012-046. 2012. URL: <http://cdsweb.cern.ch/record/1448222>.

- [90] ATLAS Collaboration. “Search for squarks and gluinos in events with isolated leptons, jets and missing transverse momentum at $\sqrt{s} = 8$ TeV with the ATLAS detector.” In: *JHEP* 1504 (2015), p. 116. doi: [10.1007/JHEP04\(2015\)116](https://doi.org/10.1007/JHEP04(2015)116). arXiv: [1501.03555 \[hep-ex\]](https://arxiv.org/abs/1501.03555).
- [91] ATLAS Collaboration. “Improved luminosity determination in pp collisions at $\sqrt{s} = 7$ TeV using the ATLAS detector at the LHC.” In: *Eur. Phys. J. C* 73 (2013), p. 2518. doi: [10.1140/epjc/s10052-013-2518-3](https://doi.org/10.1140/epjc/s10052-013-2518-3). arXiv: [1302.4393 \[hep-ex\]](https://arxiv.org/abs/1302.4393).
- [92] ATLAS Collaboration. “Luminosity determination in pp collisions at $\sqrt{s} = 8$ TeV using the ATLAS detector at the LHC.” In: *to be submitted to Eur. Phys. J. C* ().
- [93] Michael Kramer et al. *Supersymmetry production cross sections in pp collisions at $\sqrt{s} = 7$ TeV*. 2012. arXiv: [1206.2892 \[hep-ph\]](https://arxiv.org/abs/1206.2892).
- [94] W. Beenakker, R. Höpker, M. Spira, and P.M. Zerwas. “Squark and gluino production at hadron colliders.” In: *Nucl. Phys. B* 492 (1997), pp. 51–103. doi: [10.1016/S0550-3213\(97\)00084-9](https://doi.org/10.1016/S0550-3213(97)00084-9). arXiv: [hep-ph/9610490 \[hep-ph\]](https://arxiv.org/abs/hep-ph/9610490).
- [95] A. Kulesza and L. Motyka. “Threshold resummation for squark-antisquark and gluino-pair production at the LHC.” In: *Phys. Rev. Lett.* 102 (2009), p. 111802. doi: [10.1103/PhysRevLett.102.111802](https://doi.org/10.1103/PhysRevLett.102.111802). arXiv: [0807.2405 \[hep-ph\]](https://arxiv.org/abs/0807.2405).
- [96] A. Kulesza and L. Motyka. “Soft gluon resummation for the production of gluino-gluino and squark-antisquark pairs at the LHC.” In: *Phys. Rev. D* 80 (2009), p. 095004. doi: [10.1103/PhysRevD.80.095004](https://doi.org/10.1103/PhysRevD.80.095004). arXiv: [0905.4749 \[hep-ph\]](https://arxiv.org/abs/0905.4749).
- [97] W. Beenakker et al. “Soft-gluon resummation for squark and gluino hadroproduction.” In: *JHEP* 0912 (2009), p. 041. doi: [10.1088/1126-6708/2009/12/041](https://doi.org/10.1088/1126-6708/2009/12/041). arXiv: [0909.4418 \[hep-ph\]](https://arxiv.org/abs/0909.4418).
- [98] W. Beenakker et al. “Squark and gluino hadroproduction.” In: *Int. J. Mod. Phys. A* 26 (2011), pp. 2637–2664. doi: [10.1142/S0217751X11053560](https://doi.org/10.1142/S0217751X11053560). arXiv: [1105.1110 \[hep-ph\]](https://arxiv.org/abs/1105.1110).
- [99] M. Baak et al. “HistFitter software framework for statistical data analysis.” In: *Eur. Phys. J. C* 75 (2014), p. 153. doi: [10.1140/epjc/s10052-015-3327-7](https://doi.org/10.1140/epjc/s10052-015-3327-7). arXiv: [1410.1280 \[hep-ex\]](https://arxiv.org/abs/1410.1280).
- [100] Rene Brun and Fons Rademakers. “ROOT — An object oriented data analysis framework.” In: *Nuclear Instruments and Methods in Physics Research Section A: Accelerators, Spectrometers, Detectors and Associated Equipment* 389.1 (1997), pp. 81 –86. issn: 0168-9002. doi: [http://dx.doi.org/10.1016/S0168-9002\(97\)00048-X](http://dx.doi.org/10.1016/S0168-9002(97)00048-X). URL: <http://www.sciencedirect.com/science/article/pii/S016890029700048X>.
- [101] Lorenzo Moneta, Kevin Belasco, Kyle Cranmer, Sven Kreiss, Alfonso Lazzaro, Danilo Piparo, Gregory Schott, Wouter Verkerke, and Matthias Wolf. *The RooStats Project*. 2010. eprint: [arXiv:1009.1003](https://arxiv.org/abs/1009.1003).

- [102] Kyle Cranmer, George Lewis, Lorenzo Moneta, Akira Shibata, and Wouter Verkerke. "HistFactory: A tool for creating statistical models for use with RooFit and RooStats." In: (2012).
- [103] Glen Cowan, Kyle Cranmer, Eilam Gross, and Ofer Vitells. "Asymptotic formulae for likelihood-based tests of new physics." In: *Eur. Phys. J. C* 71 (2011), p. 1554. DOI: [10.1140/epjc/s10052-011-1554-0](https://doi.org/10.1140/epjc/s10052-011-1554-0). arXiv: [1007.1727 \[physics.data-an\]](https://arxiv.org/abs/1007.1727).
- [104] A. Read. "Presentation of search results: the CLs technique." In: *Journal of Physics G: Nucl. Part. Phys.* 28 (2002), pp. 2693–2704. DOI: [10.1088/0954-3899/28/10/313](https://doi.org/10.1088/0954-3899/28/10/313).
- [105] *Prospects for a search for direct pair production of top squarks in scenarios with compressed mass spectra at the high luminosity LHC with the ATLAS Detector*. Tech. rep. ATL-PHYS-PUB-2016-022. Geneva: CERN, 2016. URL: <https://cds.cern.ch/record/2220904>.